BEILSTEIN JOURNAL OF NANOTECHNOLOGY

Electrocatalysis on the nm scale

Edited by R. Jürgen Behm

Imprint

Beilstein Journal of Nanotechnology
www.bjnano.org
ISSN 2190-4286
Email: journals-support@beilstein-institut.de

The *Beilstein Journal of Nanotechnology* is published by the Beilstein-Institut zur Förderung der Chemischen Wissenschaften.

Beilstein-Institut zur Förderung der Chemischen Wissenschaften
Trakehner Straße 7–9
60487 Frankfurt am Main
Germany
www.beilstein-institut.de

BEILSTEIN JOURNAL OF NANOTECHNOLOGY

Electrocatalysis on the nm scale

R. Jürgen Behm

Editorial

Open Access

Address:
Institute of Surface Chemistry and Catalysis, Ulm University, Albert-Einstein-Allee 47, D-89081 Ulm, Germany

Email:
R. Jürgen Behm - juergen.behm@uni-ulm.de

Keywords:
electrocatalysis

Beilstein J. Nanotechnol. **2015,** *6,* 1008–1009.
doi:10.3762/bjnano.6.103

Received: 31 March 2015
Accepted: 07 April 2015
Published: 21 April 2015

This article is part of the Thematic Series "Electrocatalysis on the nm scale".

Editor-in-Chief: T. Schimmel

The past two decades have seen a renewed and rapidly growing interest in the fields of electrochemistry and electrocatalysis. This is on the one hand stimulated by applications in energy conversion and energy storage, where highly efficient electrochemical/electrocatalytic processes are considered to be an indispensable part of modern energy concepts based on the use of renewable energy sources. However, it is also pushed by the rapid development of modern in situ spectroscopy and microscopy tools, such as in situ vibrational spectroscopy, in situ X-ray spectroscopy/diffraction, and in situ scanning probe microscopy, just to name a few, as well as the enormous progress that has been made in the theoretical description of processes occurring at the electrochemical solid–liquid interface. The experimental methods provide, at least in principle, the opportunity to gain insight into the processes occurring at the solid–electrolyte interface on an unprecedented, atomic/molecular level. The theory has not only developed to a stage where a reliable description of complex surface structures and surface processes (at the solid–gas interface) is possible based on first-principles electronic structure theory (in particular, (periodic) density functional theory (DFT)), but it is also increasingly developing new approaches for a more realistic modeling of the electrochemical solid–liquid interface from first principles. Although there is still a long way to go, it is not unrealistic to assume that an atomic/molecular scale understanding of the elementary processes occurring at the electrochemical interface (similar to that developed for the solid–gas interface) is within reach, given the rapid progress in both theory and experiment. Furthermore, the employment of modern strategies from nanotechnology for the systematic fabrication of optimized, nanostructured electrodes and electrocatalysts sets the stage and provides the means for a systematic, knowledge-based optimization of electrochemical and electrocatalytic processes. This is unprecedented in this discipline and will hopefully allow us to satisfy the expectations from the technology side.

These aspects are the topics of the present Thematic Series, “Electrocatalysis on the nm scale”. This work was initiated by and is largely based on a workshop organized by the Research Group, “Elementary Reaction Steps in Electrocatalysis: Theory meets Experiment”, which was held at Reisensburg Castle (close to Ulm, Germany) in 2013. As suggested by the name of the Research Group, the topics equally cover experiment and theory. They range from fundamental aspects of electrochemistry, such as anion adsorption [1] or potential induced restruc-

turing of the electrode surface [2], to the presentation of new theoretical concepts, the mechanistic understanding [3], and the theoretical description of important electrocatalytic reactions, such as hydrogen evolution/water splitting [4,5] or electrocatalytic ammonia synthesis [6]. Additionally, mechanistic studies of electrocatalytic reactions, such as O_2 reduction [7], CO oxidation [8] or the electrooxidation of small organic molecules [9], are presented. The potential of in situ microscopy [10] and in situ spectroscopy [8,9], in addition to electrochemical measurements for the characterization of electrode surfaces/electrocatalysts and for the mechanistic understanding of electrocatalytic reactions is illustrated. Finally, the systematic use of nanostructuring strategies is outlined, both for fundamental studies [8] and for the directed design of active and stable Pt/C fuel cell catalysts [11]. In summary, despite the limited number of contributions to this Thematic Series, it provides a broad perspective covering a variety of important topics in modern electrocatalysis research, with a clear focus on the nanoscale understanding of the relevant processes.

I would like to thank all authors for their excellent contributions, as well as the referees for their valuable and prompt reports. Special thanks go to the team at the Beilstein Journal of Nanotechnology for their continuous support in the handling of this series. Finally, I would like to acknowledge the Beilstein-Institut for its support of open access policies, allowing colleagues from all over the world to freely access the contributions in this journal, as well as the financial support from the Deutsche Forschungsgemeinschaft (FOR 1376) for the initiating workshop and for part of the work.

R. Jürgen Behm

Ulm, March 2015

References

1. Gossenberger, F.; Roman, T.; Forster-Tonigold, K.; Groß, A. *Beilstein J. Nanotechnol.* **2014,** *5,* 152–161. doi:10.3762/bjnano.5.15
2. Soliman, K. A.; Kolb, D. M.; Kibler, L. A.; Jacob, T. *Beilstein J. Nanotechnol.* **2014,** *5,* 1349–1356. doi:10.3762/bjnano.5.148
3. Schneider, W. B.; Auer, A. A. *Beilstein J. Nanotechnol.* **2014,** *5,* 668–676. doi:10.3762/bjnano.5.79
4. Quaino, P.; Juarez, F.; Santos, E.; Schmickler, W. *Beilstein J. Nanotechnol.* **2014,** *5,* 846–854. doi:10.3762/bjnano.5.96
5. Lindgren, M.; Panas, I. *Beilstein J. Nanotechnol.* **2014,** *5,* 195–201. doi:10.3762/bjnano.5.21
6. Howalt, J. G.; Vegge, T. *Beilstein J. Nanotechnol.* **2014,** *5,* 111–120. doi:10.3762/bjnano.5.11
7. Gómez-Marín, A. M.; Rizo, R.; Feliu, J. M. *Beilstein J. Nanotechnol.* **2013,** *4,* 956–967. doi:10.3762/bjnano.4.108
8. Brimaud, S.; Jusys, Z.; Behm, R. J. *Beilstein J. Nanotechnol.* **2014,** *5,* 735–746. doi:10.3762/bjnano.5.86
9. Jusys, Z.; Behm, R. J. *Beilstein J. Nanotechnol.* **2014,** *5,* 747–759. doi:10.3762/bjnano.5.87
10. Nebel, M.; Erichsen, T.; Schuhmann, W. *Beilstein J. Nanotechnol.* **2014,** *5,* 141–151. doi:10.3762/bjnano.5.14
11. Meier, J. C.; Galeano, C.; Katsounaros, I.; Witte, J.; Bongard, H. J.; Topalov, A. A.; Baldizzone, C.; Mezzavilla, S.; Schüth, F.; Mayrhofer, K. J. J. *Beilstein J. Nanotechnol.* **2014,** *5,* 44–67. doi:10.3762/bjnano.5.5

License and Terms

Beilstein Journal of Nanotechnology

Some reflections on the understanding of the oxygen reduction reaction at Pt(111)

Ana M. Gómez-Marín, Ruben Rizo and Juan M. Feliu*§

Full Research Paper

Open Access

Address:
Instituto de Electroquímica, Universidad de Alicante, Apt. 99, Alicante, E-03080, Spain

Email:
Juan M. Feliu* - juan.feliu@ua.es

* Corresponding author
§ Tel.: +34 965 909 301; Fax: +34 965 903 537

Keywords:
hydrogen peroxide oxidation; hydrogen peroxide reduction; oxygen reduction; Pt(111); stepped surfaces

Beilstein J. Nanotechnol. **2013,** *4,* 956–967.
doi:10.3762/bjnano.4.108

Received: 29 May 2013
Accepted: 13 December 2013
Published: 27 December 2013

This article is part of the Thematic Series "Electrocatalysis on the nm scale".

Guest Editor: R. J. Behm

Abstract

The oxygen reduction reaction (ORR) is a pivotal process in electrochemistry. Unfortunately, after decades of intensive research, a fundamental knowledge about its reaction mechanism is still lacking. In this paper, a global and critical view on the most important experimental and theoretical results regarding the ORR on Pt(111) and its vicinal surfaces, in both acidic and alkaline media, is taken. Phenomena such as the ORR surface structure sensitivity and the lack of a reduction current at high potentials are discussed in the light of the surface oxidation and disordering processes and the possible relevance of the hydrogen peroxide reduction and oxidation reactions in the ORR mechanism. The necessity to build precise and realistic reaction models, which are deducted from reliable experimental results that need to be carefully taken under strict working conditions is shown. Therefore, progress in the understanding of this important reaction on a molecular level, and the choice of the right approach for the design of the electrocatalysts for fuel-cell cathodes is only possible through a cooperative approach between theory and experiments.

Introduction

Nowadays, the oxygen reduction reaction (ORR) is arguably one of the most important challenges in electrocatalysis and it is undoubtedly the most important cathodic process in fuel cells. It is a complex 4-electron reaction that involves the breaking of a double bond and the formation of 4 OH-bonds through several elementary steps and intermediate species. A generally accepted, classical scheme for this reaction, in which hydrogen peroxide is a stable reaction intermediate species, can be depicted by Scheme 1 [1].

However, despite the intensive experimental and theoretical ORR research for decades, which ranges from studies on idealized model electrodes up to reaction studies in technical systems, up to now the exact ORR mechanism is not clearly known. This has different reasons. First, the currently available experimental techniques are not capable of detecting all possible reaction intermediates in a complex process such as the ORR. Second, the reaction takes place at high overpotentials and the activation region is quite limited to the onset of the

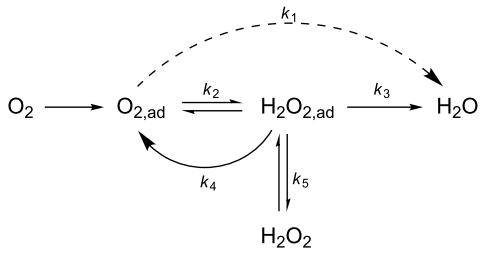

Scheme 1: Reaction pathways proposed for the ORR given by Wroblowa et al. [1].

wave. Thus, the transport-controlled region appears very soon, which limits the potential range, in which the electron transfer mechanism can really be studied. Therefore other approaches are needed that include theoretical calculations that could help to shed light on the microscopic structures and processes taking place at the surface during the reaction.

As starting point, quantum chemical models consider perfectly ideal materials. This means that, within the state of the art of the calculation, surfaces have no defects and atoms at the surface correspond to the truncation of an ideal single crystal. This is valid for the basal planes as well as for stepped or kinked surfaces. Therefore, the predictions should be compared to experiments that were performed on equally ideal electrode surfaces, e.g., single crystal electrodes. However, experimental surfaces always contain defects at the atomic level. Hence, theoretical calculation results can only be compared with samples that fulfill some quality criteria, usually inferred from comparison with stepped surfaces [2-9].

Additionally, in most of the catalysts, the ORR starts in a potential range, in which the surface is covered, at least partially, with some oxygenated species and, because the adsorption of oxygenated species may disturb the surface order [2-4], this limits the use of single crystal surfaces to understand the reaction mechanism on model surfaces. The latter aspect is especially important when comparing experimental data with theoretical calculations and creating idealized model mechanisms. Realistic model mechanisms are important because they would provide insights into the limiting steps, which could be further modified in order to enhance the overall activity of the reaction. Hence, it is essential that experiment and theory work together and assist each other to create a fundamental and strong basis about the knowledge of the reaction. It is worth to mention that, besides well-ordered monocrystals, non-contaminated working conditions, are necessary in order to get reliable data to compare and analyze against the ideal and perfect surfaces from simplified theoretical models [4,8-10]. Experimental work with non-ordered electrodes or slightly contaminated surfaces can lead to erroneous observations and conclusions.

In this presentation a critical view on the main recent experimental and theoretical findings about the ORR on Pt(111) and its vicinal stepped surfaces, in both acidic and alkaline media, is taken. The central idea is to find agreement and disagreement points that could serve to improve the current knowledge about the ORR surface reactivity. The motivation is the belief that only by building a common basis from theory and experiment we could progress in the understanding of this important reaction. The Pt(111) electrode was selected because this basal plane represents the most abundant facet on Pt nanoparticles, which are widely used as ORR catalyst in polymer electrolyte membrane fuel cells [11-13].

In addition, the role of the adsorbed oxygen-containing species and the possible relevance of the hydrogen peroxide oxidation and reduction reactions (HPORR) in the ORR mechanism are discussed. This is done specifically for high potentials, at which apparently there is no ORR current and the influence of the structure sensitivity of small particles appears [11,12,14]. This is relevant because only from a full understanding of the ORR kinetics it would be possible to unveil the identity of the rate determining step (RDS) on Pt, which would be an essential step toward an optimized design of new ORR electrocatalysts [15].

Results and Discussion

Ideally, the surface structure and composition of a catalyst remain unchanged over the whole potential range in which a probe reaction is scrutinized. However, as can be seen in Figure 1, this is not true in the case of Pt(111). At $E < 0.35$ V, hydrogen adsorption takes place, while at higher potentials, water can be considered the main species in contact with the surface. (In fact, water is always in contact with the surface regardless of the presence of adsorbates that arise from faradaic processes). In addition, if the electrode potential is increased beyond 0.6 V, the surface starts to be covered by oxygenated species. In this region, in acidic solutions the so called "butterfly" develops, which reflects the generation of PtOH, which is likely to happen in two steps [8,9]. In this case, the cyclic voltammetric profile (CV) shows a sort of passive region without significant current flow at higher potentials [6-8], until a well-defined peak starts to grow while an organized PtO adlayer is completed ($1.0 < E < 1.15$ V, Figure 1A [6-8]).

In the following we will mainly deal with acidic solutions, but we believe that the processes undergone in the butterfly and the following oxidation contributions are also likely to take place in alkaline solutions, although they have been studied less intensively (Figure 1B). Once the second oxidation is completed, the

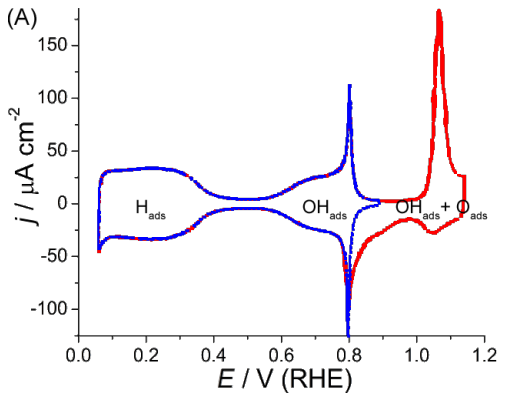

Figure 1: Stable voltammetric profile of a well-ordered Pt(111) electrode at 50 mV·s^{-1}, at two upper potential limits: 0.9 V (blue or black) and 1.15 V (red) in 0.1 M: A. $HClO_4$ (left). B. NaOH (right).

potential is close to 1.2 V and this is a strict upper potential limit (E_{up}) that ensures the surface order of the Pt(111) electrode. In this respect, a good Pt(111) blank voltammogram would have no contributions at 0.12 V nor at 0.27 V, the hydrogen adsorption energy on {110} and {100} step sites, respectively [2-5]. Besides, it would not show any current contribution in the transition region from Pt–OH to PtO in $HClO_4$ solutions [6-9] (Figure 1A) and negligible oxidation currents at potentials as high as 1.2 V in H_2SO_4 solution [2,3]. Even so, hydrogen adsorption has been proven to be less sensitive to the surface order than other probes, such as CO oxidation [10,16].

Surface order

After potential excursions higher than 1.2 V, the CV in the immediate negative potential sweep shows the presence of {110} and {100} defects in the initially featureless hydrogen adsorption region, as a result of a surface reordering after the oxygen adsorption with high coverage (Figure 2) [2,3]. In this respect, the surface is uniform from the topographic point of view between 1.20 V and the beginning of hydrogen evolution, but the surface composition changes in the potential scale.

The surface disordering kinetics has been widely studied [2-4,7] and the charge density data have been well approximated by a consecutive reaction mechanism that is slightly influenced by an autocatalytic step [2,3]. With this procedure, it was observed that the disordering kinetics on Pt(111) is faster than on Pt(20,20,19), a surface with a 40-atoms wide {111} terrace [2,3]. This was an unexpected result that takes into account the existence of the autocatalytic step in the mechanism and points out the differences in reactivity between ordered defects and randomly generated defects. The process was more conveniently studied in sulfuric acid because the peaks associated to the charge of the "disordering products" at 0.12 V and 0.27 V,

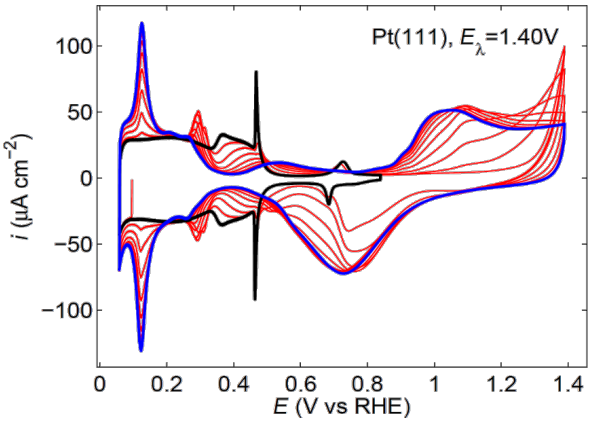

Figure 2: Evolution of the voltammetric profile of a Pt(111) electrode in 0.5 M H_2SO_4 as the electrode is cycled at 50 mV·s^{-1} between 0.06 and 1.4 V vs RHE. The black line shows the initial stable profile up to 0.85 V and the blue line the profile attained after 12 cycles (partially represented in red).

i.e., {110} and {100} defects respectively, are better defined in this media. Additionally, the decrease in the reactant domains can be easily followed by the decrease in the characteristic sulfate adsorption state at the {111} terraces [2,3].

With some limitations, the same procedure can be applied to non-adsorbing perchloric acid solutions, in which the adsorption peaks are broader, especially those corresponding to the {100} step defect [4]. In both cases, the surface disordering kinetics is faster as E_{up} increases, but the reordering rates are faster in perchloric acid than in sulfuric acid [2-4]. This result was expected and points out the effect of strongly adsorbed anions in the preservation of the metallic arrangement underneath. In contrast, when working with diluted solutions of sulfate anions (0.1 mM), it was remarked that the surface disor-

dering is faster than in pure perchloric acid [4]. This is likely due to perturbations in the water network by sulfate anions, which in turn make the surface more vulnerable to the effect of the potential in the formation of surface oxides and the subsequent reordering of the surface [4].

As it is pointed out above, models are idealized and thus state of the art experiments are required. In this respect the use of extremely clean solutions, under rotating disk electrode (RDE) experiments are necessary on well-ordered single crystal electrodes. Both Pt(111) spikes in perchloric acid (Figure 1A) and sulfuric acid (Figure 2) solutions should also be observed when the ORR is studied with the RDE configuration (Figure 3) [17,18]. Otherwise, the surfaces are probably contaminated with impurities coming from the solution that destroy these characteristic features. If both contamination and surface disorder appear, a fitting with theoretical models will be very difficult. In addition, if in this case both experimental measurements and theoretical calculations agree, one can consider that the tolerance range for the comparison is too large, and so a wide range of interpretations are possible. In order to set certain boundaries and to disentangle the details of the mechanism, it is important to use very strict experimental conditions.

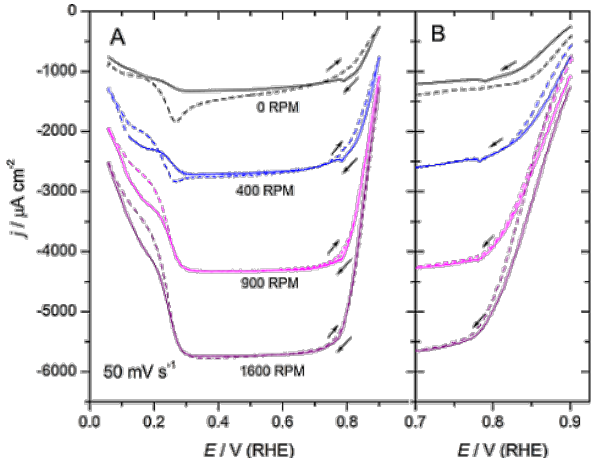

Figure 3: Oxygen reduction on a Pt(111) electrode in oxygen saturated 0.1 M $HClO_4$. (A): Cyclic voltammetric profile: Positively (dashed line) and negatively directed (solid line) sweeps. The electrode was kept at the initial potential E_i = 0.06 V for 10 s before each measurement. (B): Negatively directed sweeps when the electrode was kept at E_i = 0.06 V (solid line) and at E_i = 0.90 V (dashed line) for 10 s before each measurement [18].

First stages of surface oxidation

In addition to the governing factors of the surface order, the surface disordering experiments showed some features in the CV of Pt(111) and its stepped surfaces that could affect the surface composition to a great extent, albeit the surface order is maintained. As a consequence, it was considered necessary to carry out a deep study on the first stages of oxide formation (PtO) at potentials higher than 0.95 V, but lower than 1.15 V. For this purpose, a carefully oriented Pt(111) electrode was prepared that had an "undetectable" level of defects in the hydrogen adsorption region. The starting point was a strict charge balance between the positively and negatively directed sweeps, which indicated that the solution was clean and free of oxygen [8]. These experiments [8] demonstrated the reversibility of the butterfly, even at high sweep rates. However, the next oxidation step, which is responsible for the peak at about 1.06 V showed irreversible characteristics (Figure 1A), and consequently the peak potential strongly depends on the sweep rate. It appears that under the envelope of this peak several processes take place that can be unveiled by modifying the potential perturbation program [8,19]. In the rising part of this peak, a nucleation and growth loop was identified in a limited potential range, together with a small reversible step. The latter step was similar to that observed earlier after flame annealing studies when the first potential scan runs in the positive direction from the rest potential [6]. This suggests that chemical reaction steps that involve the so-called thermal oxides could also give rise to a significant charge fraction of the peak at about 1.06 V [19]. The corresponding reduction process involves at least three steps, which spread over a wide potential range (Figure 1A). The most positive one can be considered more or less reversible, but it evolves rapidly to generate states that undergo a charge transfer at less positive potentials. This suggests that more stable surface species are formed with increasing time. The rationale of this second oxidation step after a stable surface state is attained, i.e. the butterfly, followed by a wide potential region in which no faradaic charge is transferred, was assumed to correspond to the formation of PtO from PtOH, as a phase transition that involves the adsorption of additional OH_{ads}. This increased coverage of PtOH would destabilize the stable adlayer completed in the butterfly and generate other surface adlayers of varied composition, which finally generate a new relatively stable PtO adlayer at the end of the peak [8,19].

Theoretically, some possibilities have been suggested in order to illustrate how the different adlayers can be combined while the "total" oxygen surface coverage is increased as a charge transfer takes place [20,21] (Scheme 2).

The interconversion between these adlayers is evidenced by the different standard potential values of the different electrochemical equilibria as the oxygen coverage increases. In this scheme, the formation of PtOH at a higher coverage of that measured in the butterfly step seems to be the driving force [8,19]. Once PtO is formed, at the end of the positive branch of the peak at around 1.06 V, the stability of the adlayer increases. However, higher potentials would also generate higher PtO coverages that

$$1/2\ \text{ML}\ H_2O_{ads} + 1/6\ \text{ML}\ OH_{ads} \rightleftharpoons 1/3\ \text{ML}\ OH_{ads} + 1/3\ \text{ML}\ H_2O_{ads} + H^+ + e^-,\ E_{rev} = 0.56\ \text{V} \quad (1)$$

$$1/3\ \text{ML}\ H_2O_{ads} + 1/3\ \text{ML}\ OH_{ads} \rightleftharpoons 1/2\ \text{ML}\ OH_{ads} + 1/6\ \text{ML}\ H_2O_{ads} + H^+ + e^-,\ E_{rev} = 1.30\ \text{V} \quad (2)$$

$$1/3\ \text{ML}\ H_2O_{ads} + 1/3\ \text{ML}\ OH_{ads} \rightleftharpoons 1/6\ \text{ML}\ O_{ads} + 1/6\ \text{ML}\ OH_{ads} + 1/3\ \text{ML}\ H_2O_{ads} + H^+ + e^-,\ E_{rev} = 1.12\ \text{V} \quad (3)$$

$$1/6\ \text{ML}\ H_2O_{ads} + 1/2\ \text{ML}\ OH_{ads} \rightleftharpoons 1/6\ \text{ML}\ O_{ads} + 1/3\ \text{ML}\ OH_{ads} + 1/6\ \text{ML}\ H_2O_{ads} + H^+ + e^-,\ E_{rev} = 0.80\ \text{V} \quad (4)$$

Scheme 2: Possible adlayer reactions.

could further produce more oxidized forms. In these latter cases, however, the surface will start to disorder and would no longer be a flat, well-ordered Pt(111) surface.

Oxygen reduction reaction (ORR) on Pt(111)

The cyclic voltammetric profile (CV) for the ORR on Pt(111), in 0.1 M $HClO_4$, between 0.06 to 0.9 V, at room temperature and different rotation rates, ω, is well established (Figure 3A) [14,17,18,22,24]. In this case, the limiting current, j_{lim}, is recorded between about 0.3 and 0.75 V and the reaction onset is ca. 1.0 V vs RHE [18]. It should be noted, however, that the limiting value is progressively reached between 0.7 and 0.3 V, in contrast to other diffusion-controlled processes, such as those of H_2O_2, see below. The appearance of two current drops at $E < 0.3$ V, at which the hydrogen adsorption begins, together with the detection of H_2O_2 [14] and a similar decrease in current in this potential region during the reduction of H_2O_2 [25], suggest that adsorbed hydrogen on the electrode, H_{ads}, may prevent the O–O bond cleavage and block reactive surface sites. Therefore only two electrons are exchanged in this potential range [17,23]. This inhibition by H_{ads} depends on the surface orientation [14,17,23].

A kinetic analysis of the curves in Figure 3, either in the Tafel form or as Levich–Koutecký plots, suggested a first-order dependence with regard to the O_2 concentration [22,24]. In addition Tafel slopes that range from 60 to 88 mV between 0.8 and 0.9 V have been reported [14,17,18,22-24]. In consequence, the first charge transfer step was proposed to be the RDS. Deviations of the apparent Tafel slope from its intrinsic value of 120 mV have been explained by using either a Temkin adsorption isotherm for ORR reaction intermediates [24] or by changes in the O_2 adsorption because of changes in the coverage of chemisorbed oxygen-containing species [22,23].

On the other hand, while the superoxide anion, O_2^-, has been detected in alkaline solutions as the ORR intermediate species [15], in acidic environments the picture is not that clear. In this media, H_2O_2 has been identified under some conditions as a stable ORR intermediate product [26-31], thus indicating an incomplete electron transfer. Nevertheless, the production of hydroxyl radicals, $OH^\bullet$, during the reaction has also been reported [32], and the reduction of the soluble hydroperoxyl radical, $OOH^\bullet$, as the RDS in the ORR in acidic solutions has been also suggested [18]. In contrast, other reaction intermediates have been suggested from quantum chemical models [33-42], and two main mechanisms have been proposed, namely the "dissociative" and the "associative" mechanism. In the first case, the O–O bond is broken upon oxygen adsorption on Pt. The simplest "dissociative" mechanism proposed for the reaction at a Pt(111) surface is shown in Scheme 3 [33].

$$O_2 + 2\ Pt \longrightarrow 2\ PtO \quad (5)$$

$$PtO + H^+ + e^- \longrightarrow PtOH \quad (6)$$

$$PtOH + H^+ + e^- \longrightarrow Pt + H_2O \quad (7)$$

Scheme 3: Associative ORR mechanism.

While in the associative case the O–O bond integrity is preserved upon adsorption and would only break after electron transfer (Scheme 4) [33].

$$O_2 + Pt \longrightarrow PtO_2 \quad (8)$$

$$PtO_2 + H^+ + e^- \longrightarrow PtOOH \quad (9)$$

$$PtOOH + H^+ + e^- \longrightarrow H_2O + PtO \quad (10)$$

$$PtO + H^+ + e^- \longrightarrow PtOH \quad (11)$$

$$PtOH + H^+ + e^- \longrightarrow Pt + H_2O \quad (12)$$

Scheme 4: Dissociative ORR mechanism.

The desorption of PtOOH to H_2O_2, which would react further at another surface site, instead of Equation 10 has also been proposed [34]. In this case, the associative mechanism can also be termed as "peroxo" mechanism [33]. In fact, this happens in experiments if strong adsorbates are present in the solution, such as strongly adsorbing anions or adatoms deposited at an underpotential [26,29,30,43]. In this case, H_2O_2 is detected as the final product in RDE experiments [14,26], which proves that the surface reactivity is important and that the availability of surface sites is a key point regarding the final reaction product.

It has been claimed that the reduction of OH_{ads} or O_{ads} is the RDS of the ORR [44-46]. Hence, because Equation 11 and Equation 12 are the same as Equation 6 and Equation 7, both dissociative and associative mechanisms can occur. However, the latter assumption would not directly lead to a first-order dependence on the O_2 concentration nor to Tafel slopes between 60 and 88 mV. To account for these results, a theoretical model postulates that, together with site-blocking effects, OH_{ads} can alter the adsorption energy of ORR intermediates, and thus also have a negative energetic effect on the reaction [26,47]. However, OH_{ads} is also considered an intermediate reactive species in the H_2O_2 reduction (HPRR) on Pt [48-51], a mass-controlled reaction at potentials of up to approximately 0.95 V [25,49,51]. In consequence, the question about the real identity of the RDS in the ORR mechanism on Pt(111) still remains open. Especially because several studies have shown that improvements of the ORR at overpotentials were less than expected from the observed decrease of the OH_{ads} coverage [52-54].

Surface sensitive reactions

Since early works [55,56], it has been known that there are volcano type responses when the ORR current densities, at a chosen potential, are plotted for different electrocatalysts as a function of either the adsorption bond strength, ΔG_{ads}, of the O_{ads}, OH_{ads} and OOH_{ads} species [55], or the electronic (Pt d-band vacancies) and geometric (Pt–Pt bond length) properties of Pt and Pt alloys [56]. Numerous theoretical calculations have supported this experimental fact and proposed a scaling relationship between the ΔG_{ads} values of these species that precludes any further improvements in the ORR performance, beyond some optimal values for these adsorption bond strengths, ΔG_{OHads}, ΔG_{Oads} and ΔG_{OOHads} [33,44,45,57,59]. Similarly, for Pt(111) and its vicinal stepped surfaces a volcano type response for the ORR activity as a function of ΔG_{OHads} or ΔG_{Oads} has also been suggested, with the (111) facet at the top of this curve [13,60-62].

Following the same procedure reported in the literature and by employing the reported theoretical ΔG_{OHads}, ΔG_{Oads} and ΔG_{OOHads} values [13,33,44,58], we construct the free energy diagram at 0.9 V (vs SHE) for the ORR at the Pt(111), Pt(211), Pt(100) and Pt(110) surfaces (Figure 4). In all cases, the used adsorption free energies were calculated while assuming a low oxygen coverage [13,33,44,58]. As can be seen from Figure 4, in the absence of any activation barrier the limiting elementary step for the ORR would be the OH_{ads} desorption, Equation 7 and Equation 12, because O_{ads} and OH_{ads} are relatively strongly bound to all Pt surfaces. Hence, it would determine the upper limit of the potential for the reaction to occur. The ORR activity sequence according this figure would be Pt(111) > Pt(100) > Pt(110) > Pt(211). Incidentally, if this were true, this would be bad news for practical applications because small nanoparticles cannot contain wide {111} domains.

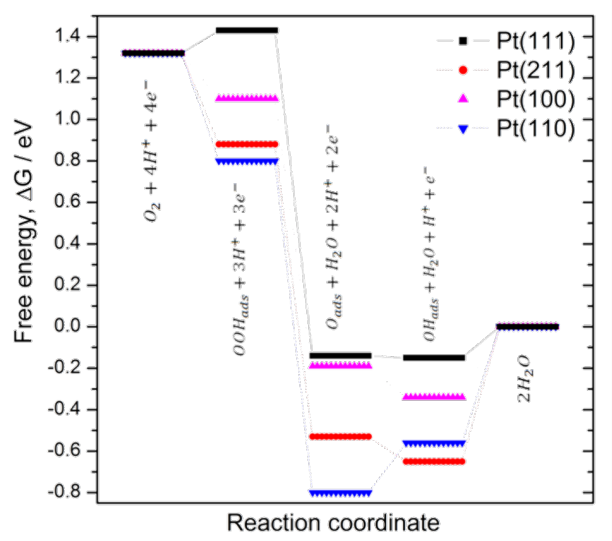

Figure 4: Potential free energy diagram for oxygen reduction over Pt(111), Pt(211), Pt(100) and Pt(110) at 0.9 V, on the basis of reported adsorption energies [13,33,44,58].

In this picture, all the electron/transfer steps before Equation 7, or Equation 12, are downhill in terms of free energy. Exceptions are Equation 8 and Equation 9 on Pt(111) and Equation 6, or Equation 11, on Pt(110) but in these electrodes the OH_{ads} desorption has the largest positive free energy change in the whole mechanism. This simple picture is, however, not sufficient to explain the ORR mechanism, because the coverage of O-containing species at the surface changes with the potential and may affect the free energy of the different reaction intermediates [33]. In addition, adsorption energies in perfect UHV atmospheres may be different from those in aqueous environments, and hence, other elementary steps that are different from Equation 5 to Equation 12 may occur during experiments [18,32,38].

In order to determine the surface sensitivity of the ORR, in our laboratory, we have approached the reactivity of the basal planes by extrapolation of the ORR activity from stepped surfaces with zero defects. In this respect, the assumption is that the steps “drain” defects in such a way that the terraces remain ordered. This was observed by STM, which shows that the defects seem to concentrate at the step lines and leave reasonably wide terraces between them [16,63,64]. Following this strategy, several experiments have shown that in acidic solutions Pt(111) is less active for the ORR than its vicinal stepped surfaces, irrespectively of the symmetry of the steps (Figure 5) [17,23]. This is in contradiction with the theoretical results

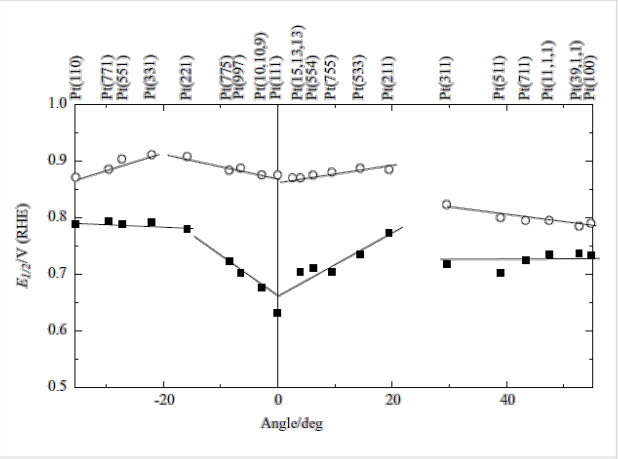

Figure 5: Plot of the half-height potential, $E_{1/2}$, for the oxygen reduction as a function of the angle of the surface with respect to Pt single crystals, basal planes and stepped surfaces, in 0.5 M H_2SO_4 (filled squares) and 0.1 M $HClO_4$ (open circles) [17,23].

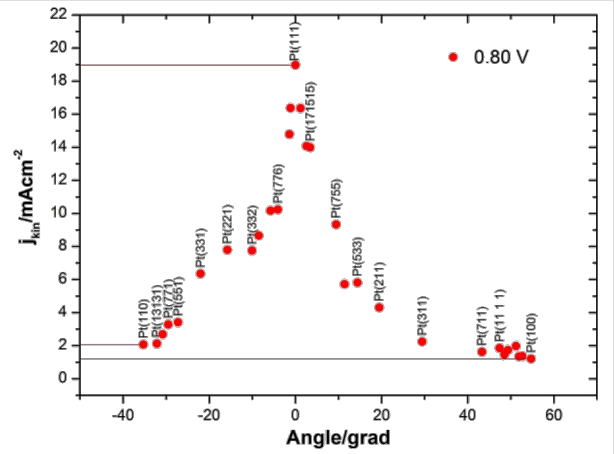

Figure 6: Plot of the kinetic currents at 0.8 V, j_{kin}(0.8 V), for the oxygen reduction as a function of the angle of the surface with respect to Pt single crystals, basal planes and stepped surfaces, in 0.1 M NaOH [66].

described above [13,60-62]. Similarly, theoretical and experimental results for Pt(110) and Pt(100) also disagrees.

This result was carefully checked and confirmed [23,65]. Taking advantage of our facet-based surface orientation system, which allows small deviations of the angles from the basal plane, we prepared stepped surfaces vicinal to Pt(111) with long (up to 50 atom wide) terraces in the [1 $\bar{1}$0] zone, which are considered to be the most stable surfaces for oxygen adsorption. The results showed again that Pt(111) is comparatively less catalytic for the ORR than the surfaces of the Pt(*S*)[*n*(111)×(111)] series [65]. This creates an inconsistent situation, because theory does apparently not fit with results that we believe are of the highest quality.

This unsatisfactory situation ended when experiments were performed in alkaline solutions (0.1 M NaOH) (Figure 6) [66]. In this case, the overall results agree well with that expected from the theoretical "correct" trend, at least in the top reactivity surface, as the Pt(111) electrode becomes the most active plane. However, stepped surfaces were still more active than the other two basal planes, Pt(100) and Pt(110), in contradiction to what would be expected from theoretical calculations [13,33,44,58,60-62]. As mentioned before, this would be a problem for fuel cells, which would require large Pt nanoparticles. Fortunately, however, in alkali solutions Pt can be replaced by Ni and thus the main challenge in alkaline fuel cells is less the catalyst in comparison to the finding of a suitable membrane.

The interesting point is that the Pt reactivity predicted by the calculations involves a material with electronic surface charge densities that are about 0.7 eV more negative than those in $HClO_4$, i.e., which is a difference of roughly 12 pH units. This raises the question of whether surface charges are appropriately included in the model. In relation to the available data, the potentials of zero total charge of Pt(111) are located at the beginning of the hydrogen adsorption and this potential shifts about 60 mV per pH unit [67]. This means that the metal side of the interface is positively charged in the potential range in which ORR starts, in both alkaline and acidic solutions that are free from dissolved species that strongly adsorb on the electrode surface and could interfere with species coming from water adsorption in the whole potential range. A cyclic voltammogram of Pt(111) in 0.1 M NaOH is depicted in Figure 1B.

However, a serious drawback in alkaline solutions deals with solution contaminants, which are more difficult to control than those in acidic solutions. This has been discussed in several cases and various interpretations were given. The first report on this problem was the result of a joint effort between Ulm and Alicante and was attributed to sulfate adsorption, while taking into account voltammetry and XPS experiments [68]. Recently, the problem was raised by Markovic et al. at the Argonne National Laboratory and it was considered to be because of metals like Ni, Co and Fe [69]. In our experiments, we have found these extra signals in the CV in some cases. To achieve the necessary voltammetric quality, it is necessary to use fresh chemicals (it is not possible to use the pellets or flakes some months after opening the flask) and solutions (daily prepared). Possible solutions to the contamination problem are currently under study in our laboratory.

Limited ORR kinetics at high potentials

The surface changes during surface oxidation and disordering may be relevant in the ORR because of the electrocatalytic

nature of this reaction, which involves adsorption steps. Results show that transport control appears at relatively high potentials of about 0.85 V (Figure 3A), but the ORR current differs between the positively and the negatively directed sweeps, the latter being higher especially at low ω (Figure 3B).That is the ORR current depends on the direction of the potential scan at 0.85 V < E < 0.9 V (Figure 3A) [18,23]. Initially, it has been suggested that surface oxides may be responsible for the discrepancies between positively and negatively directed sweeps around the onset of oxygen reduction [23]. However, under these conditions, the blank CV does not show any indication for the formation of PtO. Thus, only PtOH that comes from the reactions in the butterfly region could be expected to be on the surface, in equal amounts during both sweeps, because the butterfly is fully reversible at a sweep rate as low as 50 mV·s^{-1} [8,9].

To point out the possible effect of surface oxides on the ORR, experimental conditions can be chosen to minimize the influence of diffusional effects on the experimental response. This can be achieved by minimizing the oxygen concentration in solution and working at small rotation rates, ω. An interesting remark is that PtO formation and its reduction takes place at potentials at which the ORR just starts at Pt(111). In this respect, surface composition effects, if any, could be pointed out by comparing current densities in the positively and negatively directed sweeps in this potential region. Figure 7 shows the ORR curves at Pt(111) in 0.1 M $HClO_4$, Ar/O_2 ratio 5:1, at different ω, while Figure 8 depicts the ORR curve at 50 rpm for different upper potentials in an oxygen saturated solution.

Indeed, the presence of oxygen in the solution modifies the surface oxide dynamics, i.e., the current in the peak at about 1.06 V is decreased (Figure 7 and Figure 8) [18]. This experimental observation would suggest that molecular oxygen could participate in the formation of the adlayer, though at least one parallel path (or step) that could compete with more genuine electrochemical steps is already discussed [18]. This opens the possibility that the reverse would be also possible, i.e., the ORR could also be affected by surface oxides. Incidentally, the butterfly peaks, albeit clearly distinguished in the voltammogram, are slightly displaced (Figure 3 and Figure 7), but this could be an artifact of the combination of two independent processes. However, it should be remarked that the butterfly contribution should be observed, superimposed onto the ORR, at potentials close to its limiting diffusion-controlled value.

An interesting situation appears at high potentials with low ω and/or diluted oxygen concentrations. There is the presence of a peak, in the negatively directed sweep, with a reduction current higher than j_{lim} at E > 0.8 V, Figure 7A and Figure 8. When

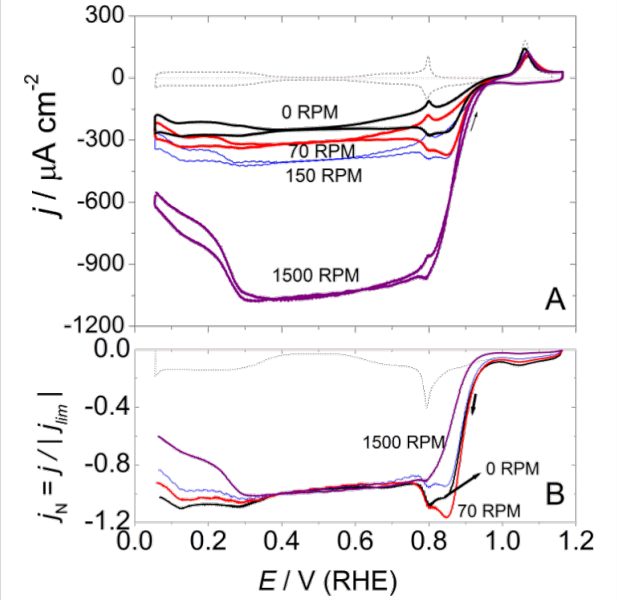

Figure 7: (A) Cyclic voltammograms for the ORR on a hanging meniscus rotating disc (HMRD) Pt(111) electrode from 0.06 to 1.15 V in 0.1 M $HClO_4$, Ar/O_2 ratio 5:1. Scan rate 50 mV·s^{-1}. (B) Negatively directed sweep normalized against the limiting currents from data in (A).

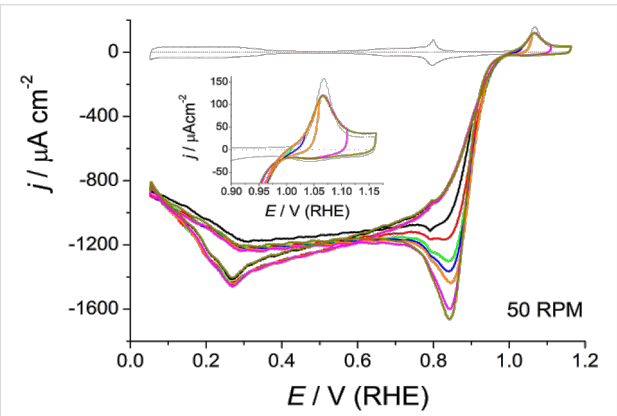

Figure 8: Cyclic voltammograms in the high potential region for the ORR on a HMRD Pt(111) electrode in oxygen saturated 0.1 M $HClO_4$, at different upper potentials and 50 rpm. Inset: Detailed view of the Pt(111) oxide formation region.

currents are normalized to j_{lim}, it can be seen that this high potential current contribution progressively disappears as ω increases (Figure 7B). This would be compatible with the formation of a soluble intermediate species in the high potential region the concentration of which at the interface vanishes as ω increases [18]. The elimination of this soluble intermediate, however, is not very fast, which suggests some interaction with the surface. We can speculate that this interaction could likely take place through the water network, because of the necessary similar molecular composition of this intermediate and water, which would enable the formation of hydrogen bonds.

It is important to remark that the formation of this soluble intermediate is dependent on the potential, i.e., at low ω, the aforementioned peak contribution at high potentials increases at higher E_{up} (Figure 8). As the upper potential limit is not too high, this observation is compatible with the preservation of the Pt(111) surface structure. It should be remarked that the product, PtO, could be formed through a chemical process that involves dissolved O_2, which could be faster than the equivalent electrochemical step that involves water. As a consequence, this complication should be considered in reaction models because it can be important in the formation of the soluble intermediate and lead to faster ORR at high potentials, which is the goal in electrocatalysis.

Hydrogen peroxide oxidation and reduction reactions (HPORR) in the ORR

From theoretical calculations, the single soluble intermediate species that could participate in the ORR mechanism is H_2O_2. However, as discussed above, H_2O_2 is a stable intermediate in ORR only under some circumstances [26-31]. It has not been detected in rotating ring-disc electrode (RRDE) experiments with either with massive Pt electrodes or Pt(111) electrodes in acidic solutions that contained moderately adsorbing anions provided that $E > 0.35$ V [1,14,22,26,70,71]. Hydrogen peroxide can be reduced and oxidized by following two different irreversible reactions that lead to water and oxygen, respectively, as final products according to Scheme 5 [25].

$$H_2O_2 + 2\,H^+ + 2\,e^- \rightleftharpoons 2\,H_2O,\ E_{rev} = 1.763\ V \quad (13)$$

$$O_2 + 2\,H^+ + 2\,e^- \rightleftharpoons H_2O_2,\ E_{rev} = 0.695\ V \quad (14)$$

Scheme 5: Reduction and oxidation of hydrogen peroxide.

It has been shown experimentally that the oxidation (HPOR) and reduction (HPRR) of H_2O_2 are fast reactions and that the total current is controlled by mass transport at any applied potential [49-51]. Hence, it has been proposed that the measured current is not resulting from the HPORRs themselves, which are considered to be purely chemical processes, but rather from the following electrochemical Pt-surface regeneration reactions [49-51]. Interestingly, on Pt(111) these reactions superimpose the CV in the potential range between the butterfly and the PtO-formation peak (Figure 9). In this potential region, the electrochemical activity is negligible in the supporting electrolyte solution, unless the upper limit becomes higher than 1.0 V at 50 mV·s^{-1}.

From Figure 9, it can be seen that the HPOR and HPRR current densities reach the same j_{lim} with opposite signs. This corresponds to controlled diffusion processes that involve the same reagent and in two reactions involve the same number of electrons. The j_{lim} values agree with those expected from the Levich equation, within the experimental error range, which takes into account that in our experiments it is less important to use exact concentrations than to preserve the purity of the solution. However, in the upper diffusion limit the surface composition is PtO with an intermediate coverage whereas in the lower diffusion limit the surface is essentially water-covered Pt.

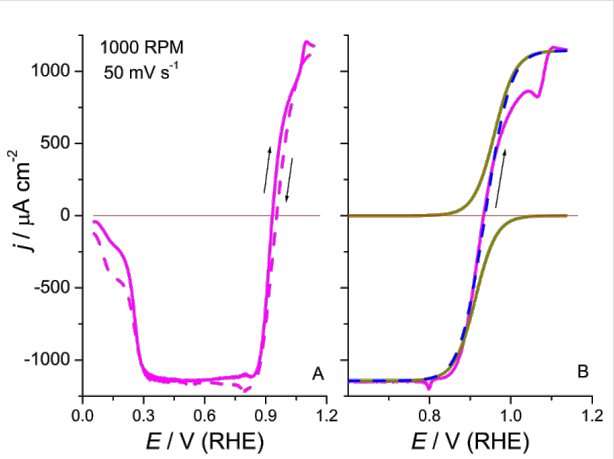

Figure 9: Hydrogen peroxide reduction and oxidation reactions on Pt(111) in 0.1 M $HClO_4$ + 1 mM H_2O_2. (A) Cyclic voltammetric profile: Positively (solid line) and negatively directed (dashed line) sweeps. (B) Adjusted curves for HPOR and HPRR (dotted lines) during the positive scan. The dashed line corresponds to the sum of currents from the fitted branches and the solid line is the experimental curve after subtracting the blank.

As in the ORR, if ω is not too high the butterfly peaks, as well as the PtO formation peak in the anodic branch, are clearly distinguished. The latter, however, is significantly reduced in charge (Figure 9A). Moreover, a clear distortion of the oxidation branch can be noticed as soon as the applied potential reaches 1.0 V (Figure 9B). This suggests that H_2O_2 can contribute to the formation of PtO through a chemical reaction, which is even faster than that by dissolved oxygen. It is interesting to remark that the inspection of the CV does not show important discontinuities when the zero current line is crossed, i.e., despite the different overpotentials for HPRR, about 800 mV, and HPOR, about 200 mV. The transition from oxidation to reduction and vice versa, which involves two different reactions, takes place without any apparent rate change in 0.1 M perchloric acid solution.

Because HPRR and HPOR are two different diffusion-controlled reactions, they can be analyzed independently under different experimental conditions in order to explore the relevant parameters that influence the mechanisms and to show

similarities and differences. It is possible to arbitrarily decompose the HPORR by using conventional equations for S-shaped electrochemical processes given by

$$E = E_{1/2} + m\log\left(\frac{j_{\lim} - j}{j}\right)$$

where m is a parameter that would depend on the particular charge transfer mechanism and $E_{1/2}$ is the potential at which the current density, j, is one half of the corresponding $j_{\lim}$ value. Following this approach, a recent study in acidic media fitted the HPORR current potential curves on Pt(111) and vicinal surfaces, in such a way that the addition of both HPRR and HPOR contributions should agree as much as possible with the overall experimental curve [51]. It has been found that at oxide-free surfaces the structure dependence of the HPRR is similar to that of the ORR in acidic solution, while at oxidized surfaces the reactivity is comparable to what is reported for the ORR in basic media [51].

Figure 9B shows the adjusted curves, with m = 60 mV, for HPOR and HPRR (dotted lines) during the positively directed scan on Pt(111). The dashed line corresponds to the sum of currents from the fitted branches and the solid line is the experimental curve after subtracting the blank. It can be seen that the fitting is particularly good for the reduction process, which is almost unaffected by the surface oxidation, this assertion being also true for the negatively directed sweep (data not shown). In contrast, the HPOR is seriously inhibited in the potential range, in which $E_{2p,a}$ appears in H_2O_2-free solutions. It seems that the formation of PtO affects the surface reactivity. However, once PtO is formed, the surface reactivity is restored and the reaction is transport controlled.

From the above, it is clear that at 1.0 V every H_2O_2 molecule that reaches the electrode will be readily oxidized. Hence, if the ORR takes place through the associative mechanism any oxygen molecule that could be reduced at potentials higher than 1.0 V, and thus yielding to H_2O_2, would be immediately re-oxidized to O_2, while it is close to the surface. This would result in a zero net current until the HPRR becomes the dominant process, i.e., at E < 0.95 V. It is interesting to remark that in any case H_2O_2 would not be detected in the ORR under the present conditions, because it should be reduced as soon as it is formed with HPRR taking place at significantly higher potentials than ORR [25,49-51].

This opens the question about the identity of the soluble species suggested by the reported experimental results discussed above [18]. Recent theoretical calculations, which consider explicitly the effect of a bulk water layer on the mechanism of the ORR, have suggested that the dissociation of OOH_{ads}, Equation 6, is much less favorable on the water covered surface as compared to the bare surface [38]. Hence, it would be possible that OOH_{ads} desorbs instead of being reduced and give rise to a soluble $OOH^{\bullet}$ radical species. Following these lines, next steps in the mechanism would be the aqueous reduction of $OOH^{\bullet}$

$$OOH^{\bullet} + H^{+} + e^{-} \rightleftharpoons PtH_2O_2$$

that will further reduce to water. Under this framework, the first–order dependence of the reaction, regarding the O_2 concentration can be also explained. It is clear that this is only one possibility and more theoretical and experimental work is still necessary for a fully understanding of the ORR mechanism. However, the experimental shift of the oxygen reduction towards higher potentials described above should be kept in mind.

Conclusion

In this work, a critical overview of the current state of the art of the oxygen reduction reaction (ORR) on Pt(111) and its vicinal surfaces has been done. Both experimental and theoretical results have been discussed and general points of agreement and disagreement highlighted.

It has been shown that despite the ORR shows a dependence on the surface structure, experimental and theoretical results disagree in acidic media while they seem to agree in alkaline solutions. The reasons behind this fact are not clearly known, but the necessity of building real and precise theoretical reaction models in order to get a fundamental knowledge about ORR mechanism is demonstrated. In contrast, the surface-structure dependence for HPOR and HPRR at oxide-free surfaces show similar trends as the ORR, despite that H_2O_2 is only produced during the ORR in acidic media when surface adsorbates are present.

The surface changes during oxidation and disordering of the surface may be relevant in the ORR because of the electrocatalytic nature of this reaction, which should involve adsorption steps. At high potentials dissolved oxygen may modify the oxide growth dynamics on Pt(111) and it is clear that both processes, ORR and oxide formation, interact. In this region, the reduction of a soluble intermediate species, different to H_2O_2, has been tentatively suggested from experiments as the rate determining step (RDS) for the ORR in Pt(111). However, there are no theoretical models that include both phenomena, yet and thus, the structures and processes at the molecular level that take place at the surface in this potential region, in which apparently there is no ORR current, are not clearly known.

More efforts are still necessary through a cooperative approach between theory and experiment in order to fully understand the ORR mechanism and to define the right approach for designing new electrocatalysts for fuel-cell cathodes. An agreement between theoretical calculations and experiments on model surfaces that describe the same process should be attained as a first step to understand the electrocatalysis at more complex surfaces such as those of dispersed nanoparticles.

Experimental

In a similar way as described earlier [8], the working electrodes were prepared from small Pt beads, approximately 2–3 mm in diameter, by the method described by Clavilier et al. [72]. All the experiments were carried out at room temperature, approximately 22 °C, in a two-compartment, three-electrode all-glass cell, by following a well detailed experimental protocol [73]. Suprapure perchloric acid (Merck) and H_2O_2 (Panreac) were used to prepare the aqueous solutions in ultrapure water (Purelab Ultra, Elga-Vivendi, 18.2 MΩ·cm^{-1}). H_2, O_2 and Ar (N50, Air Liquide) were also employed. All potentials were measured against the reversible hydrogen electrode (RHE) and a large, flame-cleaned, Pt wire coil was used as a counter electrode.

Acknowledgements

Support from the Spanish MICYNN though project CTQ2010–16271 and GV through PROMETEO/2009/045 (FEDER) is greatly acknowledged.

References

1. Wroblowa, H. S.; Yen-Chi-Pan; Razumney, G. *J. Electroanal. Chem.* **1976,** *69,* 195–201. doi:10.1016/S0022-0728(76)80250-1
2. Björling, A.; Ahlberg, E.; Feliu, J. M. *Electrochem. Commun.* **2010,** *12,* 359–361. doi:10.1016/j.elecom.2009.12.034
3. Björling, A.; Feliu, J. M. *J. Electroanal. Chem.* **2011,** *662,* 17–24. doi:10.1016/j.jelechem.2011.01.045
4. Gómez-Marín, A. M.; Feliu, J. M. *Electrochim. Acta* **2012,** *82,* 558–569. doi:10.1016/j.electacta.2012.04.066
5. Clavilier, J.; El Achi, K.; Petit, M.; Rodes, A.; Zamakchari, M. A. *J. Electroanal. Chem.* **1990,** *295,* 333–356. doi:10.1016/0022-0728(90)85026-2
6. Clavilier, J.; Armand, D.; Wu, B. L. *J. Electroanal. Chem.* **1982,** *135,* 159–166. doi:10.1016/0022-0728(82)90013-4
7. Clavilier, J.; Rodes, A.; El Achi, K.; Zamakhchari, M. A. *J. Chim. Phys. Phys.-Chim. Biol.* **1991,** *88,* 1291–1337.
8. Gómez-Marín, A. M.; Clavilier, J.; Feliu, J. M. *J. Electroanal. Chem.* **2013,** *688,* 360–370. doi:10.1016/j.jelechem.2012.07.016
9. Berná, A.; Climent, V.; Feliu, J. M. *Electrochem. Commun.* **2007,** *9,* 2789–2794. doi:10.1016/j.elecom.2007.09.018
10. Lebedeva, N. P.; Koper, M. T. M.; Feliu, J. M.; Van Santen, R. A. *Electrochem. Commun.* **2000,** *2,* 487–490. doi:10.1016/S1388-2481(00)00062-X
11. Solla-Gullón, J.; Vidal-Iglesias, F. J.; Feliu, J. M. *Annu. Rep. Prog. Chem., Sect. C: Phys. Chem.* **2011,** *107,* 263–297. doi:10.1039/c1pc90010b
12. Sánchez-Sánchez, C. M.; Solla-Gullón, J.; Vidal-Iglesias, F. J.; Aldaz, A.; Montiel, V.; Herrero, E. *J. Am. Chem. Soc.* **2010,** *132,* 5622–5624. doi:10.1021/ja100922h
13. Greeley, J.; Rossmeisl, J.; Hellman, A.; Norskov, J. K. *Z. Phys. Chem.* **2009,** *221,* 1209–1220. doi:10.1524/zpch.2007.221.9-10.1209
14. Markovic, N. M.; Gasteiger, H.; Ross, P. N. *J. Electrochem. Soc.* **1997,** *144,* 1591–1597. doi:10.1149/1.1837646
15. Shao, M.-h.; Liu, P.; Adzic, R. R. *J. Am. Chem. Soc.* **2006,** *128,* 7408–7409. doi:10.1021/ja061246s
16. Inukai, J.; Tryk, D. A.; Abe, T.; Wakisaka, M.; Uchida, H.; Watanabe, M. *J. Am. Chem. Soc.* **2013,** *135,* 1476–1490. doi:10.1021/ja309886p
17. Maciá, M. D.; Campiña, J. M.; Herrero, E.; Feliu, J. M. *J. Electroanal. Chem.* **2004,** *564,* 141–150. doi:10.1016/j.jelechem.2003.09.035
18. Gómez-Marín, A. M.; Feliu, J. M. *ChemSusChem* **2013,** *6,* 1091–1100. doi:10.1002/cssc.201200847
19. Gómez-Marín, A. M.; Feliu, J. M. *Electrochim. Acta* **2013,** *104,* 367–377. doi:10.1016/j.electacta.2012.10.075
20. Tian, F.; Jinnouchi, J.; Anderson, A. B. *J. Phys. Chem. C* **2009,** *113,* 17484–17492. doi:10.1021/jp905377d
21. Tian, F.; Anderson, A. B. *J. Phys. Chem. C* **2011,** *115,* 4076–4088. doi:10.1021/jp1100126
22. Markovic, N. M.; Adžić, R. R.; Cahan, B. D.; Yeager, E. B. *J. Electroanal. Chem.* **1994,** *377,* 249–259. doi:10.1016/0022-0728(94)03467-2
23. Kuzume, A.; Herrero, E.; Feliu, J. M. *J. Electroanal. Chem.* **2007,** *599,* 333–343. doi:10.1016/j.jelechem.2006.05.006
24. Pérez, J.; Villullas, H. M.; Gonzalez, E. R. *J. Electroanal. Chem.* **1997,** *435,* 179–187. doi:10.1016/S0022-0728(97)00303-3
25. Gómez-Marín, A. M.; Schouten, K. J. P.; Koper, M. T. M.; Feliu, J. M. *Electrochem. Commun.* **2012,** *22,* 153–156. doi:10.1016/j.elecom.2012.06.016
26. Markovic, N. M.; Ross, P. N., Jr. *Surf. Sci. Rep.* **2002,** *45,* 117–229. doi:10.1016/S0167-5729(01)00022-X
27. Seidel, Y. E.; Schneider, A.; Jusys, Z.; Wickman, B.; Kasemo, B.; Behm, R. J. *Faraday Discuss.* **2009,** *140,* 167–184. doi:10.1039/b806437g
28. Schneider, A.; Colmenares, L.; Seidel, Y. E.; Jusys, Z.; Wickman, B.; Kasemo, B.; Behm, R. J. *Phys. Chem. Chem. Phys.* **2008,** *10,* 1931–1943. doi:10.1039/b719775f
29. Schmidtz, T. J.; Stamenkovic, V.; Ross, P. N.; Markovic, N. M. *Phys. Chem. Chem. Phys.* **2003,** *5,* 400–406. doi:10.1039/b208322a
30. Schmidt, T. J.; Paulus, U. A.; Gasteiger, H. A.; Behm, R. J. *J. Electroanal. Chem.* **2001,** *508,* 41–47. doi:10.1016/S0022-0728(01)00499-5
31. Stamenkovic, V.; Markovic, N. M.; Ross, P. N., Jr. *J. Electroanal. Chem.* **2001,** *500,* 44–51. doi:10.1016/S0022-0728(00)00352-1
32. Nöel, J.-M.; Latus, A.; Lagrost, C.; Volanschi, E.; Hapiot, P. *J. Am. Chem. Soc.* **2012,** *134,* 2835–2841. doi:10.1021/ja211663t
33. Nørskov, J.; Rossmeisl, J.; Logadottir, A.; Lindqvist, L.; Kitchen, J. R.; Bligaard, T.; Jónsson, H. *J. Phys. Chem. B* **2004,** *108,* 17886–17892. doi:10.1021/jp047349j
34. Anderson, A. B.; Albu, T. V. *J. Electrochem. Soc.* **2000,** *147,* 4229–4238. doi:10.1149/1.1394046
35. Keith, J. A.; Jacob, T. *Angew. Chem., Int. Ed.* **2010,** *49,* 9521–9525. doi:10.1002/anie.201004794

36. Panchenko, A.; Koper, M. T. M.; Shubina, T. E.; Mitchell, S. J.; Roduner, E. *J. Electrochem. Soc.* **2004,** *151,* A2016–A2027. doi:10.1149/1.1809586
37. Nilekar, A. U.; Mavrikakis, M. *Surf. Sci.* **2008,** *602,* L89–L94. doi:10.1016/j.susc.2008.05.036
38. Walch, S. P. *J. Phys. Chem. C* **2011,** *115,* 7377–7391. doi:10.1021/jp106497h
39. Anderson, A. B.; Albu, T. V. *Electrochem. Commun.* **1999,** *1,* 203–206. doi:10.1016/S1388-2481(99)00039-9
40. Anderson, A. B.; Albu, T. V. *J. Am. Chem. Soc.* **1999,** *121,* 11855–11863. doi:10.1021/ja992735d
41. Tripković, V.; Skúlason, E.; Siahrostami, S.; Nørskov, J. K.; Rossmeisl, J. *Electrochim. Acta* **2010,** *55,* 7975–7981. doi:10.1016/j.electacta.2010.02.056
42. Hansen, H. A.; Rossmeisl, J.; Nørskov, J. K. *Phys. Chem. Chem. Phys.* **2008,** *10,* 3722–3730. doi:10.1039/b803956a
43. Abe, T.; Swain, G. M.; Sashikata, K.; Itaya, K. *J. Electroanal. Chem.* **1995,** *382,* 73–83. doi:10.1016/0022-0728(94)03664-O
44. Rossmeisl, J.; Logadottir, A.; Nørskov, J. K. *Chem. Phys.* **2005,** *319,* 178–184. doi:10.1016/j.chemphys.2005.05.038
45. Viswanathan, V.; Hansen, H.; Rossmeisl, J.; Nørskov, J. K. *ACS Catal.* **2012,** *2,* 1654–1660. doi:10.1021/cs300227s
46. Jinnouchi, R.; Kodama, K.; Hatanaka, T.; Morimoto, Y. *Phys. Chem. Chem. Phys.* **2011,** *13,* 21070–21083. doi:10.1039/c1cp21349k
47. Wang, J. X.; Markovic, N. M.; Adzic, R. R. *J. Phys. Chem. B* **2004,** *108,* 4127–4133. doi:10.1021/jp037593v
48. Balbuena, P. B.; Calvo, R. S.; Lamas, E. J.; Salazar, P. F.; Seminario, J. M. *J. Phys. Chem. B* **2006,** *110,* 17452–17459. doi:10.1021/jp063027z
49. Katsouraros, I.; Schneider, W. B.; Meier, J. C.; Benedikt, U.; Biedermann, P. U.; Auer, A. A.; Mayrhofer, K. J. J. *Phys. Chem. Chem. Phys.* **2012,** *14,* 7384–7391. doi:10.1039/c2cp40616k
50. Katsouraros, I.; Schneider, W. B.; Meier, J. C.; Benedikt, U.; Biedermann, P. U.; Auer, A. A.; Cuesta, A.; Mayrhofer, K. J. J. *Phys. Chem. Chem. Phys.* **2013,** *15,* 8058–8068. doi:10.1039/c3cp50649e
51. Sitta, E.; Gómez-Marín, A. M.; Aldaz, A.; Feliu, J. M. *Electrochem. Commun.* **2013,** *33,* 39–42. doi:10.1016/j.elecom.2013.04.014
52. Shao, M.; Sasaki, K.; Marinkovic, N. S.; Zhang, L.; Adzic, R. R. *Electrochem. Commun.* **2007,** *9,* 2848–2853. doi:10.1016/j.elecom.2007.10.009
53. Teliska, M.; Murthi, V.; Mukerjee, S.; Ramaker, D. *J. Phys. Chem. C* **2007,** *111,* 9267–9274. doi:10.1021/jp071106k
54. Strmcnik, D.; Escudero-Escribano, M.; Kodama, K.; Stamenkovic, V. R.; Cuesta, A.; Marković, N. M. *Nat. Chem.* **2010,** *2,* 880–885. doi:10.1038/nchem.771
55. Appleby, A. J. *Catal. Rev.* **1971,** *4,* 221–244. doi:10.1080/01614947108075490
56. Mukerjee, S.; Srinivasan, S.; Soriaga, M. P.; McBreen, J. *J. Electrochem. Soc.* **1995,** *142,* 1409–1422. doi:10.1149/1.2048590
57. Okamoto, Y.; Sugino, O. *J. Phys. Chem. C* **2010,** *114,* 4473–4478. doi:10.1021/jp9087805
58. Koper, M. T. M. *J. Electroanal. Chem.* **2011,** *660,* 254–260. doi:10.1016/j.jelechem.2010.10.004
59. Man, I. C.; Su, H.-Y.; Calle-Vallejo, F.; Hansen, H. A.; Martinez, J. I.; Inoglu, N. G.; Kitchen, J.; Jaramillo, T. F.; Nørskov, J. K.; Rossmeisl, J. *ChemCatChem* **2011,** *3,* 1159–1165. doi:10.1002/cctc.201000397
60. Tritsaris, G. A.; Greeley, J.; Rossmeisl, J.; Nørskov, J. K. *Catal. Lett.* **2011,** *141,* 909–913. doi:10.1007/s10562-011-0637-8
61. Viswanathan, V.; Wang, F. Y.-F. *Nanoscale* **2012,** *4,* 5110–5117. doi:10.1039/c2nr30572k
62. Stephens, I. E. L.; Bondarenko, A. S.; Grønbjerg, U.; Rossmeisl, J.; Chorkendorff, I. *Energy Environ. Sci.* **2012,** *5,* 6744–6762. doi:10.1039/c2ee03590a
63. Itaya, K.; Sugawara, S.; Sashikata, K.; Furuya, N. *J. Vac. Sci. Technol., A* **1990,** *8,* 515–519. doi:10.1116/1.576378
64. Herrero, E.; Orts, J. M.; Aldaz, A.; Feliu, J. M. *Surf. Sci.* **1999,** *440,* 259–270. doi:10.1016/S0039-6028(99)00813-4
65. Gómez-Marín, A. M.; Feliu, J. M. *Chem. Sci.* Submitted.
66. Rizo, R.; Herrero, E.; Feliu, J. M. *Phys. Chem. Chem. Phys.* **2013,** *15,* 15416–15425. doi:10.1039/c3cp51642c
67. Van der Niet, M. J. T. C.; Garcia-Araeza, N.; Hernández, J.; Feliu, J. M.; Koper, M. T. M. *Catal. Today* **2013,** *202,* 105–113. doi:10.1016/j.cattod.2012.04.059
68. Morallón, E.; Vásquez, J. L.; Aldaz, A.; Zhai, R. S. *J. Electroanal. Chem.* **1993,** *360,* 89–100. doi:10.1016/0022-0728(93)87006-H
69. Subbaraman, R.; Danilovic, N.; Lopes, P. P.; Tripkovic, D.; Strmcnik, D.; Stamenkovic, V. R.; Markovic, N. M. *J. Phys. Chem. C* **2012,** *116,* 22231–22237. doi:10.1021/jp3075783
70. Scherson, D. A.; Tolmachev, Y. V. *Electrochem. Solid-State Lett.* **2010,** *13,* F1–F2. doi:10.1149/1.3264089
71. Damjanovic, A.; Genshaw, M. A.; Bockris, J. O.'M. *J. Phys. Chem.* **1966,** *70,* 3761–3762. doi:10.1021/j100883a515
72. Clavilier, J.; Armand, D.; Sun, S. G.; Petit, M. *J. Electroanal. Chem.* **1986,** *205,* 267–277. doi:10.1016/0022-0728(86)90237-8
73. Korzeniewsky, C.; Climent, V.; Feliu, J. M. Electrochemistry at platinum single crystal electrodes. In *Electroanalytical Chemistry. A series of advances;* Bard, A. J.; Zoski, C. G., Eds.; CRC Press: Boca Raton, FL, USA, 2012; Vol. 24, pp 75–170.

License and Terms

Beilstein Journal of Nanotechnology

Design criteria for stable Pt/C fuel cell catalysts

Josef C. Meier[*,‡1], Carolina Galeano[‡2], Ioannis Katsounaros[1], Jonathon Witte[1], Hans J. Bongard[2], Angel A. Topalov[1], Claudio Baldizzone[1], Stefano Mezzavilla[2], Ferdi Schüth[2] and Karl J. J. Mayrhofer[*1,§]

Review

Open Access

Address:
[1]Department of Interface Chemistry and Surface Engineering, Max-Planck-Institut für Eisenforschung GmbH, Max-Planck-Strasse 1, 40237 Düsseldorf, Germany and [2]Department of Heterogeneous Catalysis, Max-Planck-Institut für Kohlenforschung, Kaiser-Wilhelm-Platz 1, 45470 Mülheim an der Ruhr, Germany

Email:
Josef C. Meier[*] - meier@mpie.de; Karl J. J. Mayrhofer[*] - mayrhofer@mpie.de

* Corresponding author ‡ Equal contributors
§ Tel.: +49 211 6792 160, Fax: +49 211 6792 218

Keywords:
catalyst design criteria; degradation mechanisms; fuel cell catalyst; nanoparticles; stability

Beilstein J. Nanotechnol. **2014,** *5,* 44–67.
doi:10.3762/bjnano.5.5

Received: 23 July 2013
Accepted: 19 December 2013
Published: 16 January 2014

This article is part of the Thematic Series "Electrocatalysis on the nm scale".

Guest Editor: R. J. Behm

Abstract

Platinum and Pt alloy nanoparticles supported on carbon are the state of the art electrocatalysts in proton exchange membrane fuel cells. To develop a better understanding on how material design can influence the degradation processes on the nanoscale, three specific Pt/C catalysts with different structural characteristics were investigated in depth: a conventional Pt/Vulcan catalyst with a particle size of 3–4 nm and two Pt@HGS catalysts with different particle size, 1–2 nm and 3–4 nm. Specifically, Pt@HGS corresponds to platinum nanoparticles incorporated and confined within the pore structure of the nanostructured carbon support, i.e., hollow graphitic spheres (HGS). All three materials are characterized by the same platinum loading, so that the differences in their performance can be correlated to the structural characteristics of each material. The comparison of the activity and stability behavior of the three catalysts, as obtained from thin film rotating disk electrode measurements and identical location electron microscopy, is also extended to commercial materials and used as a basis for a discussion of general fuel cell catalyst design principles. Namely, the effects of particle size, inter-particle distance, certain support characteristics and thermal treatment on the catalyst performance and in particular the catalyst stability are evaluated. Based on our results, a set of design criteria for more stable and active Pt/C and Pt-alloy/C materials is suggested.

Introduction

The hydrogen-fueled proton exchange membrane fuel cell (PEMFC) is a promising technology for energy conversion especially for local or portable applications [1]. PEMFC convert chemical energy stored in hydrogen into electrical energy in an electrochemical process that requires efficient catalysts for both the facile hydrogen oxidation reaction (HOR) at the anode side

as well as the more sluggish oxygen reduction reaction (ORR) at the cathode side of the fuel cell [2]. The state of the art electrocatalyst for both electrodes are Pt or Pt-alloys dispersed in the form of nanoparticles on a carbon support, in order to achieve a maximum of active sites. Practical performance, however, not only demands high activities per mass for the ORR, but also stability against the aggressive conditions that occur in the fuel cell under operation, particularly on the cathode side [3]. While significant knowledge on factors that influence the activity of the catalyst was obtained in recent years such as alloying platinum with transition metals [4-7] or varying the particle size [8-14], many questions regarding the fundamental degradation mechanisms of such systems remain [15,16].

A stable fuel cell catalyst needs to preserve its activity over an extended lifetime and to avoid degradation under operation, which is macroscopically reflected in a loss of the electrochemically active surface area (ECSA). A gradual loss of ECSA will inevitably lead to efficiency losses of the fuel cell and can eventually reach an unacceptable level, thus determining the end of fuel cell life as a whole. The degradation of fuel cell catalysts depends on multiple parameters linked to the operation conditions of the cell as well as the structure and composition of the electrocatalyst material. Temperature, pH value, potential as well as the humidity and purity of fuel and oxidant feeds are just a few operation parameters that influence the degradation behavior of the catalyst [3,17]. One mode of operation that was found to be particularly harmful for the electrocatalyst are start-up/shut-down conditions, as they can lead to severe potential changes at the cathode, which result in a rapid degradation of the catalyst [17-22]. Over recent years, attempts to circumvent the severe loss of ECSA and the degradation under various conditions have been mainly based on approaches to enhance materials, predominantly by modifying the properties of the support. Finding substitutes for the commonly used carbon black supports is a demanding task, as only few materials present similar electronic conductivities in combination with high surface areas and comparable chemical inertness at the same time [23]. Due to the large versatility of carbon structures, many research groups have focused on a variety of alternative carbon materials [24] as supports for fuel cell applications such as single walled and multi-walled carbon nanotubes (SWCNTs, MWCNTs) [25,26], graphene [27], carbon nanofibers [28], nanohorns [29], ordered mesoporous carbons (OMCs) [30,31], carbon aerogels [32], carbon shells [33-36], colloid-imprinted carbon supports (CIC) [37] and even boron-doped diamond structures [38,39]. Alternatively, certain non-carbon materials (e.g., oxides, carbides and nitrides of metals such as Ti, W, Mo etc.) exhibit promising corrosion resistances under fuel cell conditions. However, most of these non-carbon materials suffer from low conductivities and/or poor platinum dispersion, thus limiting the efficiency of the fuel cell [17]. Despite the demonstration of an improved stability as electrocatalyst under particular conditions, a general and comprehensive performance gain for these advanced materials is still missing. Moreover, in most cases no detailed understanding is available on how the material design influences the degradation pathways that are responsible for the macroscopically observed platinum surface area loss. For standard Pt/C catalysts, indications for a variety of different degradation mechanisms are reported and summarized in the literature [3,15-17,40-42]. In Figure 1 we provide a short summary of catalyst degradation mechanisms that have been suggested to occur in hydrogen fuel cells.

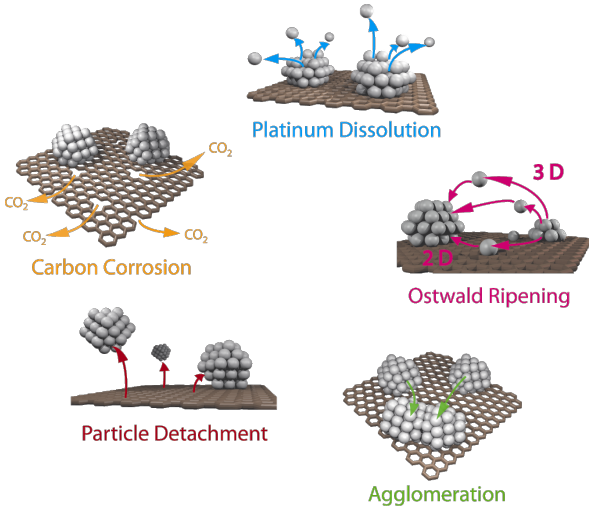

Figure 1: Simplified representation of suggested degradation mechanisms for platinum particles on a carbon support in fuel cells.

A variety of studies have demonstrated that **platinum dissolution** can occur in PEMFCs during operation, as dissolved platinum was detected in the water stream that exited the fuel cells [43]. Platinum was also found to redeposit in the membrane of PEMFCs as a consequence of the reduction with hydrogen that permeates the ionomer from the anode chamber of the cell [44-46]. Platinum dissolution is expected to be especially severe for smaller platinum particles, which have a higher surface energy and are thus considered to dissolve already at lower potentials than bulk platinum (Gibbs–Thomson effect) [14,15]. If the dissolved platinum is redeposited on larger platinum particles, significant particle growth can occur and the according degradation mechanism is called **Ostwald ripening** (3D Ostwald ripening, if the dissolved platinum species travel through the electrolyte, and 2D Ostwald ripening – as known from high temperature TEM studies in the absence of an electrolyte – if platinum atoms are believed to diffuse along the carbon

support) [44,45,47,48]. Another possible explanation for the growth of platinum particles in the catalyst layer is **coalescence** [17,49]. This may be either due to migration and collision of platinum particles on the surface of the carbon support with successive coalescence, or due to strong carbon corrosion. In the second case, neighboring but initially separated particles come into contact with each other because of a successive shrinkage of the carbon support on which they are located [49]. However, also in the first possible case of agglomeration and coalescence due to migration, carbon corrosion may be involved and lead to a weakening of the interactions between platinum particles and support. Alternatively a preferential local corrosion of the support in the surrounding of the platinum particles may facilitate particle movement [50]. A weakening of the interaction between particle and support due to carbon corrosion is also believed to be the cause for the observed **detachment** of whole platinum particles from the support [51,52]. In this context, the ability of platinum to catalyze the oxidation of carbon was suggested to play a decisive role [50,53]. Finally, severe **carbon corrosion** can lead to a loss of the structural integrity of the catalyst layer, which reduces the porosity and thus can result, besides triggering the above catalyst degradation pathways, in mass transport limitations for the reactants [54]. It is also assumed that the formation of excessive oxygenated functional groups at the carbon surface can increase the hydrophilicity of the support and thus enhance flooding effects that can hamper the transport of oxygen to platinum within the catalyst layer and thus lead to a decline in performance [17]. In the light of the aforementioned reasons for the deterioration of the catalyst performance, it is worth distinguishing conceptually between **primary** and **secondary degradation phenomena**. In this sense, carbon corrosion is a primary degradation process and can be the cause for secondary processes such as platinum particle detachment or agglomeration. Moreover, dissolution of platinum can be considered as another primary degradation phenomenon, which is the precondition for secondary degradation phenomena such as Ostwald ripening or platinum deposition in the ionomer.

Much of the up-to-date knowledge on degradation mechanisms of standard fuel cell catalysts has been derived from post-mortem analyses of membrane electrode assemblies (MEAs) after fuel cell operation. Electron-microscopic techniques played a crucial role in such investigations [44,45,55-58]. However, any catalyst testing within a real fuel cell is time demanding and ambiguous because of the high complexity of cell manufacturing [17,59]. Furthermore, standard electron-microscopic post-mortem analysis demands for extensive statistical evaluations in order to obtain meaningful information. Because of the above reasons, several groups recently highlighted the importance of studying changes in the electrocatalyst microstructure by visualizing one specific catalyst location and its transformation under certain imposed aging conditions. Such investigations follow the example of the well-established high temperature in-situ transmission electron microscopy (TEM) measurements, which is utilized to study the behavior of various kinds of catalyst materials at elevated temperatures [60]. More recently, TEM stability studies under environmental conditions, for instance in moisturized air, were also reported [50],[61-63]. Aiming for a visualization of the degradation processes that electrocatalysts undergo under electrochemical conditions, our group has developed an electron microscopic method to study identical locations of catalysts before and after electrochemical aging (i.e., post mortem) while simulating the operation conditions in a fuel cell [51,52]. The identical location transmission electron microscopy (IL-TEM) approach was recently extended to other electron microscopic techniques, such as scanning electron microscopy (IL-SEM) or electron tomography (IL-tomography) [16,40,64,65], and it has been applied in several studies on the degradation behavior of standard fuel cell catalysts that used accelerated-aging protocols [41,42,49,65-70]. These studies have provided direct visual evidence for all of the above mentioned processes under aggressive potential cycling conditions, namely platinum dissolution [16,68], coalescence [16,41,42], particle detachment [42,51,52], carbon corrosion [16,49,70] and Ostwald ripening (3D) [64]. In many cases, several of the discussed mechanisms were observed to occur simultaneously and their contribution to the overall surface area loss seems to vary depending on the applied protocols and the structural properties of the catalyst [16,42,66,67].

In this study, we use identical location electron microscopic techniques in combination with standard electrochemical techniques to provide an in-depth understanding of degradation phenomena under accelerated-aging conditions at low-temperatures. We investigate the electrochemical activity and the macroscopic as well as nanoscale stability of three different Pt/C materials, i.e., Pt/Vulcan 3–4 nm, Pt@HGS 1–2 nm and Pt@HGS 3–4 nm (with Pt@HGS meaning platinum nanoparticles confined within the carbon support HGS) and compare the results with the performance of other conventional fuel cell catalysts. In this context, we will evaluate possible causes for the previously reported excellent stability of the Pt@HGS 3–4 nm material [71]. We therefore summarize and deepen some of our earlier findings and use them as a basis for a broader discussion about design principles for stable Pt/C materials. In particular the impact of the size of the platinum particles, the inter-particle distances, the structure of the support, and of a thermal treatment will be discussed and we provide guidelines for the design of stable nanostructured fuel cell catalysts.

Materials

Two HGS-based catalysts, Pt@HGS 1–2 nm and Pt@HGS 3–4 nm, were selected as model nanostructured materials and compared to Pt/Vulcan 3–4 nm. Each of the three materials is characterized by a platinum content of 20 wt %. The comparison of any set of catalysts reveals a different particle size or a different carbon support. While Pt@HGS 1–2 nm and Pt@HGS 3–4 nm both have the same carbon support they can be distinguished by their particle size distribution. Pt@HGS 3–4 nm and Pt/Vulcan 3–4 nm on the other hand offer a comparable particle size distribution, but the structure of the carbon support is different. An in-depth characterization of the degradation behavior of all three materials, thus, promises insight into the effect of both particle size and support structure on the underlying degradation mechanisms.

The hollow graphitic spheres (HGS) provide a mesoporous, three-dimensional interconnected support structure with a high degree of graphitization and a high BET surface area (ca. 1200 $m^2 \cdot g^{-1}$) at the same time. The synthesis was described previously in detail, however a short summary of the synthesis approach is provided in Scheme S1 (Supporting Information File 1). The majority of the pores in the shell of the hollow spheres are in the size range of 3–4 nm while some are larger, about 8–10 nm. The spheres have an average diameter of about 360 nm with an average shell thickness of approximately 50 nm. The mesoporous network is intended to provide a good separation and encapsulation of the particles without losing accessibility to the Pt particles. The access is also facilitated by the short diffusion pathways through the shell, which are a result of the large void in the middle of the sphere. Graphitization is intended to slow down carbon corrosion and the high specific carbon surface area in combination with the three dimensional network is intended to offer large inter-particle distances and a good particle separation [71].

Because of the large surface area and the mesoporous structure, the platinum deposition results in a high dispersion of platinum particles within the network with platinum nanoparticles in a size range of approximately 1–2 nm (Pt@HGS 1–2 nm). An increase in particle size was possible through a thermal-treatment step up to 900 °C for several hours. The annealing step results in a minor sintering of the initial clusters and leads to an average particle size of about 3–4 nm, which is in the range of the pore size distribution. The particle growth is remarkably well-controlled in the mesoporous network and gives a monodisperse distribution of the particle sizes after the sintering (Pt@HGS 3–4 nm). A first investigation of the electrochemical properties of the Pt@HGS 3–4 nm material has been described before [71]. The synthesis of the Pt/Vulcan 3–4 nm material was also described previously [16]. Contrary to the HGS-based catalysts, colloidal deposition was utilized for platinum deposition in the Pt/Vulcan material. This allowed us to obtain a comparable and defined particle size distribution to the one of Pt@HGS 3–4 nm. Another Pt/Vulcan material with an average particle size of 5–6 nm was used for the activity comparison and was manufactured by mild thermal treatment of the Pt/Vulcan 3–4 nm material.

Results and Discussion

Activity of Pt/C materials

Before focusing on stability, it is essential to compare the activity of the synthesized materials for the ORR (Pt@HGS 1–2 nm, Pt@HGS 3–4 nm and Pt/Vulcan 3–4 nm) with a small library of reference Pt/C catalysts, all measured under the same conditions. Apart from polycrystalline platinum (Pt-poly) and unsupported Pt-black catalyst, all other catalysts consist of platinum nanoparticles supported on carbon in the form of HGS (BET ≈ 1200 $m^2 \cdot g^{-1}$), Vulcan (BET ≈ 250 $m^2 \cdot g^{-1}$) or high-surface-area carbon black (hereafter denoted as HSA, BET ≈ 800 $m^2 \cdot g^{-1}$) in the case of commercial catalysts. Furthermore, the used catalysts have varying platinum contents as well as different platinum particle sizes and thus provide an overview of the impact of various parameters on the activity properties of standard platinum catalysts (see Table 1).

The ORR activities in this study were determined by using the so called thin film method [72,73] in a rotating disk electrode (RDE) setup, in two different electrolytes (0.1 M $HClO_4$ and 0.1 M H_2SO_4). Additionally, compensation for the resistance of the electrolyte by positive feedback has been applied to avoid errors when comparing catalysts with different platinum and carbon content [74]. A representative set of ORR measurements is provided for one of the catalysts studied (Pt@HGS 1–2 nm catalyst) in Figure 2A and Figure 2B. The blue hydrodynamic voltammograms in Figure 2A were recorded in oxygen-saturated 0.1 M $HClO_4$ at different rotation rates (400, 900, 1600, 2500 rpm), while the black curve in the same Figure was recorded in argon-saturated electrolyte to estimate the background response. The latter, which remains unaffected by rotation, is subtracted from the curves recorded in oxygen to receive the response entirely due to the ORR (Figure 2B), thus avoiding an overestimation of kinetic currents due to contributions from the capacitive background. The shape of the ORR voltammograms for both Pt@HGS materials are typical for standard platinum catalysts, with the only difference being that the thermal-treated Pt@HGS 3–4 nm material requires electrochemical activation prior to the activity measurement (ca. 200–300 potential cycles between 0.05 and 1.35 V_{RHE} at 0.2 $V \cdot s^{-1}$). The obtained values for the electrochemical active surface area (ECSA), the specific activity (i.e., kinetic current per platinum surface area) as well as the economically relevant

Table 1: The material and activity data of a small library of reference catalysts is summarized and compared to the three model Pt/C materials. TEM images of the reference catalysts with larger magnification are available in Supporting Information File 1 (see Figure S1). The particle diameters of Pt/C 5 nm, Pt/C 3 nm were provided by the manufacturer. The size derived from XRD is in good agreement with the results from TEM. The particle size for Pt-black was calculated from its ECSA, while all other particle sizes were obtained from TEM.

material	manufacturer	particle size [nm]	Pt content [wt %]	electrochemical active surface area [$m^2 \cdot g^{-1}$]	specific activity in $HClO_4/(H_2SO_4)$ [$mA \cdot cm^{-2}_{Pt}$]	mass activity in $HClO_4/(H_2SO_4)$ [$A \cdot mg^{-1}_{Pt}$]
Poly-Pt	MaTeck	—	100	—	1.8 ± 0.27 (0.43 ± 0.039)	—
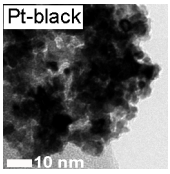	Umicore	10–15	98	18 ± 2	1.4 ± 0.22 (0.27 ± 0.024)	0.26 ± 0.07 (0.049 ± 0.010)
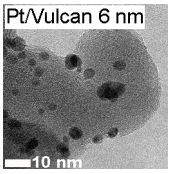	authors' lab	5–6	21	52 ± 6	0.66 ± 0.10 (0.14 ± 0.013)	0.34 ± 0.09 (0.073 ± 0.015)
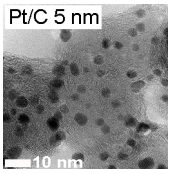	TKK	4.8	51	56 ± 8	0.46 ± 0.07 (0.11 ± 0.012)	0.26 ± 0.08 (0.062 ± 0.014)
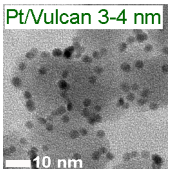	authors' lab	3–4	20	67 ± 6	0.49 ± 0.06 (—)	0.32 ± 0.07 (—)
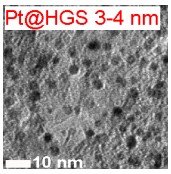	authors' lab	3–4	20	75 ± 11	0.47 ± 0.07 (0.095 ± 0.009)	0.35 ± 0.09 (0.071 ± 0.017)
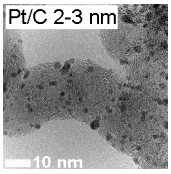	TKK	2.6	46	99 ± 15	0.38 ± 0.06 (0.093 ± 0.008)	0.37 ± 0.11 (0.092 ± 0.022)
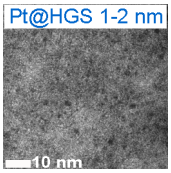	authors' lab	1–2	20	108 ± 16	0.41 ± 0.06 (0.10 ± 0.009)	0.44 ± 0.13 (0.11 ± 0.026)
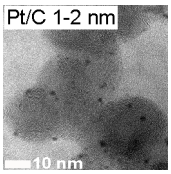	TKK	1–2	10	116 ± 18	0.41 ± 0.06 (0.084 ± 0.008)	0.47 ± 0.14 (0.097 ± 0.024)

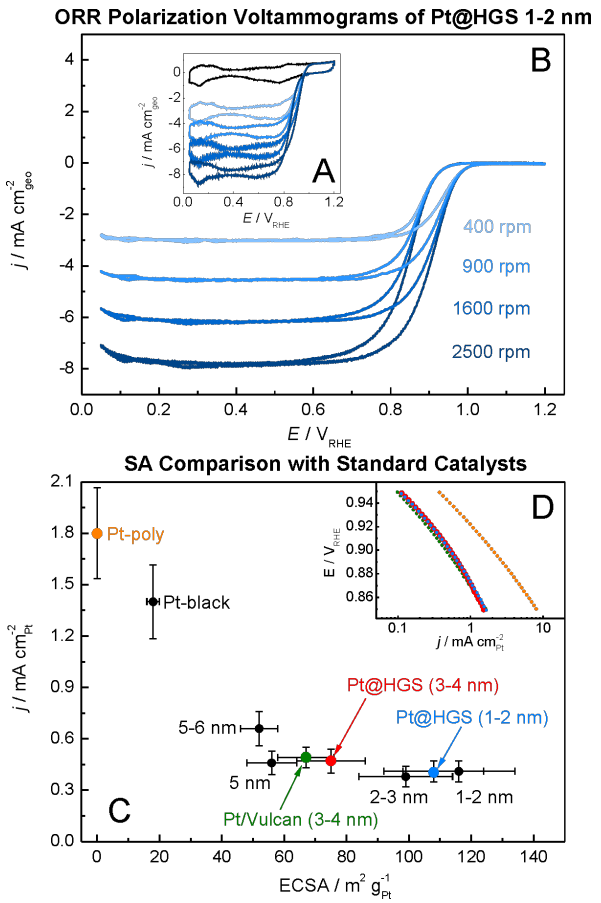

Figure 2: A) ORR cyclic voltammograms of Pt@HGS 1–2 nm in 0.1 M $HClO_4$ saturated with Ar (black) and with oxygen at (400–2500 rpm, blue) recorded at room temperature with a sweep rate of 0.05 V·s^{-1}. B) Same as in A) after subtraction of capacitive currents. C) Plot of the specific activity as derived from the anodic scan at 0.9 V_{RHE} versus the electrochemically active surface area of platinum illustrating the particle size dependent changes in activity. D) Tafel plots from a representative measurement of Pt-poly (orange), Pt@HGS 1–2 nm (blue), Pt@HGS 3–4 nm (red) and Pt/Vulcan 3–4 nm (green). The three Tafel plots of the Pt/C catalysts are almost identical, which indicates comparable specific activities of Pt@HGS based catalysts with standard high surface area fuel cell catalysts.

mass activity (i.e., kinetic current per mass of platinum) for all catalysts in both electrolytes are all summarized in Table 1, together with the most important material properties.

The specific activity values as a function of the ECSA in 0.1 M $HClO_4$ are plotted in Figure 2C (for the according plot in 0.1 M H_2SO_4 see Figure S2 in Supporting Information File 1). The unsupported Pt-poly and Pt-black catalysts clearly present a higher specific activity than all supported platinum nanoparticles-based catalysts, and the activity rapidly drops when the particle size decreases down to 5 nm. For the catalysts below this particle size (i.e., in the region 1–5 nm), changes in the specific activity are minor or even within the error of the measurement, which is in line with previous observations [12,14]. The 5–6 nm Pt/Vulcan catalyst exhibits a slightly increased specific activity compared to all other Pt/C catalysts with smaller sizes, however, this may also be an artifact due to the very broad particle size distribution (ranging from 3–13 nm) of this particular catalyst.

The Pt@HGS 1–2 nm and the Pt@HGS 3–4 nm catalysts are characterized by a specific activity comparable with the other catalysts in the particle size range between 1 and 5 nm. This is also evident from Figure 2D, which depicts representative Tafel plots for polycrystalline platinum, Pt/Vulcan 3–4 nm and both Pt@HGS catalysts. The obtained values for the ECSA (see Figure 2C) are in good agreement with the expected values for catalysts of the according nanoparticle diameters, thus indicating that the platinum nanoparticles confined in the mesoporous shell of the HGS are as well accessible as the platinum on other types of carbon supports. As the specific activity does not change significantly even when going to particle sizes as small as 1 nm, the mass activity increases continuously with decreasing particle sizes. The same trends in specific activity, ECSA and mass activity were also confirmed in sulfuric acid (see Table 1 and Figure S2 in Supporting Information File 1).

Macroscopic stability investigation

While cathode electrocatalysts are rather stable under constant fuel cell operating conditions for hundreds or even thousands of hours, they can degrade rapidly if subjected to more harmful conditions that can for instance occur during start-up and shut-down or in the case of local fuel starvation. Reiser et al. [75] pointed out that potentials at the cathode in this case may locally even exceed values as high as 1.5 V for short periods of time, and already Kinoshita et al. [18] reported that such transitions in potential result in more severe catalyst surface area losses compared to constantly high potentials. These drastic conditions, which can be simulated in electrochemical half-cell experiments by, e.g., subjecting the catalyst to cyclic voltammetry, are a demanding challenge for designing a stable cathode catalyst. Even though it has to be highlighted that the according potential cycling experiments cannot directly reproduce all the phenomena that occur in a real fuel cell as for instance demonstrated recently by Durst et al. [76], they can provide valuable insights about the catalyst performance under well controllable and reproducible conditions.

According potential changes were thus employed in this work by imposing potential cycles between 0.4 and 1.4 V_{RHE} (1 V·s^{-1}, 0.1 M $HClO_4$, room temperature) on the three catalyst materials (Figure 3). In this context it has to be emphasized that all three materials, Pt@HGS 1–2 nm, Pt@HGS 3–4 nm and Pt/Vulcan, were tested with an equal amount of platinum on the working electrode, i.e., 30 $\mu g_{Pt} \cdot cm^{-2}$. Namely the amount of

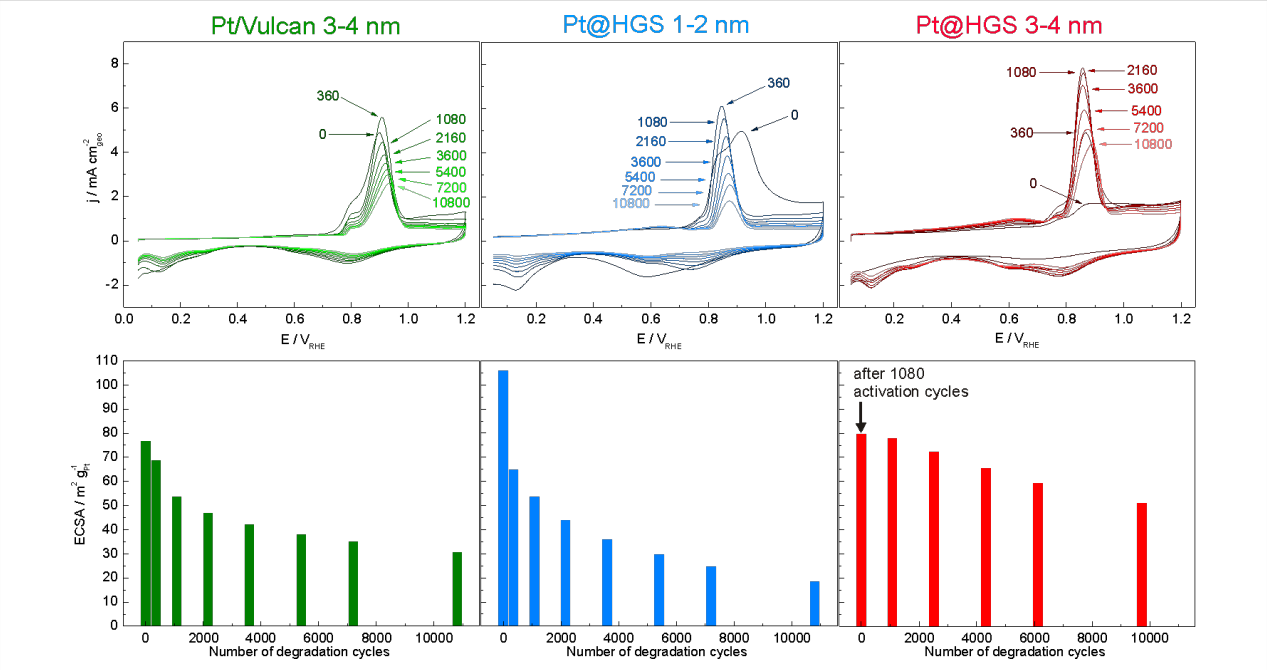

Figure 3: Electrochemical oxidation of a carbon monoxide monolayer (CO-stripping curves) after 0, 360, 1080, 2160, 3600, 5400, 7200 and 10800 degradation cycles for Pt/Vulcan 3–4 nm, Pt@HGS 1–2 nm and Pt@HGS 3–4 nm. The degradation cycles are performed between 0.4 and 1.4 V_{RHE} with a scan rate of 1 $V \cdot s^{-1}$ without rotation at room temperature in argon-saturated 0.1 M $HClO_4$ (not shown). CO-stripping voltammograms (top) were recorded between 0.05 and 1.2 V_{RHE} at a scan rate of 0.05 $V \cdot s^{-1}$ to measure the ECSA versus the number of cycles (bottom). The CO-stripping voltammograms of Pt@HGS 3–4 nm are reprinted with permission from [71]. Copyright 2012 American Chemical Society.

catalyst deposited on the electrode can have a significant influence on catalyst stability in thin film degradation tests and thus needs to be considered to enable a fair comparison. The changes in the platinum surface area of the three catalysts were monitored in between the degradation test via electrochemical oxidation of an adsorbed carbon monoxide monolayer, as described in the Experimental section ("Activity measurements"). A typical CO-stripping voltammogram exhibits no current between 0.05 and approximately 0.6 V_{RHE}. The features of hydrogen desorption in the hydrogen underpotential deposition (H_{UPD}) region, which are typical for cyclic voltammograms of platinum, are not present in that case as the complete platinum surface is covered with adsorbed carbon monoxide, which suppresses the adsorption of hydrogen or other species. The oxidation of the adsorbed CO to CO_2 finally starts in the positively directed scan at potentials around 0.7 V_{RHE} and results in a pronounced CO-stripping peak. Beyond the CO-stripping peak, the current does not decay to zero, which is due to the formation of platinum oxide on the now CO-free surface. The reduction of the formed platinum oxide in the negatively directed scan (ca. 1.0–0.5 V_{RHE}) is followed by the low capacitive currents in the double layer region (ca. 0.5–0.3 V_{RHE}) and the adsorption of hydrogen in the H_{UPD} region (ca. 0.3–0.05 V_{RHE}). The integration of the area under the CO oxidation signal between the CO-stripping voltammogram and the successive voltammogram in CO-free argon atmosphere (background) is a measure of the active surface area.

According CO-stripping experiments were carried out after 0, 360, 1080, 2160, 3600, 5400, 7200 and 10800 degradation cycles. A representative measurement for each of the three catalysts is depicted in Figure 3. For the Pt/Vulcan catalyst, the most rapid decrease in ECSA occurs at the beginning of the degradation test and, in particular, almost half of the total losses in ECSA take place in the first thousand degradation cycles, which corresponds to a tenth of the total amount of imposed potential cycles on the catalyst. After 10800 degradation cycles, the remaining ECSA is 30 $m^2 \cdot g^{-1}$ compared to initially 77 $m^2 \cdot g^{-1}$, corresponding to a loss of about 61% of the original ECSA.

The ECSA loss is more severe for the Pt@HGS 1–2 nm catalyst. The smaller particle size is reflected in the higher initial ECSA of 106 $m^2 \cdot g^{-1}$. However, already after the first 360 degradation cycles, the ECSA of the Pt@HGS 1–2 nm catalyst falls below the ECSA value of the Pt/Vulcan 3–4 nm catalyst. After 10800 degradation cycles, only 18 $m^2 \cdot g^{-1}$ are left, i.e. the total loss of ECSA of the Pt@HGS 1–2 nm catalyst corresponds to 83%. The high initial loss of ECSA for this material, already within the first 360 degradation cycles, is accompanied with a characteristic change of the shape of the carbon monoxide oxi-

dation peak. In particular, before the degradation cycles, the oxidation peak spans a very broad potential range from 0.72 V_{RHE} to potentials above 1.0 V_{RHE}, and has a pronounced shoulder at about 0.85 V_{RHE} and a maximum at 0.91 V_{RHE}. After 360 degradation cycles, the peak has become sharper, the maximum shifts to a more negative potential (0.85 V_{RHE}), while no significant carbon monoxide oxidation is observed anymore above 0.91 V_{RHE}. Since the peak potential of the CO oxidation is more positive for smaller particles [77-79], the described changes of shape and the peak potential shift indicate that the CO oxidation before the treatment takes place mainly on small nanoparticles, which are not present anymore after the first 360 degradation cycles. Thus, the initial drastic surface area loss is most likely linked to a loss/rearrangement of the smallest platinum nanoparticles of the Pt@HGS 1–2 nm catalyst. Moreover, the increase of the current and the evolution of a maximum in the CO-stripping current after 360 degradation cycles at 0.85 V_{RHE}, at which a peak shoulder was observed before degradation, can be interpreted as an indication for an increase of the amount of larger particles. This analysis is also confirmed by the shift of the oxide reduction peak toward more positive potentials after 360 degradation cycles, which is characteristic for the reduction of platinum oxide formed at less oxophilic, larger particles [11].

To confirm that these observations are not related to the support, we imposed the same degradation protocol on a commercial Pt/C catalyst with an average platinum particle size of 1–2 nm (TKK, 10 wt % platinum, see also Table 1), and the same characteristic shape changes in the CO-stripping voltammograms were observed (see supporting Figure S3). Thus, the above mentioned observations are solely due to the initially present small platinum particles, which are not stable even if subjected to only a few degradation cycles, leading to rapid ECSA losses for both the Pt@HGS and the commercial Pt/C catalysts of 1-2 nm size.

A different picture evolves for the Pt@HGS 3–4 nm catalyst, for which no strong CO oxidation, but also no pronounced platinum features are observed before the degradation cycles. This indicates that platinum is initially not accessible to the electrolyte, and that the first potential cycles are necessary for the "activation" of the catalyst material, which is reflected in the increase of both the CO-stripping signal, as well as the characteristic platinum features in the H_{UPD} and platinum oxide regions. This activation process is initially fast, so that about 90% of the catalyst surface is accessible already after less than 500 potential cycles, while afterwards the ECSA increases slowly and reaches its maximum value only after 1080 potential cycles. The need for this harsh activation is attributed to the cleaning of the platinum from carbon impurities that are introduced upon thermal treatment during the material synthesis. The accessibility of the platinum particles in the network is limited by pores that might be blocked by the sintered platinum nanoparticles, as the average particle diameter after the thermal treatment is in the range of the pore size distribution in the mesoporous network. Potential cycling may help to corrode the carbon that is in contact with the sintered platinum particles allowing the recovery of accessibility. The ECSA obtained after 1080 activation/degradation cycles is 80 $m^2 \cdot g^{-1}$, which is comparable to the initial ECSA of the Pt/Vulcan 3–4 nm catalyst and in agreement with what is expected for a catalyst of the according platinum particle size. Throughout the remaining 9720 degradation cycles, the ECSA decays with a lower rate compared to the other two catalysts. The final ECSA of the Pt@HGS 3–4 nm material is 51 $m^2 \cdot g^{-1}$, i.e., the total loss after 9720 cycles is less than 36%, which is much lower than the 83% for the Pt@HGS 1–2 nm catalyst. Even more important, the Pt@HGS 3–4 nm catalyst maintains a significantly higher absolute ECSA than the Pt/Vulcan 3–4 nm catalyst (30 $m^2 \cdot g^{-1}$) after the same number of cycles, which would correspond to a higher voltage and power output in fuel cell operation over an extended time.

Interestingly, the sharp initial decay of the surface area is completely absent for the Pt@HGS 3–4 nm catalyst, while it is quite severe for the other two materials. The reasons for this have not been completely resolved so far, but two likely contributions shall be mentioned here. Shao-Horn et al. [15] suggested, that this fast initial degradation may be explained by the loss of the smallest platinum particles as a result of a rapid dissolution. This suggestion is in agreement with our observations for the Pt@HGS 1–2 nm catalyst, which shows very high initial degradation rates, due to a massive loss of the smallest particles. In contrast, the coalescence of particles being initially in contact can also lead to fast initial degradation for many materials even with larger particle size. This would explain the behavior of the Pt/Vulcan 3–4 nm catalyst and might be important for comparable fuel cell catalysts with high platinum loadings on carbon supports with low surface areas. At a later stage in the degradation process, when particles in close vicinity to each other have already merged into larger ones or when the distances between the platinum particles have increased also due to other degradation mechanisms, further agglomeration and coalescence becomes less likely. The overall degradation becomes less severe since effectively only dissolution remains. These changes in the individual contributions of certain degradation pathways (particle detachment and coalescence) to the overall surface area loss over time seem to be absent in the case of the Pt@HGS 3–4 nm. Thus the stability is only limited by the dissolution of Pt particles from the beginning on, which is in general hard to circumvent. A more detailed microstructural

analysis, as presented in the next section is, therefore, necessary to support this hypothesis.

Stability investigation on the nanoscale

The above described tests focused on the macroscopic differences in loss of ECSA for catalysts with different material properties. To gain insight into the underlying reasons for the different stability characteristics and thus into the impact of the material design on the degradation pathways, investigations at the nanoscale -level are explored in the same manner as described in [71]. IL-SEM was used to study morphological and structural aspects of the support for the Pt/Vulcan 3–4 nm, Pt@HGS 1–2 nm and Pt@HGS 3–4 nm catalysts before and after 3600 potential cycles between 0.4 and 1.4 V_{RHE} (scan rate 1 $V \cdot s^{-1}$, room temperature) in 0.1 M $HClO_4$. Three representative catalyst locations are shown in Figure 4, with the catalysts before and after electrochemical treatment always on top and below, respectively.

The dissimilarity of the two types of employed carbon supports, Vulcan and HGS, becomes evident from Figure 4. While Vulcan is made of primary carbon particles of 10–40 nm that form aggregates with the typical branched chain-like structure of carbon black materials, HGS are characterized by their ball-shaped morphology. The interior of the latter is hollow and thus every sphere contains one large macropore, while the approximately 50 nm thick shell – where the platinum nanoparticles are confined – consists of a three-dimensional interconnected mesoporous network with two maxima in the pore size distribution around 4 and 10 nm [71]. When comparing the untreated and the electrochemically treated catalyst locations in Figure 4, the major observation is that no significant changes take place, neither in the morphology nor in the external surface topology of any of the three samples under investigation. Thus, a structural breakdown of the carbon support due to strong carbon corrosion is not a dominant degradation mechanism for the three materials under these conditions. This is in good agreement with previous IL-TEM studies [40], in which indications for massive carbon corrosion have been found only rarely and at a few catalyst locations at room temperature, while structural breakdown of the carbon support is to be expected mainly at elevated temperatures [49,54]. Even if a loss of structural integrity of the support is not observed, carbon corrosion especially in proximity to platinum cannot be excluded.

While an identification of the platinum nanoparticles on the rough and porous carbon surface of the two Pt@HGS samples via SEM at this magnification is not straightforward, the platinum particles can be readily identified on the Pt/Vulcan 3–4 nm material. Most remarkably, a clear increase in the average particle size for the Pt/Vulcan is already visible from the SEM micrographs. A still better visualization of the platinum nanoparticles can be achieved with the higher resolution in TEM, where a 2D projection of the complete object under investigation discloses also the platinum nanoparticles inside and on the back side of the porous network. Figure 5 shows dark field scanning transmission electron microscopy (DF-STEM) images for all three materials at the same locations as in Figure 4, before (top) and after (middle) the above described electrochemical treatment. A first glance at the three materials before electrochemical treatment indicates that for all of them the platinum particles are well dispersed over the complete carbon support. The impression of the high particle density in the Pt@HGS materials originates from the particles

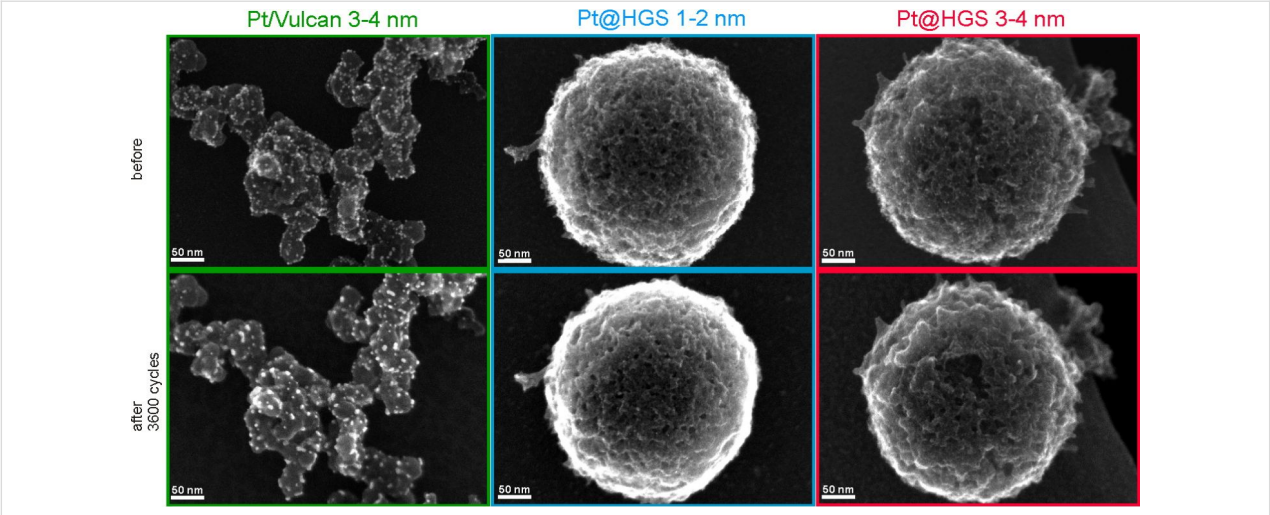

Figure 4: IL-SEM of Pt/Vulcan 3–4 nm (green), Pt@HGS 1–2 nm (blue) and Pt@HGS 3–4 nm (red) after 0 (top) and after 3600 (bottom) potential cycles between 0.4 and 1.4 V_{RHE} in 0.1 M $HClO_4$ at a scan rate of 1 $V \cdot s^{-1}$. IL-SEM visualizes the surface morphology of the materials, in particular the support structure, which is demonstrated not to undergo significant changes during potential cycling at room temperature.

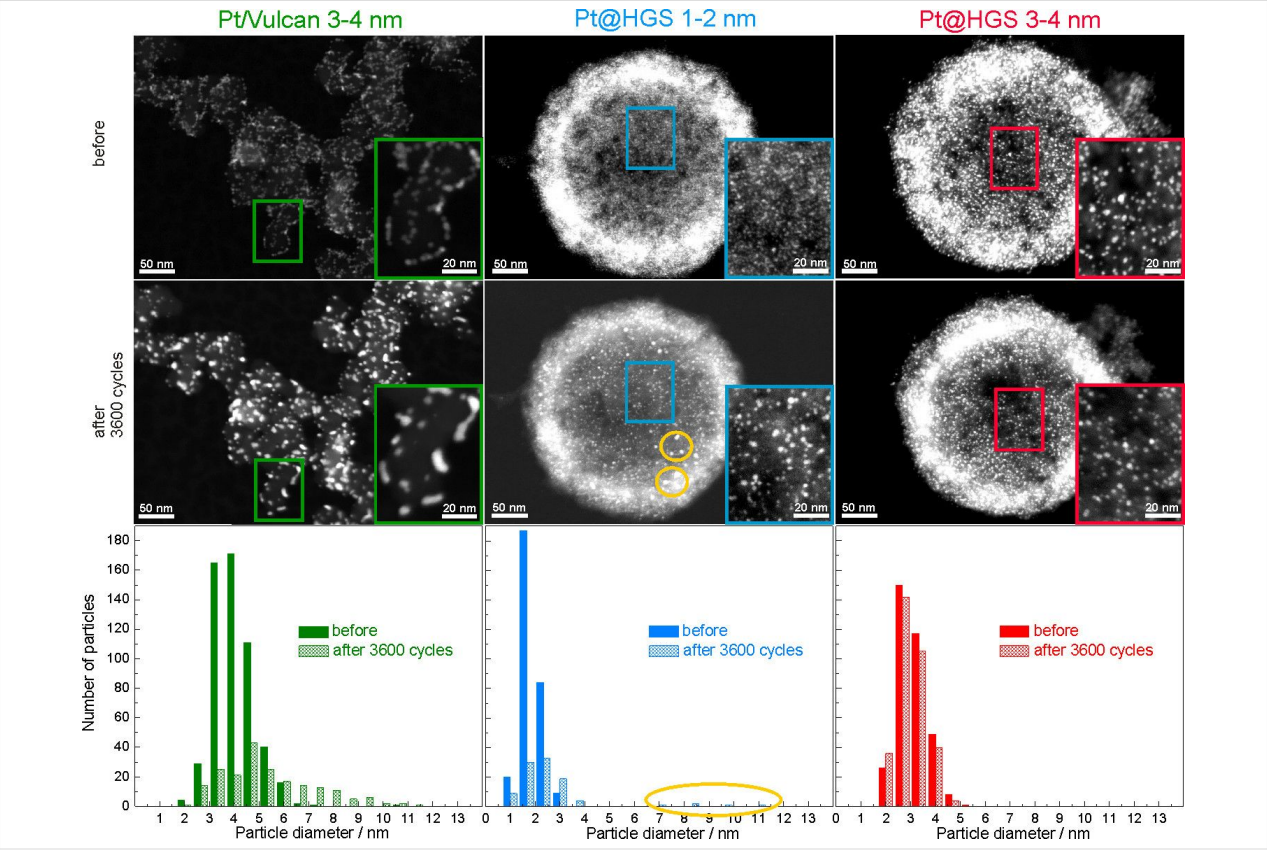

Figure 5: Identical location dark field IL-STEM of Pt/Vulcan 3–4 nm (green), Pt@HGS 1–2 nm (blue) and Pt@HGS 3–4 nm (red) after 0 (top) and after 3600 (middle) potential cycles between 0.4 and 1.4 V_{RHE} in 0.1 M $HClO_4$ at a scan rate of 1 $V \cdot s^{-1}$ at room temperature. The insets highlight sub-regions in the micrograph. The yellow circles for the Pt@HGS 1–2 nm material mark several particles which result from untypical, strong particle growth. The change in particle size distribution for all three Pt/C materials is additionally depicted at the bottom. Bars referring to the same particle diameter before (filled) and after degradation (shaded) are pictured next to each other.

being located at different "levels" throughout the 50 nm thick shell, i.e., some of the particles that appear to be close to each other are tens or hundreds of nanometers (if located at the other side of the sphere) apart. The dispersion of platinum is especially fine for the Pt@HGS 1–2 nm catalyst, as reflected in the blue inset and in the particle size distribution before the degradation test. The Pt@HGS 3–4 nm material (which is produced from the Pt@HGS 1–2 nm material through a thermal-treatment step up to 900 °C for several hours in an inert atmosphere) has clearly undergone a mild sintering of the smaller platinum nanoparticles that led to an average particle size of about 3–4 nm, as can be seen in the red inset and the according particle size distribution before the electrochemical treatment. The particle growth due to the thermal treatment is remarkably well-controlled and the resulting particle size distribution is very monodisperse compared to what is known for other Pt/C materials that have undergone a comparable treatment. This well-defined particle growth is attributed to the defined pore size distribution within the mesoporous network. The comparison between the DF-STEM images before and after degradation shown in Figure 5 provides various insights into the degradation behavior of the three catalysts, which is summarized below.

Description and interpretation of Pt/Vulcan 3–4 nm degradation

A significant alteration of the Pt/Vulcan 3–4 nm catalyst is shown in Figure 5, with a decrease in the total amount of platinum particles and an increase in the average platinum particle size. The strong particle growth is the most obvious occurring degradation process and the shape of the formed clusters in the insets with higher magnification indicates coalescence to be an important degradation mechanism. The particle growth is also clearly reflected in the change in particle size distribution with a tailing towards larger particle sizes, which is frequently interpreted as evidence for agglomeration and coalescence in post-mortem TEM investigations of fuel cell catalysts. However, particle growth is not the only pathway responsible for the loss of platinum ECSA for the Pt/Vulcan 3–4 nm catalyst. Figure 6 is a standard IL-TEM image of another location of Pt/Vulcan 3–4 nm, which reveals that several degradation processes are taking place in parallel. Particle growth is accompanied by

detachment of particles from the Vulcan support, likely as a consequence of the corrosion of carbon in direct contact with platinum (red circle), and dissolution of platinum particles (blue arrow).

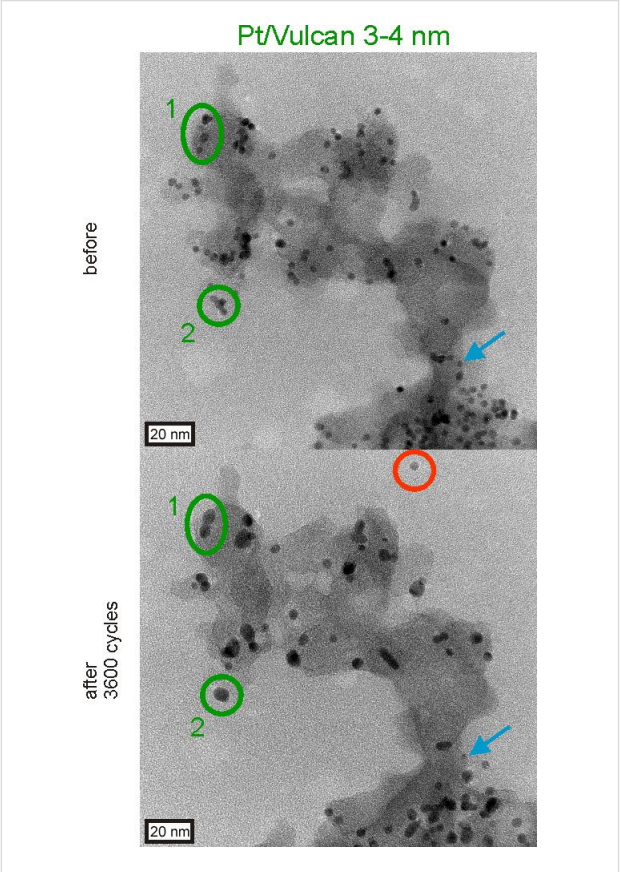

Figure 6: IL-TEM micrographs of Pt/Vulcan 3–4 nm after 0 and after 3600 potential cycles between 0.4 and 1.4 V_{RHE} in 0.1 M $HClO_4$ (scan rate 1 $V \cdot s^{-1}$, room temperature). Blue, red and green symbols mark dissolving, detached and coalescing platinum particles.

Coalescence can originate from particles that migrate on the carbon support during the degradation test, collide and "melt" together when they come into contact, as pointed out by the 1st green circle where "necking" (i.e. a thin bridge between two particles) can be identified. We hereafter refer to this type of particle growth mechanism as agglomeration due to migration, as it is often found in the literature [15]. The situation is slightly different for the platinum particles depicted by the 2nd green circle, where the particles are already in contact with each other from the very beginning and coalescence is immediately possible resulting in larger particles with reduced surface area. We hereafter refer to this type of mechanism as *coalescence due to initial contact*. In this case, coalescence is most likely controlled by surface diffusion processes of platinum atoms of the touching particles. This mechanism seems to be the dominant process also in Figure 5, in which a large number of particles are close to each other already before the degradation test, despite the comparatively good dispersion of particles. To investigate the contribution of the initially dominating coalescence to the overall surface area loss at a different stage we also recorded IL-TEM micrographs on Pt/Vulcan 3–4 nm after 5000 degradation cycles (between 0.4 and 1.4 V_{RHE}, scan rate 1 $V \cdot s^{-1}$, 0.1 M $HClO_4$, room temperature), as shown in Figure 7.

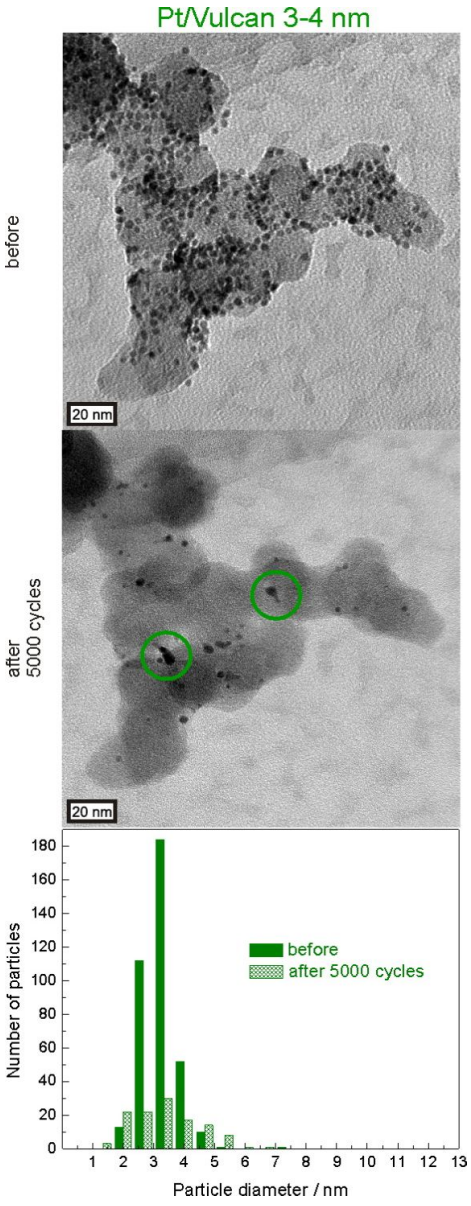

Figure 7: IL-TEM micrographs of the Pt/Vulcan 3–4 nm catalyst before and after 5000 potential cycles between 0.4 and 1.4 V_{RHE} in 0.1 M $HClO_4$ (scan rate 1 $V \cdot s^{-1}$, room temperature). Green circles indicate examples for agglomeration of platinum nanoparticles. The particle size distributions before and after 5000 degradation cycles indicate both particle growth and dissolution to occur. Bars referring to the same particle diameter before (filled) and after degradation (shaded) are pictured next to each other.

Naturally the changes in microstructure are more severe at this later stage in the degradation process and the increase in interparticle distances becomes even more obvious than after 3600 cycles. As can be seen from the representative catalyst location depicted in Figure 7 and based on the shape of the formed clusters, traces of coalescence can still be observed. However, while after 3600 degradation cycles (see Figure 5 and Figure 6) particle growth due to coalescence appears to play the prevailing role and the average particle size increases strongly, no further increase in average particle size is observed when the degradation test is performed for a total of 5000 degradation cycles. In fact, a large number of platinum particles decrease in size due to dissolution, which appears to be the more important degradation pathway regarding its relative contribution to surface area loss at this later stage in the degradation process. Moreover, many clusters that were formed via coalescence are small compared to what would be expected on the basis of the amount of platinum particles initially present in that region, which indicates that also the formed clusters shrink as a consequence of dissolution. These observations are also reflected in the comparison of particle size distributions before and after 5000 degradation cycles. While the number of medium sized particles has decreased, both the amount of larger and smaller particles has increased, confirming that not only coalescence, but also dissolution of platinum is taking place.

It needs to be emphasized that considering the presence of dissolution it cannot be excluded that Ostwald ripening may contribute to the observed particle growth. Namely, in a real fuel cell electrode dissolved platinum ions could either precipitate in the ionomer or on larger particles within the extended 3D structure of the catalyst layer, besides being washed out with the exhaust water. In an IL-TEM experiment, however, only a very small quantity of electrocatalyst is deposited on the TEM grid and thus no extended 3D catalyst layer is present. The catalyst on the grid is exposed to a large volume of electrolyte and thus the concentration of dissolved platinum species remains low, which makes platinum re-deposition less likely to occur. Only for cases in which high amounts of platinum dissolve in a very short period of time, the dissolved platinum concentration at the interface may be sufficient to observe re-deposition and Ostwald ripening in an IL-TEM experiment. The importance of the 3D structure of the catalyst layer for the observation of significant re-deposition as highlighted previously [16,40], was recently confirmed by the investigation of catalyst layers with thicknesses of several micrometers by using IL-SEM [64].

Description and interpretation of Pt@HGS 1–2 nm degradation

As already seen from the macroscopic stability test, the Pt@HGS 1–2 nm catalyst is the least stable of the three catalyst materials, which was attributed to a massive loss of the smallest platinum particles in the initial degradation stage based on an analysis of the CO-stripping features. An unambiguous identification of the underlying degradation mechanisms for the Pt@HGS 1–2 nm material cannot be easily accomplished, because of the complex structure of the HGS support and the small particle size. Nevertheless, the IL-STEM picture in Figure 5 confirms this picture, as a very large amount of the smallest platinum particles is not present anymore after 3600 degradation cycles, while the overall particle density is decreased. The drastic loss of small particles is furthermore reflected in the particle size distribution, in which more than 60% of the particles are gone after the accelerated-aging test and the average particle size has moderately increased from 1.8 nm to 2.5 nm. Indeed platinum dissolution (possibly with successive re-deposition of some of the dissolved platinum) appears as the most likely cause for the strong ECSA losses of the Pt@HGS 1–2 nm material.

In addition, the formation of large platinum particles with a size of about 10 nm highlights a minor contribution of particle growth to the overall degradation. As major dissolution is observed under these conditions in conjunction with the particle growth, a dissolution/re-deposition mechanism may occur. However, coalescence is an at least as likely contributor to the observed particle growth. In particular, the fact that the Pt@HGS 3–4 nm catalyst is prepared by sintering upon thermal treatment of the Pt@HGS 1–2 nm catalyst, shows that coalescence is feasible and that enough platinum nanoparticles are initially in sufficient proximity to each other to allow agglomeration and coalescence. Moreover, coalescence can take place for the Pt/Vulcan 3–4 nm material under exactly the same aging conditions. Therefore it is reasonable to assume that it also plays an important role in the particle growth observed for the Pt@HGS 1–2 nm material.

Description and interpretation of Pt@HGS 3–4 nm degradation

As shown already in the “macroscopic stability test”, the Pt@HGS 3–4 nm catalyst is the most stable of the three investigated Pt/C materials, as it is able to preserve a high ECSA throughout the whole degradation test. The high stability of this catalyst under the aggressive potential cycling treatment is confirmed via IL-STEM in Figure 5, which indicates that there are no significant changes in the catalyst material after 3600 cycles and that the changes in the particle size distribution are less significant compared to the other two materials. Only a very slight increase in the number of the smallest particles and a concomitant minor decrease in the number of larger particles can be interpreted as an indication of dissolution.

In this context, it is important to emphasize that the Pt@HGS 3–4 nm catalyst requires several hundreds of activation cycles, and therefore Figure 5 depicts a somewhat favorable situation for the Pt@HGS 3–4 nm material. Therefore, we additionally performed IL-TEM before and after 5000 degradation cycles (Figure 8) instead of 3600 cycles only, to take the necessary activation amply into account. The comparison of the degradation observed after 5000 cycles for the Pt@HGS 3–4 nm material with the other two materials after 3600 cycles reveals that the Pt@HGS 3–4 nm material is still significantly less degraded, which confirms the findings of the "macroscopic stability tests". The particle size distribution before and after 5000 cycles depicts more clearly now that the number of small particles increases while the number of larger particles decreases, which is evidence for platinum dissolution to occur. It also cannot be excluded that the detachment of platinum particles from the external surface of the HGS catalyst, which are not incorporated in the mesoporous network, may contribute to the modest decrease in total number of platinum particles. While the Pt/Vulcan catalyst of the same particle size shows particle growth and particularly coalescence as a dominant process, no particle growth is observed for the Pt@HGS 3–4 nm catalyst under the applied conditions. Even though a few platinum particles appear to move slightly in the mesoporous network, the majority of particles can be identified separated one by one after the aging test (see Figure S4 in Supporting Information File 1). Thus also the IL-measurements confirm the improved stability behavior of Pt@HGS 3–4 nm. It is worth to mention in this context that first measurements in real fuel cells also indicate an improved stability in line with these findings [71].

Design considerations

The results presented so far, can be summarized in the following. A structural breakdown of the carbon support is not playing a dominant role at room temperature for the three investigated catalysts. Nevertheless, the importance of such a mechanism may strongly increase with increasing temperature [54]. Platinum dissolution is an important degradation mechanism for all three investigated catalysts. The massive loss of smallest particles for the Pt@HGS 1–2 nm catalyst indicates that dissolution is most severe for materials with very small platinum particle size. Pt/Vulcan 3–4 nm and to some extent Pt@HGS 1–2 nm suffer from particle growth, which is mainly attributed to coalescence especially at the initial stage of the degradation process. In contrast, Pt@HGS 3–4 nm does not show any significant particle growth.

Despite some similarities, there are distinct differences in the degradation behavior of the three materials. In order to understand how materials can be designed to mitigate degradation mechanisms and still maintain high ORR activities, it is important to analyze which properties are responsible for the

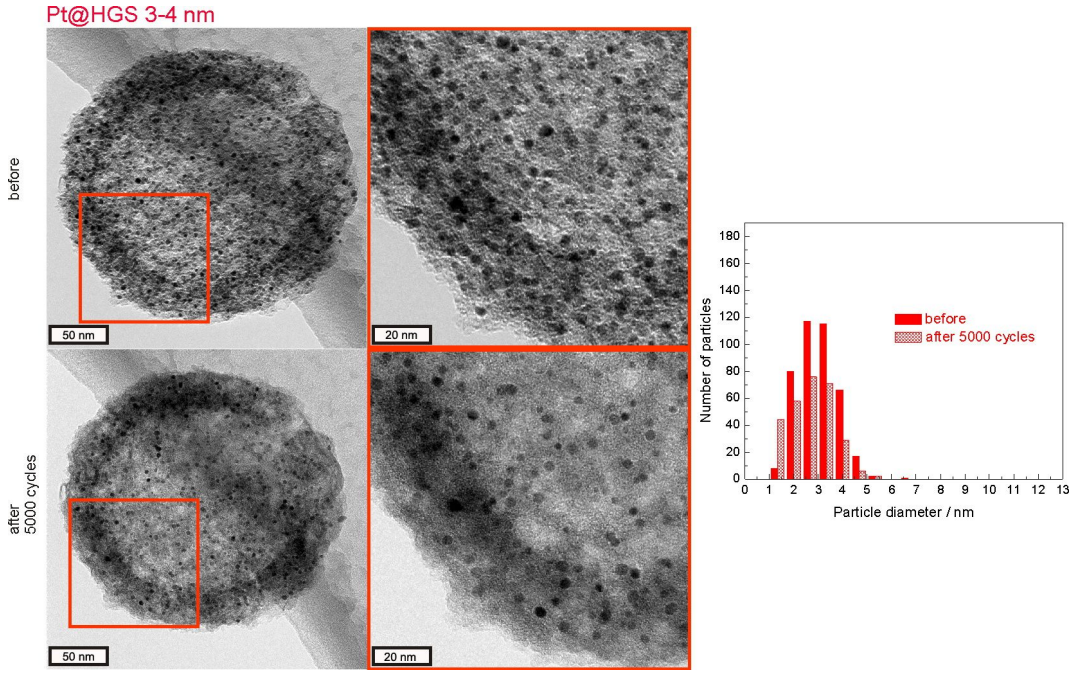

Figure 8: IL-TEM micrographs of the Pt@HGS 3–4 nm catalyst before and after 5000 potential cycles between 0.4 and 1.4 V_{RHE} in 0.1 M $HClO_4$ (scan rate 1 $V \cdot s^{-1}$, room temperature). The red rectangles in the micrographs mark regions, which are magnified on the right. Filled bars refer to the particle size before, shaded bars to the particle size after degradation.

observed differences in the degradation behavior. In the following, we will use the activity data presented in Table 1 and Figure 2 along with the degradation data for the herein investigated catalysts, as well as data from catalysts from other IL-TEM studies, to evaluate the effect of material properties on the activity and degradation behavior of Pt/C catalysts.

Effect of inter-particle distance

Particles can agglomerate due to migration on or shrinkage of the carbon support. When particles establish contact or are already in contact after synthesis, coalescence due to surface diffusion of platinum atoms during potential cycling leads to successive decrease in surface area. The probability of agglomeration and coalescence increases with decreasing distance between particles on the support, since shorter travelling is required to establish contact. As degradation proceeds, the distance between the particles will increase and the contribution of agglomeration and coalescence in the overall surface area loss should decrease over time. Agglomeration and in particular coalescence due to initial contact are not only of importance for the homemade Pt/Vulcan 3–4 nm material, but also for many commercial catalysts. Figure 9 summarizes IL-TEM data from three different studies [52,66,67] for four different Pt/C fuel cell catalysts, which were subjected to the same accelerated-aging test as the three Pt/C catalysts in this study (0.4–1.4 V_{RHE}, 1 $V \cdot s^{-1}$, 0.1 M $HClO_4$, room temperature). More details about the characteristics of these Pt/C materials (as well as others that will be described later) are available in Table 2 (see below). While no agglomeration and coalescence is seen for the Pt/C 5 nm catalyst, particle growth is present for the Pt/C 3 nm catalyst, and even stronger particle growth can be found for the Pt/LSA-C II and Pt/graph-C materials. Pt/LSA-C II is described as a catalyst with a transition-metal modified low surface area (LSA) carbon support, while Pt/graph-C is a catalyst with a graphitized carbon support. Indeed, it can be qualitatively seen in the IL-TEM micrographs (Figure 9) that the largest initial inter-particle distances are observed for the Pt/C 5 nm, followed by the Pt/C 3 nm catalyst, and only very small inter-particle distances are present for the Pt/LSA-C II and the Pt/graph-C materials. In fact, for the latter two catalysts, a large fraction of platinum nanoparticles are in contact already from the beginning and thus coalescence due to initial contact appears to be the likely cause for the massive particle growth of these materials.

It needs to be noted that highly graphitized supports are often used to prevent carbon corrosion however such supports quite commonly exhibit small specific surface areas. At the same time, high platinum loadings are often desirable to reduce the thickness of the catalyst layer in the fuel cell, and thus to reduce the mass transport limitations in the catalyst layer. The combination of the two – high platinum loadings and small carbon surface areas – inevitably leads to Pt/C catalysts with many platinum particles in close proximity or even in contact to each

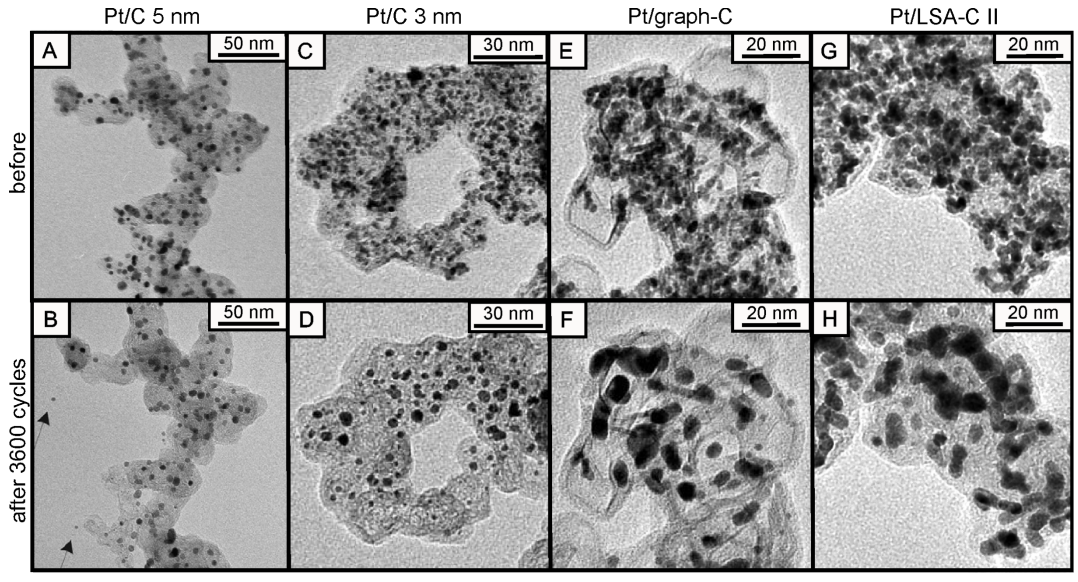

Figure 9: IL-TEM micrographs from degradation studies on four Pt/C fuel cell catalysts. Pt/C 5 nm (A,B) and Pt/C 3nm (C,D) are the same catalysts as depicted in Table 1 and Figure 2. Pt/graph-C (E,F) is a catalyst with graphitized carbon support and Pt/LSA-C II (G,H) is a catalyst with a (transition-metal modified) low surface area support. More information about these and further catalysts can be found in Table 2. A), C), E) and G) depict the catalysts before potential cycling, while B), D), F) and H) are micrographs of the identical locations after 3600 potential cycles between 0.4 and 1.4 V_{RHE} (scan rate 1 $V \cdot s^{-1}$; 0.1 M $HClO_4$, room temperature). A) and B) were reprinted from [52] with permission; Copyright 2008 Elsevier. C)–F) were reproduced from [67] with permission; Copyright 2012 The Electrochemical Society. G) and H) were kindly provided by Arenz and co-workers.

other. Both Pt/LSA-C II and Pt/graph-C are good examples in this respect. While such materials appear susceptible towards agglomeration and coalescence, they do show high carbon corrosion tolerance.

The determination of the inter-particle distance along the surface of the support is not straightforward, as TEM only provides a 2D projection of a 3D reality. Thus a rough estimation of the inter-particle distance of various Pt/C catalysts can only be achieved by taking certain material properties into account, i.e., (i) the platinum content (ii) the surface area of the support (iii) the platinum particle size and (iv) the homogeneity of the distribution of the platinum nanoparticles. Assuming a two-fold monodisperse Pt/C catalyst, i.e., a Pt/C catalyst consisting of both platinum nanoparticles of the same diameter and a perfectly equidistant distribution of those particles on the carbon support, then an equation can be derived from pure geometric considerations to estimate the "average inter-particle distance", l, as a function of the above mentioned parameters (Equation 1):

$$l = \sqrt{\frac{\pi}{3\sqrt{3}} \cdot 10^{-3} \cdot \rho_{Pt} \cdot \left(\frac{100 - L_{Pt}}{L_{Pt}} \right) \cdot A_S \cdot d^3} - d \qquad (1)$$

Where l is the "average inter-particle distance" (nm), ρ_{Pt} is the density of platinum (21.45 $g \cdot cm^{-3}$), L_{Pt} is the platinum content (wt %), A_s is the specific surface area of the support ($m^2 \cdot g^{-1}$), and d is the platinum particle diameter (nm). The derivation and a more detailed explanation of the equation are provided in Supporting Information File 1. It should be noted that a similar equation was derived by Watanabe et al. [80] to study the impact of inter-particle distances on catalyst activity, however, Equation 1, which is provided here to study the probability of agglomeration and coalescence, additionally considers the extension of the platinum particles (i.e., the inter-particle distance is estimated between the surfaces of the particles rather than between their centers).

The average inter-particle distance (AID) corresponds to the length a particle has to travel along the support surface to meet the next platinum particle. Of course, the AID has to be understood as an indicative average value, for the following reasons: (i) since a two-dimensional ideally homogeneous distribution was assumed, the heterogeneity in the distribution of particles, which is clearly present in real systems, is not considered; (ii) a single particle size is considered in the model, while in reality the platinum particle size and also the inter-particle distances, both are subject to a natural distribution; (iii) the model assumes that the distribution of particles on the support is neither affected by favorable sites on the support, nor by any interactions between platinum particles; (iv) the model considers only the initial inter-particle distance before the degradation starts, even though the inter-particle distance (as for instance described earlier in this work for the Pt/Vulcan 3–4 nm material) is a function of time throughout the degradation process. Despite all these simplifications, the AID can be used as a rule of thumb to identify trends in the initially present inter-particle distance and thus for the likelihood for a Pt/C catalyst to suffer from coalescence and/or agglomeration under simulated start-stop conditions. This is for example demonstrated in Table 2, in which the calculated initial AID can be correlated with the extent of particle growth observed.

Almost all of the investigated materials included in Table 2 showed particle growth that was predominantly a result of coalescence, like in the case of the Pt/Vulcan 3–4 nm catalyst. Only for two materials, i.e., Pt/C 5 nm and Pt@HGS 3–4 nm, no observable particle growth after several thousands of potential cycles at room temperature was found. The calculated average inter-particle distances for these two particular catalysts are the largest among all depicted catalysts (i.e., about 28 nm for Pt/C 5 nm and about 48 nm for Pt@HGS 3–4 nm). Note that even though the AID of 28 nm is sufficient for the Pt/C 5 nm catalyst to prevent coalescence at room temperature, this is not the case at higher temperatures. Schlögl et al. [49] investigated the stability of this particular catalyst under constant potential (1.3 V_{RHE}) and at 75 °C (Figure 10). At these elevated temperatures, carbon corrosion played a much more dominant role, and the shrinkage of the carbon support led to a decrease of the inter-particle distances and to successive coalescence as a secondary degradation process.

For all other catalysts depicted in Table 2 the inter-particle distances are much shorter and thus agglomeration and coalescence are already possible at room temperature without the need for strong carbon corrosion. Most remarkably, materials with very small inter-particle distances like Pt/graph-C (<<10 nm) or Pt/LSA-C I and II (2 nm both) (LSA-C I is a standard low surface area support, LSA-C II was described before) are characterized by the most severe particle growth. Even though the inter-particle distance is not the only important parameter to improve catalyst stability, an indication can be provided with the aid of Equation 1 on whether a catalyst with a known support, particle size and loading would offer sufficient inter-particle distances to make coalescence less likely to occur. Figure 11 illustrates how the AID depends on the platinum content for various platinum particle sizes (Figure 11A) and for various specific support surface areas (Figure 11B).

A value of zero for the inter-particle distance in the model would correspond to a densely packed monolayer of platinum

Table 2: Stability data of the three Pt/C catalysts of this study, as well as data from the four catalysts depicted in Figure 9 are summarized. Additionally, three further catalyst materials are included. Information about particle growth was deduced from IL-TEM, while the ECSA loss was determined via thin-film half-cell tests. The data from investigations of Schlögl et al. [49,67], Mayrhofer et al. [51], Hartl et al. [66] and Perez-Alonso et al. [68] were included in the comparison, and the AID was also calculated for these studies by using Equation 1. "rt" indicates experiments at room temperature.

material	publication (catalyst manufacturer)	particle diameter [nm]	Pt content [wt %]	BET support [$m^2 \cdot g^{-1}$]	aging protocol	ECSA loss [%]	calculated AID [nm]	particle growth
Pt/C 3 nm	Schlögl et al. [49,67] (TKK)	2.6	46	800	0.4–1.4 V_{RHE} 3600 cycles 1 $V \cdot s^{-1}$; rt 0.1 M $HClO_4$	55	12	strong
Pt/C 5 nm (heat-treatment)	Mayrhofer et al. [51] (TKK)	4.8	51	800	0.4–1.4 V_{RHE} 3600 cycles 1 $V \cdot s^{-1}$; rt 0.1 M $HClO_4$	31	28	none
	Schlögl et al. [49,67] (TKK)				1.3 V_{RHE} 16 h hold 348 K (75 °C) 0.1 M $HClO_4$	24	<<28 (support shrinks)	strong
Pt/graph-C (graphitized)	Schlögl et al. [49,67] (TKK)	2-3	47	—	0.4–1.4 V_{RHE} 3600 cycles 1 $V \cdot s^{-1}$; rt 0.1 M $HClO_4$	40	<<10	very strong
Pt/LSA-C I	Hartl et al. [66]	3	30	30	0.4–1.4 V_{RHE} 3600 cycles 1 $V \cdot s^{-1}$; rt 0.1 M $HClO_4$	48	2	very strong
Pt/LSA-C II	Hartl et al. [66]	3	28	28	0.4–1.4 V_{RHE} 3600 cycles 1 $V \cdot s^{-1}$; rt 0.1 M $HClO_4$	38	2	very strong
Pt/C 2.3 nm	Perez-Alonso et al. [68]	2.3	10	250	0.6–1.2 V_{RHE} 3000 cycles 0.2 $V \cdot s^{-1}$; rt 0.1 M $HClO_4$	—	17	mild
Pt/C 2 nm	Schlögl et al. [49,67] (TKK)	2	20	—	0.4–1.4 V_{RHE} 3600 cycles 1 $V \cdot s^{-1}$; rt 0.1 M $HClO_4$	58	—	strong
Pt/Vulcan 3–4 nm	current study (authors' lab)	3–4	20	250	0.4–1.4 V_{RHE} 3600 cycles 1 $V \cdot s^{-1}$; rt 0.1 M $HClO_4$	45	20	strong
Pt@HGS 1–2 nm (graphitized)	current study (authors' lab)	1–2	20	1200	0.4–1.4 V_{RHE} 3600 cycles 1 $V \cdot s^{-1}$; rt 0.1 M $HClO_4$	66	13	strong
Pt@HGS 3–4 nm (graphitized, heat-treatment)	current study (authors' lab)	3–4	20	1200	0.4–1.4 V_{RHE} 5000 cycles 1 $V \cdot s^{-1}$; rt 0.1 M $HClO_4$	19	48	none

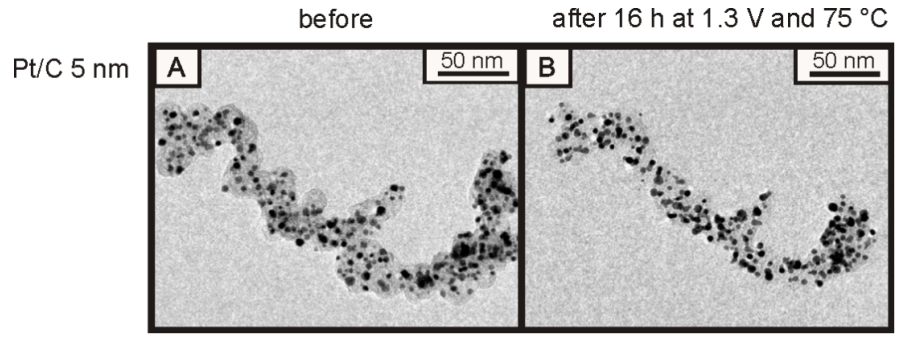

Figure 10: IL-TEM micrograph of Pt/C 5 nm subjected to 1.3 V_{RHE} at 348 K (75 °C) for 16 h in 0.1 M $HClO_4$. A shrinkage of the carbon support due to carbon corrosion with successive decrease in inter-particle distances and coalescence can be observed. The images were reprinted with permission from [49]. Copyright 2011 Elsevier.

nanoparticles on the carbon surface, while negative values indicate that this monolayer would even be exceeded and further particles would be stacked on top. It is noteworthy how strongly the AID decreases with decreasing platinum particle size in Figure 11. While a Pt/C catalyst (with BET of ca. 250 $m^2 \cdot g^{-1}$ as typical for standard Vulcan supports) with a particle size in the

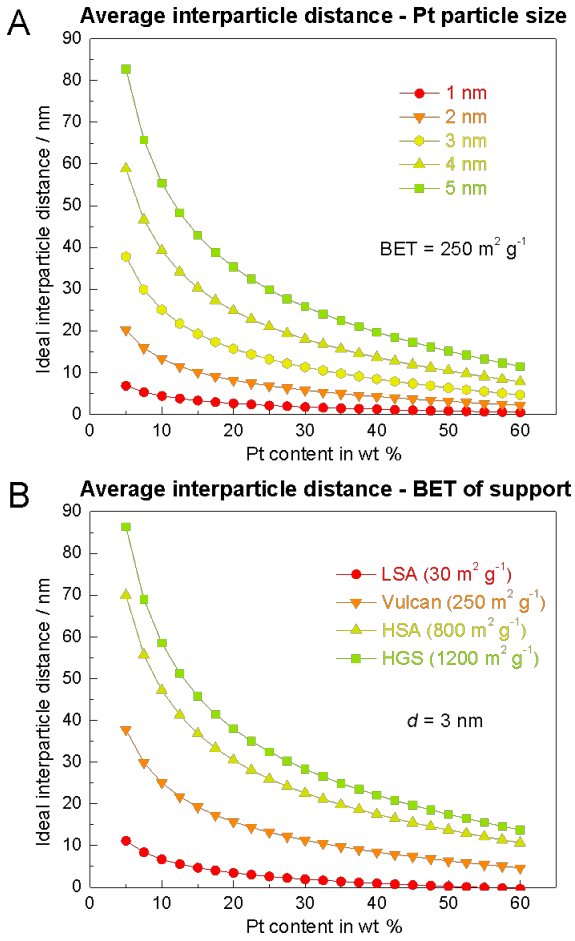

Figure 11: A) Dependence of the AID on platinum content for various platinum particle sizes, calculated for a Vulcan support (BET ca. 250 $m^2 \cdot g^{-1}$) using Equation 1. B) Dependence of the AID on platinum content for various specific support surface areas, calculated for a platinum particle diameter of 3 nm, by using Equation 1.

range of 1–2 nm is already in a regime of small inter-particle distances at low platinum loadings such as 10 wt %, catalysts with platinum particle sizes between 4–5 nm require loadings of 40 wt % or higher to reduce the average inter-particle distance to a similar degree. Moreover, the specific surface area of the carbon support has a strong impact on the AID, as shown in Figure 11B. It can be concluded from that figure that the low surface area supports (LSA) with a BET surface area of around 30 $m^2 \cdot g^{-1}$ (as explored by Hartl et al. [66]), despite providing an improved resistance against carbon corrosion, cannot sufficiently separate the platinum nanoparticles from each other. On the contrary, remarkably larger average inter-particle distances are offered by high surface area carbon supports (HSA), e.g., those for Pt/C 5 nm, 3 nm and 1–2 nm catalysts (all manufactured by TKK), and even more by HGS. This indicates that carbon supports with a high specific surface area have the advantage that higher platinum loadings (or smaller platinum particle sizes) can be used without ending up in inter-particle distances below the critical value at which coalescence is expected.

Apart from agglomeration and coalescence, it needs to be mentioned that small inter-particle distances may similarly enhance an Ostwald-ripening type of mechanism, because large concentrations of dissolved platinum can be expected in close proximity to other particles in regions with high particle density, acting as sites for redeposition. However, while coalescence due to initial contact occurs most likely during the initial stage of catalyst degradation, redeposition of dissolved platinum requires a significant dissolution first, so it probably has a stronger contribution to the overall surface area loss at a later degradation stage, as the findings of Hodnik et al. by using IL-SEM [64] may suggest.

Applying the above findings for the interpretation of the different degradation behavior of Pt/Vulcan 3–4 nm (AID = 20 nm), Pt@HGS 1–2 nm (AID = 13 nm) and Pt@HGS 3–4 nm (AID = 48 nm), helps to understand why the Pt@HGS 3–4 nm material is more stable towards agglomeration and coalescence. Even though Pt/Vulcan 3–4 nm has the same Pt content and a comparable particle size distribution, its inter-particle distance is comparatively small, which has its origin in the small specific surface area of the Vulcan carbon support compared to the HGS support. The Pt@HGS 1–2 nm catalyst on the other side, which again has the same Pt content as the Pt@HGS 3–4 nm catalyst along with the same carbon support, cannot reach a sufficient inter-particle separation due to the dispersion of the platinum into very small particles. The total number of platinum nanoparticles and thus their average distance is thus much smaller for the Pt@HGS 1–2 nm compared to the Pt@HGS 3–4 nm catalyst.

Overall under potential cycling conditions (between 0.4–1.4 V_{RHE} at 1 $V \cdot s^{-1}$) in 0.1 M $HClO_4$ and at room temperature, three regimes for different AID, l, can be roughly identified: (i) $l > 25$ nm → no coalescence; (ii) 10 nm < l < 25 nm → some coalescence (extent dependent on quality and homogeneity of distribution of particles); and (iii) $l < 10$ nm → strong coalescence. Even though a distance of for instance 20 nm may appear as sufficiently large to prevent coalescence, it is crucial to understand that a certain fraction of nanoparticles will be in closer proximity, because the distance l is only an average value, which in reality corresponds to an inter-particle size distribution. In this case the fraction of smallest inter-particle distances (i.e., the number of particles in direct contact or close vicinity) is most likely the decisive parameter for the extent to which coalescence occurs. The above mentioned regimes should be seen as a first guideline, however they require confir-

mation and refinement on the basis of larger data sets. Note that as implied by the discussion of the degradation of Pt/C 5 nm at higher temperatures, the suggested regimes may change significantly under a different set of applied aging conditions.

Effect of particle size

When a defined mass of platinum is dispersed on a given carbon support, decreasing the platinum particle size on a nanometer scale implicates (i) an alteration of electronic properties of platinum (ii) an increasing ECSA and (iii) decreasing inter-particle distances. These implications have a severe impact on the ORR activity as well as on the stability of Pt/C materials under fuel-cell operation conditions. The so called "particle/crystallite size effect" on the ORR (specific) activity was investigated in various studies [8-14] and thus is not at the focus of this work. However, it needs to be mentioned that the activity investigations on a broader basis of catalysts (Table 1 and Figure 2) in the current study confirm recent findings [12,14]. Changes in specific activity for carbon supported catalysts in a range of particle sizes between 1 and 5 nm were found to be within the error of the measurement, whereas a significant increase of specific activity is observed for Pt/C materials with particles larger than 5 nm. This observation was discussed and investigated in more detail in several recent works [12,14] and indicates that an increase in initial mass activity for supported catalysts is optimized by aiming for very small particle sizes.

However, the measurements on Pt@HGS 1–2 nm shown above or on the commercial Pt/C 1–2 nm catalyst (Figure S3 in Supporting Information File 1) demonstrate that catalysts with such small particles are not able to maintain their high initial ECSA, as they degrade very fast because of the rapid loss of the small particles. The low stability of small particles is reflected in Table 2, in which the most severe losses in ECSA are in general observed for catalysts with the smallest particle size. The comparison indicates that besides the AID, the particle size has an outstanding impact on catalyst stability, which is, for instance, also supported by the findings of Shao-Horn and coworkers [14] or Makharia et al. [81] (see below in Figure 12). According to these studies especially catalysts with a large fraction of platinum particles smaller than 2 nm suffer from the most severe surface area losses. A typical explanation for this is that with decreasing size of the platinum particles the curvature of the particles increases and thus the surface energy rises, which can impact the dissolution thermodynamics according to the so-called Gibbs–Thomson effect. This is expected to result in a negative shift of the Nernst potential of platinum dissolution for these particles compared to bulk platinum [15].

Recent observations on the dissolution of polycrystalline platinum with an electrochemical flow cell and online detection of dissolved platinum in the electrolyte via inductively coupled plasma mass spectrometry (ICP-MS) [82] have resulted in three major conclusions: (i) platinum dissolution is a transient process that occurs only when the potential changes cause a substantial change in the platinum surface state, while at constant potential conditions no platinum dissolution was observed; (ii) platinum dissolution can be separated into anodic and cathodic dissolution; and (iii) the amount of anodically dissolved Pt is linked to low-coordinated surface atoms and the amount of cathodically dissolved platinum is linked to the extent of oxidation. In the light of these observations the impact of particle size on platinum dissolution could be explained by the enhanced oxophilicity and thus increased oxide content at a given potential with decreasing particle size [11,14]. Additionally, the contribution of under-coordinated edge and corner sites to the overall surface area is rising for smaller particles. For platinum particles with a diameter of about 2 nm (assuming a cubo-octahedral shape) the surface already consists of more than 50% of under-coordinated edge and corner sites and their contribution drastically increases for even smaller particles, which is why especially Pt/C materials with a large fraction of particles below this size degrade so rapidly. Still, more quantitative investigations will be necessary to resolve the effect of particle size on dissolution, while particularly taking into account the increase in ECSA. Namely, a larger ECSA naturally implicates that more platinum atoms are available for both the desired oxygen reduction reaction as well as the undesirable dissolution of platinum.

The observation that catalysts with a significant amount of platinum particles smaller than 2 nm degrade much faster, suggests that the synthesis of stable Pt/C catalysts should rather aim for larger sizes. Considering that significantly larger particles lead to low mass activities, an average particle size of about 3–4 nm, as often employed anyway in commercial systems, seems to be indeed a reasonable choice for fuel cell materials. Moreover, a narrow particle size distribution, in order to neither waste platinum for unstable smaller particles nor for too large particles with low mass activity, are a precondition for the efficient utilization of platinum.

Effect of thermal-treatment

Makharia et al. [81] performed an extensive study on the effect of thermal treatment, the larger average particle size (as a result of the heat treatment), and additionally on the intrinsic properties induced by alloying. They compared the surface area loss of four catalyst materials (Figure 12), namely Pt/C (2–3 nm), a "poorly dispersed" Pt/C (4–5 nm), a "well-dispersed" heat-treated Pt/C-HT (4–5 nm) catalyst and a platinum-alloy catalyst, i.e., PtCo/C (4–5 nm). All catalysts were subjected to the same single-cell aging test, namely potential cycling between 0.6 and 1.0 V (at 80 °C, 100% RH, 0.02 $V \cdot s^{-1}$).

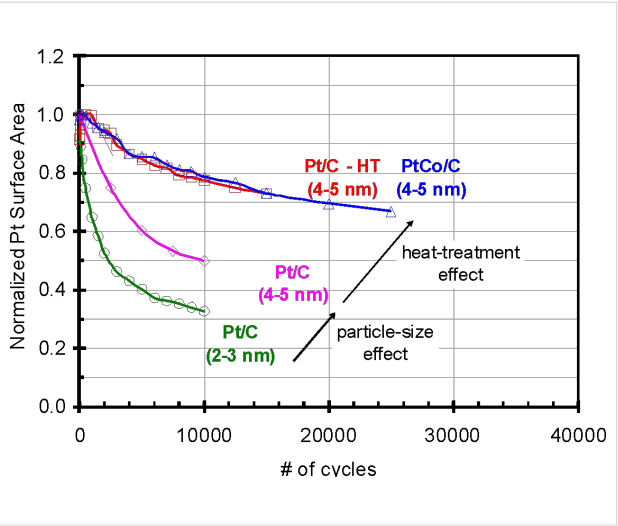

Figure 12: Impact of catalyst particle size and post-synthesis heat treatment on the normalized platinum surface area loss. The test was performed with H_2 on the anode and N_2 on the cathode at 80 °C, 100% RH. The cathode side of the membrane electrode assembly (MEA) is cycled between 0.6 and 1.0 V_{RHE} at 0.02 $V \cdot s^{-1}$. The graph was reproduced from [81] with permission. Copyright 2006 The Electrochemical Society.

First, the findings of Makharia et al. [81] indicate that the improvement of the stability of the alloy catalyst is due to a "heat-treatment effect" (direct or indirect) and not due to an improved intrinsic material stability of the alloy, as both the Pt/C-HT (4–5 nm) and the PtCo/C (4–5 nm) material show an almost identical surface area loss. Furthermore, it is remarkable that their thermally treated Pt/C-HT (4–5 nm) catalyst is significantly more stable than the Pt/C (4–5 nm) reference material, which was synthesized without a thermal-treatment step. Therefore, the stabilization due to thermal treatment cannot merely be attributed to an increase in average particle size, but also other aspects contribute to the effect of the thermal treatment. However, an explanation for the origin of the improved stability upon thermal treatment was not provided. In this context, Shao-Horn et al. [15] emphasized that it is important to take into account the complete particle size distribution and not only the average particle size when comparing thermally treated and non-treated materials. In particular the fraction of smaller particles of Pt/C catalysts is decreased significantly during thermal treatment, as small platinum particles will presumably migrate on the carbon support and coalesce into larger particles. Thus the fraction of platinum particles smaller than 2 nm in the overall particle size distribution will be smaller than for other Pt/C catalysts of comparable average particle size. Since those smaller particles are expected to dissolve faster under degradation conditions, the improved stability of the thermally treated catalyst materials with a smaller fraction of small particles could be explained with the particle size effect, as described above, however, while taking the distribution into account.

This is well in line with our investigations of the Pt/Vulcan 3–4 nm, Pt@HGS 1–2 nm and Pt@HGS 3–4 nm catalysts. However a further effect that contributes to the thermal-treatment effect, which is linked again to the inter-particle distance, was not considered so far. The Pt@HGS 3–4 nm catalyst is produced from the Pt@HGS 1–2 nm material in the process of a thermal-treatment step up to 900 °C. As can be seen from the comparison of the two Pt@HGS materials, not only the particle size increases from 1–2 nm to 3–4 nm during the thermal treatment, but also the AID changes from about 13 nm to about 48 nm after thermal treatment (see magnified insets for both materials in Figure 5). This is probably because particles in close proximity to each other (or even in direct contact) will preferentially already coalesce during the thermal treatment step. Therefore, the fraction of small inter-particle distances will decrease substantially and thus degradation due to agglomeration in general and coalescence due to initial contact in particular will be less likely to occur under fuel-cell operation conditions. The comparison of the degradation of the Pt/Vulcan 3–4 nm catalyst and the Pt@HGS 3–4 nm material as depicted in Figure 5, Figure 6 and Figure 7 supports this interpretation of the thermal-treatment effect due to different inter-particle distances. The Pt/Vulcan 3–4 nm catalyst does not only have a similar average particle size as the Pt@HGS 3–4 nm catalyst, but also a comparable particle size distribution, thus the number of particles smaller than 2 nm is about the same for both materials. However, the particle separation is improved for the thermally treated Pt@HGS 3–4 nm, and this catalyst is also much more stable toward coalescence compared to the Pt/Vulcan 3–4 nm catalyst. Similarly, the commercial Pt/C 5 nm catalyst with an AID of 28 nm (Figure 9 and Table 2) results from a thermal treatment of the Pt/C 3 nm material with an AID of ca. 12 nm [67]. Again, the non-treated catalyst shows significant coalescence among other degradation mechanisms, contrary to the thermally treated catalyst that shows no signs of coalescence during potential cycling at room temperature. It is noteworthy that the effect of thermal treatment was recently also addressed by Stephens et al. [83], who suggested that the heating results in a smoothening of the catalyst surface and the removal of defects or under-coordinated sites, which are most prone to corrosion. It can therefore be summarized that a decrease in the fraction of smallest particles in the particle size distribution, as well as a decrease of the smallest inter-particle distances, eventually together with a decrease of the number of under-coordinated sites, all contribute to the increased stability of thermally treated Pt/C catalysts. It is remarkable that the Pt/C 5 nm catalyst and the Pt@HGS 3–4 nm catalyst, i.e., the only two materials that were synthesized through a thermal treatment, are those with the lowest relative ECSA loss. This emphasizes that the thermal-treatment step to high temperatures is indeed a valuable option to improve the stability of the

material, as long as the particle size can be kept in the desirable range for a high mass activity.

Effects of carbon support: graphitization, specific surface area, surface structure, and pore confinement

While the activity for the ORR (Table 1 and Figure 2) is not significantly influenced by the type of carbon support for the tested Pt/C catalysts in thin-film RDE experiments (a study of mass transport effects would require fuel cell measurements), strong differences in the stability of the catalysts become obvious (see Table 2). Especially the small losses in ECSA for the catalysts with graphitized support (Pt/graph-C) and low surface area supports (Pt/LSA-C I and Pt/LSA-C II) all depict quite good stabilities considering their comparatively small platinum particle sizes, and the initial agglomeration and coalescence due to the very small inter-particle distances as a consequence of their low specific support surface areas. This observation is in good agreement with literature reports that emphasize the positive effect of graphitization on the resistance against carbon corrosion [23,67,84]. The effect of the surface structure of the carbon supports for fuel cell catalysts was demonstrated by Reetz et al. [85] in a separate study. Platinum particles have a lower tendency to agglomerate during the synthesis process of a Pt/C catalyst, if the support surface depicts a pronounced tortuosity. In general micro- and mesopores in carbon support materials are believed to act as a kind of physical barrier [86]. The concept of using the support surface structure to separate the platinum particles can be extended to the extreme case of a 3D interconnected mesoporous network. Here the platinum particles are confined to the mesoporous structure that provides various hosting sites. These hosting sites also play a crucial role during the heat-treatment step and the control of the particle growth via confinement of Pt in pores [71]. Overall, the Pt@HGS 3–4 nm material can thus be considered as an extension of the graphitized catalysts offering not only a high degree of graphitization, but also a high specific surface area and stabilization by a confinement to the pores, which results in a highly active and stable catalyst.

The combination of the graphitization, the thermal-treatment effect and the pore-confinement opens up also an interesting option for highly stable and active Pt-alloy fuel cell catalysts. The disadvantage of a pronounced thermal-treatment step for standard supports, i.e., an increased particle size and thus decreased ECSA and mass activity, generally limits the beneficial effects of alloying on the specific activity. The extraordinary control of the particle growth in the HGS support can help to circumvent this issue and thus offers an excellent opportunity for the synthesis of a new class of high-temperature annealed platinum-alloy catalysts with high ECSA and stability.

Conclusion

Detailed investigations on the activity and the stability of electrochemical half-cells with three selected Pt/C catalysts and comparisons with a library of further Pt/C materials provided insights into several parameters that influence the performance of the catalysts. In particular identical location electron microscopy revealed how the material design can impact the degradation behavior of electrocatalysts under accelerated-aging conditions. Coalescence of not sufficiently well separated platinum nanoparticles on the support often plays a major role, especially at the initial stage of catalyst degradation. The average inter-particle distance (AID), which depends on the surface area of the carbon support, the platinum content of the catalyst, the platinum particle size as well as the quality of the distribution of the platinum particles on the support, was derived as a simple quantity that aids to evaluate an eventual impact of coalescence. Moreover, it was demonstrated that the platinum particle size is one of the most dominant parameters for the stability of the Pt/C catalyst. While a surprisingly small influence of the platinum particle size on the specific activity of the catalyst was found for Pt/C materials based on supported nanoparticles in a range of 1–5 nm, a strong impact on the stability is evident especially when large fractions of the platinum particles are smaller than 2 nm. A thermal treatment of Pt/C catalysts is quite beneficial in this aspect, as it reduces the amount of the smallest particles, which would be otherwise lost during operation, and it also leads to larger AIDs and thus a better separation of the resulting larger particles. In order to optimize carbon-supported catalysts for both, activity and mass activity, it is thus necessary to thoroughly consider all of these aspects. In particular the transformation of the catalyst material during long-term operation should already be taken into account at the stage of materials design.

Experimental

The details of the synthesis and characterization of the HGS support as well as the pore-confinement of the Pt nanoparticles can be found in our previous publication [71]. The electrochemical procedures are shortly summarized in the following, as they have been previously described more extensively [12,16,40,72,73]. All electrochemical measurements were performed in a three-compartment electrochemical Teflon cell, while using a rotating disk electrode (RDE) setup, a radiometer analytical rotation controller and a Gamry Reference 600 potentiostat. A graphite rod was used as counter electrode and an Ag/AgCl electrode (Metrohm) as reference. However, all potentials were referenced to the reversible hydrogen electrode (RHE), which was determined prior to every measurement. The rotator, the potentiostat and the gas flow were automatically regulated by using a LabVIEW based software that was developed in-house [87]. The Ag/AgCl electrode compartment was

separated from the main compartment of the cell via a Nafion membrane to prevent the tested materials from contamination with chlorides during the activity and stability tests [88]. The working electrode was made of a Teflon tip with an embedded glassy carbon disc (5 mm diameter, 0.196 cm^2 geometrical surface area) onto which the catalyst suspension was directly pipetted to form films for the activity or macroscopic stability tests, or on which a gold finder grid was contacted for identical location electron microscopy measurements. In the latter case the catalyst was pipetted on the grid after contacting. The standard electrolyte volume was about 150 mL and all tests were performed at room temperature. The electrolytes, i.e., 0.1 M $HClO_4$ and 0.1 M H_2SO_4, were prepared with ultrapure water (18 MΩ·cm, ELGA) and conc. $HClO_4$ (Merck, Suprapur) or conc. H_2SO_4 (Prolabo, Normapur). The resistance of the solution was taken into account by positive feedback compensation so that the residual uncompensated resistance was less than 4 Ω in all measurements. Catalyst suspensions were made by dispersing the catalyst powders ultrasonically in ultrapure water for at least 30 minutes.

Activity measurements

Activity measurements were carried out for different loadings of catalyst on the working electrode to exclude mass transport limitations as a result of a too thick catalyst film. Freshly sonicated catalyst suspensions (at least 5 minutes prior to application) were pipetted onto the glassy carbon disc and dried in air or under mild vacuum. Typical loadings for the commercial and self-made Pt/C materials were in the range of 2.5 to 40 $\mu g_{Pt} \cdot cm^{-2}$ at the electrode in order to obtain thin and well-dispersed catalyst films. Typical loadings for Pt-black to achieve good films were in the range of 40–80 $\mu g_{Pt} \cdot cm^{-2}$. The materials were subjected to potential cycles before activity and ECSA measurements in order to clean the catalyst surface until stable cyclic voltammograms were obtained. Significantly more cleaning cycles were necessary for the Pt@HGS 3–4 nm catalyst (typically 200–300 cleaning cycles, 0.05–1.35 V_{RHE}, 0.2 $V \cdot s^{-1}$) as a consequence of the heat-treatment procedure during the synthesis. General guidelines for activity measurements were followed as described previously [12,72,73]. Specific activities were calculated from the positively directed scan of the RDE polarization curves at 0.9 V_{RHE}, a rotation rate of 1600 rpm and a scan rate of 0.05 $V \cdot s^{-1}$.The RDE polarization curves were corrected for capacitive processes to consider only the current that was related to the ORR. For this purpose, a cyclic voltammogram recorded with the same scan rate and potential window but in argon-saturated electrolyte was subtracted from the ORR polarization curves.

The platinum surface area was determined by electrochemical oxidation of pre-adsorbed carbon monoxide (CO-stripping). In each CO-stripping measurement, carbon monoxide was adsorbed on platinum in a potential region (e.g., 0.05 V_{RHE}) at which carbon monoxide is stable at the surface, until the saturation coverage was reached. Afterwards, the electrolyte was purged with argon until all carbon monoxide was removed from the electrolyte, while still the same potential was held. Finally, the adsorbed carbon monoxide was oxidized electrochemically in stagnant electrolyte, and the charge corresponding to the oxidation was measured by the area of the oxidation peak. Mass activities were calculated be multiplying the specific activity and ECSA, which was determined independently with several CO-stripping experiments for at least three different catalyst loadings at the working electrode.

“Macroscopic stability tests”

The macroscopic stability tests, i.e., thin-film degradation tests, for the three Pt/C materials were performed on thin films with the same catalyst loading (i.e., the same amount of catalyst on the working electrode) for each of the three materials, namely 30 $\mu g_{Pt} \cdot cm^{-2}$. The tests were done in 0.1 M $HClO_4$, at room temperature and without rotation. The accelerated-aging protocol consisted of 10800 potential cycles (triangular wave) between 0.4 and 1.4 V_{RHE} with a sweep rate of 1 $V \cdot s^{-1}$. The surface of the catalysts was not subjected to potential cycles for cleaning before the test, to report the surface area changes from the start. CO-stripping was used to monitor changes in ECSA after 0, 360, 1080, 2160, 3600, 5400, 7200 and 10800 potential cycles.

“Nanoscale stability test”

The catalyst suspensions as used for the thin-film degradation experiments were diluted by a factor of 5 with ultrapure water. A drop of the suspension was loaded on the front side of a gold finder grid (NHA7, Plano) coated with a holey carbon film (Quantifoil R2/2). To avoid high catalyst loadings, which can result in overlapping catalyst particles, the drop was absorbed off the grid with a tissue after a few seconds. IL-SEM and IL-STEM experiments were performed with a Hitachi S-5500 ultra-high resolution cold field emission scanning electron microscope at 30 kV, which allows SEM as well as STEM measurements. All other IL-TEM measurements were carried out with a JEM-2200FS (Jeol, Japan) transmission electron microscope, operated at an acceleration voltage of 200 kV. The catalyst deposited on the TEM grid was treated electrochemically by immobilizing the gold finder grid on the glassy carbon disc working electrode with the help of a Teflon cap as reported previously [16,40]. The aging procedures were designed analogous to the macroscopic degradation study. Tests after 0 and 3600 or 5000 degradation cycles between 0.4 and 1.4 V_{RHE} with a sweep rate of 1 $V \cdot s^{-1}$ without rotation were applied in 0.1 M $HClO_4$ saturated with argon. The measurements were

again performed at room temperature and IR-compensation was achieved via positive feedback. CO-stripping experiments were not carried out between the degradation cycles for the identical location studies, because it is not possible to determine the area of such low amounts of catalyst as dispersed on the TEM finder grid. All particle size distributions were determined from the 2D IL-TEM and IL-STEM images. As the particles are not spherical, the shape was approximated with ellipses. A diameter corresponding to an ideal circle was calculated for every single particle from the area obtained from the ellipse, and this was used to calculate the average spherical diameter. Further information regarding the basic identical location electron microscopy method can be found in the literature [40,51,71].

Supporting Information

Supporting Information features a schematic illustration of the most important steps in the synthesis process of HGS, Pt@HGS 1–2 nm and Pt@HGS 3–4 nm. TEM images of reference materials, activity data in sulphuric acid, thin-film degradation tests on a commercial Pt/C 1–2 nm catalyst as well as further IL-TEM data are also available together with the derivation of the equation for the average inter-particle distance.

Supporting Information File 1

Further experimental data.
[http://www.beilstein-journals.org/bjnano/content/supplementary/2190-4286-5-5-S1.pdf]

Author contributions

J.C.M. and C.G. contributed equally to the achievement of this work. Nanostructured HGS-based materials and non-commercial Pt/Vulcan electrocatalysts were designed and developed by C.G. Activity measurements were performed by J.C.M. and J.W. Thin-film degradation tests and the nanoscale degradation via the IL-approach were performed by J.C.M. IL-SEM/STEM investigations were developed by C.G, H.B. and J.C.M. The manuscript was written by J.C.M. All authors contributed to scientific discussions and in proof reading of the manuscript.

Acknowledgements

J.C.M. acknowledges financial support by the Kekulé Fellowship from the Fonds der Chemischen Industrie (FCI). We thank Dr. Aleksander Kostka for providing access to the electron microscopy facility and discussions. We furthermore acknowledge Dr. Volker Peinecke and Dr. Ivan Radev from the Zentrum für Brennstoffzellentechnik (ZBT) in Duisburg as well as Prof. Matthias Arenz from Technical University of Denmark in Copenhagen for contributing to scientific discussions.

References

1. Debe, M. K. *Nature* **2012,** *486,* 43–51. doi:10.1038/nature11115
2. Marković, N. M.; Ross, P. N., Jr. *Surf. Sci. Rep.* **2002,** *45,* 117–229. doi:10.1016/S0167-5729(01)00022-X
3. Borup, R.; Meyers, J.; Pivovar, B.; Kim, Y. S.; Mukundan, R.; Garland, N.; Myers, D.; Wilson, M.; Garzon, F.; Wood, D.; Zelenay, P.; More, K.; Stroh, K.; Zawodinski, T.; Boncella, J.; McGrath, J. E.; Inaba, M.; Miyatake, K.; Hori, M.; Ota, K.; Ogumi, Z.; Miyata, S.; Nishikata, A.; Siroma, Z.; Uchimoto, Y.; Yasuda, K.; Kimijima, K.-i.; Iwashita, N. *Chem. Rev.* **2007,** *107,* 3904–3951. doi:10.1021/cr050182l
4. Gasteiger, H. A.; Kocha, S. S.; Sompalli, B.; Wagner, F. T. *Appl. Catal., B* **2005,** *56,* 9–35. doi:10.1016/j.apcatb.2004.06.021
5. Greeley, J.; Stephens, I. E. L.; Bondarenko, A. S.; Johansson, T. P.; Hansen, H. A.; Jaramillo, T. F.; Rossmeisl, J.; Chorkendorff, I.; Nørskov, J. K. *Nat. Chem.* **2009,** *1,* 552–556. doi:10.1038/nchem.367
6. Stamenkovic, V. R.; Fowler, B.; Mun, B. S.; Wang, G.; Ross, P. N.; Lucas, C. A.; Marković, N. M. *Science* **2007,** *315,* 493–497. doi:10.1126/science.1135941
7. Stamenkovic, V. R.; Mun, B. S.; Arenz, M.; Mayrhofer, K. J. J.; Lucas, C. A.; Wang, G.; Ross, P. N.; Marković, N. M. *Nat. Mater.* **2007,** *6,* 241–247. doi:10.1038/nmat1840
8. Bregoli, L. J. *Electrochim. Acta* **1978,** *23,* 489–492. doi:10.1016/0013-4686(78)85025-7
9. Sattler, M. L.; Ross, P. N. *Ultramicroscopy* **1986,** *20,* 21–28. doi:10.1016/0304-3991(86)90163-4
10. Kinoshita, K. *J. Electrochem. Soc.* **1990,** *137,* 845–848. doi:10.1149/1.2086566
11. Mayrhofer, K. J. J.; Blizanac, B. B.; Arenz, M.; Stamenkovic, V. R.; Ross, P. N.; Marković, N. M. *J. Phys. Chem. B* **2005,** *109,* 14433–14440. doi:10.1021/jp051735z
12. Nesselberger, M.; Ashton, S.; Meier, J. C.; Katsounaros, I.; Mayrhofer, K. J. J.; Arenz, M. *J. Am. Chem. Soc.* **2011,** *133,* 17428–17433. doi:10.1021/ja207016u
13. Perez-Alonso, F. J.; McCarthy, D. N.; Nierhoff, A.; Hernandez-Fernandez, P.; Strebel, C.; Stephens, I. E. L.; Nielsen, J. H.; Chorkendorff, I. *Angew. Chem., Int. Ed.* **2012,** *51,* 4641–4643. doi:10.1002/anie.201200586
14. Sheng, W.; Chen, S.; Vescovo, E.; Shao-Horn, Y. *J. Electrochem. Soc.* **2012,** *159,* B96–B103. doi:10.1149/2.009202jes
15. Shao-Horn, Y.; Sheng, W. C.; Chen, S.; Ferreira, P. J.; Holby, E. F.; Morgan, D. *Top. Catal.* **2007,** *46,* 285–305. doi:10.1007/s11244-007-9000-0
16. Meier, J. C.; Galeano, C.; Katsounaros, I.; Topalov, A. A.; Kostka, A.; Schüth, F.; Mayrhofer, K. J. J. *ACS Catal.* **2012,** *2,* 832–843. doi:10.1021/cs300024h
17. Mench, M. M.; Kumbur, E. C.; Veziroglu, T. N. *Polymer Electrolyte Fuel Cell Degradation;* Academic Press: Amsterdam, The Netherlands, 2012.
18. Kinoshita, K.; Lundquist, J. T.; Stonehardt, P. *J. Electroanal. Chem. Interfacial Electrochem.* **1973,** *48,* 157–166. doi:10.1016/S0022-0728(73)80257-8
19. Kreitmeier, S.; Wokaun, A.; Büchi, F. N. *J. Electrochem. Soc.* **2012,** *159,* F787–F793. doi:10.1149/2.019212jes
20. Shen, Q.; Hou, M.; Liang, D.; Zhou, Z.; Li, X.; Shao, Z.; Yi, B. *J. Power Sources* **2009,** *189,* 1114–1119. doi:10.1016/j.jpowsour.2008.12.075
21. Rabis, A.; Rodriguez, P.; Schmidt, T. J. *ACS Catal.* **2012,** *2,* 864–890. doi:10.1021/cs3000864
22. Hartnig, C.; Schmidt, T. J. *J. Power Sources* **2011,** *196,* 5564–5572. doi:10.1016/j.jpowsour.2011.01.044

23. Kinoshita, K. *Carbon: Electrochemical and Physicochemical Properties;* Wiley & Sons: New York, NY, USA, 1988.
24. Sheng, W.; Lee, S. W.; Crumlin, E. J.; Chen, S.; Shao-Horn, Y. *J. Electrochem. Soc.* **2011,** *158,* B1398–B1404. doi:10.1149/2.066111jes
25. Hasché, F.; Oezaslan, M.; Strasser, P. *Phys. Chem. Chem. Phys.* **2010,** *12,* 15251–15258. doi:10.1039/c0cp00609b
26. Kou, R.; Shao, Y.; Wang, D.; Engelhard, M. H.; Kwak, J. H.; Wang, J.; Viswanathan, V. V.; Wang, C.; Lin, Y.; Wang, Y.; Aksay, I. A.; Liu, J. *Electrochem. Commun.* **2009,** *11,* 954–957. doi:10.1016/j.elecom.2009.02.033
27. Biddinger, E. J.; Ozkan, U. S. *J. Phys. Chem. C* **2010,** *114,* 15306–15314. doi:10.1021/jp104074t
28. Brandão, L.; Passeira, C.; Gattia, D. M.; Mendes, A. *J. Mater. Sci.* **2011,** *46,* 7198–7205. doi:10.1007/s10853-010-4638-6
29. Shrestha, S.; Mustain, W. E. *J. Electrochem. Soc.* **2010,** *157,* B1665–B1672. doi:10.1149/1.3489412
30. Meng, Y.; Gu, D.; Zhang, F. Q.; Shi, Y. F.; Yang, H. F.; Li, Z.; Yu, C. Z.; Tu, B.; Zhao, D. Y. *Angew. Chem., Int. Ed.* **2005,** *44,* 7053–7059. doi:10.1002/anie.200501561
31. Job, N.; Maillard, F.; Marie, J.; Berthon-Fabry, S.; Pirard, J.-P.; Chatenet, M. *J. Mater. Sci.* **2009,** *44,* 6591–6600. doi:10.1007/s10853-009-3581-x
32. Smirnova, A.; Dong, X.; Hara, H.; Vasiliev, A.; Sammes, N. *Int. J. Hydrogen Energy* **2005,** *30,* 149–158. doi:10.1016/j.ijhydene.2004.04.014
33. Carroll, N. J.; Pylypenko, S.; Atanassov, P. B.; Petsev, D. N. *Langmuir* **2009,** *25,* 13540–13544. doi:10.1021/la900988j
34. Fang, B.; Kim, J. H.; Lee, C.; Yu, J.-S. *J. Phys. Chem. C* **2008,** *112,* 639–645. doi:10.1021/jp710193s
35. Fang, B.; Kim, J. H.; Kim, M.; Yu, J.-S. *Chem. Mater.* **2009,** *21,* 789–796. doi:10.1021/cm801467y
36. Banham, D.; Feng, F.; Fürstenhaupt, T.; Ye, S.; Birss, V. *J. Mater. Chem.* **2012,** *22,* 7164–7171. doi:10.1039/c2jm00137c
37. Wang, J.; Swain, G. M. *J. Electrochem. Soc.* **2003,** *150,* E24–E32. doi:10.1149/1.1524612
38. Fischer, A. E.; Swain, G. M. *J. Electrochem. Soc.* **2005,** *152,* B369–B375. doi:10.1149/1.1984367
39. Shrestha, S.; Liu, Y.; Mustain, W. E. *Catal. Rev. - Sci. Eng.* **2011,** *53,* 256–336. doi:10.1080/01614940.2011.596430
40. Meier, J. C.; Katsounaros, I.; Galeano, C.; Bongard, H. J.; Topalov, A. A.; Kostka, A.; Karschin, A.; Schüth, F.; Mayrhofer, K. J. J. *Energy Environ. Sci.* **2012,** *5,* 9319–9330. doi:10.1039/c2ee22550f
41. Zana, A.; Speder, J.; Roefzaad, M.; Altmann, L.; Bäumer, M.; Arenz, M. *J. Electrochem. Soc.* **2013,** *160,* F608–F615. doi:10.1149/2.078306jes
42. Nikkuni, F. R.; Ticianelli, E. A.; Dubau, L.; Chatenet, M. *Electrocatalysis* **2013,** *4,* 104–116. doi:10.1007/s12678-013-0126-5
43. Mukerjee, S.; Srinivasan, S. *Handbook of Fuel Cells - Fundamentals, Technology and Applications;* Wiley and Sons: Chichester, UK, 2003.
44. Ferreira, P. J.; La O', G. J.; Shao-Horn, Y.; Morgan, D.; Makharia, R.; Kocha, S.; Gasteiger, H. A. *J. Electrochem. Soc.* **2005,** *152,* A2256–A2271. doi:10.1149/1.2050347
45. Shao-Horn, Y.; Ferreira, P. J.; La O', G. J.; Morgan, D.; Gasteiger, H.; Makharia, R. *ECS Trans.* **2006,** *1,* 185–195. doi:10.1149/1.2214553
46. Aragane, J.; Urushibata, H.; Murahashi, T. *J. Appl. Electrochem.* **1996,** *26,* 147–152. doi:10.1007/BF00364064
47. Ross, P. N.; Petersen, E. E.; Bell, A. T. *Catalyst Deactivation;* M. Dekker: New York, NY, USA, 1987.
48. Bett, J.; Lundquist, J.; Washington, E.; Stonehart, P. *Electrochim. Acta* **1973,** *18,* 343–348. doi:10.1016/0013-4686(73)85002-9
49. Schlögl, K.; Mayrhofer, K. J. J.; Hanzlik, M.; Arenz, M. *J. Electroanal. Chem.* **2011,** *662,* 355–360. doi:10.1016/j.jelechem.2011.09.003
50. Yaguchi, T.; Kanemura, T.; Shimizu, T.; Imamura, D.; Watabe, A.; Kamino, T. *J. Electron Microsc.* **2012,** *61,* 199–206. doi:10.1093/jmicro/dfs041
51. Mayrhofer, K. J. J.; Meier, J. C.; Ashton, S. J.; Wiberg, G. K. H.; Kraus, F.; Hanzlik, M.; Arenz, M. *Electrochem. Commun.* **2008,** *10,* 1144–1147. doi:10.1016/j.elecom.2008.05.032
52. Mayrhofer, K. J. J.; Ashton, S. J.; Meier, J. C.; Wiberg, G. K. H.; Hanzlik, M.; Arenz, M. *J. Power Sources* **2008,** *185,* 734–739. doi:10.1016/j.jpowsour.2008.08.003
53. Linse, N.; Gubler, L.; Scherer, G. G.; Wokaun, A. *Electrochim. Acta* **2011,** *56,* 7541–7549. doi:10.1016/j.electacta.2011.06.093
54. Schulenburg, H.; Schwanitz, B.; Linse, N.; Scherer, G. G.; Wokaun, A.; Krbanjevic, J.; Grothausmann, R.; Manke, I. *J. Phys. Chem. C* **2011,** *115,* 14236–14243. doi:10.1021/jp203016u
55. Yasuda, K.; Taniguchi, A.; Akita, T.; Ioroi, T.; Siroma, Z. *Phys. Chem. Chem. Phys.* **2006,** *8,* 746–752. doi:10.1039/b514342j
56. Yasuda, K.; Taniguchi, A.; Akita, T.; Ioroi, T.; Siroma, Z. *J. Electrochem. Soc.* **2006,** *153,* A1599–A1603. doi:10.1149/1.2210590
57. Wang, Z.-B.; Zuo, P.-J.; Wang, X.-P.; Lou, J.; Yang, B.-Q.; Yin, G.-P. *J. Power Sources* **2008,** *184,* 245–250. doi:10.1016/j.jpowsour.2008.06.037
58. Yoda, T.; Uchida, H.; Watanabe, M. *Electrochim. Acta* **2007,** *52,* 5997–6005. doi:10.1016/j.electacta.2007.03.049
59. Zhang, S.; Yuan, X.-Z.; Hin, J. N. C.; Wang, H.; Friedrich, K. A.; Schulze, M. A. *J. Power Sources* **2009,** *194,* 588–600. doi:10.1016/j.jpowsour.2009.06.073
60. Lee, J.-G.; Lee, J.; Tanaka, T.; Mori, H. *Phys. Rev. Lett.* **2006,** *96,* 075504. doi:10.1103/PhysRevLett.96.075504
61. Simonsen, S. B.; Chorkendorff, I.; Dahl, S.; Skoglundh, M.; Sehested, J.; Helveg, S. *J. Am. Chem. Soc.* **2010,** *132,* 7968–7975. doi:10.1021/ja910094r
62. Simonsen, S. B.; Chorkendorff, I.; Dahl, S.; Skoglundh, M.; Sehested, J.; Helveg, S. *J. Catal.* **2011,** *281,* 147–155. doi:10.1016/j.jcat.2011.04.011
63. Yoshida, K.; Xudong, Z.; Bright, A. N.; Saitoh, K.; Tanaka, N. *Nanotechnology* **2013,** *24,* 065705. doi:10.1088/0957-4484/24/6/065705
64. Hodnik, N.; Zorko, M.; Jozinović, B.; Bele, M.; Dražič, G.; Hočevar, S.; Gaberšček, M. *Electrochem. Commun.* **2013,** *30,* 75–78. doi:10.1016/j.elecom.2013.02.012
65. Yu, Y.; Xin, H. L.; Hovden, R.; Wang, D.; Rus, E. D.; Mundy, J. A.; Muller, D. A.; Abruña, H. D. *Nano Lett.* **2012,** *12,* 4417–4423. doi:10.1021/nl203920s
66. Hartl, K.; Hanzlik, M.; Arenz, M. *Energy Environ. Sci.* **2011,** *4,* 234–238. doi:10.1039/C0EE00248H
67. Schlögl, K.; Hanzlik, M.; Arenz, M. *J. Electrochem. Soc.* **2012,** *159,* B677–B682. doi:10.1149/2.035206jes
68. Perez-Alonso, F. J.; Elkjaer, C. F.; Shim, S. S.; Abrams, B. L.; Stephens, I. E. L.; Chorkendorff, I. *J. Power Sources* **2011,** *196,* 6085–6091. doi:10.1016/j.jpowsour.2011.03.064
69. Dubau, L.; Castanheira, L.; Berthomé, G.; Maillard, F. *Electrochim. Acta* **2013,** *110,* 237–281. doi:10.1016/j.electacta.2013.03.184
70. Liu, Z. Y.; Zhang, J. L.; Yu, P. T.; Zhang, J. X.; Makharia, R.; More, K. L.; Stach, E. A. *J. Electrochem. Soc.* **2010,** *157,* B906–B913. doi:10.1149/1.3391737

71. Galeano, C.; Meier, J. C.; Peinecke, V.; Bongard, H.; Katsounaros, I.; Topalov, A. A.; Lu, A.; Mayrhofer, K. J. J.; Schüth, F. *J. Am. Chem. Soc.* **2012,** *134,* 20457–20465. doi:10.1021/ja308570c
72. Paulus, U. A.; Schmidt, T. J.; Gasteiger, H. A.; Behm, R. J. *J. Electroanal. Chem.* **2001,** *495,* 134–145. doi:10.1016/S0022-0728(00)00407-1
73. Schmidt, T. J.; Gasteiger, H. A.; Stab, G. D.; Urban, P. M.; Kolb, D. M.; Behm, R. J. *J. Electrochem. Soc.* **1998,** *145,* 2354–2358. doi:10.1149/1.1838642
74. van der Vliet, D.; Strmcnik, D. S.; Wang, C.; Stamenkovic, V. R.; Marković, N. M.; Koper, M. T. M. *J. Electroanal. Chem.* **2010,** *647,* 29–34. doi:10.1016/j.jelechem.2010.05.016
75. Reiser, C. A.; Bregoli, L.; Patterson, T. W.; Yi, J. S.; Yang, J. D. L.; Perry, M. L.; Jarvi, T. D. *Electrochem. Solid-State Lett.* **2005,** *8,* A273–A276. doi:10.1149/1.1896466
76. Durst, J.; Lamibrac, A.; Charlot, F.; Dillet, J.; Castanheira, L. F.; Maranzana, G.; Dubau, L.; Maillard, F.; Chatenet, M.; Lottin, O. *Appl. Catal., B* **2013,** *138-139,* 416–426. doi:10.1016/j.apcatb.2013.03.021
77. Cherstiouk, O. V.; Simonov, P. A.; Zaikovskii, V. I.; Savinova, E. R. *J. Electroanal. Chem.* **2003,** *554-555,* 241–251. doi:10.1016/S0022-0728(03)00198-0
78. Maillard, F.; Eikerling, M.; Cherstiouk, O. V.; Schreier, S.; Savinova, E.; Stimming, U. *Faraday Discuss.* **2004,** *125,* 357–377. doi:10.1039/b303911k
79. Arenz, M.; Mayrhofer, K. J. J.; Stamenkovic, V.; Blizanac, B. B.; Tomoyuki, T.; Ross, P. N.; Markovic, N. M. *J. Am. Chem. Soc.* **2005,** *127,* 6819–6829. doi:10.1021/ja043602h
80. Watanabe, M.; Sei, H.; Stonehart, P. *J. Electroanal. Chem. Interfacial Electrochem.* **1989,** *261,* 375–387. doi:10.1016/0022-0728(89)85006-5
81. Makharia, R.; Kocha, S.; Yu, P.; Sweikart, M. A.; Gu, W.; Wagner, F.; Gasteiger, H. A. *ECS Trans.* **2006,** *1,* 3–18. doi:10.1149/1.2214540
82. Topalov, A. A.; Katsounaros, I.; Auinger, M.; Cherevko, S.; Meier, J. C.; Klemm, S. O.; Mayrhofer, K. J. J. *Angew. Chem., Int. Ed.* **2012,** *51,* 12613–12615. doi:10.1002/anie.201207256
83. Stephens, I. E. L.; Bondarenko, A. S.; Grønbjerg, U.; Rossmeisl, J.; Chorkendorff, I. *Energy Environ. Sci.* **2012,** *5,* 6744–6762. doi:10.1039/c2ee03590a
84. Xia, B. Y.; Wang, J. N.; Teng, S. J.; Wang, X. X. *Chem.–Eur. J.* **2010,** *16,* 8268–8274. doi:10.1002/chem.201000758
85. Reetz, M. T.; Schulenburg, H.; Lopez, M.; Spliethoff, B.; Tesche, B. *Chimia* **2004,** *58,* 896–899. doi:10.2533/000942904777677083
86. Rodríguez-Reinoso, F. *Carbon* **1998,** *36,* 159–175. doi:10.1016/S0008-6223(97)00173-5
87. Topalov, A. A.; Katsounaros, I.; Meier, J. C.; Klemm, S. O.; Mayrhofer, K. J. J. *Rev. Sci. Instrum.* **2011,** *82,* 114103. doi:10.1063/1.3660814
88. Mayrhofer, K. J. J.; Ashton, S. J.; Kreuzer, J.; Arenz, M. *Int. J. Electrochem. Sci.* **2009,** *4,* 1–8.

License and Terms

Beilstein Journal of Nanotechnology

The role of oxygen and water on molybdenum nanoclusters for electro catalytic ammonia production

Jakob G. Howalt[1,2] and Tejs Vegge[*1]

Full Research Paper

Open Access

Address:
[1]Department of Energy Conversion and Storage, Technical University of Denmark, DK-4000 Roskilde, Denmark and [2]Center for Atomic-scale Materials Design, Department of Physics, Technical University of Denmark, DK-2800 Kgs. Lyngby, Denmark

Email:
Tejs Vegge[*] - teve@dtu.dk

* Corresponding author

Keywords:
ammonia; density functional theory; electrocatalysis; nanoparticles; oxygen poisoning

Beilstein J. Nanotechnol. **2014,** *5,* 111–120.
doi:10.3762/bjnano.5.11

Received: 30 September 2013
Accepted: 17 January 2014
Published: 31 January 2014

This article is part of the Thematic Series "Electrocatalysis on the nm scale".

Guest Editor: R. J. Behm

Abstract

The presence of water often gives rise to oxygen adsorption on catalyst surfaces through decomposition of water and the adsorbed oxygen or hydroxide species often occupy important surfaces sites, resulting in a decrease or a total hindrance of other chemical reactions taking place at that site. In this study, we present theoretical investigations of the influence of oxygen adsorption and reduction on pure and nitrogen covered molybdenum nanocluster electro catalysts for electrochemical reduction of N_2 to NH_3 with the purpose of understanding oxygen and water poisoning of the catalyst. Density functional theory calculations are used in combination with the computational hydrogen electrode approach to calculate the free energy profile for electrochemical protonation of O and N_2 species on cuboctahedral Mo_{13} nanoclusters. The calculations show that the molybdenum nanocluster will preferentially bind oxygen over nitrogen and hydrogen at neutral bias, but under electrochemical reaction conditions needed for nitrogen reduction, oxygen adsorption is severely weakened and the adsorption energy is comparable to hydrogen and nitrogen adsorption. The potentials required to reduce oxygen off the surface are −0.72 V or lower for all oxygen coverages studied, and it is thus possible to (re)activate (partially) oxidized nanoclusters for electrochemical ammonia production, e.g., using a dry proton conductor or an aqueous electrolyte. At lower oxygen coverages, nitrogen molecules can adsorb to the surface and electrochemical ammonia production via the associative mechanism is possible at potentials as low as −0.45 V to −0.7 V.

Introduction

Molybdenum nanoclusters have been identified as a prime candidate for electrochemical ammonia production with seemingly low Faradaic losses to hydrogen evolution [1,2]. To produce ammonia electrochemically, one can either use a liquid or a solid electrolyte, but these effectively require wet conditions to obtain sufficient protonic conduction [3,4]. The pres-

ence of water may give rise to oxygen or hydroxide adsorption on the surface, which can occupy or block important surfaces sites. The adsorbed oxygen species can either decrease or totally hinder other chemical reactions taking place at that site. Oxygen poisoning of the surface is indeed a main inhibitor for ammonia production [5,6]. In this paper, the presence of oxygen species, e.g., resulting from a dehydrogenation reaction of residual water from a solid electrolyte or an aqueous electrolyte, will be investigated to understand the implications it has on the catalytic properties for electrochemical ammonia production. In addition, the blocking of active sites by oxygen species has been explored; together with a determination of reduction pathways to electrochemically reduce the blocking oxygen off the surface.

Computational Method

DFT calculations

The calculations were carried out with density functional theory (DFT) calculations [7,8] using the RPBE exchange correlation functional [9] along with the projector augmented wave method [10,11] as implemented in the GPAW code [12-14]. A grid of (3,3) for the finite difference stencils have been used together with a grid spacing of 0.18 Å and a minimum of 20 free bands above the Fermi level. Periodic boundary conditions with a Monkhorst–Pack [15] k-point sampling of 2 × 2 × 2 were used to perform a methodological consistent comparison with previously obtained results on stepped and flat surfaces [1,16]. A 7 Å vacuum layer on all sides of the nanocluster is applied, giving a separation of 14 Å between the clusters. When solving the electronic density self-consistently, the convergence criteria have been chosen such that the changes were $\leq 10^{-5}$ eV for the energy and 10^{-4} electrons per valence electron for the density. In all calculations, a Fermi smearing of 10^{-4} eV has been used. The atomic simulation environment ASE [17] was used to set up the atomic structure of these systems. All calculations were performed without spin polarization in order to enable full structural (and atomic) relaxation of the full Mo_{13} nanocluster together with the adsorbates (N, H, O, NH, etc.); these were carried out using the BFGS and FIRE [18] optimizers within ASE.

Electrochemical modelling

The procedure for electrochemical reduction of nitrogen molecules through the associative mechanism is outlined in [2,16]. It was shown that the associative mechanism is the preferred route for electrochemical ammonia production, where the protonation of the nitrogen molecules give rise to a weakened N–N bond and subsequent splitting at the third or fourth protonation step. The dissociative mechanism, the other route for electrochemical ammonia production, is due to high dissociation barriers (1.8 eV) of N_2 not taking place at the surface.

For the purposes of analyzing the reduction of oxygen, a two-step electron-transfer process was assumed and simulated using the Heyrovsky-type [19] reaction. In an acidic environment, the reaction comprises of these elementary reaction steps:

$$\mathrm{O}^* + 2\left(\mathrm{H}^+ + \mathrm{e}^-\right) \rightleftharpoons \mathrm{OH}^* + \left(\mathrm{H}^+ + \mathrm{e}^-\right)$$

$$\mathrm{OH}^* + \left(\mathrm{H}^+ + \mathrm{e}^-\right) \rightleftharpoons \mathrm{H_2O}^*$$

$$\mathrm{H_2O}^* \rightleftharpoons \mathrm{H_2O(g)} + ^*,$$

where e^- is an electron in the electrode, H^+ is a proton in the electrolyte and * is a surface site. The reference potential is set to that of the standard hydrogen electrode, and through the computational hydrogen electrode approach the electrons and protons are introduced into the analysis, where $1/2\ H_2 \rightleftharpoons H^+ + e^-$. Hereby, a description of the effects of an external applied potential U on the electrons and the concentration of protons in the electrolyte [20-24] are implemented.

The adsorption energy of O* under electrochemical reaction conditions under an applied potential U are calculated as $\Delta E_0(U) = E_{\mathrm{surface/O}} - E_{\mathrm{surface}} - E_{\mathrm{H_2O(g)}} + 2E_{\mathrm{H^+ + e^-}}(U)$, where $E_{\mathrm{surface/O}}$ and E_{surface} are the total energies of the molybdenum nanocluster with and without the specific oxygen atom adsorbed, and $E_{\mathrm{H_2O(g)}}$ is the gas phase energy of water and $E_{\mathrm{H^+ + e^-}}(U)$ are the energy of protons and electrons with an applied potential defined by the computational hydrogen electrode approach. Molecular O_2 is not expected to be present under operating conditions and the sole contributor of O atoms is water. At standard ambient temperature and pressure the adsorption energies are corrected with zero-point energy, E_{ZPE}, and entropy, TS, contributions at room temperatures.

$$\begin{aligned}\Delta G &= \Delta E + \Delta E_{\mathrm{ZPE}} - T\Delta S - neU + kT \cdot \ln\left[\mathrm{H}^+\right] \\ &= \Delta E + \Delta E_{\mathrm{ZPE}} - T\Delta S - neU + 2.3 \cdot kT \cdot \mathrm{pH}\end{aligned} \quad (1)$$

In this paper the pH value is set to 0 and the values of the free energy corrections for all the oxygen containing species were found in literature [25], were the $\Delta E_{\mathrm{ZPE}} - T\Delta S$ corrections for O is 0.05 eV, for OH is 0.35 eV and for H_2O is 0.67 eV. A pH of, e.g., 7 would change the energy by 0.41 eV for all the reduction mechanisms, leaving the relative activity unchanged.

Results and Discussion

Oxygen adsorbed in nitrogen vacancies

We have previously shown that partially reduced nitrogen covered molybdenum nanoclusters are promising catalysts for

electrochemical production of ammonia [2]. N_2 adsorption is preferred over H in nitrogen vacancy sites at lower nitrogen coverages at the potential of $U = -0.6$ V needed for electrochemical ammonia production through the associative mechanism [2]. Adsorption of oxygen atoms at nitrogen vacancy sites is presented in Figure 1, where they have been adsorbed at the vacant bridge site.

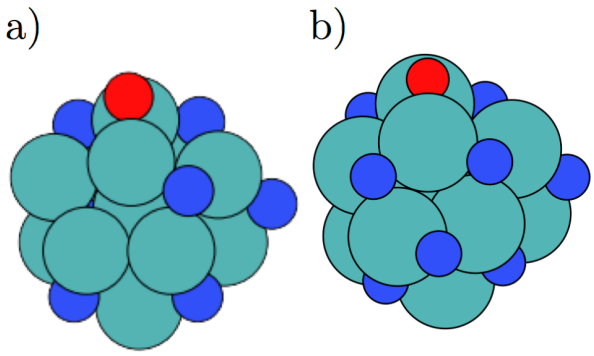

Figure 1: (a) Adsorption of oxygen at a nitrogen vacancy site on $Mo_{13}N_{10}$, and (b) adsorption of oxygen at a nitrogen vacancy site on $Mo_{13}N_{12}$. Oxygen is adsorbed in the bridge site in both cases.

The free energies for oxygen absorption are shown in Table 1 for neutral bias and the potential needed for ammonia production, and listed together with the energies for nitrogen and hydrogen (from [2]). At neutral bias, oxygen is the preferred adsorbate with adsorption energies of −1.58 eV increasing to −2.15 eV. Under these conditions, the vacancy sites will be filled with oxygen and block nitrogen molecules from adsorbing to the active sites and stop the electrochemical formation of ammonia.

At the potentials needed for ammonia production (−0.6 V), the adsorption of oxygen is weakened by 1.2 eV, due to the change in energy from oxidation of water at the applied potential, i.e., $-2U$. Under these conditions, the adsorption of oxygen has a comparable stability to nitrogen and hydrogen.

The strong preference for oxidation at neutral bias means that the particles will often be (partially) oxidized during synthesis or sample transfer [24]. To free the active sites for N_2 adsorption and subsequent electrochemical ammonia production, the adsorbed oxygen atoms needs to be removed from the surface sites. One way of re-activating the molybdenum nanocluster for electrochemical ammonia production is therefore to reduce the oxygen electrochemically to water, which will be less strongly bound to the active site and make it possible to bind N_2 preferentially.

In the case of oxygen adsorption on the more nitrogen rich molybdenum nanoclusters, Table 2 shows the required potentials for the two-proton transfer steps in the reduction of oxygen.

Table 2: Reduction of oxygen adsorbed on the $Mo_{13}N_x$ nanocluster.

	$U_{O\rightarrow OH}$ [V]	$U_{OH\rightarrow H2O}$ [V]
$Mo_{13}N_{12}O$	−0.35	−1.62
$Mo_{13}N_{11}O$	−0.97	−1.25
$Mo_{13}N_{10}O$	−1.18	−1.28
$Mo_{13}N_9O$	−0.72	−1.41

The potentials range from −1.28 to −1.62 V for the second protonation step, where the formation of H_2O is hindered by the adsorbed nitrogen atoms in the three fold hollow sites, surrounding the adsorption site of O, OH and H_2O. The high potential needed for the formation of H_2O is due to the repositioning of the adsorption site of OH (bridge site) to the adsorption site of H_2O (ontop site), which is structurally hindered by the nearby adsorbed nitrogen atoms. The removal of oxygen from the partially nitrogen covered molybdenum surface and oxygen will therefore constitute a strong blocking of the active sites and subsequently limit the ammonia production rate through the associative mechanism on partially oxidized nitrogen covered molybdenum nanoclusters.

Table 1: Stability of nitrogen, hydrogen and oxygen with ($U = -0.6$ V) and without ($U = 0$ V) an applied potential at nitrogen vacancy sites on $Mo_{13}N_x$ nanoclusters. The potential required to produce ammonia electrochemically at partially nitrogen covered molybdenum nanoclusters was shown to be $U = -0.6$ V [2]. The energies are given with respect to H_2O (g), H_2 (g) and N_2 (g). (The values for ΔG_{N2}, ΔG_H ($U = 0$ V) and ΔG_H ($U = -0.6$ V) are taken from [2]).

	ΔG_{N2} [eV]	ΔG_H [eV] ($U = 0$ V)	ΔG_O [eV] ($U = 0$ V)	ΔG_H [eV] ($U = -0.6$ V)	ΔG_O [eV] ($U = -0.6$ V)
$Mo_{13}N_{12}$	−0.06	−0.66	−1.58	−1.26	−0.38
$Mo_{13}N_{11}$	−0.43	−0.71	−2.24	−1.31	−1.04
$Mo_{13}N_{10}$	−1.2	−0.73	−2.33	−1.33	−1.13
$Mo_{13}N_9$	−1.13	−0.59	−2.15	−1.19	−0.95

Direct reduction of the residual nitrogen skin will, however, still be possible and the potential will not be influenced by the presence of oxygen and the nitrogen skin will be reduced electrochemically at −0.6 V as shown in [2].

An oxygen skin

The electrochemical production of ammonia will not only occur on nitrogen covered molybdenum clusters, but could also take place at very low or no nitrogen coverage [2]. A clean molybdenum nanocluster in contact with nitrogen, hydrogen and water at neutral bias will also adsorb oxygen from water on the surface, see Figure 2. The figure shows the total adsorption free energies of oxygen, nitrogen and hydrogen as the coverage evolves and until saturation of oxygen and nitrogen is obtained on the surface. This oxygen skin is approximate 1–2 eV more energetically favoured than a nitrogen skin at low coverage. At higher coverage, the oxygen skin becomes even more energetically favoured. However, an applied potential of $U = -0.6$ V, destabilizes oxygen (dashed blue line) significantly with respect to nitrogen and hydrogen (dashed red line), such that an overlayer of oxygen arising from electrochemical splitting of water should not be expected.

A cyclic pattern is seen in the binding energy for both nitrogen and oxygen adatoms, and the distance between the cycles correspond roughly to an addition of 10 electrons, corresponding to the filling of a d-shell. Figure S1 in Supporting Information File 1 shows the d-band of the molybdenum nanocluster as the oxygen coverage increases and it is observed that the d-band broadens and the energetically lower lying d-orbitals are filled additionally as the coverage of oxygen is increased.

The preferred adsorption sites for the oxygen atoms are the three fold hollow sites, see Figure 3a. When all the three fold sites are filled, the oxygen atoms will adsorb in the four fold hollow sites, see Figure 3c, where additional adsorption of a few oxygen atoms greatly distorts the surface; this restructuring allows a higher filling of oxygen on the surface, see Figure 3d. The maximum filling of the surface increases to 16 oxygen atoms and further additions of oxygen atoms are energetically unfavourable. Close to a full overlayer, the binding sites of oxygen becomes asymmetrically and the oxygen atoms now binds in a mix of a three fold hollow site and a bridge site.

Reduction of the oxygen overlayer

For a fully oxygen covered molybdenum nanocluster, nitrogen molecules cannot adsorb to the surface. Therefore, a full oxygen skin eliminates electrochemical ammonia production. It is therefore necessary to reduce the surface, in order to create active sites for nitrogen adsorption. To investigate the reduction of oxygen on a partially or fully oxygen covered molybdenum

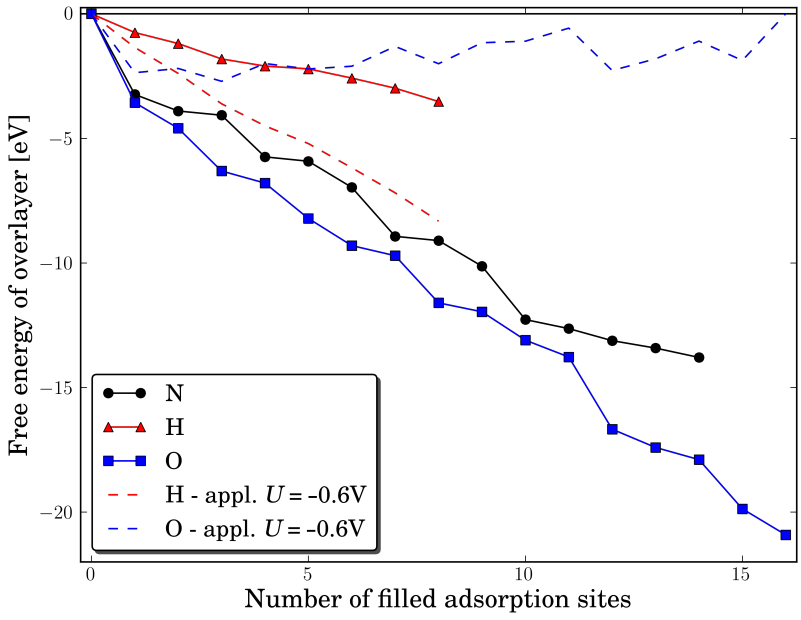

Figure 2: The total free energy for covering the Mo_{13} nanocluster with nitrogen, oxygen or hydrogen. The filled black line shows the filling of the nitrogen skin, while the filled blue line shows the evolution of oxygen coverage at neutral bias. The red coloured line shows the adsorption of hydrogen, while the dashed red coloured line shows adsorption of hydrogen and the dashed blue line shows the adsorption of oxygen at an external applied potential of −0.6 V, which is the potential needed for electrochemically ammonia production previously determined for the clean and nitrogen covered molybdenum nanocluster [2].

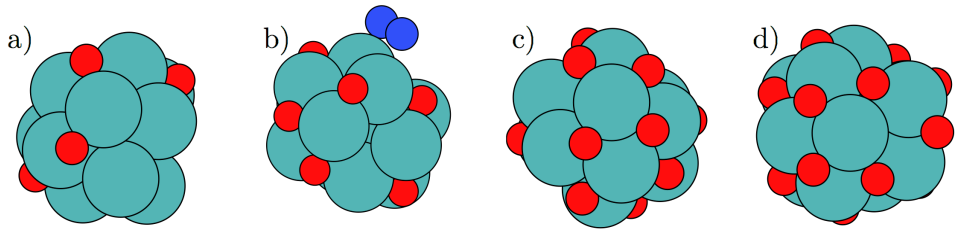

Figure 3: (a) The $Mo_{13}O_6$ nanocluster, (b) the $Mo_{13}O_9$ nanocluster with N_2 adsorbed, (c) the $Mo_{13}O_{12}$ with an almost filled oxygen skin, (d) the $Mo_{13}O_{16}$ with a filled oxygen skin. At the $Mo_{13}O_{16}$, the oxygen adsorption sites are a mix of three fold hollow sites and bridge sites.

nanocluster, the reduction of all adsorbed oxygen atoms should, in principle, be analysed. This is, however, not computationally feasible and instead up to three representative adsorbed oxygen atoms are reduced at each investigated oxygen coverage. Each of the selected oxygen atoms represents a unique oxygen adsorption position and the coverage ranges from 16 oxygen atoms to only one oxygen atom. The potentials needed for the two proton transfer processes are presented in Table 3. For other proton transfer processes (not shown), the local geometries around the adsorption site can hinder both protonation steps, but most often the second protonation is hindered. One such hindrance can be the movements from the adsorption site of the OH species to an on top site, where the H_2O species is energetically most stable. Such movement requires a restructuring of the local environment, and hence the protonation step can become strongly endothermic. The largest variation is therefore seen for the second protonation step. For the presented reduction steps of OH to H_2O, the required potentials are in the range of −0.2 to −0.7 V. The formation of OH from O will require a negative potential to stabilize the OH specie compared to the O atom, and in most cases the potential required are in the range of −0.3 V to −0.7 V.

For most of the studied coverages, the reaction free energies for desorption of H_2O off the surface are either low or exergonic. In general, desorption energies are lower than 0.4 eV, but for a single adsorbed H_2O molecule, it is as high as 1.2 eV. Water should therefore desorb thermally from the surface, except at very low oxygen coverages.

Table 3: Reduction of an oxygen overlayer on molybdenum nanoparticles. Multiple adsorbed oxygen atoms have been reduced at the studied oxygen coverage. This is done to probe the reduction of all the unique adsorption sites at the studied oxygen coverage.

	$U_{O\rightarrow OH}$ [V]	$U_{OH\rightarrow H2O}$ [V]
$Mo_{13}O_{16}$	−0.49	−0.44
$Mo_{13}O_{14}$	0.04	−0.47
$Mo_{13}O_{12}$	−0.64	−0.66
$Mo_{13}O_9$	−0.27	−0.67
$Mo_{13}O_6$	−0.29	−0.24
$Mo_{13}O_2$	−0.44	−0.31
$Mo_{13}O$	−0.67	−0.72

The study of oxygen reduction produces adsorption energies for O, OH, H_2O at different coverages. No apparent correlation is found between the adsorption energies of E_O, E_{OH} and E_{H2O} on the cluster, see Figure S2 and Figure S3 in Supporting Information File 1, in contrast to what has previously been observed on metal surfaces, where scaling relations are applicable for OH species on close-packed and stepped surfaces for low coverages [26]. The close packed and stepped surfaces typically have less restructuring during the adsorption of O, OH and H_2O.

On the molybdenum nanocluster surface, larger local restructuring takes place when either O is added or removed and when either O or OH is protonated. The restructuring of the molybdenum cluster involves all atoms in the nanocluster. This is an effect of the small size of the nanocluster, where the local impact from an adsorption or a reduction step influences the whole nanocluster.

The lowest required potential for water formation at the different coverages is in the range of −0.3 V to −0.7 V. These values are lower or comparable to the required potential needed to form ammonia on the molybdenum nanocluster [2]. Overall, it seems that it is possible to reduce oxygen of the surface at moderate potential of −0.72 V. The potential required for reduction of a surface oxygen atom indicates that the nanoclusters can be reactivated after exposure to water from the electrolyte or the fabrication process.

Formation of ammonia at relative high oxygen coverage

Nitrogen molecules are not able to adsorb to neither an oxygen vacancy site nor ontop of an oxygen atom at high oxygen coverages. Once the oxygen skin has been partially reduced, the nitrogen molecules adsorb onto the surface at the oxygen

vacancy sites, see Figure 3b. The adsorption of nitrogen become stable at a coverage of less than 10 oxygen atoms, see Table 4. The adsorption energies of N_2 range from −1.0 eV to −1.8 eV depending on the oxygen coverage. The corresponding hydrogen adsorption energies are lower, ranging from −0.65 eV to −0.86 eV, and nitrogen molecules are therefore preferred over hydrogen on the surface at neutral bias. At an applied potential of −0.6 V, which is the potential shown to electrochemically produce ammonia on the clean molybdenum nanocluster, the reaction free energy of adsorbing either a hydrogen atom (coming from H^+ and e^-) or a nitrogen molecule will at certain coverages be in favour of H ($Mo_{13}O_8$ and $Mo_{13}O_6$) and others of N_2 ($Mo_{13}O_9$ and $Mo_{13}O_7$).

For nitrogen molecules adsorbed at a vacancy site on either $Mo_{13}O_9$ or $Mo_{13}O_6$, the potential for driving the electrochemical production of ammonia has been determined. These nanoclusters were selected to describe the two regimes with either strong or weak N_2 adsorption compared to hydrogen adsorption, respectively. On the $Mo_{13}O_9$ nanocluster, N_2 is bound most strongly at an applied potential of −0.6 V, while hydrogen is bound stronger on the $Mo_{13}O_6$ nanocluster. Investigations of the associative pathway on the $Mo_{13}O_9$ nanocluster, shows the first protonation step to require an onset potential of −0.7 V similar to that needed to reduce oxygen (see Table 3). The onset potentials are shown in Figure 4 for the following electrochemical reaction steps:

Table 4: The adsorption free energies of nitrogen and hydrogen with and without an applied potential on a partly oxygen covered Mo_{13} nanocluster.

	ΔG_{N2} [eV]	ΔG_H [eV] (U = 0 V)	ΔG_H [eV] (U = −0.6 V)
$Mo_{13}O_{12}$	No binding	−0.23	−0.83
$Mo_{13}O_{10}$	0.33	−0.84	−1.44
$Mo_{13}O_9$	−1.82	−0.72	−1.32
$Mo_{13}O_8$	−1.02	−0.75	−1.35
$Mo_{13}O_7$	−1.77	−0.86	−1.46
$Mo_{13}O_6$	−0.93	−0.65	−1.25

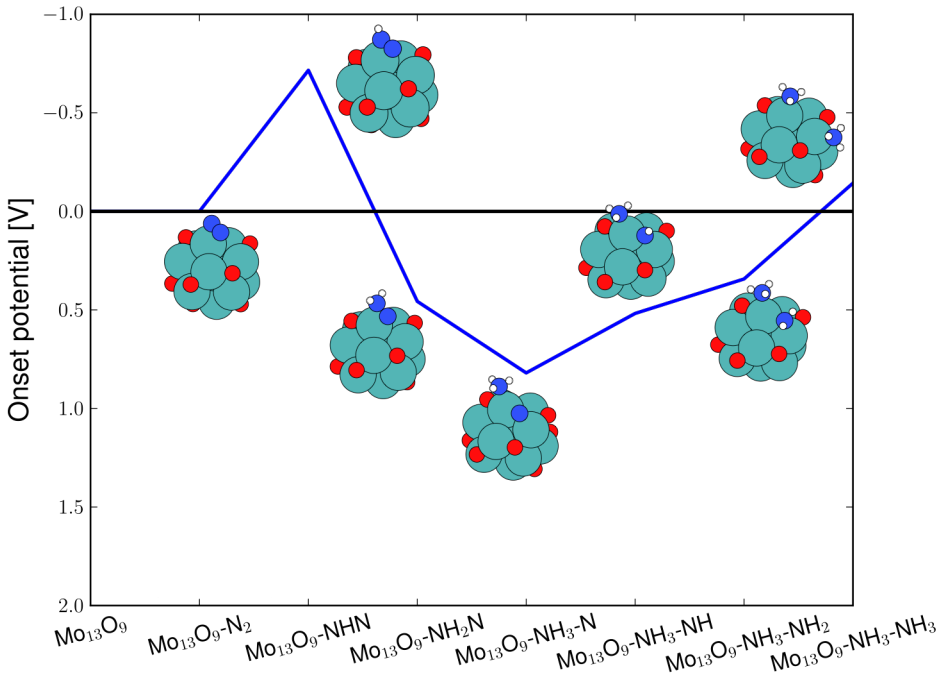

Figure 4: Diagram of the required applied potential to make each reaction step exergonic for electrochemical ammonia production on the $Mo_{13}O_9$ through the associative mechanism. For all five studied reaction pathways, the highest required potential is −0.7 V for the first protonation step.

$$NN^* + 6(H^+ + e^-) \rightarrow$$
$$NHN^* + 5(H^+ + e^-) \rightarrow$$
$$NH_2N^* + 4(H^+ + e^-) \rightarrow$$
$$NH_3{}^* + N^* + 3(H^+ + e^-) \rightarrow$$
$$NH_3{}^* + NH^* + 2(H^+ + e^-) \rightarrow$$
$$NH_3{}^* + NH_2{}^* + (H^+ + e^-) \rightarrow$$
$$NH_3{}^* + NH_3{}^*$$

The x-axis show the adsorbed reaction intermediate for each protonation step and NH_2N denotes a doubly protonated nitrogen molecule with the N–N backbone intact, while NH_3–NH denotes NH_3 and NH adsorbed on the surface and the N–N backbone has been dissociated. Five pathways were studied, and all of them had the first initial protonation step to be the potential limiting step with identical required onset potentials.

For a more reduced oxygen skin, e.g., the $Mo_{13}O_6$ nanocluster, the energetics of the electrochemical production of ammonia are much more diverse. Here, two routes are very favourably, demanding only potentials of around −0.45 V, to drive the electrochemical production of ammonia, see Figure 5. The routes not shown require potentials of −0.85 V to −1.3 V. The reaction intermediates for the preferred ammonia formation route have been used as the bottom x-axis. The blue filled line on Figure 5 shows that the rate-limiting step is the last protonation; while for the alternative route, marked with the green dashed line and the corresponding reaction intermediates have been used as the top x-axis in Figure 5, the rate-limiting steps are found to be both the third and the last protonation step. The limiting step for this reaction path is the formation of the NH_2–NH intermediate on the surface. The reaction is then followed by a very exergonic reaction step, where the N–N bond breaks. In both pathways, the N–N bond breaking in the associative process is very exergonic and no apparent activation barrier is observed for the N–N cleavage at either the third or fourth protonation step. The onset potential presented here for electrochemical ammonia production is similar to those obtained in previous studies on both clean and nitrogen covered molybdenum nanoclusters [2].

Instead of protonating the adsorbed nitrogen molecule, the potential could drive the reduction of oxygen. In Table 5, the potentials for driving the oxygen reduction processes are presented. Here, a potential of −0.77 V is required for the high oxygen coverage case, while the last reduction step for the lower oxygen coverage requires significantly larger potentials,

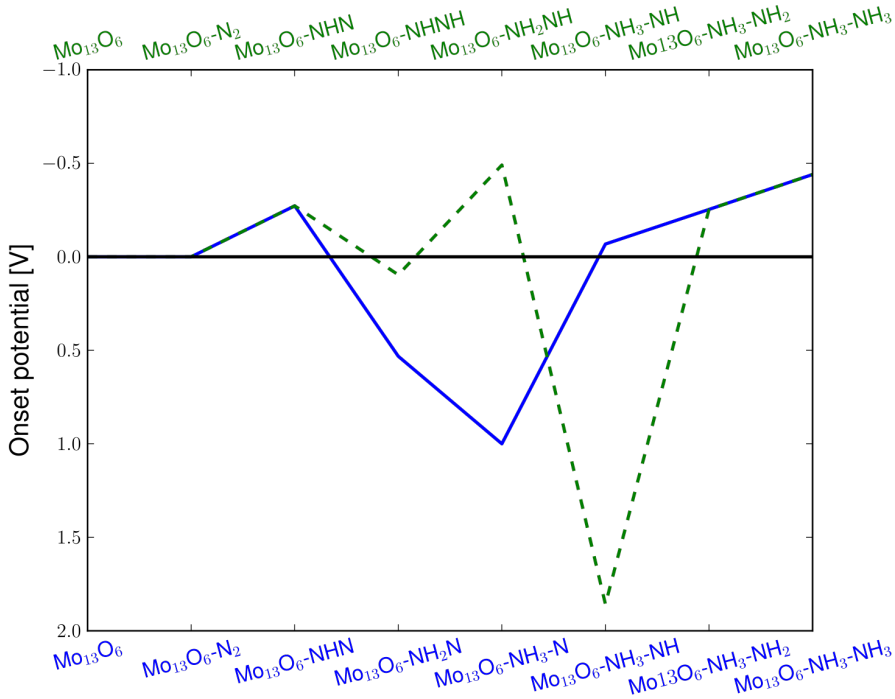

Figure 5: Diagram of the required applied potential to make each reaction step exergonic for electrochemical ammonia production on the $Mo_{13}O_6$ through the associative mechanism. The limiting reaction is the last protonation to form the second ammonia on the surface requiring a potential of −0.45 V to become exergonic.

i.e., −1.3 V to −1.75 V, to make the reaction exergonic, H_2O is found to be unstable on $Mo_{13}O_6$, while $Mo_{13}O_9$ has a stable adsorption of water.

Table 5: The required potentials for reducing oxygen at two oxygen coverages, when nitrogen molecules are present on the partly covered oxygen surfaces.

	$U_{O\rightarrow OH}$ [V]	$U_{OH\rightarrow H2O}$ [V]
$Mo_{13}O_9$-N_2	−0.53	−0.77
$Mo_{13}O_6$-N_2	−0.26	−1.30

Competing reaction mechanisms

Here, a possible reaction pathway is presented for electrochemical ammonia production on the $Mo_{13}O_9$ nanocluster with adsorbed N_2 at an applied potential $U = -0.7$ V. Three possible mechanisms must be considered: the reduction of N_2 to ammonia, hydrogen adsorption and evolution, and last the reduction of oxygen and subsequently formation of water. Here, we assume that the adsorption of H with N_2 present on the surface will be equal to adsorption of H on a surface without N_2 present.

The reaction free energies of forming H, OH, and N_2H at $U = -0.7$ V are: $\Delta G[N_2* + (H^+ + e^-) \rightarrow N_2H*] = 0$ eV, $\Delta G[(H^+ + e^-) \rightarrow H*] = -1.42$ eV, $\Delta G[O* + (H^+ + e^-) \rightarrow OH*] = -0.17$ eV, respectively. The reaction step with the lowest reaction free energy is hydrogen adsorption on the surface. For adsorbed hydrogen, the next step will be formation of $H_2(g)$ with a reaction free energies of $\Delta G[H* + (H^+ + e^-) \rightarrow H_2(g)] = 0.02$ eV. The next reaction to occur on the surface will therefore be the reduction of O to OH at −0.17 V. For this reaction intermediate, the next step will produce H_2O with a reaction free energy of $\Delta G[OH* + (H^+ + e^-) \rightarrow H_2O*] = 0.08$ eV. Small energy differences exist for the next protonation step, but N_2H will be formed on the surface.

The subsequent reaction intermediates for ammonia formation are exergonic at $U = -0.7$ V. The initial production of an overlayer of H is followed by reduction of O into OH, until the electrochemical reduction of N_2 becomes possible. When the ammonia molecules have desorbed from the surface, adsorption of N_2 is 0.4 eV more stable than H, which would make the adsorption of nitrogen at a vacancy site energetically favourable. At higher pH-values this difference would increase in favour of N_2 adsorption because a pH relatively destabilizes the adsorption of H, see Equation 1. Because of the very small difference between the formation of N_2H, H_2O and $H_2(g)$ a Faradaic loss due to hydrogen evolution should be expected and a reduction of the oxygen skin on the surface would also be expected at this oxygen coverage and potential.

For the $Mo_{13}O_6$ nanocluster with N_2 adsorbed at an applied potential of $U = -0.45$ V, the preferred mechanism is the following. First hydrogen is bound to the surface, then O is reduced to OH and then finally the reduction of N_2 can take place. Here, the reaction free energy for production of gas phase hydrogen is $\Delta G[H* + (H^+ + e^-) \rightarrow H_2(g)] = 0.20$ eV and for water formation is $\Delta G[OH + (H^+ + e^-) \rightarrow H_2O*] = 0.59$ eV, while ΔG for all electrochemical reaction steps for ammonia production, see Figure 5, are zero or lower as in the previous example on the $Mo_{13}O_9$ nanocluster.

In the discussion of the preferential reactions on the $Mo_{13}O_9$ and $Mo_{13}O_6$ nanoclusters, all possible adsorbate–adsorbate interactions are not included due to the large computational cost associated with a comprehensive investigation. This is a potentially significant assumption, since the adsorption energies may decrease with higher coverage of certain species [27]. For hydrogen evolution on the $Mo_{13}O_6$ nanocluster, this could, e.g., have the consequence that the free energy barrier for producing gas phase hydrogen molecules is lowered.

The results for ammonia production on a partially oxidized molybdenum nanocluster indicates that the formation of ammonia on the molybdenum nanocluster is possible at a low onset potential, but with a low Faradaic efficiency due to the parasitic formation of both adsorbed H or OH on $Mo_{13}O_9$ and $Mo_{13}O_6$. Adsorption of nitrogen seems to hinder the further reduction of OH at lower oxygen coverages. This indicates that the nanocluster should be fully reduced, i.e., no oxygen present on the surface, before nitrogen is able to reach the catalyst surface. Small amounts of oxygen present at the molybdenum nanocluster surface, arising from either the electrolyte or from the preparation of the electrocatalyst, should therefore not affect the electrochemical production of ammonia.

Conclusion

Density functional theory calculations have been employed to investigate the adsorption and reduction of oxygen on molybdenum nanoclusters. The computational hydrogen electrode was used to determine potentials for reduction of nitrogen and oxygen and the hydrogen evolution reaction.

First, a partially nitrogen covered molybdenum nanocluster was exposed to gaseous water, showing preferential adsorption of oxygen atoms compared to both hydrogen atoms and nitrogen molecules at neutral bias ($U = 0$ V), while the adsorption energies are comparable at the potential needed to produce ammonia ($U = -0.6$ V). The consequence is that the presence of water will lead to preferential oxygen adsorption at the nitrogen vacancy sites unless a negative bias is applied. The reduction of the oxygen atoms at the nitrogen rich molybdenum nanocluster

was studied, and potentials more negative than −1.25 V is required to reduce the oxygen atoms into water. The main challenge is the second protonation step, where the reaction step is very dependent on the local environment. The oxygen atom will bind to the vacancy site blocking the adsorption of nitrogen molecules and thereby greatly reduce the efficiency of the nitrogen rich molybdenum nanocluster as an electro catalyst for ammonia production through the associative mechanism. A direct reduction of the nitrogen skin will, however, still be possible at $U = -0.6$ V [2].

A clean molybdenum nanocluster in contact with oxygen, hydrogen and nitrogen will preferentially form an oxygen skin at neutral bias and nitrogen adsorption on an oxygen covered molybdenum nanocluster is found to be impossible. The reduction of an oxygen overlayer was therefore studied and it was found that the reduction requires potentials of −0.29 V to −0.72 V to successfully produce water from adsorbed oxygen atoms.

For oxygen coverages of nine or less oxygen atoms, adsorption of nitrogen and hydrogen becomes possible. The electrochemical production of ammonia for adsorbed nitrogen molecules at partial oxygen coverage will only require potentials of −0.45 V to −0.7 V to make the reaction exergonic. These onset potentials are similar to values reported in earlier studies of electrochemical ammonia production on molybdenum nanocluster with or without a nitrogen skin [2]. At the potentials needed to make the ammonia production exergonic, hydrogen is found to be present on the surface, and a reduction of oxygen to OH is observed, before electrochemical production of ammonia is possible.

On the basis of the work presented here, we propose that (partially) oxidized and nitrided molybdenum nanoclusters can be re-activated for ammonia production by electrochemical reduction of the adsorbed oxygen resulting from, e.g., the catalyst synthesis procedure or the presence of water in the electrolyte, at a potential of approximate −0.7 V. This makes molybdenum nanoclusters a highly promising catalyst for electrochemical ammonia production via the associative mechanism.

Supporting Information

Supporting Information File 1

Additional Figures.
[http://www.beilstein-journals.org/bjnano/content/supplementary/2190-4286-5-11-S1.pdf]

Acknowledgements

The authors would like to acknowledge the the Danish Center for Scientific Computing, the Catalysis for Sustainable Energy (CASE) initiative, the Center of Atomic-Scale Materials Design (CAMD) and the National Danish Advanced Technology Foundation. CASE is funded by the Danish Ministry of Science, Technology and Innovation, and CAMD is funded by the Lundbeck Foundation.

References

1. Howalt, J. G.; Bligaard, T.; Rossmeisl, J.; Vegge, T. *Phys. Chem. Chem. Phys.* **2013,** *15,* 7785–7795. doi:10.1039/c3cp44641g
2. Howalt, J. G.; Vegge, T. *Phys. Chem. Chem. Phys.* **2013,** *15,* 20957–20965. doi:10.1039/c3cp53160k
3. Sone, Y.; Ekdunge, P.; Simonsson, D. *J. Electrochem. Soc.* **1996,** *143,* 1254–1259. doi:10.1149/1.1836625
4. Kreuer, K.-D.; Paddison, S.; Spohr, E.; Schuster, M. *Chem. Rev.* **2004,** *104,* 4637–4678. doi:10.1021/cr020715f
5. Fastrup, B.; Nygård Nielsen, H. *Catal. Lett.* **1992,** *14,* 233–239. doi:10.1007/BF00765236
6. Kuchaev, V. L.; Shapatina, E. N.; Avetisov, A. K. *Russ. J. Electrochem.* **2009,** *45,* 983–995. doi:10.1134/S1023193509090031
7. Hohenberg, P.; Kohn, W. *Phys. Rev.* **1964,** *136,* B864–B871. doi:10.1103/PhysRev.136.B864
8. Kohn, W.; Sham, L. J. *Phys. Rev.* **1965,** *140,* A1133–A1138. doi:10.1103/PhysRev.140.A1133
9. Hammer, B.; Hansen, L. B.; Nørskov, J. K. *Phys. Rev. B* **1999,** *59,* 7413–7421. doi:10.1103/PhysRevB.59.7413
10. Blöchl, P. E. *Phys. Rev. B* **1994,** *50,* 17953–17979. doi:10.1103/PhysRevB.50.17953
11. Blöchl, P. E.; Först, C. J.; Schimpl, J. *Bull. Mater. Sci.* **2003,** *26,* 33–41. doi:10.1007/BF02712785
12. Mortensen, J. J.; Hansen, L. B.; Jacobsen, K. W. *Phys. Rev. B* **2005,** *71,* 035109. doi:10.1103/PhysRevB.71.035109
13. Enkovaara, J.; Rostgaard, C.; Mortensen, J. J.; Chen, J.; Dułak, M.; Ferrighi, L.; Gavnholt, J.; Glinsvad, C.; Haikola, V.; Hansen, H. A.; Kristoffersen, H. H.; Kuisma, M.; Larsen, A. H.; Lehtovaara, L.; Ljungberg, M.; Lopez-Acevedo, O.; Moses, P. G.; Ojanen, J.; Olsen, T.; Petzold, V.; Romero, N. A.; Stausholm-Møller, J.; Strange, M.; Tritsaris, G. A.; Vanin, M.; Walter, M.; Hammer, B.; Häkkinen, H.; Madsen, G. K. H.; Nieminen, R. M.; Nørskov, J. K.; Puska, M.; Rantala, T. T.; Schiøtz, J.; Thygesen, K. S.; Jacobsen, K. W. *J. Phys.: Condens. Matter* **2010,** *22,* 253202. doi:10.1088/0953-8984/22/25/253202
14. The GPAW code is available as a part of the CAMPOS software: http://wiki.fysik.dtu.dk/gpaw/
15. Monkhorst, H.; Pack, J. D. *Phys. Rev. B* **1976,** *13,* 5188–5192. doi:10.1103/PhysRevB.13.5188
16. Skúlason, E.; Bligaard, T.; Gudmundsdóttir, S.; Studt, F.; Rossmeisl, J.; Abild-Pedersen, F.; Vegge, T.; Jónsson, H.; Nørskov, J. K. *Phys. Chem. Chem. Phys.* **2012,** *14,* 1235–1245. doi:10.1039/c1cp22271f
17. The ASE code is available as a part of the CAMPOS software: http://wiki.fysik.dtu.dk/ase/
18. Bitzek, E.; Koskinen, P.; Gähler, F.; Moseler, M.; Gumbsch, P. *Phys. Rev. Lett.* **2006,** *97,* 170201. doi:10.1103/PhysRevLett.97.170201

19. Heyrovský, J. *Recl. Trav. Chim. Pays-Bas* **1927,** *46,* 582–585. doi:10.1002/recl.19270460805
20. Rossmeisl, J.; Logadottir, A.; Nørskov, J. K. *J. Chem. Phys.* **2005,** *319,* 178–184. doi:10.1016/j.chemphys.2005.05.038
21. Rossmeisl, J.; Qu, Z.-W.; Kroes, G.-J.; Nørskov, J. K. *J. Electroanal. Chem.* **2007,** *607,* 83–89. doi:10.1016/j.jelechem.2006.11.008
22. Hummelshøj, J. S.; Blomquist, J.; Datta, S.; Vegge, T.; Rossmeisl, J.; Thygesen, K. S.; Luntz, A. C.; Jacobsen, K. W.; Nørskov, J. K. *J. Chem. Phys.* **2010,** *132,* 071101. doi:10.1063/1.3298994
23. Reuter, K.; Scheffler, M. *Phys. Rev. B* **2001,** *65,* 035406. doi:10.1103/PhysRevB.65.035406
24. Rossmeisl, J.; Nørskov, J. K.; Taylor, C. D.; Janik, M. J.; Neurock, M. *J. Phys. Chem. B* **2006,** *110,* 21833–21839. doi:10.1021/jp0631735
25. Nørskov, J. K.; Rossmeisl, J.; Logadottir, A.; Lindqvist, L.; Kitchin, J. R.; Bligaard, T.; Jónsson, H. *J. Phys. Chem. B* **2004,** *108,* 17886–17892. doi:10.1021/jp047349j
26. Abild-Petersen, F.; Greeley, J.; Studt, F.; Rossmeisl, J.; Munter, T. R.; Moses, P. G.; Skúlason, E.; Bligaard, T.; Nørskov, J. K. *Phys. Rev. Lett.* **2007,** *99,* 016105. doi:10.1103/PhysRevLett.99.016105
27. Getman, R. B.; Schneider, W. F. *ChemCatChem* **2010,** *2,* 1450–1460. doi:10.1002/cctc.201000146

License and Terms

Beilstein Journal of Nanotechnology

Constant-distance mode SECM as a tool to visualize local electrocatalytic activity of oxygen reduction catalysts

Michaela Nebel[1,2], Thomas Erichsen[2] and Wolfgang Schuhmann[*1]

Full Research Paper

Open Access

Address:
[1]Lehrstuhl für Analytische Chemie; Ruhr-Universität Bochum, D-44780 Bochum and [2]Sensolytics GmbH, Universitätsstr 142, D-44799 Bochum

Email:
Wolfgang Schuhmann[*] - wolfgang.schuhmann@rub.de

* Corresponding author

Keywords:
electrocatalysis; oxygen reduction; recessed microelectrodes; redox-competition SECM; SECM; scanning electrochemical microscopy; shearforce-based constant-distance mode

Beilstein J. Nanotechnol. **2014,** *5,* 141–151.
doi:10.3762/bjnano.5.14

Received: 16 August 2013
Accepted: 20 January 2014
Published: 07 February 2014

This article is part of the Thematic Series "Electrocatalysis on the nm scale".

Guest Editor: R. J. Behm

Abstract

Multidimensional shearforce-based constant-distance mode scanning electrochemical microscopy (4D SF/CD-SECM) was utilized for the investigation of the activity distribution of oxygen reduction catalysts. Carbon-supported Pt model catalyst powders have been immobilized in recessed microelectrodes and compared to a spot preparation technique. Microcavities serve as platform for the binder-free catalyst sample preparation exhibiting beneficial properties for constant-distance mode SECM imaging concerning modified surface area and catalyst loading. The integration of the redox competition mode of SECM into the detection scheme of the 4D SF/CD mode is demonstrated for specifically adapting high-resolution SECM experiments to powder-based catalyst preparations.

Introduction

In scanning electrochemical microscopy (SECM) [1,2] an ultramicroelectrode, which is referred to as the SECM tip, is moved in close distance in a grid-wise manner over a sample surface. The resulting tip current is detected as a function of the tip position within the scanned grid, thus enabling visualization of the local electrochemical activity of the investigated sample surface caused by local variations of reaction rates. The tip current is, however, distance dependent and variations in the topography as well as in the local reactivity of the sample surface may both affect the tip response. Therefore, an unambiguous interpretation of the current response can only be realized by discrimination between the impact of topography and local reactivity by means of a constant-distance mode (cd-mode) positioning of the SECM tip in known and constant distance to the sample surface. The basis of cd-mode scanning is the control of the tip-to-sample separation by means of an additional electrochemistry-independent but distance-dependent analytical signal. Among other strategies for cd-mode imaging like the tip-pos-

ition modulation mode (TPM) [3], AFM-SECM [4,5] and SECM-SICM [6,7], AC-SECM [8], the soft stylus probe [9,10] and the intermitted contact mode (IC-SECM) [11], the shearforce-based constant-distance mode [12-14] has been widely used and demonstrated its feasibility for high-resolution SECM. Furthermore, decoupling of the working distance of the electrochemical detection from the typically very short working distances required for cd-mode imaging was established recently proposing a 4D shearforce-based constant-distance mode (4D SF/CD-SECM) [15]. As a general strategy of tip movement it provides a tool to increase the analytical content of a single cd-mode SECM experiment and it is independent of the applied distance control mechanism. The concept of 4D CD-SECM was recently extended to intermittent contact-SECM [16].

Here, we describe the adaptation of the 4D SF/CD-SECM to the investigation of the activity of powdery oxygen reduction catalysts. In order to understand the properties of catalyst powders on a local scale, like, e.g., the distribution of activity within the catalyst material or initial processes of degradation, experiments have to be conceived which allow investigating the catalysts as close as possible to the conditions at which they are intended to be used. SECM is a promising tool in that respect. Typically, catalyst powders as samples for SECM investigations are immobilized as spots onto conductive plates such as, e.g., glassy carbon or conducting glasses. An example for such an investigation of catalyst libraries can be found in [17] and the local investigation of the activity of catalyst spots at elevated temperatures was recently described in [18].

In this contribution, we demonstrate the feasibility of 4D SF/CD-SECM to the topography-corrected investigation of the oxygen consumption profile of catalyst spots using commercially available model catalyst for the oxygen reduction reaction (ORR). Furthermore, recessed microelectrodes fabricated by etching inlayed Au disk microelectrodes are demonstrated as a flexible platform for immobilization of catalyst powders for cd-mode SECM experiments. The microcavities (also referred to as micropores) have already demonstrated their applicability for integral investigations of the activity of catalyst powders [19-26]. More recently recessed microelectrodes were already used for the visualization of powder catalyst activity using SECM [27,28]; however, cd-mode imaging and consequently topography-corrected activity determination was not described until now. Furthermore, the proposed 4D SF/CD mode provides the possibility to perform various complex electrochemical experiments at each grid point and in several known and constant distances to the contour of the sample surface. The combination of the transient redox competition mode (RC-SECM) [29,30] with the 4D SF/CD mode (by analogy named as 4D SF/CD-RC-SECM) for high-resolution SECM investigations of heterogeneous oxygen reduction catalysts is introduced as a strategy to further adapt the SECM detection scheme towards local visualization of ORR catalyst activity with high resolution.

Results and Discussion

Constant-distance mode imaging of catalyst spots

The investigation of the activity of catalysts for ORR using SECM is commonly performed in a competition arrangement. A scheme of this variation of the generator/collector mode is shown in Figure 1a. The sample is polarized at a sufficiently low potential to reduce oxygen. Due to the catalyst reaction, oxygen is consumed and a gradual depletion of oxygen in front of the sample area occurs (consumption profile). Simultaneously, the tip is also polarized at a potential to reduce oxygen. Thus, sample and tip compete for the oxygen inside the gap between tip and sample which represents a leaking thin layer electrochemical cell. Due to the depletion of oxygen in the gap, a diffusion gradient is established leading to an in-diffusion of oxygen into the gap. Thus, depending on the tip-to-sample distance and the rates for oxygen reduction at tip and sample a stationary oxygen concentration is established within the gap. Hence, the tip current is modulated by the rate of oxygen reduction at the sample. The magnitude of current decrease at the tip in a competition experiment is visualizing the sample activity.

The topography image of a catalyst spot prepared from a commercially available ORR catalyst (Pt/C with 20 wt % Pt on Vulcan XC72 from ETEK) in a 4D SF/CD-SECM scan is shown in Figure 1b. The linescan started at a position above the glassy carbon plate and was performed towards the centre of the catalyst spot. Beside the formed outer ring with high catalyst loading due to a coffee drop effect [31,32], the topography of the catalyst spot was successfully visualized using shearforce-based positioning. The topographic features of the catalyst spot are also seen in the micrograph in the insert of Figure 1b. The oxygen consumption profile obtained during the same linescan is displayed in Figure 1c. The oxygen reduction current at the tip substantially decreases when the tip passes the border between glassy carbon plate and catalyst spot indicative for the ORR activity of the deposited powder catalyst. Variations of the tip current within the spot were detected showing a higher catalytic activity at positions with higher catalyst loading. Due to the cd-mode scanning, the current decrease above positions with higher catalyst thickness is independent from changes in the tip-to-sample distance and the observed tip response is therefore unambiguously allocated to the local catalyst activity for ORR. This experiment demonstrates the feasibility of the 4D SF/CD mode for studying the local activity of catalyst spots

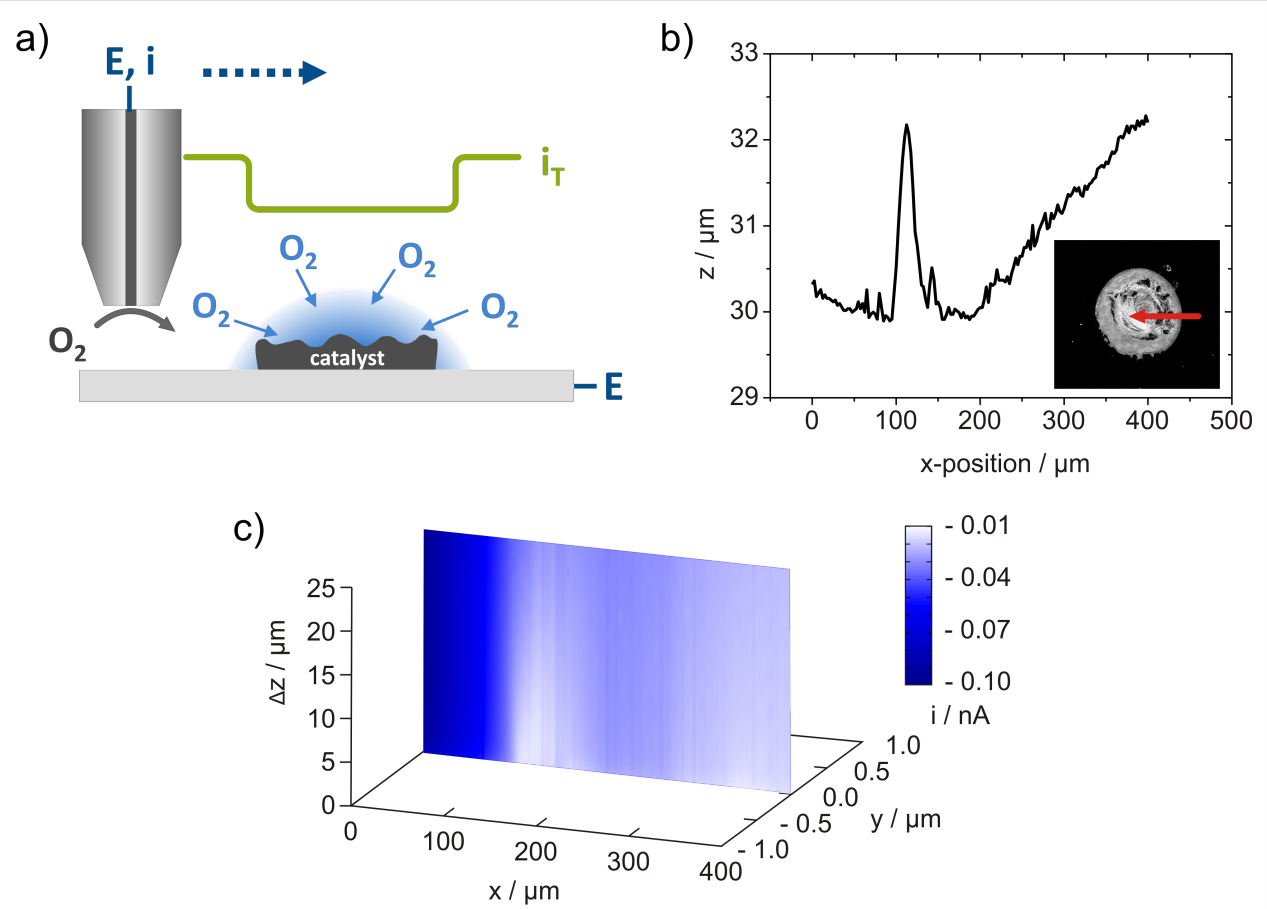

Figure 1: 4D SF/CD-SECM for the investigation of the catalytic activity towards oxygen reduction. a) Scheme of the competition mode. b) Topographic linescan across a spot of Pt/C catalyst with 20 wt % Pt on a glassy carbon plate obtained in the shearforce-based cd-mode of SECM. The topography is displayed as the z-piezo position of the tip after reaching the predefined stop criterion of the shearforce interaction (point of closest approach). The insert shows an optical micrograph of the investigated spot and the arrow marks the scan position and direction. c) Oxygen consumption profile above the line displayed in b) visualized as a x,Δz,i-image, where Δz represents the distance of the current detection from the point of shearforce interaction. E_{sample} = −300 mV, E_{tip} = −600 mV, d_{tip} = 0.8 µm, f_{osc} = 356.7 kHz, stop criterion: 5% change of the lock-in signal in bulk.

removing any impact from the sample topography. The accuracy of the shearforce-based tip positioning enables to follow the contour of the catalyst spot using comparatively stiff glass-insulated Pt tips in non-optical cd-mode. However, the visualization of the local catalytic activity of complete catalyst spots using SECM tips with sizes <5 µm is practicable only to a limited extent. The large size of the spots considerably increases the duration of cd-mode SECM experiments and electrolyte evaporation or electrode fouling may lead to unpredictable errors. The reduction of the time needed for a single SECM experiment using larger tip electrodes and/or increased distances between the grid points contradict the demand for high-resolution investigations. Using established spot preparation methods such as ink-jet dispensing it is possible to reduce the spot diameter to about 100 µm concomitantly depositing a substantially smaller catalyst loading leading to a decreased contrast in related SECM images. In order to overcome these drawbacks, an alternative sample preparation protocol based on the utilization of recessed microelectrodes as flexible platform for catalyst immobilization was applied for cd-mode SECM imaging.

Microcavities as flexible platform for sample preparation in constant-distance mode SECM

The requirement of a small catalyst-modified area with simultaneously high catalyst loadings are met by the application of recessed microelectrodes whose cavities are filled with the desired catalyst powder. The bottom of the microcavity forms the electrical contact and the thickness of the investigated catalyst material is determined by the depth L of the cavity (see Figure 2a). This sample preparation is fast, enables an easy exchange of catalyst powder, is applicable for quantitative studies and the modified surface area is determined by the opening of the cavity [25,26]. The fabrication of nanometre-sized recessed electrodes have already been reported [33,34] and a further miniaturization of the modified surface area is

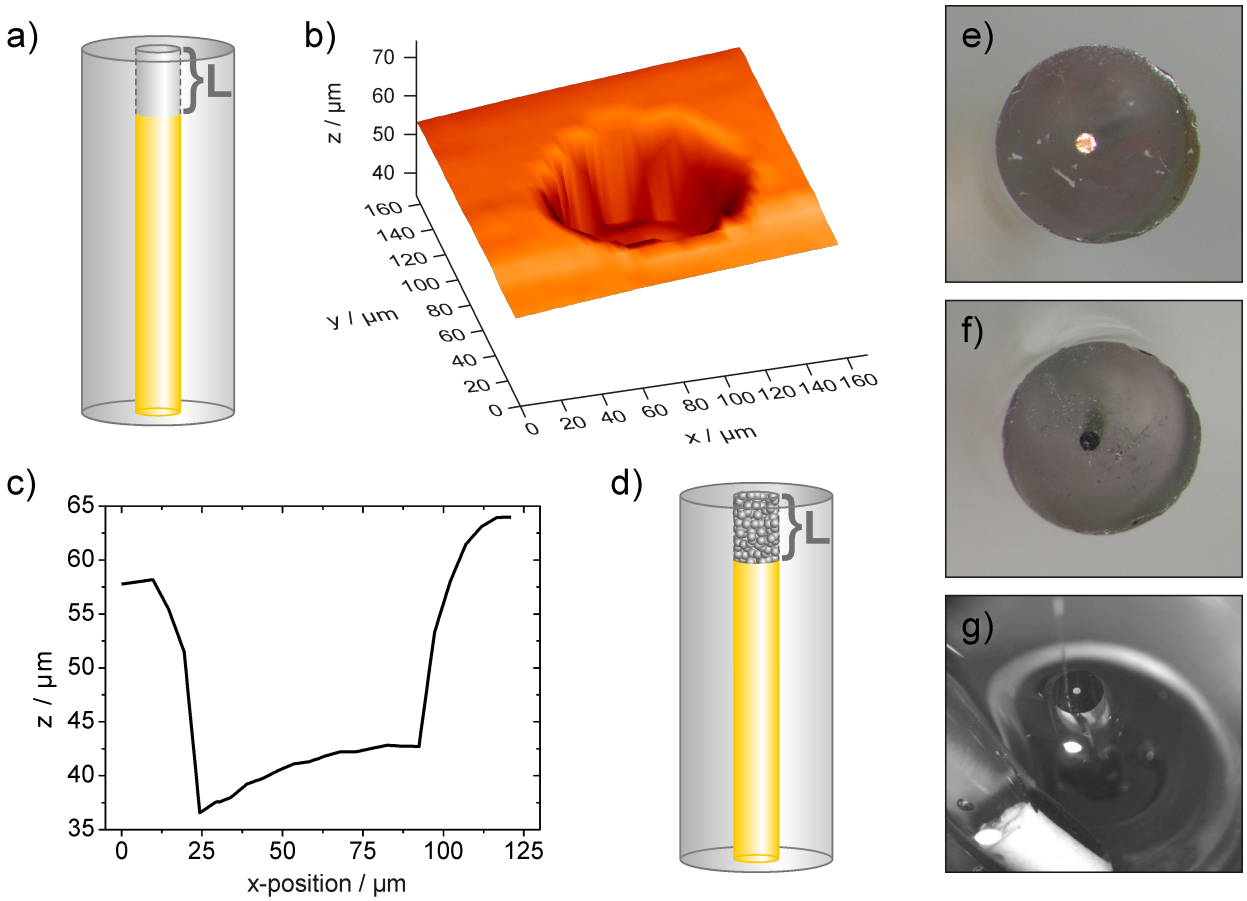

Figure 2: a) Scheme of a microcavity used as platform for catalyst immobilisation in cd-mode SECM investigations. b) Topography of the cavity obtained by means of shearforce-based cd-scanning and a corresponding linescan shown in c). d) Scheme of the microcavity electrode filled with catalyst powder. Optical micrographs of the cavity electrode before e) and after f) filling with catalyst powder. Residues of the black Pt/C catalyst are visible at the glass insulation and are removed before the filled cavity is inserted in the SECM measuring cell. g) Micrograph of the setup for 4D SF/CD-SECM experiments with the tip positioned next to the microcavity. The glass body of the used reference electrode is visible in the front.

therefore possible. Furthermore, immobilization of the catalyst powder within the cavity of the recessed microelectrode allows for avoiding any binder additive such as, e.g., Nafion that is commonly used for rotating disk electrode studies or spot preparation [23]. Since the influence of Nafion on the catalytic activity is still not fully understood [35-37], the investigation of the catalyst material in absence of any binder is an additional advantage of this sample preparation method. In order to generate a microcavity, polished disk-shaped gold electrodes with a diameter of 100 µm were electrochemically etched in HCl using 10 potentiodynamic cycles. The depth of the formed cavity was investigated by shearforce-based cd-mode scanning and a complete topography image and a corresponding topographic linescan across the centre of the cavity are displayed in Figure 2b and Figure 2c, respectively.

The depth L was determined to be about 19 µm with an inhomogenous contour of the bottom of the microcavity. Obviously, the material removal at the edges of the cavity was more efficient than at the centre leading to a protruding structure of the cavity bottom. Similar results were previously shown for chemically etched Pt disk electrodes [25]. However, the non-flat cavity bottom does not impede with the function as a conductive contact for the catalyst powder filled into the cavity. The depth of about 19 µm allows high catalyst loadings making any impact of bottom irregularities on the activity determination being negligible. The microcavities were further used for catalyst immobilization and manually filled with the catalyst powder (Figure 2d). The result of the filling procedure was examined by means of optical microscopy (Figure 2e and Figure 2f). Subsequently, the prepared catalyst-filled microcavity electrode was integrated into a specifically designed measuring cell for cd-mode SECM experiments (Figure 2g). As a matter of fact, it is important to elucidate that the Au bottom of the recessed microelectrode does not have a major impact on the measured catalytic activity for ORR. A partly filled micro-

cavity (Figure 3a) was analysed by means of 4D SF/CD-SECM in the competition arrangement. Although the tilt between the scanning plane and the surface of the microcavity electrode was compensated by the distance control it was visible in the topography image displaying the z-position of the tip when the stop criterion of the shearforce signal was obtained. In order to enhance the contrast, the tilt was subtracted and the visualization of the resulting sample topography is shown in Figure 3b. The lateral inhomogeneous filling of the microcavity with the catalyst powder is clearly visible. With respect to the surrounding glass plane the catalyst filling is elevated by about 1 to 2 µm. Additionally, the unfilled part of the cavity can be distinguished, however, due to the size of the glass sheath of the tip, an edge effect is obtained allowing the tip only to move into the cavity at distances from the edge being larger than half of the overall tip diameter. The tip current at closest tip approach is displayed in Figure 3c showing a decrease of the tip current exclusively above areas filled with catalyst material. The current detection of the 4D SF/CD mode is sensitive enough to visualize the fine structure of the filling and even the thin catalyst layer at the left side of the cavity was distinguished as a location of higher catalytic activity. No interference of the free Au bottom was detected at an applied sample potential of -300 mV.

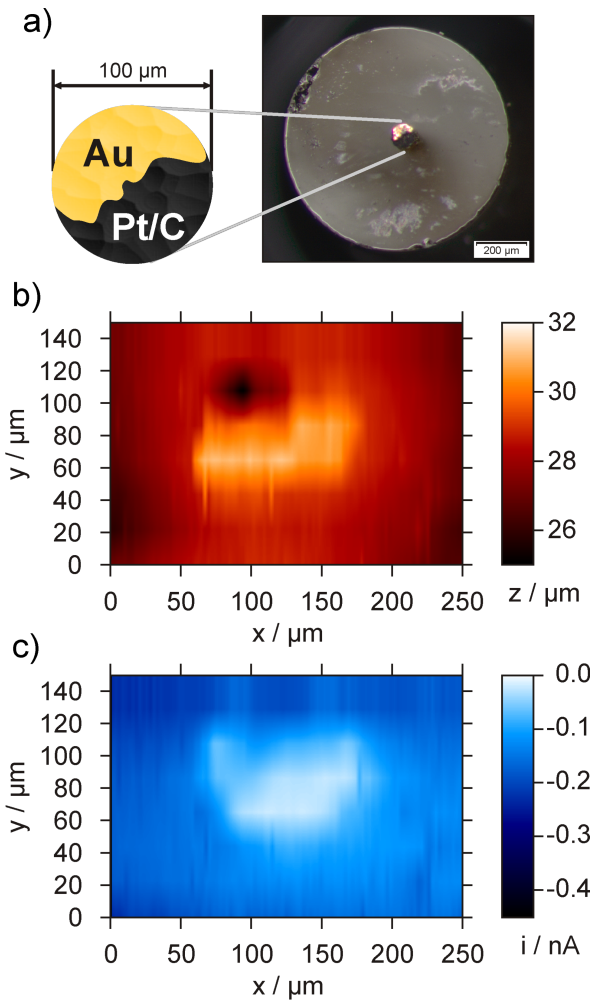

Figure 3: 4D SF/CD-SECM experiment at a partly filled microcavity. a) Optical micrograph with a scheme of the catalyst filling, b) topography and c) current image at the point of closest approach. E_{sample} = −300 mV, E_{tip} = −600 mV, d_{tip} = 1.6 µm, f_{osc} = 299.4 kHz, stop criterion: 15%.

4D constant-distance mode RC-SECM (4D SF/CD-RC-SECM)

The redox competition mode of scanning electrochemical microscopy (RC-SECM) is a specially designed SECM detection mode for the investigation of oxygen reduction catalysts [29,30]. The current measurement is performed at the tip and a further increase of the lateral resolution by utilization of smaller electrodes is therefore possible [29]. In order to enable a precise positioning of small electrodes also for the RC mode, the detection scheme was integrated in the 4D SF/CD-SECM. This combination leads to the concept of 4D SF/CD-RC-SECM as illustrated in Figure 4. As a variation of the 4D shearforce-based constant-distance mode the tip is vibrated at its own resonance frequency and approached towards the sample surface under shearforce control until the predefined stop criterion is reached (Figure 4a). After precise positioning of the tip within the shearforce interaction regime, the resulting z-position is stored to visualize the sample topography (Figure 4b). The concept of 4D SF/CD-SECM provides the possibility to perform any anticipated electrochemical experiment at each grid point and each tip-to-sample separation. Integration of the transient redox competition mode of SECM is performed by implementing a potential pulse profile that is applied at the tip and the time-resolved detection of the current response is performed (Figure 4c and 4d). After completion of the stepwise retraction the tip is moved to the next grid point (Figure 4e) and the procedure of shearforce-based positioning and retraction with simultaneous data acquisition is repeated. By using the constant-distance mode RC-SECM, local chronoamperograms are recorded at different but constant tip-to-sample separations at each point of the scanned grid. This enables the determination of the complete time-depended oxygen consumption profile in constant tip-to-sample separations far outside the restricted range of the shearforce interaction. In accordance with the previously proposed terminology of multidimensional SECM and the transient character of the 4D SF/CD-RC-SECM, this mode is a 5D measuring technique (i vs t vs x-, y-, z-position). The representation of the multidimensional data set is optionally realized by horizontally sliced current images in different tip-to-sample distances at discrete points of time. Alternatively, a set of vertical oxygen consumption profiles can be extracted.

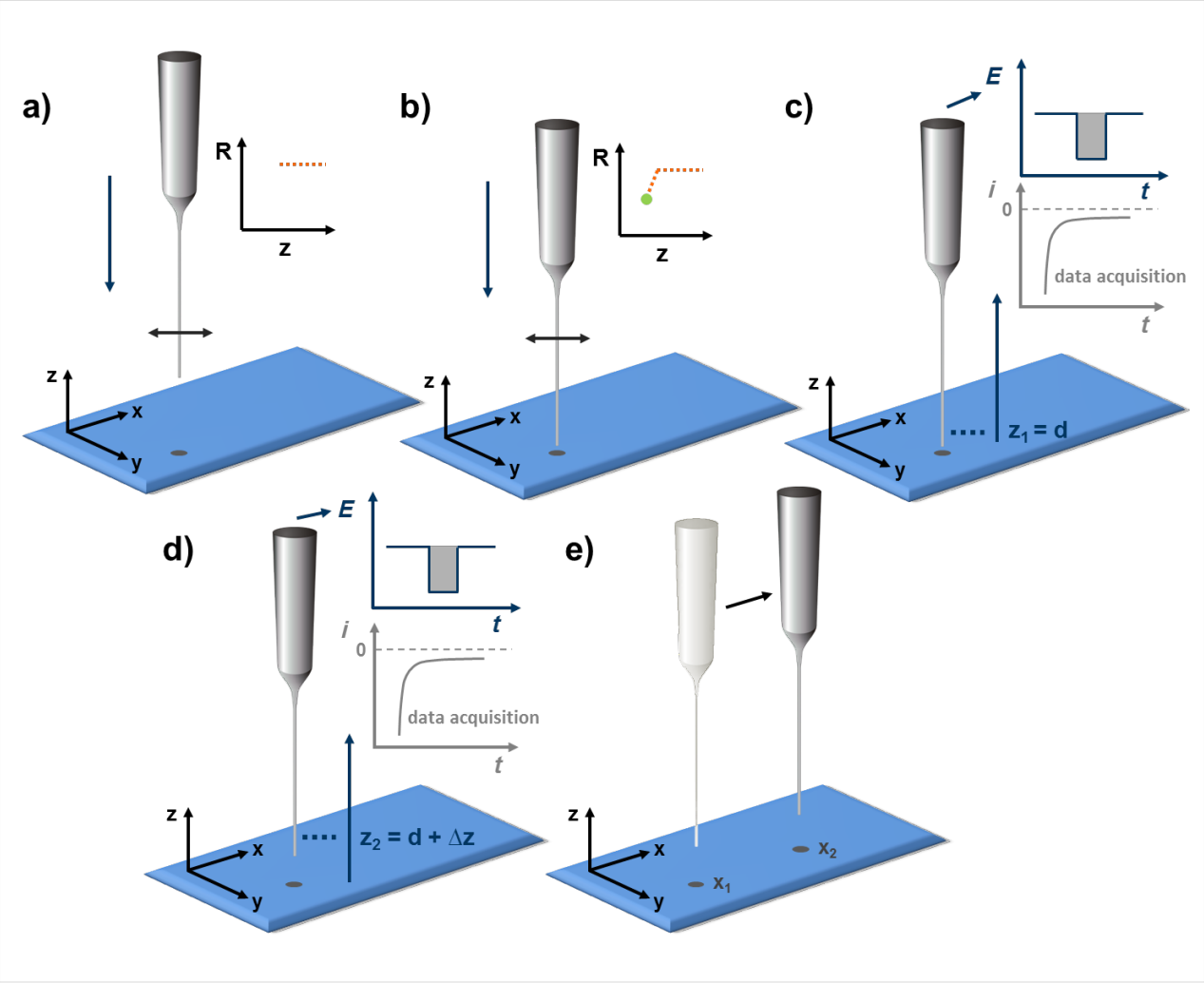

Figure 4: Concept of the 4D SF/CD-RC-SECM. Similar to the 4D SF/CD mode the tip is positioned within the shearforce-interaction regime by means of a z-approach curve (a and b). Data acquisition is performed in subsequent retraction steps (c and d) set out from the point of closest approach. To additionally implement the redox competition mode, a variable potential pulse profile is performed at each tip-to-sample distance. During a competition pulse tip and sample compete for the oxygen inside the gap and a time-dependent current decay curve is recorded at the tip enabling a time-resolved analysis of the oxygen concentration within the gap. After completion of the retraction the tip is moved to the next grid point (e) and the procedure is repeated starting with the shearforce-based positioning (a).

Figure 5 shows the application of the 4D SF/CD-RC mode to a polished Pt disk electrode as model sample for an ORR catalyst.

A tilt of the surface is visible in the topography image (Figure 5a) and the Pt surface is elevated by about 200 nm above the glass insulation. The area above the active Pt disk is clearly distinguishable as a location with increased oxygen consumption (Figure 5b–e). The contrast decreases with larger working distances representing the diminution of the vertical oxygen consumption profile as displayed in Figure 5f. This result shows the feasibility of the proposed 4D SF/CD-RC-SECM for the visualization of the local catalyst activity for ORR. In order to proof the applicability of the 4D SF/CD-RC-SECM for the evaluation of the catalytic activity of powder catalysts, a Pt/C filled microcavity was investigated (Figure 6). The filled cavity is visible as a maximal 3 µm recessed area in the topography image displayed in Figure 6a. A decreased oxygen concentration was successfully detected above the filled cavity and the current images at increasing tip-to-sample separations (Figure 6c and d) show the expansion of the oxygen consumption profile into the electrolyte solution.

Apart from the local catalytic activity, the contrast of a RC-SECM experiment depends on several parameters like, e.g., the RG value and the size of the tip, the tip-to-sample separation, the applied pulse profile and the time of data acquisition [29]. Due to this complex multiparameter system, the experimental conditions for the best data acquisition varies for each measurement. By means of the 4D SF/CD-RC-SECM a technique is accessible that enables a time-dependent data

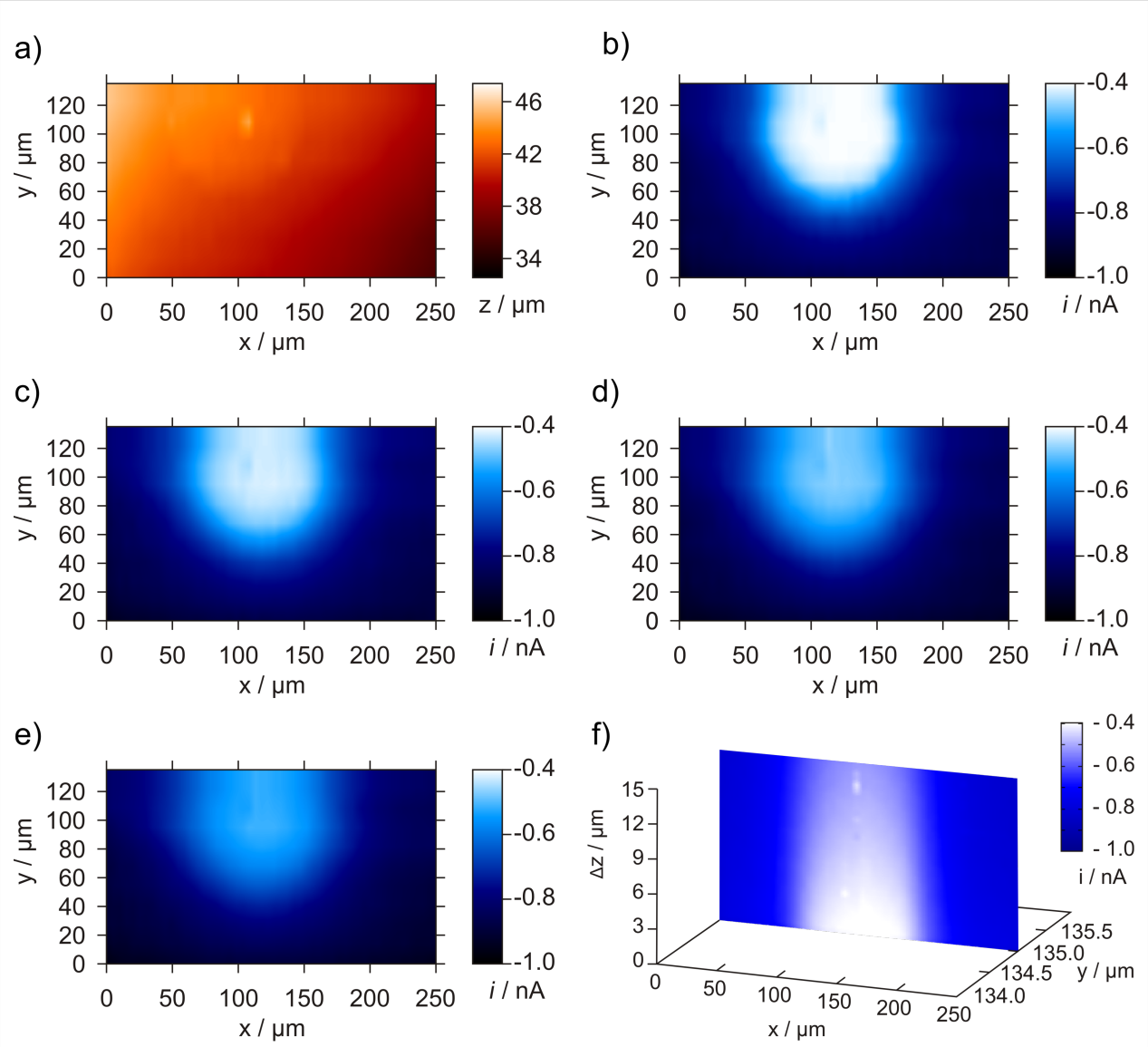

Figure 5: 4D SF/CD-RC-SECM experiment at a 100 µm diameter Pt disk electrode as model sample for an ORR catalyst. a) Topography image, b)–e) horizontal current image at the point of shearforce contact and in increments of 5 µm after tip retraction. f) Oxygen consumption profile (vertically-sliced current image). E_{sample} = −600 mV, $E_{tip,base}$ = 0 mV, $E_{tip,pulse1}$ = 0 mV, t_{pulse1} = 0.5 s, $E_{tip,pulse2}$ = −600 mV, t_{pulse2} = 0.5 s, pictures displayed at t = 0.25 s, d_{tip} = 3.4 µm, f_{osc} = 318.2 kHz, stop criterion: 5%.

acquisition at various constant working distances. As a result, the conditions for the best contrast of a SECM experiment are chosen after the SECM investigation is completed without the demand of knowing the exact contribution of each parameter beforehand. Moreover, we recently demonstrated that the reaction at a continuously polarized tip may actively influence the detection of the local oxygen concentration inside the gap between tip and sample [38,39]. As a consequence, the oxygen detection is superimposed by effects caused by the tip reaction and the tip is not acting as a passive spectator. Using the flexible potential pulse profile of the 4D SF/CD-RC mode the tip can be polarized to the oxygen reduction potential for only a very short time. Thus, the diffusion field in front of the electrode is restricted and an influence of the tip reaction on the imaging result is minimized.

Conclusion

The application of the 4D shearforce-based constant-distance mode for the investigation of the activity of ORR catalyst powders enables the visualization of the activity distribution within a catalyst spot avoiding any convolution due to topography effects. Catalyst-filled microcavities were successfully used as platform for the immobilization of catalyst powders. No influence of the underlying gold support on the determined

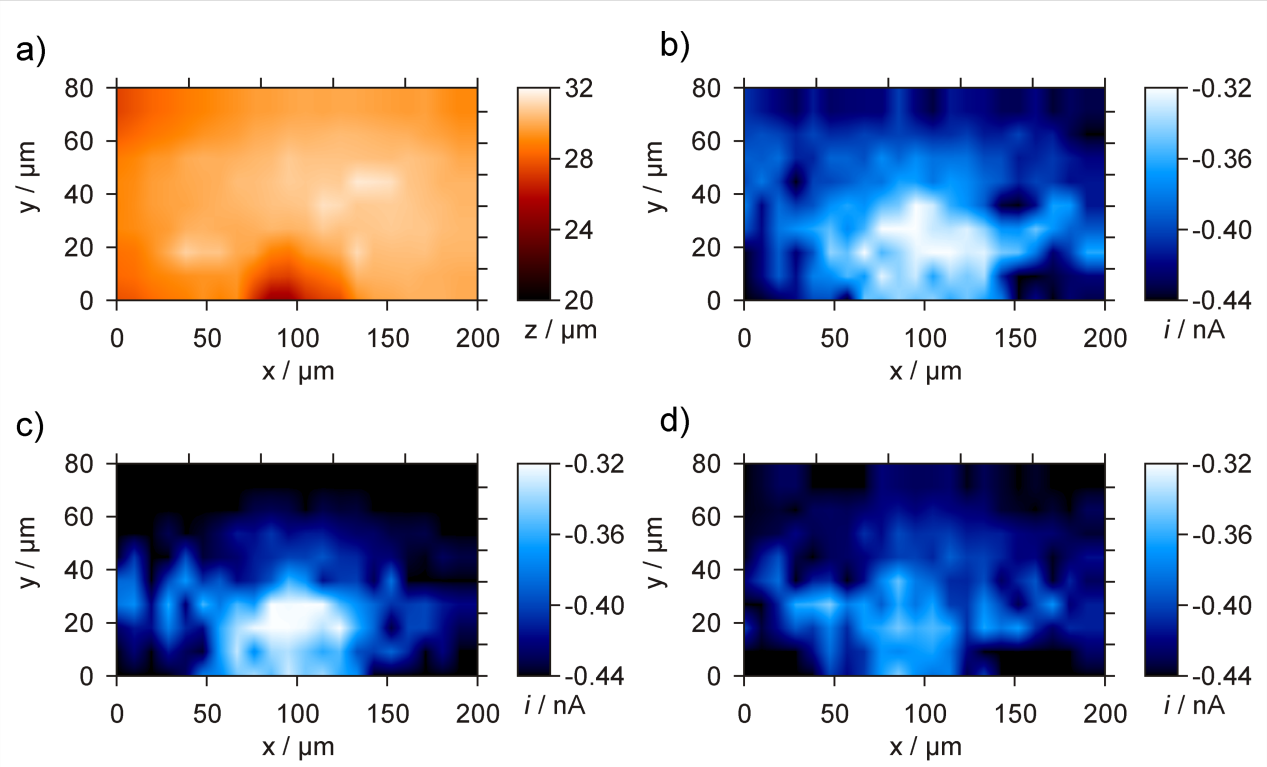

Figure 6: 4D SF/CD-RC-SECM experiment at a microcavity filled with a Pt/C model catalyst. Topography image a) and current images at b) the point of shearforce-contact *d*, c) *d* + 4 µm, and d) *d* + 20 µm. E_{sample} = −300 mV, $E_{tip,base}$ = 500 mV, $E_{tip,pulse1}$ = 500 mV, t_{pulse1} = 0.5 s, $E_{tip,pulse2}$ = −600 mV, t_{pulse2} = 0.5 s, images displayed at t = 0.25 s, d_{tip} = 1.9 µm, f_{osc} = 366.7 kHz, stop criterion: 5%.

local catalyst activity has been detected. Additionally, integration of RC-SECM in the detection scheme of the 4D SF/CD mode was successfully applied for the investigation of catalyst filled microcavities.

Catalysts for industrial applications are typically operated at elevated temperatures. Due to the availability of a temperature-controlled SECM setup [18] and the recently demonstrated capability of the tip-to-sample distance determination via shear-force-based approach curves in front of a heated surface [40], future work aims towards the high-resolution detection of catalytic activity at elevated temperatures.

Experimental

Chemicals and materials

All chemicals were used as received without further purification and all aqueous solutions were prepared using ultrapure water (Siemens Water Technologies, Barsbüttel, Germany). The electrochemical characterization of the SECM tips, microelectrodes, and recessed microelectrodes as sample surfaces were performed by means of cyclic voltammetry in an electrolyte containing 5 mM $[Ru(NH_3)_6]Cl_3$ (ABCR, Karlsruhe, Germany) and 100 mM KCl (Riedel-de Haën, Seelze, Germany) as background electrolyte. As a model catalyst a commercial nanoporous ORR catalyst from ETEK (Natick, USA) with 20 wt % Pt on Vulcan XC72 was used. An air saturated 0.1 M sodium phosphate buffer (pH 7, VWR International, Darmstadt, Germany) was used for all investigations of the catalytic activity towards ORR.

Platinum wires with diameters of 25 µm, 100 µm and 250 µm and a gold wire with a diameter of 100 µm were from Goodfellow (Bad Nauheim, Germany). Borosilicate glass capillaries (length 100 mm, outside Ø 1.5 mm, inside Ø 0.75 mm) were purchased from Hilgenberg (Malsfeld, Germany) while quartz glass capillaries (length 95 mm, outside Ø 0.9 mm, inside Ø 0.3 mm) were from Quarzschmelze Illmenau (Illmenau, Germany).

SECM instrumentation and tip preparation

A specifically designed SECM setup was used for all experiments and the main components have been described previously [15]. The SECM tip was stationary and the electrochemical measuring cell with the sample at the bottom movable by a stage of three joined stepper motors (SPI Robot Systems, Oppenheim, Germany). The nominal resolution in x-, y-, and z-direction was 10 nm per microstep. Additionally, a three axis piezo-positioning system (Nanocube P-611.3S, Physik Instru-

mente, Waldbronn, Germany) with strain gauge position sensors was used. The total travel length was 100 µm in each direction with a minimum step width of 1 nm and a reproducibility <10 nm.

The 4D shearforce-based constant-distance mode [15] with non-optical shearforce detection was used for all SECM measurements. A piezoelectric detection system (Sensolytics, Bochum, Germany) that consists of two piezoelectric plates each of them glued onto a brass holder was used for the detection of the shearforce interaction. For the piezo-piezo detection these piezo elements have been directly attached to the electrode body as reported in [13,41]. The needle shaped electrode is set into vibration at its own resonance frequency (f_{osc}) by means of the first attached piezo element. Changes of the vibration magnitude and phase shift are detected by the second piezo element that is closely positioned at the very end of the non-tapered electrode body. Excitation and low-noise determination of the tip vibration were realized by a lock-in amplifier (model 7280, Signal Recovery, Wokingham, UK). Electrode potentials and data acquisition were controlled by a bipotentiostat model PG 100 (Jaissle Elektronik, Waiblingen, Germany) in combination with a 16 bit AD/DA board (PCI-2517, Plug-In Electronics, Eichenau, Germany). In order to minimize electrostatic noise, the whole system was placed in a Faraday cage. The in-house written software for controlling the SECM setup was programmed in Visual Basic 6.0 (Microsoft, Unterschleissheim, Germany). The tip movement of the 4D shearforce-based constant-distance mode includes a shearforce-based approach curve until a predefined vibration change (stop criterion, typically in the range of 5–15%) is reached. Subsequently, a stepwise retraction of the tip with simultaneous data acquisition at each pre-defined tip-to-sample separation is performed. Diffusion profiles exceed far the geometric dimensions of the investigated surface structure. The collection of electrochemical data in z-direction requires therefore comparable large distances towards the sample surface. After lateral displacement, the tip is approached until the shearforce interaction range (usually observed at distances <300 nm) is reached again. In order to decrease the timescale of the tip approach, the procedure of the 4D SF/CD-SECM was supplemented with a predefined distance that is approached with a fast speed (typically 10 µm/s). Only the last few microns are afterwards approached at slow speed (e.g., 0.5 µm/s) that is required for the accurate shearforce-based positioning.

Vibratory needle shaped SECM tips were fabricated by means of a laser puller P-2000 from Sutter Instruments (Novato, USA) following an earlier published procedure [42]. Parameters for the sealing step were: Heat 810, Filament 5, Velocity 100, Delay 120, Pull 1 (repetition of 8–11 cycles, 20 s on and 40 s off). For the pulling step Heat 870, Filament 5, Velocity 130, Delay 150, Pull 220 was used. The platinum of the fabricated SECM tips was exposed by cutting the very end of the pulled Pt/capillary assembly with a blade under microscopic control (BX41, Olympus, Hamburg, Germany). For polishing a machine like in [42] was used. The electrodes were characterized by means of optical inspection under the microscope and by cyclic voltammetry with $[Ru(NH_3)_6]^{3+}$ as redox mediator. The size of the disk shaped electrodes was calculated using the diffusion limited steady state current and $i = 4nFDcr$ (n: number of electrons transferred per molecule, F: Faraday constant, D: diffusion coefficient, c: bulk concentration of the electroactive species and r: radius of the active electrode surface). A diffusion coefficient of 9.1×10^{-6} cm^2s^{-1} for $[Ru(NH_3)_6]^{3+}$ in KCl [43] was used. In all experiments a coiled Pt-wire (Ø 250 µm) counter electrode and a home build miniaturized Ag/AgCl (3 M KCl) reference electrode was used.

Sample Preparation

Catalyst spots

Spots of ORR catalyst powders were prepared by using a catalyst suspension applied by means of a piezoceramic spotter (model SciFA DW with tip PDC 80 from Scienion; Dortmund, Germany) onto polished (0.3 µm alumina paste) glassy carbon plates (Sigradur G, 1 mm thickness, HTW, Thierhaupten, Germany). 1 mL of the catalyst suspension consisted of 2.5 mg catalyst powder in a solution of 49.5% ethanol, 49.5% water and 1% Nafion (solution of 5 wt % Nafion from Sigma-Aldrich, Steinheim, Germany). The spot was prepared by 3200 droplets dispensing 45 pL of catalyst suspension per droplet.

Microelectrodes and microcavities

All SECM investigations of microelectrodes and microcavities as SECM sample were performed with a specifically designed measuring cell that enables an upstanding positioning of the electrode relative to the SECM tip (see also Figure 2g). All electrodes used as sample surface in SECM experiments had a total length of 2.5 cm. They were screwed upright inside the bottom of the measuring cell via a fitting and a corresponding O-ring. A polished Pt disk electrode with a diameter of 100 µm embedded in a large glass sheath with an overall outer diameter of 1.5 mm was used as a model sample for 4D SF/CD-RC-SECM experiments. Microcavities as platforms for catalyst immobilization were prepared via electrochemical etching of Au microelectrodes with diameters of 100 µm. After polishing of the initial Au disc electrode and cleaning for 15 min in distilled water in an ultrasonic bath electrochemical cleaning by means of potentiodynamic cycling (potential range: 0 mV to 1700 mV, scan rate: 200 mV s^{-1}, 20 cycles) in 0.5 M sulfuric acid and subsequent electrochemical characterisation of the cleaned disk electrode was performed. Electrochemical etching

was performed in 6 M HCl by cyclic voltammetry (potential range: 100 mV to 1300 mV, scan rate: 500 mV s^{-1}, 10 cycles). The chloride ions act as a complexing agent and at a potential of about 1100 mV etching of gold is performed [44]. After completion of the etching remaining impurities were removed by an ultrasound washing step in water and electrochemical cleaning in H_2SO_4. The recessed electrode was characterised by means of CV in 5 mM $[Ru(NH_3)_6]Cl_3$ and 100 mM KCl. The formed microcavity was filled with the catalyst powder by pressing the etched electrode in a small amount of catalyst material on a glass slide. Circular movements of the electrode on the glass plate lead to a homogeneous filling of the cavity. Excess catalyst material was removed with a tissue under microscopy control until the catalyst filling was lined up precisely with the surrounding glass sheath.

Acknowledgements

The authors are grateful to Dr Kathrin Eckhard for discussions at the beginning of the project, to Dr Andrea Puschhof for preparation of the Pt/C catalyst spots, and Alexander Botz for his contribution during his practical work. Financial support in the framework of the Helmholtz-Energie-Allianz "Stationäre elektrochemische Speicher und Wandler" (HA-E-0002) and from the Cluster of Excellence RESOLV (DFG EXC 1069) is gratefully acknowledged.

References

1. Bard, A. J.; Fan, F. R. F.; Kwak, J.; Lev, O. *Anal. Chem.* **1989,** *61,* 132–138. doi:10.1021/ac00177a011
2. Engstrom, R. C.; Weber, M.; Wunder, D. J.; Burgess, R.; Winquist, S. *Anal. Chem.* **1986,** *58,* 844–848. doi:10.1021/ac00295a044
3. Wipf, D. O.; Bard, A. J.; Tallman, D. E. *Anal. Chem.* **1993,** *65,* 1373–1377. doi:10.1021/ac00058a013
4. Macpherson, J. V.; Unwin, P. R. *Anal. Chem.* **2000,** *72,* 276–285. doi:10.1021/ac990921w
5. Kranz, C.; Friedbacher, G.; Mizaikoff, B.; Lugstein, A.; Smoliner, J.; Bertagnolli, E. *Anal. Chem.* **2001,** *73,* 2491–2500. doi:10.1021/ac001099v
6. Comstock, D. J.; Elam, J. W.; Pellin, M. J.; Hersam, M. C. *Anal. Chem.* **2010,** *82,* 1270–1276. doi:10.1021/ac902224q
7. Takahashi, Y.; Shevchuk, A. I.; Novak, P.; Murakami, Y.; Shiku, H.; Korchev, Y. E.; Matsue, T. *J. Am. Chem. Soc.* **2010,** *132,* 10118–10126. doi:10.1021/ja1029478
8. Alpuche-Aviles, M. A.; Wipf, D. O. *Anal. Chem.* **2001,** *73,* 4873–4881. doi:10.1021/ac010581q
9. Cortés-Salazar, F.; Träuble, M.; Li, F.; Busnel, J.-M.; Gassner, A.-L.; Hojeij, M.; Wittstock, G.; Girault, H. H. *Anal. Chem.* **2009,** *81,* 6889–6896. doi:10.1021/ac900887u
10. Cortés-Salazar, F.; Momotenko, D.; Lesch, A.; Wittstock, G.; Girault, H. H. *Anal. Chem.* **2010,** *82,* 10037–10044. doi:10.1021/ac1019304
11. McKelvey, K.; Edwards, M. A.; Unwin, P. R. *Anal. Chem.* **2010,** *82,* 6334–6337. doi:10.1021/ac101099e
12. Ludwig, M.; Kranz, C.; Schuhmann, W.; Gaub, H. E. *Rev. Sci. Instrum.* **1995,** *66,* 2857–2860. doi:10.1063/1.1145568
13. Ballesteros Katemann, B.; Schulte, A.; Schuhmann, W. *Chem.–Eur. J.* **2003,** *9,* 2025–2033. doi:10.1002/chem.200204267
14. James, P. I.; Garfias-Mesias, L. F.; Moyer, P. J.; Smyrl, W. H. *J. Electrochem. Soc.* **1998,** *145,* L64–L66. doi:10.1149/1.1838417
15. Nebel, M.; Eckhard, K.; Erichsen, T.; Schulte, A.; Schuhmann, W. *Anal. Chem.* **2010,** *82,* 7842–7848. doi:10.1021/ac1008805
16. Lazenby, R. A.; McKelvey, K.; Unwin, P. R. *Anal. Chem.* **2013,** *85,* 2937–2944. doi:10.1021/ac303642p
17. Fernández, J. L.; Walsh, D. A.; Bard, A. J. *J. Am. Chem. Soc.* **2005,** *127,* 357–365. doi:10.1021/ja0449729
18. Schäfer, D.; Puschhof, A.; Schuhmann, W. *Phys. Chem. Chem. Phys.* **2013,** *15,* 5215–5223. doi:10.1039/c3cp43520b
19. Cha, C. S.; Li, C. M.; Yang, H. X.; Liu, P. F. *J. Electroanal. Chem.* **1994,** *368,* 47–54. doi:10.1016/0022-0728(93)03016-I
20. Vivier, V.; Cachet-Vivier, C.; Cha, C. S.; Nedelec, J.-Y.; Yu, L. T. *Electrochem. Commun.* **2000,** *2,* 180–185. doi:10.1016/S1388-2481(00)00004-7
21. Cachet-Vivier, C.; Vivier, V.; Cha, C. S.; Nedelec, J.-Y.; Yu, L. T. *Electrochim. Acta* **2001,** *47,* 181–189. doi:10.1016/S0013-4686(01)00549-7
22. Umeda, M.; Kokubo, M.; Mohamedi, M.; Uchida, I. *Electrochim. Acta* **2003,** *48,* 1367–1374. doi:10.1016/S0013-4686(03)00002-1
23. Guilminot, E.; Corcella, A.; Chatenet, M.; Maillard, F. *J. Electroanal. Chem.* **2007,** *599,* 111–120. doi:10.1016/j.jelechem.2006.09.022
24. Vertova, A.; Barhdadi, R.; Cachet-Vivier, C.; Locatelli, C.; Minguzzi, A.; Nedelec, J.-Y.; Rondinini, S. *J. Appl. Electrochem.* **2008,** *38,* 965–971. doi:10.1007/s10800-008-9507-5
25. Locatelli, C.; Minguzzi, A.; Vertova, A.; Cava, P.; Rondinini, S. *Anal. Chem.* **2011,** *83,* 2819–2823. doi:10.1021/ac200286q
26. Minguzzi, A.; Locatelli, C.; Cappelletti, G.; Bianchi, C. L.; Vertova, A.; Ardizzone, S.; Rondinini, S. *J. Mater. Chem.* **2012,** *22,* 8896–8902. doi:10.1039/c2jm15750k
27. Kishi, A.; Inoue, M.; Umeda, M. *J. Phys. Chem. C* **2010,** *114,* 1110–1116. doi:10.1021/jp909010q
28. Kishi, A.; Shironita, S.; Umeda, M. *J. Power Sources* **2012,** *197,* 88–92. doi:10.1016/j.jpowsour.2011.08.010
29. Eckhard, K.; Chen, X.; Turcu, F.; Schuhmann, W. *Phys. Chem. Chem. Phys.* **2006,** *8,* 5359–5365. doi:10.1039/B609511A
30. Eckhard, K.; Schuhmann, W. *Electrochim. Acta* **2007,** *53,* 1164–1169. doi:10.1016/j.electacta.2007.02.028
31. Deegan, R. D.; Bakajin, O.; Dupont, T. F.; Huber, G.; Nagel, S. R.; Witten, T. A. *Nature* **1997,** *389,* 827–829. doi:10.1038/39827
32. Deegan, R. D. *Phys. Rev. E* **2000,** *61,* 475–485. doi:10.1103/PhysRevE.61.475
33. Zhang, B.; Zhang, Y.; White, H. S. *Anal. Chem.* **2004,** *76,* 6229–6238. doi:10.1021/ac049288r
34. Zhang, B.; Galusha, J.; Shiozawa, P. G.; Wang, G.; Bergren, A. J.; Jones, R. M.; White, R. J.; Ervin, E. N.; Cauley, C. C.; White, H. S. *Anal. Chem.* **2007,** *79,* 4778–4787. doi:10.1021/ac070609j
35. Lee, S. J.; Mukerjee, S.; McBreen, J.; Rho, Y. W.; Kho, Y. T.; Lee, T. H. *Electrochim. Acta* **1998,** *43,* 3693–3701. doi:10.1016/S0013-4686(98)00127-3
36. Thompson, S. D.; Jordan, L. R.; Forsyth, M. *Electrochim. Acta* **2001,** *46,* 1657–1663. doi:10.1016/S0013-4686(00)00767-2
37. Gasteiger, H. A.; Kocha, S. S.; Sompalli, B.; Wagner, F. T. *Appl. Catal., B* **2005,** *56,* 9–35. doi:10.1016/j.apcatb.2004.06.021

38. Nebel, M.; Grützke, S.; Diab, N.; Schulte, A.; Schuhmann, W. *Angew. Chem., Int. Ed.* **2013,** *52,* 6335–6338. doi:10.1002/anie.201301098
39. Nebel, M.; Grützke, S.; Diab, N.; Schulte, A.; Schuhmann, W. *Faraday Discuss.* **2013,** *164,* 19–32. doi:10.1039/C3FD00011G
40. Sode, A.; Nebel, M.; Pinyou, P.; Schmaderer, S.; Szeponik, J.; Plumeré, N.; Schuhmann, W. *Electroanalysis* **2013,** *25,* 2084–2091. doi:10.1002/elan.201300258
41. Ballesteros Katemann, B.; Schulte, A.; Schuhmann, W. *Electroanalysis* **2004,** *16,* 60–65. doi:10.1002/elan.200302918
42. Ballesteros Katemann, B.; Schuhmann, W. *Electroanalysis* **2002,** *14,* 22–28. doi:10.1002/1521-4109(200201)14:1<22::AID-ELAN22>3.0.CO;2-F
43. Marken, F.; Eklund, J. C.; Compton, R. G. *J. Electroanal. Chem.* **1995,** *395,* 335–339. doi:10.1016/0022-0728(95)04268-S
44. Hu, Z.; Ritzdorf, T. *J. Electrochem. Soc.* **2007,** *154,* D543–D549. doi:10.1149/1.2768901

License and Terms

Beilstein Journal of Nanotechnology

Change of the work function of platinum electrodes induced by halide adsorption

Florian Gossenberger[1], Tanglaw Roman[*1], Katrin Forster-Tonigold[2] and Axel Groß[1,2]

Full Research Paper

Open Access

Address:
[1]Institute of Theoretical Chemistry, Ulm University, 89069 Ulm, Germany and [2]Helmholtz Institute Ulm (HIU) for Electrochemical Energy Storage, 89069 Ulm, Germany

Email:
Tanglaw Roman[*] - tanglaw.roman@uni-ulm.de

* Corresponding author

Keywords:
density functional theory; ionicity; polarizability; surface dipole; work function

Beilstein J. Nanotechnol. **2014,** *5,* 152–161.
doi:10.3762/bjnano.5.15

Received: 22 August 2013
Accepted: 21 January 2014
Published: 10 February 2014

This article is part of the Thematic Series "Electrocatalysis on the nm scale".

Guest Editor: R. J. Behm

Abstract

The properties of a halogen-covered platinum(111) surface have been studied by using density functional theory (DFT), because halides are often present at electrochemical electrode/electrolyte interfaces. We focused in particular on the halogen-induced work function change as a function of the coverage of fluorine, chlorine, bromine and iodine. For electronegative adsorbates, an adsorption-induced increase of the work function is usually expected, yet we find a decrease of the work function for Cl, Br and I, which is most prominent at a coverage of approximately 0.25 ML. This coverage-dependent behavior can be explained by assuming a combination of charge transfer and polarization effects on the adsorbate layer. The results are contrasted to the adsorption of fluorine on calcium, a system in which a decrease in the work function is also observed despite a large charge transfer to the halogen adatom.

Introduction

In electrochemistry, processes at the interface between an electron conductor, the electrode, and an ion conductor, the electrolyte, are studied [1]. In order to be charge neutral, the electrolyte contains equal amounts of anions and cations. In aqueous electrolytes, protons acting as cations are always present [2] whereas halides are often chosen as anions. The contact of a particular solvent with an electrode surface can lead to a rather complex situation at the electrode surface [3,4]. The characteristics of the solvent significantly affects processes such as adsorption and desorption. Because of the strong interaction of halogen atoms with metal electrodes, the metal electrodes typically become halogen-covered through specific adsorption. These adsorbed anions are not only part of the electrochemical double layer, in general they also change the work function of

the electrode, which is directly related to the electrode potential [5]. Furthermore, they also affect the chemical properties of the electrodes [6].

In spite of the importance of the specific adsorption of anions in electrochemistry, atomistic details of the role of anions in surface electrochemistry are still poorly understood [7]. Here, surface science studies focusing on the change of the properties of metal surfaces upon halide adsorption can help to elucidate the role of anionic specific adsorption at electrode/electrolyte interfaces, in particular with respect to the adsorption-induced change of the work function. It is known that the work function is strongly influenced by the adsorption of ions, which can lead to both an increase and a decrease of the work function [8-17]. In a previous study, we have addressed the adsorption of iodine and chlorine on Cu(111) [9] by using periodic density functional theory (DFT) calculations. Whereas chlorine causes the expected increase of the work function upon adsorption of an electronegative adsorbate, iodine leads to a surprising decrease of the work function for coverages up to approximately 0.4 ML. By analyzing the underlying electronic structure, we were able to show that this behavior can be explained through a combination of charge transfer and polarization effects of the adsorbate layer.

We have now extended this previous study by considering the adsorption of fluorine, chlorine, bromine and iodine on Pt(111) in order to check whether the findings for halogen adsorption on Cu(111) are also valid for the technologically important electrode material platinum. It has already been observed experimentally [18-20] as well as theoretically [11,13,17] that the adsorption of chlorine, bromine and iodine on Pt(111) leads to an unexpected decrease of the work function. Based on calculations for several adsorbates on tungsten surfaces, Leung, Kao and Su pointed out that it is possible to relate the electronegativity scale to the direction of the charge transfer but not necessarily to the induced work function change. It has also been shown that the formation of halogen oxides at the surface of a metal oxide leads to a decrease in the work function [21]. The problem of the unexpected decrease of the work function was also tackled by Michaelides et al. [8] for a system of nitrogen adsorbed on a tungsten (100) surface. They showed that the decrease of the work function depends strongly on the length of the chemisorption bond. If the adatom is located close to the surface, it is in the region of the overspill electron density of the metal. This leads to an area of electron depletion far from the surface, and in combination with an electron buildup in the area around the adsorbed ion, to a decrease of the work function.

In this paper we present a detailed study of the halogen-induced change of the work function on Pt(111) as a function of the halogen coverage, which has still been missing. We will show that the observed decrease of the work function upon the adsorption of chlorine, bromine and iodine on Pt(111) at low coverages can be explained by the strong polarization of the adsorbed halogen atoms, as in the case of I/Cu(111) [9]. We contrast these results with findings obtained for fluorine adsorption on calcium, for which an adsorption-induced decrease of the work function is also observed. However, due to the particular geometric conditions in this system, the spillout mechanism [8,22] is operative.

Methods

For the following calculations, the periodic density functional theory (DFT) program Vienna Ab initio Simulation Package (VASP) was used. The exchange and correlation energy was calculated by using the generalized gradient approximation (GGA) with the PBE functional, developed by Perdew, Burke and Ernzerhof [23]. This functional is widely used, as it has been shown to give reliable results in terms of atomization energy, chemisorption energies [24,25], work function changes [26], and good estimates of bulk properties of metals [27]. Hybrid functionals are not necessarily improvements to PBE; for example they do not yield a satisfactory description of the characteristics of transition metals [27].

To describe the ionic cores of the atoms, we used the projector augmented wave potentials (PAW) constructed by Kresse and Joubert [28]. The electronic wave functions were expanded in a plane wave basis set up to an energy cutoff of 400 eV. For the calculations, a periodic slab with a thickness of 7 atomic layers and 4 × 4 lateral periodicity was chosen. All calculations were done by using a symmetric setup of the slab, i.e., the halogen atoms were adsorbed on both sides of the slab, the middle three layers of the slab were kept fixed and the outermost two layers of both sides of the slab together with the adatoms were relaxed. Thus no dipole correction was necessary in order to derive the work function of the surface terminations. The unit cell was computed with a gamma-centered 4 × 4 × 1 *k*-point mesh.

The optimized lattice constant for platinum was found to be $a = 3.98$ Å, which is only 1.48% larger than the standard experimental value [29]. For low coverages the halogens iodine, bromine and chlorine adsorb most stably at the fcc threefold-hollowsite position on a platinum (111) surface. Since the hcp threefold-hollow position is also quite stable, the halogens were ordered in symmetric patterns on the surface with the highest possible nearest neighbor distance to other adsorbed atoms in hcp and fcc positions. The threefold-hollow adsorption positions are considered as the most probable adsorption sites for halogens on metals [9,10,14,30]. In this manner, six different coverages – 1/16 ML, 2/16 ML, 3/16 ML, 4/16 ML, 6/16 ML

and 8/16 ML – were created, which are illustrated in Figure 1. The structures of iodine, bromine and chlorine were relaxed completely.

Interestingly enough, fluorine atoms adsorb more stably at the on-top position of platinum. At this position, the average distance to the topmost surface layer is larger than on the threefold-hollow sites. Since we are interested in getting trends among the halogen atoms in order to understand and predict adsorption processes, we kept the fluorine in the threefold-hollow site positions, but allowed for vertical relaxation, which made a better comparison with the results for the chlorine, bromine and iodine adsorption structures possible.

Results and Discussion

Of central importance for this particular work is the determination of the change of the work function as a function of the halogen coverage. In periodic slab calculations, the work function is given by the difference between the Fermi energy and the value of the one-electron potential in vacuum. Vacuum is reached when the potential does not change anymore with increasing distance from the surface.

Figure 2 shows the work function of halogen-covered Pt(111) as a function of the halogen coverage. For clean Pt(111), the calculations yield a value of 5.71 eV. Various experimental measurements in the last decades do not agree well with each other. They are in the range of 5.6 eV to 6.1 eV [20,31-37]. The presence of fluorine on Pt(111) always increases the work function, which is qualitatively consistent with what one expects from a dipole involving a negative charge on the adsorbate. The adsorption of chlorine, bromine or iodine on a platinum (111) surface reduces the work function at low coverages. While the trend reverses at 0.25 ML, ΔΦ becomes positive not until the coverage reaches half a monolayer. The experimental trends [18-20] as well as theoretical values by Migani et al. [10] agree with the calculated results.

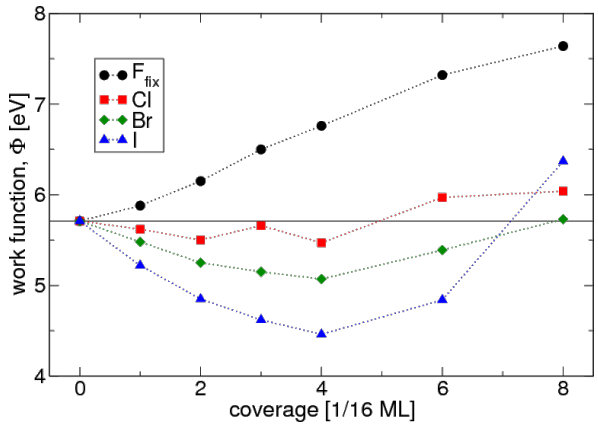

Figure 2: Calculated change of the work function vs coverage for the adsorption of fluorine, chlorine, bromine and iodine on Pt(111). The high value for the 0.5 ML calculation of iodine is due to a double layer structure of the adsorbates, caused by the larger size of iodine atoms.

Aside from the sign of the work function change, the dependence of ΔΦ on the halogen coverage is another aspect that needs

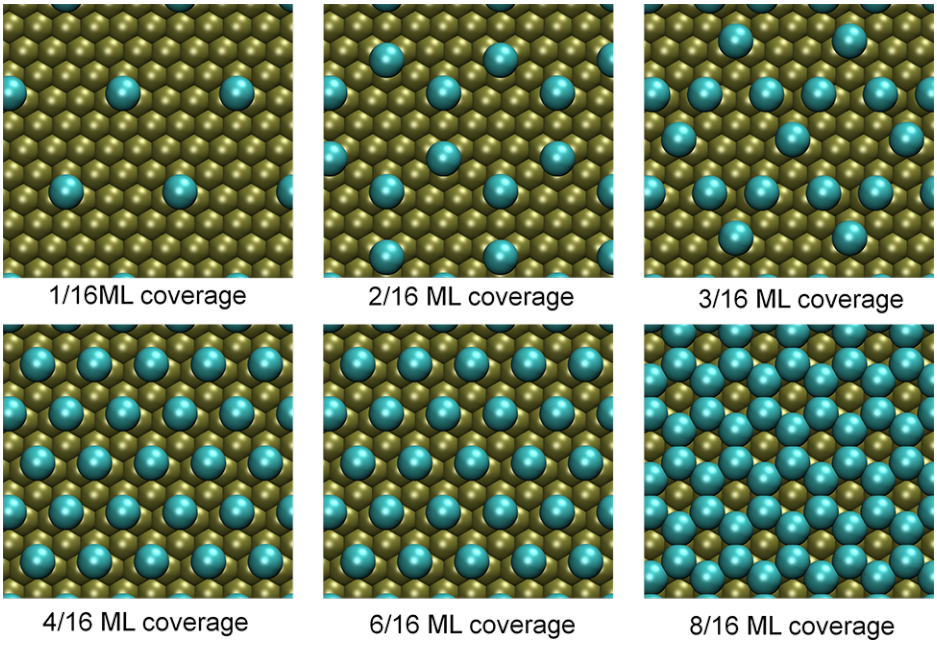

Figure 1: The figures show the relaxed structures of different coverages of chlorine on a Pt(111) surface.

to be clarified. In a simple model, one may completely neglect the interaction between the adsorbates. In this case, a linear trend $\Delta\Phi(\theta) \propto -\theta\Delta\mu$ would be expected, where θ is the surface coverage and Δμ is the change in the surface dipole moment brought about by the adsorption of a halogen atom. Obviously, this model is applicable only at low coverages in Figure 2. In a more advanced model, the electrostatic interaction between adjacent dipoles is taken into account by assuming that the mutual repulsion of the dipoles leads to a decrease in the polarity of the halogen–metal bond. The term Δμ thus becomes dependent on the halogen coverage, which causes a saturation of ΔΦ at high coverages. However, this does not explain the observed non-monotonic behavior of the work function change and so a more comprehensive explanation is needed.

In general, an adsorbate layer that involves charge transfer in the adsorption reaction can produce an observable change in the work function of the metal surface since electrons, in leaving the metal surface, will have to pass through the resulting interface dipole layer. Depending on the orientation of the dipole, this can either make removing electrons easier or harder. More precisely, the connection between work function change and surface dipole moment change is given by

$$\Delta\Phi = -\frac{e}{\varepsilon_0}\left(\mu_z - \mu_{z,0}\right) = -\frac{e}{\varepsilon_0}\Delta\mu\,, \qquad (1)$$

where $\mu_{z,0}$ is the surface-normal dipole moment per unit area of the clean surface, μ_z is the surface-normal dipole moment per unit area for the adsorbate-covered surface. A positive value of μ has traditionally been assigned to a dipole pointing away from the bulk, which leads to a decrease of the work function ($\Delta\Phi < 0$). Conversely, a negative μ points into the bulk and increases the work function ($\Delta\Phi > 0$). The surface dipole moment changes when the electron density close to the surface becomes redistributed upon bond formation. The most straightforward description of this redistribution is through the electron density difference that is given by the difference of the electron density of the interacting system with the total electron density of the non-interacting metal slab and halogen layer at the same atomic positions, $\rho_{\text{diff}} = \rho_{\text{Hal+Pt}} - (\rho_{\text{Hal}} + \rho_{\text{Pt}})$. The electron density difference profile $\Delta\lambda(z)$ along the z direction corresponds to the lateral sum of the electron density difference in the x and y directions,

$$\Delta\lambda = \frac{1}{N}\iint_{\text{cell}} \rho_{\text{diff}}\, dx\, dy\,, \qquad (2)$$

where N is the number of halogen atoms adsorbed on one side of the slab per unit cell. The Δλ profiles for a coverage of 1/16 ML of the four halogens are shown in Figure 3. The shape of the diagrams for higher coverages look similar. The profiles illustrate how the electron density is reorganized along the z direction when the adatoms adsorb. The gray area on the left hand side denotes the metal slab. The topmost metal atoms are centered at z = 0 Å. The electron density difference profile shows a significant electron depletion far from the surface for the case of chlorine, bromine and iodine, followed by an electron buildup close to the surface, and oscillations in the metal. In the case of fluorine, there is just an electron buildup around the fluorine atom, followed by oscillations into the bulk. This electron buildup around the fluorine atom indicates an ionic state. Fluorine is partially constrained to remain at the threefold-hollow sites, where the average distance from the center of the adsorbates to the topmost surface layer is smaller than for fluorine adsorbed at the on-top position. Calculations for F atoms at the most stable adsorption site may give slightly different results in charge transfer and dipole moments.

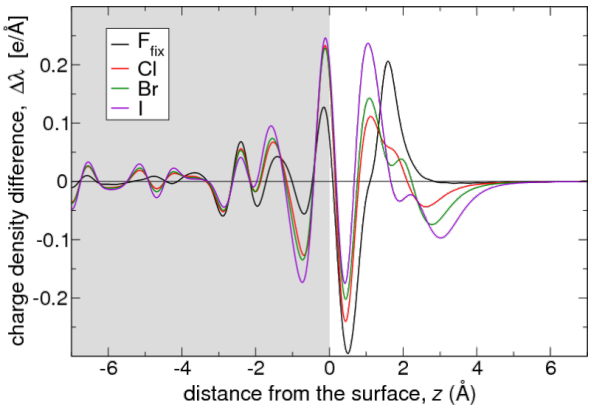

Figure 3: Charge density difference Δλ(z) for the adsorption of fluorine, chlorine, bromine, and iodine on Pt(111) at the fcc hollow position for a coverage of 1/16 ML. The subsurface region corresponds to the gray-shaded area at z < 0.

In the next step, the resulting surface dipole moment change $\Delta\mu_N$ can be determined by analyzing Δλ, as in [9] for the adsorption of iodine and chlorine on Cu(111). The N indicates that this is the total surface dipole moment of N atoms adsorbed in the unit cell. The dipole moment change due to the adsorption process can be calculated by integration of $\Delta\lambda_N(z) = N\Delta\lambda(z)$ along the z direction, perpendicular to the surface,

$$\Delta\mu_N = -\int_{\text{bulk}}^{\text{vac}} z\Delta\lambda_N(z)\, dz \qquad (3)$$

where the negative sign is introduced because positive regions of $\Delta\lambda_N$ (i.e., electron buildup) are in fact negatively charged. The integration runs from the central layer of the platinum slab

to the middle of the vacuum. Figure 4 shows the good correlation between the calculated work function and the dipole moment derived from the charge distribution, which verifies the assumptions that underlie Equation 3.

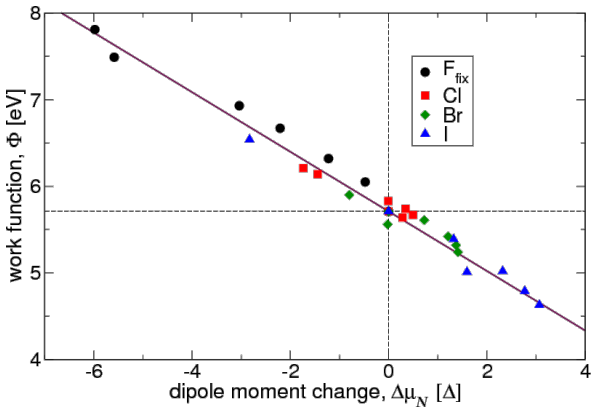

Figure 4: Calculated work function versus dipole moment. The solid line corresponds to the expectation according to Equation 1.

Since Δλ of the fluorine-covered platinum slab shows for all coverage values the structure of an electron buildup far from the surface, followed by an electron depletion close to the surface, the dipole moment on each face of the slab becomes more negative as a function of the coverage, which is consistent with a work function increase. For the other three halogens, the electron density difference profile looks more complicated. There is an electron depletion far from the surface, followed by an electron buildup. This structure is sufficiently strong to invert the dipole moment, so that $\Delta\mu_N$ changes sign as a function of the coverage.

It has been suggested that adsorbates that are located rather close to a surface can decrease the electron spillout at the surface. This can cause unexpected changes of the work function, such as the decrease of the work function observed for N on the W(100) surface [8] or the small dipole moment for O on Al(111) [22]. However, the area of electron depletion for chlorine, bromine and iodine is approximately 2.5–4.0 Å away from the center of the topmost platinum atoms, far beyond the region of a sizable electron spillout for the uncovered surface. This electron density shift rather corresponds to a redistribution of the electron density in the adatom layer, which can be associated with a covalent character of the chemisorption bond. This rearrangement is particularly strong for the adsorption of iodine, and slightly weaker for bromine and chlorine. The character of the chemisorption bond between iodine and platinum was discussed in the past [10,17] and conflicting results in terms of the charge of the adatom were presented. In this study, we find that the charge buildup between the iodine and the Pt surface indicates the presence of a covalent bond. Similar conclusions have been found, for example for the adsorption of I on Cu [9] or Cl on Au [14]. Furthermore, in a chronocoulometric study [38] it was found that the adsorbed species is basically a neutral chlorine atom which agrees nicely with our findings. Fluorine, on the other hand, tends to adsorb to the Pt(111) surface mainly in the ionic form.

Coverage trends

Our calculations confirm the experimental observations [18-20] of a work function minimum as a function of the halogen coverage. Several mechanisms have been proposed to explain its occurrence. For cationic adsorbates, the subsequent increase of Φ beyond the work function minimum was attributed to a reduction of the ionicity of the cationic adsorbate [39]. This explanation, however, does not apply to the halogen adsorption considered here as we still find no indication of cationic adsorption.

The work function minimum has also been explained through differences in site occupancies that occur as halogen coverage increases. Subsurface penetration followed by surface adsorption was one of the possibilities considered in explaining the work function minimum for chlorine on platinum [18]. This was based on the assumption that subsurface penetration and surface adsorption lead to opposite dipole moments at the surface. In contrast, for iodine on platinum, an adsorption site effect was suggested under the assumption that threefold-site adsorption decreases the work function, while adding iodine to top sites increases it [20]. As the coverage increases, more top sites get occupied by iodine, which leads to the increase in Φ beyond the minimum. Still, the change of the surface work function remained negative over the entire coverage range that was considered.

A more recent computational study has shown that the adsorption of isolated iodine atoms at the hollow or top sites both lead to $\Delta\Phi < 0$, although the decrease in the work function is larger for the adsorption of iodine at the hollow site [17]. Another explanation for the minimum of the work function was proposed, namely changes in the polarization of the metal substrate. The authors found that the polarization in the platinum substrate that is induced by the presence of the iodine anion adsorbate is reduced with increasing coverage, hence explaining the non-monotonic behavior in ΔΦ.

While changing site occupancy with increasing coverage can and will lead to observable changes in the work function, in this study we focus on changes of the work function that are caused by effects that are primarily electronic in nature, i.e., that are not due to changes in the adsorption or absorption site. Hence a

deeper analysis of charge transfer, internal redistribution of charge in the metal substrate, and redistribution of charge on the halogen adatoms is needed. To analyze the surface dipole moments in detail, we use the total surface dipole moment per unit cell normalized to the number of adatoms to define the dipole moment change created per adsorbed atom,

$$\Delta\mu_{\mathrm{q}} = -\bar{z}_{\mathrm{X}} \int_{z_{\mathrm{q}}}^{\mathrm{vac}} \Delta\lambda(z)dz\,, \tag{4}$$

The normalized dipole moments are shown in Figure 5. The plots are nowhere flat, suggesting the presence of considerable neighboring adatom interactions even at the lowest coverages. There is also a clear tendency for the dipole moment induced by the adsorption of a single halogen atom to be reduced as the concentration of adatoms increases at the Pt surface. Note that the 0.5 ML coverage of iodine is so closely packed that the repulsion of the electron shells induces a two-layer structure of the adsorbate layer. Every second iodine atom becomes a part of a second adsorbate layer, which is positioned about 1.7 Å farther from the surface than the first layer of iodine atoms.

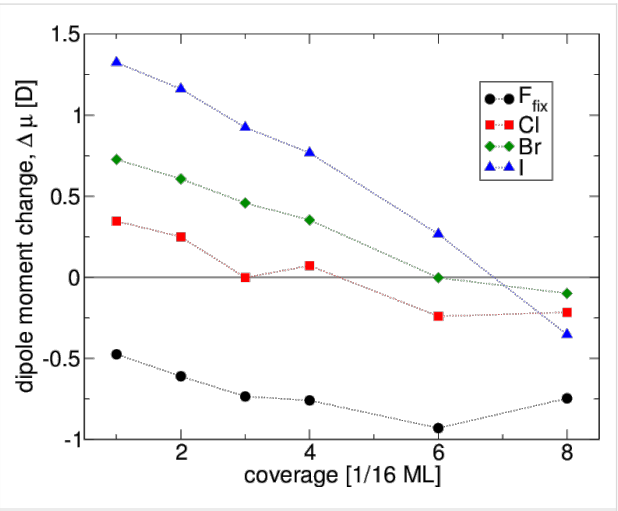

Figure 5: Calculated normalized dipole moment as a function of the coverage of fluorine, chlorine, bromine and iodine on Pt(111).

Looking at the charge transfer as a function of the coverage is useful to understand the negative slopes of Δμ for the adsorption of halogens. Quantifying charge transfer between atoms however always involves a more or less ambivalent choice as far as associating the electron density to a particular atom is concerned. We have therefore considered two limits: a maximum-charge-transfer picture, and a zero-charge-transfer picture of halogen adsorption on platinum.

The maximum charge transfer is obtained by assuming that the complete electron buildup between an adatom and the surface is always counted to the adsorbate. In practice, this is done by determining the plane $z = z_q$ between the metal and the adatom that maximizes the area under $\Delta\lambda(z)$ at the halogen side. The charge transfer from the metal surface to the adatoms gives rise to a change of the dipole moment, $\Delta\mu_{\mathrm{q}}$. By using a simple model that assumes charge transfer from the topmost Pt layer to the halogen adlayer, the contribution of the electron transfer to the surface dipole moment can be quantified,

$$\Delta\mu_{\mathrm{q}} = -\bar{z}_{\mathrm{X}} \int_{z_{\mathrm{q}}}^{\mathrm{vac}} \Delta\lambda(z)dz\,, \tag{5}$$

where $\bar{z}_{\mathrm{X}}$ is the average distance of the halogen adatoms from the metal surface. We combine all other parts contributing to the total dipole moment in the term $\Delta\mu_{\mathrm{pol}}$, because it involves polarization effects in the metal and in the adlayer. The combination of both contributions leads to the total dipole moment change,

$$\Delta\mu = \Delta\mu_{\mathrm{q}} + \Delta\mu_{\mathrm{pol}}\,. \tag{6}$$

These contributions are plotted in Figure 6a and Figure 6b, respectively. The effect of the charge transfer $\Delta\mu_{\mathrm{q}}$ to the surface dipole is nearly zero for iodine. For fluorine, however, charge transfer plays a significant role, which can be expected since it is more electronegative than the other halogens, as also reported by Migani et al. [10]. Moreover, the negative dipole moment change for the adsorption of fluorine decreases even more with increasing coverage, which is due to the fact that the adsorption distance and charge transfer to the F adatoms increase with increasing coverage.

The results also suggest that higher surface concentrations of adatoms decrease the dipole moment change per adatom through mutual depolarization. This effect is most pronounced for iodine, as well as for a low-coverage adsorption of bromine and chlorine, but not for fluorine because of the low polarizability of small atoms. Besides the repulsion of the dipoles, the electron shells of adsorbed atoms at a higher coverage start to repel.

Another interesting question concerns the importance of the electron density oscillations in the subsurface, as shown in Figure 3. It might be speculated that these oscillations could be responsible for the significant polarization part, $\Delta\mu_{\mathrm{pol}}$, of the total dipole moment Δμ. To answer this question, we have divided Δλ into two parts, one representing the dipole moment change due to polarization in the adsorbate layer and the other part representing the dipole moment change due to polarization in the substrate,

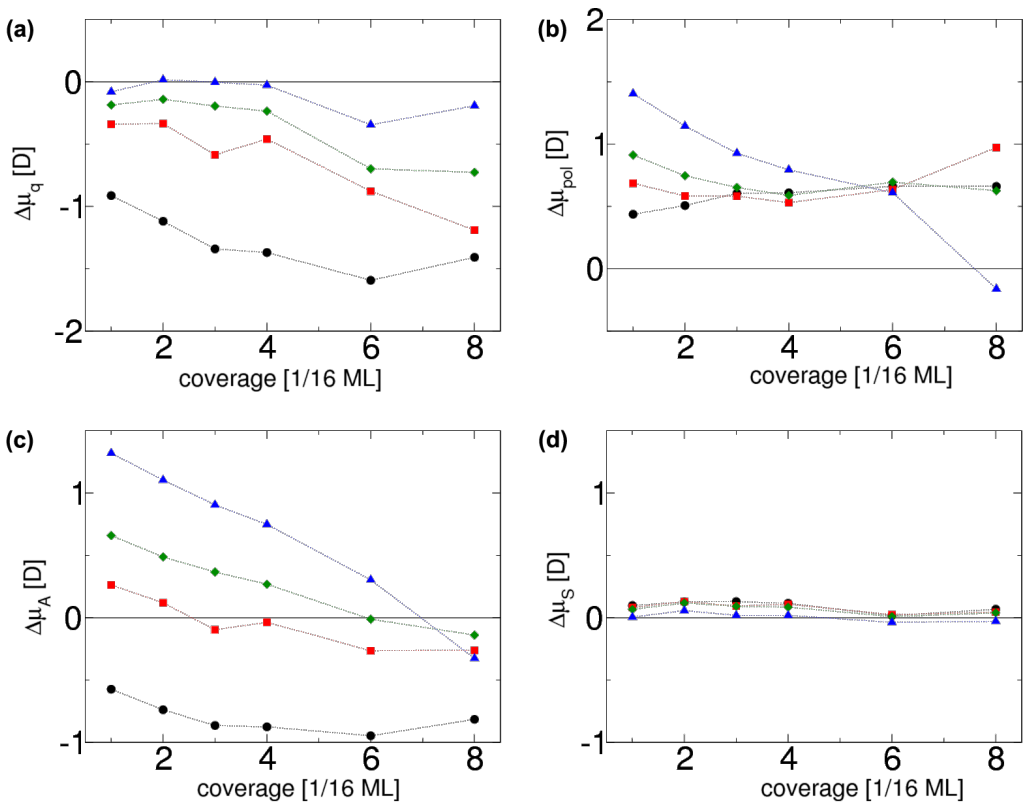

Figure 6: Contributions to the total dipole moment change $\Delta\mu$ according to Equation 6 and Equation 7 as a function of halogen coverage. The term $\Delta\mu_q$ describes the purely charge transfer induced dipole moment and $\Delta\mu_{pol}$ the polarization induced dipole moment; $\Delta\mu_A$ shows the effect of the adsorbate layer on the total dipole moment and $\Delta\mu_S$ indicates substrate effects. The color code denoting the different halogen atoms is the same as used in the previous figures.

$$\Delta\mu = \Delta\mu_A + \Delta\mu_S \,. \tag{7}$$

This zero-charge transfer picture for breaking down polarization is especially effective for iodine adsorption on platinum. Such a distinction between pure substrate and adsorbate contributions is again an arbitrary choice. In order to obtain trends, the integration was started from the point z_0, at which the unit cell is divided exactly into the charge neutral part of the adlayer and the charge neutral part of the platinum slab, defined by the condition

$$\int_{z_0}^{\text{vac}} \Delta\lambda(z)\,dz = 0 \,. \tag{8}$$

For this choice, the analogous integral on the metal side is also zero due to the overall charge neutrality of the supercell. It is then possible to estimate the surface dipole moment μ_S and the adsorbate dipole moment μ_A by using

$$\Delta\mu_S = \int_{\text{bulk}}^{z_0} z\Delta\lambda(z)\,dz \tag{9}$$

and

$$\Delta\mu_A = \int_{z_0}^{\text{vac}} z\Delta\lambda(z)\,dz \,. \tag{10}$$

We briefly summarize the difference in the integration limits z_q and z_0 of Equation 5 and Equation 9, respectively: These equations have the purpose of dividing the unit cell into two parts, but it is not clear where exactly the adatom ends and where the platinum begins or vice versa. The two integration limits mark special points in the graph of $\Delta\lambda$. The limit z_q divides the unit cell at the point of maximum charge at the adatom, in contrast to z_0 which divides at the point of zero charge at the adatom.

The adsorbate and the substrate dipole moments, which are plotted in Figure 6c and Figure 6d, respectively, indicate that the contribution of the change of the metal substrate dipole moment $\Delta\mu_S$ to the total change of the dipole moment $\Delta\mu$ is minor compared with the impact of adsorbate polarization $\Delta\mu_A$, which affects the total dipole moment change quite dramatically. This also means that our analysis does not support the

view [17] that substrate polarization plays an important role in explaining the halogen-induced work function decrease.

Additionally, it is noticeable that the decrease in the total change of the dipole moment in the case of iodine and chlorine at around 0.25 ML is much more significant on platinum compared with the total change of the dipole moment of copper [9]. The work function of the copper surface is about 1 eV smaller, thus the charge transfer is larger from copper than from the platinum surface to the halogen adatom. It is for this reason that the adsorption of chlorine on copper does not exhibit a work function minimum with increasing adsorption coverage [9,40], similar to the work function plot of F on Pt in the current study.

Fluorine on calcium

We have shown that the strong polarizability of large atoms such as iodine leads to a considerable buildup of charge in the adatom–surface bonding regions, which is consistent with covalent bonding, and an accompanying electron depletion region far from the surface which creates a net dipole on the adatom that in turn promotes a decrease in the work function. Here we show that the adsorption of fluorine can also decrease the work function of a metal surface, namely calcium, but through a different mechanism. Calcium is considered to be an attractive electrode material in electrochemical energy storage because of its low electronegativity, earth abundance, and low cost [41]. Fluorine adsorbs stably at a threefold hollow site on calcium, which is a metal with fcc structure and a calculated lattice constant that is 39% larger than that of platinum. At its equilibrium adsorption position, fluorine is only 0.73 Å from the topmost layer of Ca atoms. In contrast, iodine adsorbs 2.07 Å from the platinum surface.

In Figure 7, we compare two systems, in which halogen adsorption decreases the work function of the metal substrate. The left panel shows the adsorption of iodine on Pt(111) at a coverage of 1/9 ML. The right panel shows fluorine adsorption on Ca(111) at a coverage of 1/4 ML. This yields similar absolute values for the coverage per area for the two systems given the stark difference between the lattice constants of Pt and Ca. At these adsorption coverages, iodine reduces the platinum work function by 0.79 eV, while fluorine reduces the calcium work function by 0.20 eV.

Figure 7 shows that halogen adsorption can create a surface dipole that reduces the work function in two very distinct mechanisms, namely adatom polarization and spillout depletion. Iodine on platinum is characterized by a negligible charge transfer, covalent bonding, and polarization on the adatom. There is no evidence for a dominantly ionic bond for I/Pt(111)

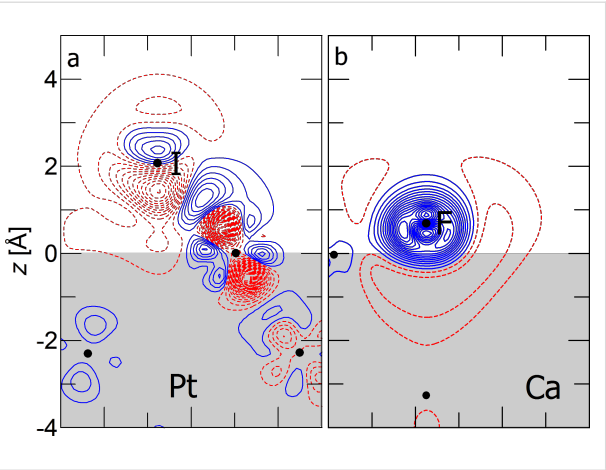

Figure 7: Cross sections of electron density difference $\rho_{diff}(\mathbf{r})$ at the surface. Solid-blue (dashed-red) contours denote regions of electron buildup (depletion). The interval between contours of constant electron density is 0.01 electrons/Å^3. The region of the metal slab is shaded gray as a visual aid.

reported in [17]. Fluorine adsorption on calcium on the other hand is characterized by a large charge transfer to the adatom with negligible polarization, creating a system, which is comprised of a negative ion enveloped by electron depletion. Since fluorine is adsorbed very close to the surface, it is embedded within the electron spillout region of calcium. The depletion of electron density in the spillout region not only reduces the effect of the strongly negative fluorine on the net dipole, but even overcompensates it, resulting in a decrease of the work function.

Conclusion

The change of the work function induced by halogen adsorption on Pt(111) as a function of the coverage was studied by electronic structure calculations. In general, because of their electronegativity, the adsorption of halogens is associated with a charge transfer from the metal substrate to the adsorbate layer. In the case of fluorine adsorption, this leads to the expected increase in the work function. However, for chlorine, bromine and iodine adsorption on Pt(111), the charge transfer effect is overcompensated by a significant polarization of the adsorbate, causing a work function decrease. The decreasing change of the dipole moment per adatom with an increasing adsorption coverage leads to a maximum in the total surface dipole moment and a minimum in the work function at a coverage of approximately 0.25 ML. The mutual depolarization within the adsorbate layer contributes to the eventual work function increase.

The anomalous work function change on platinum is large because of the high work function of clean platinum, which favors only a small electron transfer to the halogen adatoms

compared with other metals. Therefore, polarization effects that reverse the dipole moment attributed to charge transfer are more pronounced than on metals with smaller work functions such as copper.

Furthermore, we showed that fluorine adsorption can also lead to an anomalous work function decrease, but through a different mechanism. On calcium, fluorine is adsorbed close to the surface because of the large spacing between the calcium atoms. This causes a depletion of the electron density in the spillout region, which results in a decrease of the work function.

Acknowledgements

This research has been supported by the German Science Foundation (DFG) through the research unit FOR 1376 (DFG contract GR 1503/21-1). Computer time has been provided by the BW-Grid of the federal state of Baden-Württemberg and by a computer cluster financed through the stimulus programme "Electrochemistry for Electromobility" of the German Ministry of Education and Science (BMBF).

References

1. Kolb, D. M. *Surf. Sci.* **2002,** *500,* 722–740. doi:10.1016/S0039-6028(01)01583-7
2. Quaino, P.; Luque, N. B.; Soldano, G.; Nazmutdinov, R.; Santos, E.; Roman, T.; Lundin, A.; Groß, A.; Schmickler, W. *Electrochim. Acta* **2013,** *105,* 248–253. doi:10.1016/j.electacta.2013.04.084
3. Schnur, S.; Groß, A. *Catal. Today* **2011,** *165,* 129–137. doi:10.1016/j.cattod.2010.11.071
4. Roman, T.; Groß, A. *Catal. Today* **2013,** *202,* 183–190. doi:10.1016/j.cattod.2012.06.001
5. Trasatti, S. *Pure Appl. Chem.* **1986,** *58,* 955–966. doi:10.1351/pac198658070955
6. Groß, A. *Surf. Sci.* **2013,** *608,* 249–254. doi:10.1016/j.susc.2012.10.015
7. Tripkovic, D. V.; Strmcnik, D.; van der Vliet, D.; Stamenkovic, V.; Markovic, N. M. *Faraday Discuss.* **2009,** *140,* 25–40. doi:10.1039/B803714K
8. Michaelides, A.; Hu, P.; Lee, M.-H.; Alavi, A.; King, D. A. *Phys. Rev. Lett.* **2003,** *90,* 246103. doi:10.1103/PhysRevLett.90.246103
9. Roman, T.; Groß, A. *Phys. Rev. Lett.* **2013,** *110,* 156804. doi:10.1103/PhysRevLett.110.156804
10. Migani, A.; Illas, F. *J. Phys. Chem. B* **2006,** *110,* 11894–11906. doi:10.1021/jp060400u
11. Migani, A.; Sousa, C.; Illas, F. *Surf. Sci.* **2005,** *574,* 297–305. doi:10.1016/j.susc.2004.10.041
12. Leung, T. C.; Kao, C. L.; Su, W. S.; Feng, Y. J.; Chan, C. T. *Phys. Rev. B* **2003,** *68,* 195408. doi:10.1103/PhysRevB.68.195408
13. Pašti, I. A.; Mentus, S. V. *Electrochim. Acta* **2010,** *55,* 1995–2003. doi:10.1016/j.electacta.2009.11.021
14. Baker, T. A.; Friend, C. M.; Kaxiras, E. *J. Am. Chem. Soc.* **2008,** *130,* 3720–3721. doi:10.1021/ja7109234
15. Bagus, P. S.; Staemmler, V.; Wöll, C. *Phys. Rev. Lett.* **2002,** *89,* 096104. doi:10.1103/PhysRevLett.89.096104
16. Bagus, P. S.; Käfer, D.; Witte, G.; Wöll, C. *Phys. Rev. Lett.* **2008,** *100,* 126101. doi:10.1103/PhysRevLett.100.126101
17. Bagus, P. S.; Wöll, C.; Wieckowski, A. *Surf. Sci.* **2009,** *603,* 273–283. doi:10.1016/j.susc.2008.11.021
18. Erley, W. *Surf. Sci.* **1980,** *94,* 281–292. doi:10.1016/0039-6028(80)90007-2
19. Bertel, E.; Schwaha, K.; Netzer, F. P. *Surf. Sci.* **1979,** *83,* 439–452. doi:10.1016/0039-6028(79)90055-4
20. Jo, S. K.; White, J. M. *Surf. Sci.* **1992,** *261,* 111–117. doi:10.1016/0039-6028(92)90222-R
21. Hansen, H. A.; Man, I. C.; Studt, F.; Abild-Pedersen, F.; Bligaard, T.; Rossmeisl, J. *Phys. Chem. Chem. Phys.* **2010,** *12,* 283–290. doi:10.1039/B917459A
22. Lang, N. D. *Surf. Sci.* **1983,** *127,* L118–L122. doi:10.1016/0039-6028(83)90409-0
23. Perdew, J. P.; Burke, K.; Ernzerhof, M. *Phys. Rev. Lett.* **1996,** *77,* 3865–3868. doi:10.1103/PhysRevLett.77.3865
24. Paier, J.; Hirschl, R.; Marsman, M.; Kresse, G. *J. Chem. Phys.* **2005,** *122,* 234102. doi:10.1063/1.1926272
25. Hammer, B.; Hansen, L. B.; Nørskov, J. K. *Phys. Rev. B* **1999,** *59,* 7413–7421. doi:10.1103/PhysRevB.59.7413
26. Lischka, M.; Groß, A. *Phys. Rev. B* **2002,** *65,* 075420. doi:10.1103/PhysRevB.65.075420
27. Stroppa, A.; Kresse, G. *New J. Phys.* **2008,** *10,* 063020. doi:10.1088/1367-2630/10/6/063020
28. Kresse, G.; Joubert, D. *Phys. Rev. B* **1999,** *59,* 1758–1775. doi:10.1103/PhysRevB.59.1758
29. Kittel, C. *Introduction to Solid State Physics,* 7th ed.; John Wiley & Sons, 1996.
30. Ignaczak, A.; Gomes, J. A. N. F. *J. Electroanal. Chem.* **1997,** *420,* 71–78. doi:10.1016/S0022-0728(96)04815-2
31. Collins, D. M.; Spicer, W. E. *Surf. Sci.* **1977,** *69,* 114–132. doi:10.1016/0039-6028(77)90164-9
32. Fisher, G. B. *Chem. Phys. Lett.* **1981,** *79,* 452–458. doi:10.1016/0009-2614(81)85013-0
33. Nieuwenhuys, B. E.; Sachtler, W. M. H. *Surf. Sci.* **1973,** *34,* 317–336. doi:10.1016/0039-6028(73)90121-0
34. Nieuwenhuys, B. E.; Meijer, D. T.; Sachtler, W. M. H. *Phys. Status Solidi A* **1974,** *24,* 115–122. doi:10.1002/pssa.2210240108
35. Nieuwenhuys, B. E. *Surf. Sci.* **1976,** *59,* 430–446. doi:10.1016/0039-6028(76)90027-3
36. Salmerón, M.; Ferrer, S.; Jazzar, M.; Somorjai, G. A. *Phys. Rev. B* **1983,** *28,* 6758–6765. doi:10.1103/PhysRevB.28.6758
37. Derry, G. N.; Ji-Zhong, Z. *Phys. Rev. B* **1989,** *39,* 1940–1941. doi:10.1103/PhysRevB.39.1940
38. Garcia-Araez, N.; Climent, V.; Herrero, E.; Feliu, J.; Lipkowski, J. *J. Electroanal. Chem.* **2005,** *576,* 33–41. doi:10.1016/j.jelechem.2004.10.003
39. Bonzel, H. P. *Surf. Sci. Rep.* **1988,** *8,* 43–125. doi:10.1016/0167-5729(88)90007-6
40. Peljhan, S.; Kokalj, A. *J. Phys. Chem. C* **2009,** *113,* 14363–14376. doi:10.1021/jp902273k
41. Kim, H.; Boysen, D. A.; Ouchi, T.; Sadoway, D. R. *J. Power Sources* **2013,** *241,* 239–248. doi:10.1016/j.jpowsour.2013.04.052

Beilstein Journal of Nanotechnology

Confinement dependence of electro-catalysts for hydrogen evolution from water splitting

Mikaela Lindgren* and Itai Panas

Full Research Paper

Open Access

Address:
Department of Chemical and Biological Engineering, Chalmers University of Technology, S-412 96 Gothenburg, Sweden

Email:
Mikaela Lindgren* - mikaela.lindgren@chalmers.se

* Corresponding author

Keywords:
confinement; corrosion; DFT; electro-catalysis; hydrogen evolution

Beilstein J. Nanotechnol. **2014,** *5,* 195–201.
doi:10.3762/bjnano.5.21

Received: 05 September 2013
Accepted: 21 January 2014
Published: 24 February 2014

This article is part of the Thematic Series "Electrocatalysis on the nm scale".

Guest Editor: R. J. Behm

Abstract

Density functional theory is utilized to articulate a particular generic deconstruction of the electrode/electro-catalyst assembly for the cathode process during water splitting. A computational model was designed to determine how alloying elements control the fraction of H_2 released during zirconium oxidation by water relative to the amount of hydrogen picked up by the corroding alloy. This model is utilized to determine the efficiencies of transition metals decorated with hydroxide interfaces in facilitating the electro-catalytic hydrogen evolution reaction. A computational strategy is developed to select an electro-catalyst for hydrogen evolution (HE), where the choice of a transition metal catalyst is guided by the confining environment. The latter may be recast into a nominal pressure experienced by the evolving H_2 molecule. We arrived at a novel perspective on the uniqueness of oxide supported atomic Pt as a HE catalyst under ambient conditions.

Introduction

Molecular hydrogen produced by water splitting constitutes the archetypical energy carrier in chemistry and is a main target process for the future harvesting of solar energy. Today, water splitting represents large economical values, i.e., it comprises a significant fraction of the total industrial electric energy consumption in the USA [1]. Decisive factors jointly determining the efficiency of the electrochemical process are the reactions at the oxidizing anode as well as at the hydrogen evolving cathode. In two inspiring experimental studies [2,3], Subbaraman et al. reported enhanced hydrogen evolution activity in water splitting by tailoring $TM(OH)_2$-Pt electro-catalyst/electrode assemblies, where TM represents Mn^{2+}, Fe^{2+}, Co^{2+} and Ni^{2+}. The role of these hydroxides was to catalyze water dissociation. In this context, the objective of the present study is to contribute a novel descriptor for the electro-catalytic hydrogen evolution reaction (HER). It offers a complementary

perspective on a recent study addressing the oxidation of zirconium alloys by water [4,5]. The overall reaction

$$\tfrac{1}{2}\,\mathrm{Zr} + \mathrm{H_2O} \rightarrow \tfrac{1}{2}\,\mathrm{ZrO_2} + \mathrm{H_2} \tag{1}$$

is taken to occur by water utilizing hydrolysis to penetrate the oxide scale along hydroxylated grain boundaries, see Figure 1a,

$$\begin{aligned}&\left[\mathrm{Zr^{IV}-O-\ Zr^{IV}}\right]_{\text{grain boundary}} + \mathrm{H_2O}\\ &\rightarrow \left[\mathrm{Zr^{IV}-O-H\quad HO-Zr^{IV}}\right]_{\text{hydroxylated grain boundary}}\end{aligned} \tag{2}$$

These hydroxide ions subsequently react with transition metal decorated sites (see Figure 1a) and zirconium metal to produce ZrO_2 in conjunction with transient transition metal associated hydride-proton (hydroxide) pairs (see Figure 1b) to restore the ZrO_2 grain boundary according to

$$\begin{aligned}&\left[\mathrm{Zr^{IV}-O-H\quad HO-Zr^{IV}}\right]+\left[\mathrm{Zr^{IV}-O-M^{X}}\right]+\tfrac{1}{2}\mathrm{Zr}\\ &\rightarrow\left[\mathrm{Zr^{IV}-O-\ Zr^{IV}}\right]+\left[\mathrm{HO-Zr^{IV}-H-M^{X}}\right]+\tfrac{1}{2}\mathrm{ZrO_2}.\end{aligned} \tag{3}$$

This can be subdivided into an anode process

$$\begin{aligned}&\tfrac{1}{2}\mathrm{Zr} + \left[\mathrm{Zr^{IV}-O-H\quad HO-Zr^{IV}}\right]\\ &\rightarrow \tfrac{1}{2}\,\mathrm{ZrO_2} + \left[\mathrm{Zr^{IV}-O-\ Zr^{IV}}\right] + 2\mathrm{H^+} + 2\mathrm{e^-}\end{aligned} \tag{4}$$

where the [Zr^{IV}–O–Zr^{IV}] oxide grain boundary is recovered, and a cathode process

$$\begin{aligned}&\left[\mathrm{Zr^{IV}-O-M^{X}}\right] + 2\mathrm{H^+} + 2\mathrm{e^-}\\ &\rightarrow \left[\mathrm{Zr^{IV}-O-M^{X-2}}\right] + 2\mathrm{H^+}\\ &\rightarrow \left[\mathrm{HO-Zr^{IV}-H-M^{X}}\right]\end{aligned} \tag{5}$$

is employed to decide the oxidation state X. The subsequent chemical drive for H_2 release into the confining grain boundary determines M and recovers the [Zr^{IV}–O–M^X] site (cf. Figure 1c)

$$\begin{aligned}&\left[\mathrm{HO-Zr^{IV}-H-M^{X}}\right]\\ &\rightarrow\left[\mathrm{Zr^{IV}-O-M^{X}}\right]+\left[\mathrm{H_2}\right]_{\text{grain boundary}}\end{aligned} \tag{6}$$

Indeed, Equation 6 was found to be decisive for the fraction of hydrogen atoms not forming H_2 but being absorbed in the Zr alloy according to

$$\begin{aligned}&\left[\mathrm{HO-Zr^{IV}-H-M^{X}}\right]+\ \mathrm{aZr}\\ &\rightarrow\left[\mathrm{Zr^{IV}-O-M^{X}}\right]+\mathrm{Zr_aH_2(s)}.\end{aligned} \tag{7}$$

For completeness, a 1.1 eV/H_2 drive to release H_2 from the confining grain boundary was computed according to

$$\left[\mathrm{H_2}\right]_{\text{grain boundary}} \rightarrow \mathrm{H_2(g)} + \left[\ \right]_{\text{grain boundary}}. \tag{8}$$

Utilization of the hydride-proton recombination channel (see Figure 1b), the correlation between the computed reaction energies for the HER, Equation 6, and the experimental hydrogen pick-up fractions (HPUF), i.e., the fraction of the hydrogen, which does not undergo hydrogen evolution but are instead picked-up by the alloy during zirconium oxidation by water, leads to a model as displayed in Figure 1e. It is noteworthy, that the energetics for the chemical reaction step in Equation 6 offers a measure of the confinement-dependent cathodic overpotential for the HER along the reaction channel (Equations 2–6). The relevance of the reversible hydride-proton recombination reaction (Equation 6) has recently been proposed in case of a nickel electro-catalyst supported by seven-membered cyclic diphosphine ligands containing one pendant amine, with the Ni supporting the hydride and the amine providing the proton in the hydride-proton recombination reaction [6].

Results and Discussion

In the following we introduce and employ the notion of "confinement effect" as a steric Pauli repulsion type interaction between H_2 and a hydroxylated interface (see Figure 1c) upon hydride-proton recombination. First, we employ this notion in the context of hydride-proton recombination reactions to demonstrate how it decides which oxidation state X of metal ion M minimizes the overpotential for the HER, as quantified by the reaction Equation 6 (cf. Figure 1d,e). Second, it is shown how the emerging understanding is naturally extended to include electro-catalysts for HER under ambient conditions.

Impact of confinement on HER during zirconium oxidation by water

To investigate the confinement effect on the HER, we consider the zirconium oxidation by water (see Figure 1d). The difference between the two horizontal lines at 2.9 eV and at −0.2 eV corresponds to the 3.1 eV/H_2 [9] thermodynamic drive for HER in case of Zr oxidation by water under ambient conditions

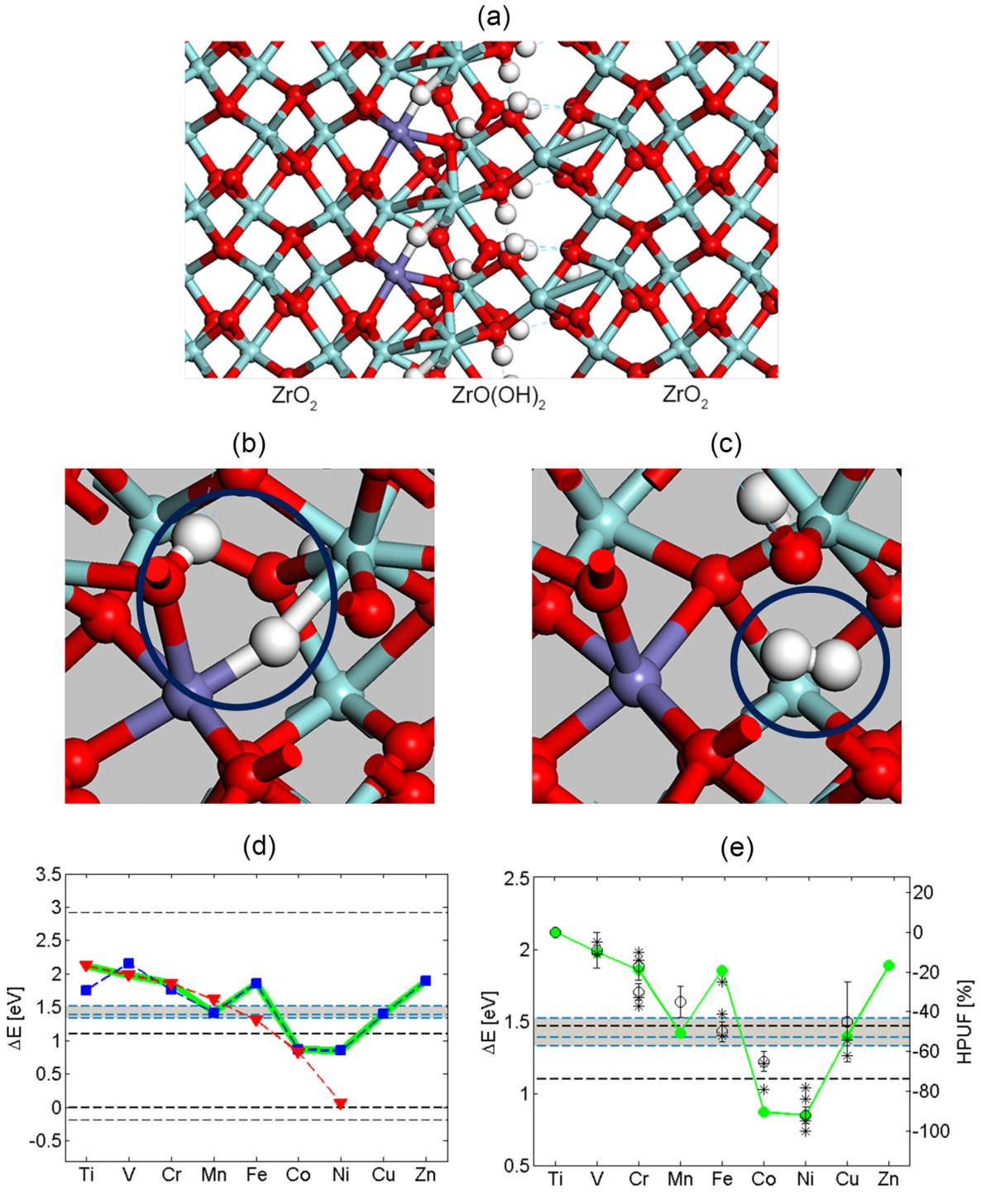

Figure 1: (a) Representative structure for a model of a hydroxylated inter-grain interface comprising $ZrO(OH)_2$ on ZrO_2. Here, this interface is decorated with Fe ions with the oxidation state +2. Oxygen is represented as red, zirconium as light blue, iron as purple, and hydrogen as white. (b) One hydride ion and one hydroxide moiety prior to the hydride-proton recombination to form H_2 is displayed, reactant in Equation 6. (c) The product in Equation 6 is displayed, including M^X coordination to the additional oxygen ion replacing the hydride ion and the released grain boundary H_2. (d) Hydride-proton recombination energies for H_2 release into said interface (dashed black line at 1.1 eV), enthalpy change for H_2 release at ambient pressure (dashed black line at 0 eV), and corresponding Gibbs energy change (dashed black line at −0.2 eV). TM^{2+} blue, TM^{3+} red, weighted average green. (e) Comparison of theoretical data (green) and experimental HPUF data (black); * from [7] and ^{o} from [8]. The theoretical data is a weighted average between TM^{2+} and TM^{3+}. The black dashed line is HPUF in pure ZrO_2 from [7]. The blue dashed line corresponds to HE from Zr^{4+} hydride at GB with Na^+, Ca^{2+} and Sc^{3+} spectator. Sc^{3+} corresponds to the top line, Na^+ to the middle line and Ca^{2+} to the bottom line.

(Figure 2). The line at 0 eV represents the energy of a free H_2 molecule at 0 K. The line at 1.1 eV represents the energy cost at 0 K for bringing a free H_2 molecule into the confinement represented by Figure 1c. The line at −0.2 eV is owing to the increase in entropy when a water molecules $H_2O(l)$ is consumed ($-70.0\ Jmol^{-1}K^{-1}$ [10]) and a $H_2(g)$ molecule is formed ($130.7\ Jmol^{-1}K^{-1}$ [10]) at 298 K and 100 kPa (compare Equation 1), while neglecting changes in entropy in Zr upon oxidation.

Thus, a perfect electro-catalyst would exhibit an enthalpy change of 0 eV for the HER under ambient conditions. Moreover, it is inferred that a perfect electro-catalyst, which passes the HER into this hydroxylated interface via Equation 6 prior to the subsequent H_2 release under ambient conditions, must display 1.3 eV/H_2 overpotential, i.e., (1.1 − (−0.2)) eV/H_2. Equivalently, in case of the HER into the interface, any residual drive towards H_2 formation relative to the line at 1.1 eV/H_2 corresponds to a local overpotential for the HER into the confining interface. A correlation emerges between a greater overpotential and a lower hydrogen pick-up fraction (HPUF, see Figure 1d and 1e). Thus the well-known effect of Ni^{2+} to cause detrimental hydrogen pick-up was explained by its reluctance to release H_2 into the hydroxylated internal inter-grain interface [4,5]. From the overall agreement between reaction energies for Equation 6 and the experimentally reported HPUF's, it was concluded that "anti-catalysts" are preferred in order to mitigate the HPUF. In case of zirconium oxidation by water, these "anti-catalysts" are ions, which conserve significant fractions of the drive for hydrogen evolution by forming highly reactive metastable hydrides. These species are contrasted by Co^{2+} and Ni^{2+}, which catalyze the HER when H_2 is released into the highly constraining interface (see Figures 1d and 1e).

A stability check on the semi-quantitative validity of the model was offered by a comparison of the experimental 44% hydrogen pick-up fraction of pure zirconium (corresponding to the black horizontal dashed line at 1.5 eV/H_2) and model calculations for the hydride-proton recombination energetics employing the inert Na^+, Ca^{2+}, and Sc^{3+} as "dummy" ions in the positions of the transition metal ions (see the three blue horizontal dashed lines in Figure 1e).

On HER at ambient conditions – a consistency check

According to the above understanding, which ions constitute viable electro-catalysts in the absence of confinement or at atmospheric pressure? In as much as the drive for HER comprises the relaxation of the resulting oxy-hydroxy ions coordinating the transition metal ion [4], it is suggested that besides being able to form the hydride intermediate, metals with low oxidation states and large ionic radii should be considered in order to minimize their affinities to the oxide surrounding. This characterization clearly points to the noble metal ions as candidates for electro-catalysts. Additional requirements for any successful electro-catalyst include sufficient electron conductivity of the oxide matrix supporting the catalyst as well as electric contact to the electrode itself. Finally, the "water dissociation catalysis" put forward by Subbaraman et al. [2,3] is used to infer that hydroxylated interfaces provide natural channels for proton transport to the oxy-hydroxide supported electro-

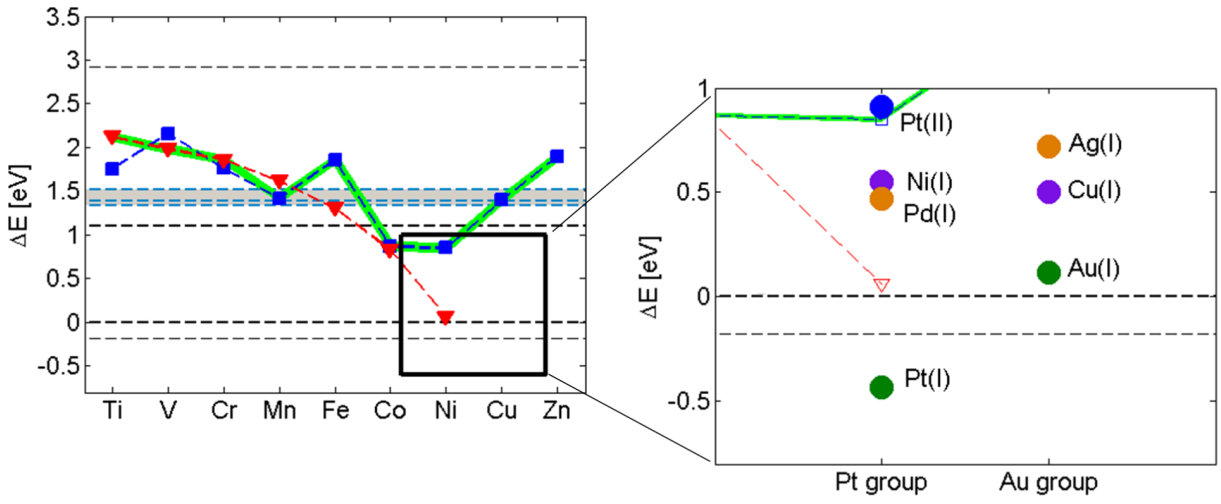

Figure 2: The diagram on the left is identical to Figure 1d. The enlarged region exposes the overpotentials for the elements in the Pt and Au groups. Note that Pt^+ associated hydride displays a negative overpotential implying that it is more stable than the $H_2(g)$ asymptote (lower dashed line).

catalytic site. A schematic representation of this understanding of the electrode/electro-catalyst assembly is provided in Figure 3.

Employing the above described hydroxylated inter-grain interface model as a generic supporting matrix for the eletrocatalytic process, we evaluate the energetics for the hydride-proton recombination reaction and arrive at a possible descriptor for the HER, which is also applicable under ambient conditions. This facilitates a procedure for the screening among candidate electro-catalysts.

Indeed, in Figure 2, a descending staircase-like curve for electro-catalysts is arrived at for the reaction energy corresponding to Equation 6. Starting at the hydroxylated zirconia inter-grain confinement, where Co^{2+} and Ni^{2+} are the obvious candidate catalysts, we approach the ambient conditions step by step by considering the embedded Ag^{+}, Ni^{+}, Cu^{+}, Pd^{+}, Au^{+} and eventually Pt^{+}. The Sabatier principle applies in two ways. Firstly, X in M^{X} can be made to satisfy the requirement that the reactant in Equation 6 forms spontaneously [4,5]. Secondly, the environment confining H_2 in Equation 6 can be tuned to equalize the stabilities of reactants and products, so that any drive to release H_2 into a confinement is balanced owing to the replacement of the three-centered hydride by an oxy-bridge (Equation 6). It is gratifying to find that the oxy-hydroxide supported Au^{+} and Pt^{+} sites become preferred only when approaching ambient conditions, as oxides of noble metals are generally unstable, a property which is often associated with their softness. Consequently, the drive to replace the hydride ion by an oxygen ion is weak, and hence the H_2 release is expected to require a loose confinement for these systems. This is in contrast to harder ions, which form more stable oxides. Interestingly, in case of Pt^{+}, the hydride comes out more stable than the H_2(g) limit. This implies that the embedded Pt^{+} site could constitute an efficient absorber of H_2 in the gas phase under ambient conditions - a purely chemical property. The semi-quantitative nature of the methodology does not allow for precise predictions of absolute numbers (see horizontal "error bar" in Figure 1e). However, it may be that the overpotentials reported for the Pt-based catalysts are related to the coverage dependence of the electrochemical decomposition of the Pt^{+}

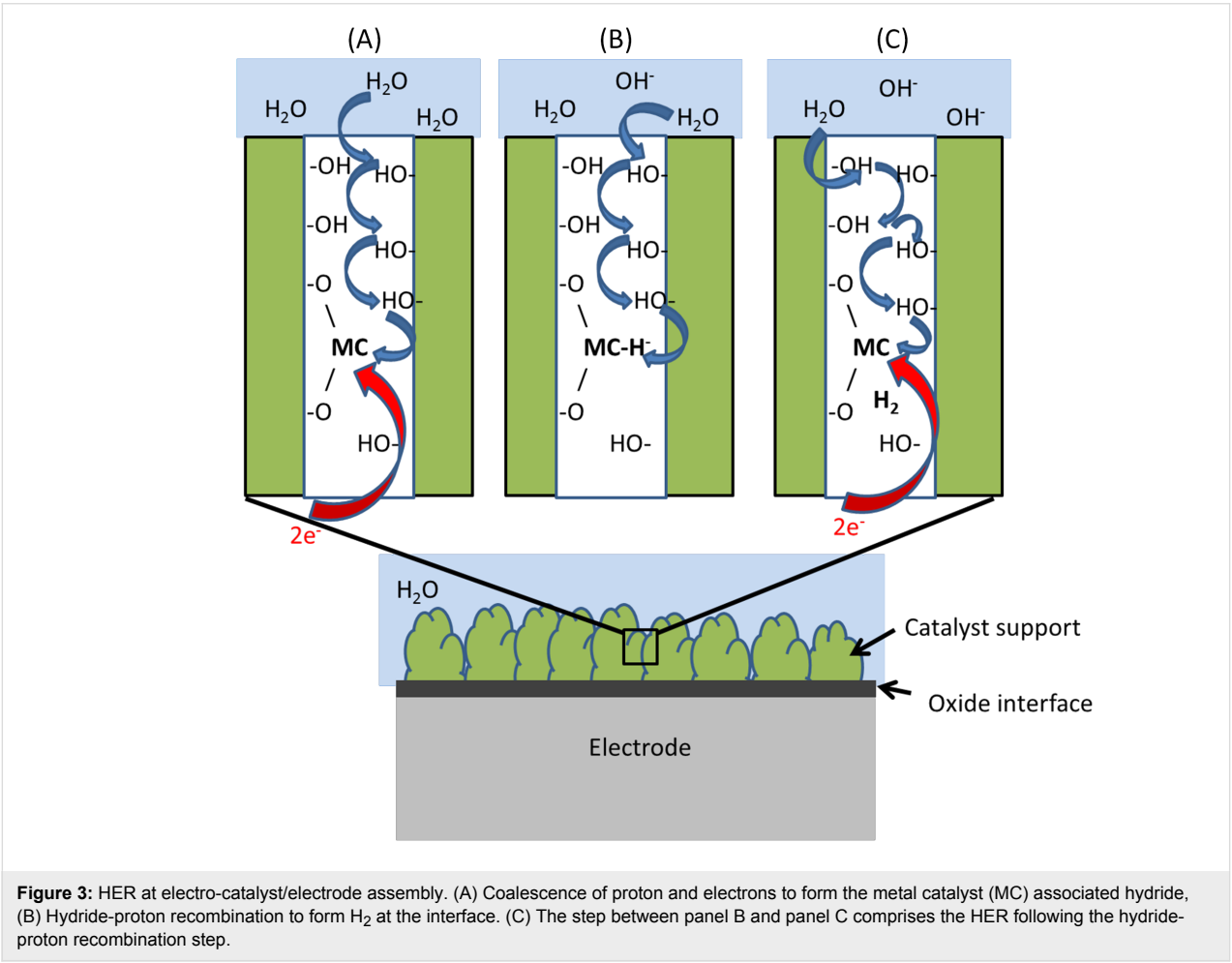

Figure 3: HER at electro-catalyst/electrode assembly. (A) Coalescence of proton and electrons to form the metal catalyst (MC) associated hydride, (B) Hydride-proton recombination to form H_2 at the interface. (C) The step between panel B and panel C comprises the HER following the hydride-proton recombination step.

associated hydride compound. Detailed properties of the embedding materials (e.g., electron conductivity) could cause the additional variations of the overpotential observed by Subbaraman et al. [2].

Interestingly, +2 is not considered a relevant oxidation state in case of Pt under ambient conditions for the electro-catalytic reaction path involving the hydride-proton recombination reaction (see Figure 2). This result is due to the strong binding of +2 to the oxy-hydroxide ligands upon H_2 release, violating Sabatiers principle.

In conclusion, the present approach offers a complementary computational strategy to rank catalysts for HER from water splitting. The complex modelling of heterogeneous HER electro-catalysis at the interface between composite catalyst/support and a water based electrolyte is subdivided into a chemical oxide hydrolysis step (Equation 2), an electro-chemical redox step (Equation 3, Equation 4 and Equation 5), followed by the chemical hydride-proton recombination step (Equation 6). This conceptual deconstruction aims for supporting the prediction of novel approaches to improve on existing electro-catalyst/electrode assemblies. Thus, the design of the aqueous electrolyte/substrate system impacts only the hydrolysis step (Equation 2). The oxidation state X of M^X is decided by Equation 5, while the choice of supported HER catalyst M^X is determined according to Equation 6 by the confinement effect in conjunction with Sabatier's principle.

For the HER step, a recently proposed alternative to the Volmer–Heyrovsky mechanism was employed [4,5]. Rather than electron-proton discharge over an M–H moiety resulting in the conversion of 2H into H_2, the HER investigated here results from a hydride-proton recombination reaction. While the protons constitute hydroxides in Equation 6, which is non-significant due to their ubiquity in aqueous media, an observation of three-center hydride intermediates is the sought-after "smoking-gun" evidence for the proposed mechanism.

Computational details

The Perdew–Burke–Ernzerhof generalized gradient approximation PBE GGA [11] as implemented in the DMOL3 engine [12,13] in the Material Studios program package [14] was employed in conjunction with a double-ζ numerical basis set with an extra polarization function on each heavy atom and a p-function on each hydrogen atom. Systematic spin polarized calculations were performed. A 4 × 4 × 1 k-point set for sampling the Brillouin zone was compared to a 2 × 2 × 1 k-point set, and the latter was found to suffice. In order to reduce the computational effort, inert electron shells were described effectively by means of the semi-core pseudopotentials. Zero-point corrected free energies were compared to non-corrected reaction energies and the differences were deemed negligible.

The grain boundary model (cf. Figure 1a) was constructed by inserting one unit cell of monoclinic $ZrO(OH)_2$ (5.4 Å × 10 Å × 5.4 Å) in between two supercells of monoclinic ZrO_2 (5.4 Å × 10.8 Å × 5.4 Å), where the unit cell doubling is in the b-direction. The stability of the model has been extensively investigated, including full geometry optimization, when arriving at the foundation of [4]. The choice of the grain boundary model is far from unique. Here, it is the success in reproducing the experimental volcano shape curve (cf. Figure 1d) which renders the present investigation meaningful.

The grain boundary model employed to evaluate the reaction energy of Equation 6 was subjected to periodic boundary conditions, where the studied super-cell contained approximately 50 atoms. The number of hydrogen atoms, i.e., hydroxides and hydride, varied. This was because the oxidation states of the transition metal ions were controlled by adding (removing) hydrogen atoms to (from) the super-cell. This way, neutral super-cells were employed in all cases. When evaluating Equation 6, all bond distances and bond angles associated with atoms in the super-cell were optimized, while the super-cell dimensions were kept constant.

Acknowledgements

The Swedish Research Council, Westinghouse Electric Sweden, Sandvik Materials Technology, Vattenfall and the EPRI are gratefully acknowledged for financial support.

References

1. Chlistunoff, J. *Final Technical Report - Advanced Chlor-Alkali Technology;* Los Alamos National Laboratory: Los Alamos, NM, 2004.
2. Subbaraman, R.; Tripkovic, D.; Chang, K.-C.; Strmcnik, D.; Paulikas, A. P.; Hirunsit, P.; Chan, M.; Greeley, J.; Stamenkovic, V.; Markovic, N. M. *Nat. Mater.* **2012,** *11,* 550–557. doi:10.1038/nmat3313
3. Subbaraman, R.; Tripkovic, D.; Strmcnik, D.; Chang, K.-C.; Uchimura, M.; Paulikas, A. P.; Stamenkovic, V.; Markovic, N. M. *Science* **2011,** *334,* 1256–1260. doi:10.1126/science.1211934
4. Lindgren, M.; Panas, I. *RSC Adv.* **2013,** *3,* 21613–21619. doi:10.1039/c3ra42941e
5. Lindgren, M.; Sundell, G.; Panas, I.; Hallstadius, L.; Thuvander, M.; Andrén, H. O. Zirconium in the Nuclear Industry: Seventeenth International Symposium, Hyderabad, Feb 3–7, 2013; Comstock, R. J., Ed.; ASTM: West Conshohocken, PA; tentatively accepted.
6. Stewart, M. P.; Ho, M.-H.; Wiese, S.; Lindstrom, M. L.; Thogerson, C. E.; Raugei, S.; Bullock, R. M.; Helm, M. L. *J. Am. Chem. Soc.* **2013,** *135,* 6033–6046. doi:10.1021/ja400181a
7. Parfenov, B. G.; Gerasimov, V. V.; Venediktova, G. I. *Corrosion of Zirconium and Zirconium Alloys (Korroziya tsirkoniya i ego splavov);* Atomizdat: Moskva, 1976; pp 118–120.

8. Cox, B. In *Advances in Corrosion Science and Technology;* Fontana, M. G.; Staehle, R. W., Eds.; Plenum: New York, 1976; Vol. 5, pp 173–391. doi:10.1007/978-1-4615-9062-0_3
9. *Electrochemical Series*. In *CRC Handbook of Chemistry and Physics Online,* 94th ed.; Haynes, W. M., Ed.; 2013.
10. Standard Thermodynamic Properties of Chemical Substances. In *CRC Handbook of Chemistry and Physics Online,* 94th ed.; Haynes, W. M., Ed.; 2013.
11. Perdew, J. P.; Burke, K.; Ernzerhof, M. *Phys. Rev. Lett.* **1996,** *77,* 3865–3868. doi:10.1103/PhysRevLett.77.3865
12. Delley, B. *J. Chem. Phys.* **1990,** *92,* 508–517. doi:10.1063/1.458452
13. Delley, B. *J. Chem. Phys.* **2000,** *113,* 7756–7764. doi:10.1063/1.1316015
14. *Materials Studio 6.0;* Accelrys Software Inc., 2011.

Beilstein Journal of Nanotechnology

Constant chemical potential approach for quantum chemical calculations in electrocatalysis

Wolfgang B. Schneider and Alexander A. Auer*

Full Research Paper

Open Access

Address:
Max-Planck-Institute for Chemical Energy Conversion, Stiftstraße 34–36, D-45470 Mülheim an der Ruhr, Germany

Email:
Alexander A. Auer* - alexander.auer@cec.mpg.de

* Corresponding author

Keywords:
density functional theory; electrocatalysis; electrochemistry; electronic strutcture theory; nanoparticles; quantum chemistry

Beilstein J. Nanotechnol. **2014,** *5,* 668–676.
doi:10.3762/bjnano.5.79

Received: 04 December 2013
Accepted: 23 April 2014
Published: 20 May 2014

This article is part of the Thematic Series "Electrocatalysis on the nm scale".

Guest Editor: R. J. Behm

Abstract

In order to simulate electrochemical reactions in the framework of quantum chemical methods, density functional theory, methods can be devised that explicitly include the electrochemical potential. In this work we discuss a Grand Canonical approach in the framework of density functional theory in which fractional numbers of electrons are used to represent an open system in contact with an electrode at a given electrochemical potential. The computational shortcomings and the additional effort in such calculations are discussed. An ansatz for a SCF procedure is presented, which can be applied routinely and only marginally increases the computational effort of standard constant electron number approaches. In combination with the common implicit solvent models this scheme can become a powerful tool, especially for the investigation of omnipresent non-faradaic effects in electrochemistry.

Introduction

In October 2012 the workshop “Elementary reaction steps in electrocatalysis: Theory meets experiment” was held in Reisensburg, Germany. Alongside exquisite experimental work on electrochemistry, numerous prominent contributions displayed the range of modern developments and applications of theory in electrochemistry. This included the application of solid state approaches [1-4], investigations on the role of the solvent [5-9] or simulations including explicit dynamics of reactants [10]. Furthermore, several contributors presented work in which cluster models were applied in the framework of electronic structure theory in order to assess the properties of nanoparticles, nanostructures or interfaces [11-15].

Today, several approaches are available for modelling the full details of the electronic structure in electrochemical phenomena. The most common approach is to describe faradaic processes by using a thermodynamic scheme in which reaction energy differences are corrected a posteriori by the number of

electrons transferred times the electrochemical potential the simulation is supposed to refer to [16-19]. This allows to monitor the changes in the system behavior depending on the electrochemical potential without having to include the electrochemical potential of the electrons in the calculation explicitly. As a consequence, this "pure thermodynamic" approximation, which is often also referred to as "computational hydrogen electrode" [16], and which we previously denoted as "constant charge approach" [13], allows to use the results of a single electronic structure calculation for all potentials [20,21]. Furthermore, this approach is also very convenient for periodic boundary calculations as in this case the models are restricted to a neutral unit cell.

However, there are several electrochemical phenomena for which it is clear that the explicit inclusion of the electrochemical potential is vital, namely the broad family of non-faradaic processes. This induces potential induced or lifted surface reconstructions [22] or the prominent non-faradaic electrochemical modification of catalytic activity (NEMCA) effect [23]. Only in recent years, attempts have been made to go beyond the pure thermodynamical approximation, explicitly including the electrochemical potential into the electronic structure calculation by means of adding or removing fractions of electrons or the introduction of electric fields included explicitly or via counter charges. For this reason, the effect of the explicit inclusion of the electrochemical potential in the electronic structure calculation for phenomena from electrocatalysis has yet to be quantified, and it is currently still open to debate if the pure thermodynamic approach is sufficient for certain processes.

Generally, electronic structure methods can roughly be divided in two subcategories, i.e., methods that treat the system within a unit cell by using periodic boundary conditions and methods that restrict the description of the system to the finite model chosen. In this work, we focus on finite systems approaches from quantum chemistry for treating electrochemical phenomena. These methods, especially in the framework of density functional theory (DFT), have in recent decades been applied for a broad variety of problems related to electrochemistry. This includes for example cluster models, that are applied to model reactions on surfaces [18,19,24], it includes the calculation of molecular properties to understand the redox properties of organic molecules and it includes the simulation of small to medium sized nanoparticles to explore their stability and the role of their atomic and electronic structure in electrocatalysis.

In a recent publication we have presented a constant potential scheme for calculating the electronic structure of a system at a given electrochemical potential [25]. This scheme is the quantum chemical equivalent to an approach by Alavi et al. [26], that focused on constant electrochemical potential schemes in the framework of periodic boundary condition DFT calculations. Based on the possibility to calculate the electronic structure of a finite system after adding or removing fractions of electrons, various quantities like the Fermi level (in that case the HOMO energy) or the numerical derivative of the energy with respect to the number of electrons can be used to associate a specific charge state of the system with its electrochemical potential. This, however, necessitates a complex computational scheme, for which several calculations have to be carried out in combination with an interpolation scheme that is far from the convenience of a black box application inherent to standard electronic structure calculations.

In the literature, only very few examples for constant potential schemes in the framework of quantum chemical approaches can be found: Bureau and Lécayon [27] describe the basic principles for devising an algorithm in which the target quantity is the chemical potential rather then the number of the electrons. After discussing the necessity and possibility to carry out constant-μ calculations, the authors lay out the theoretical underpinning in the framework of linear response theory and variational DFT schemes. They describe a variational procedure in which the Kohn–Sham equations are solved in the framework of a Grand-Potential approach with a variable number of electrons and a fixed μ. Finally, a scheme is proposed, in which a series of standard calculations with a given number of electrons are carried out and for each fixed electron number the chemical potential is evaluated afterwards. While this approach is conceptually simple, the computational effort can be immense if larger systems like nanoparticles are investigated [25]. Shiratori et al. [28,29] presented a scheme for carrying out constant-μ calculations based on a finite temperature Grand Canonical ansatz. They propose to optimize the wave function parameters explicitly including the chemical potential of the electrons, keeping the number of electrons variable through the SCF cycles. While this approach seems a promising solution for an algorithm to calculate the electronic structure of a system at a given potential, it has some pitfalls as we shall discuss in the following sections. Furthermore, Bonnet et al. showed that it is possible to calculate the properties of a system for a given potential in the framework of ab-initio molecular dynamics [30]. In this work, we present an algorithm that allows to calculate the electronic structure for a given system not with a fixed number of electrons, but with a given target chemical potential. We outline the problems of previously devised schemes and arrive at an algorithm that has the potential for a black-box scheme that can be applied for systems ranging from small molecules (insulators) up to metallic nanoparticles.

Theory

In principle, there are several ways to evaluate the chemical potential μ for a given system: A rough estimate can be obtained by the negative of the electronegativity of Pauling and Mulliken [31], calculated by the ionisation potential (I) and electronegativity (A) of the system or its approximations by the orbital energies.

$$\mu = -\frac{I + A}{2} \approx \frac{E_{\mathrm{HOMO}} + E_{\mathrm{LUMO}}}{2} \tag{1}$$

Furthermore, in calculating the free energy of a system, a Fermi–Dirac distribution function is applied to obtain the occupation numbers at a given temperature ("Fermi smearing"). Here, the chemical potential appears as a parameter for the Fermi smearing in the form of the Lagrangian multiplier for the number of electrons.

$$F = E - k_{\mathrm{b}}T\sum_i \left(f_i \ln f_i + \left(1 - f_i\right)\ln\left(1 - f_i\right)\right) - \mu\left(\sum_i f_i - N\right) \tag{2}$$

$$\text{with} \quad f_i = \frac{1}{e^{\beta\left(\varepsilon_i - \mu\right)} + 1} \quad \beta = \frac{1}{k_{\mathrm{b}}T} \quad N = \sum_i f_i \tag{3}$$

By definition, μ is the derivative of the energy with respect to the number of electrons (Equation 4). Hence, it can be evaluated either analytically (for example as an analytic derivative or by linear response theory) [27] or numerically by calculating E for various electron numbers [26].

$$\mu = \frac{\partial E}{\partial N} \tag{4}$$

At this point the basic difference between a Canonical and a Grand Canonical Ensemble should be emphasized. In a Canonical Ensemble, a constant number of electrons is assumed for each micro system, while the chemical potential is an average over the micro systems. In a Grand Canonical Ensemble the chemical potential is constant for each micro system and the number of electrons per micro system is an average. In this context, constant charge calculations as typically carried out in electronic structure theory can be attributed to a Canonical Ensemble ansatz at zero temperature. This can be extended to finite temperatures (Equation 2) by using a Fermi–Dirac distribution for the electronic degrees of freedom. This introduces fractional occupation numbers and the chemical potential of the electrons as a Lagrangian multiplier that ensures a constant number of electrons in the treatment. The Grand Canonical approach differs from this by fixing the chemical potential of the system while allowing electron exchange with an external bath.

$$\Omega = E - T\cdot S - \mu\cdot N \tag{5}$$

Bureau et al. [27] showed, that the chemical potential and the corresponding number of electrons obtained by calculating the free energy of a Canonical Ensemble equals the values that are obtained by calculating the grand potential (Equation 5) of the corresponding Grand Canonical Ensemble. Thus, the free energy and the Grand Potential can easily be converted (Equation 6).

$$\min_N \left\{E[N, \rho]\right\} + N\mu = \min_{\rho'} \left\{\Omega[\rho']\right\} \tag{6}$$

By calculating the electronic structure of an oxygen atom for different fractional numbers of electrons, Vuilleumier et al. showed that the three approaches yield comparable results for the calculation of the electrochemical potential [32]. Hence most of the constant potential schemes are derived from calculations with a constant number of electrons. An iterative procedure to directly calculate the energy of a system depending on the chemical potential was for example discussed by Shiratori et al. [28]: After converging the energy with an initial number of electrons, the number of electrons is changed by ΔN and a new value for μ is obtained. This procedure is carried out until a converged wave function is obtained at the desired value of the chemical potential. The disadvantage of this approach is that the number of iterations needed can be fairly high. Thus, the approach is associated with a considerable computational overhead.

In principle, an algorithm for the iterative calculation with varying number of electrons and given chemical potential can be constructed based on Equation 2. Instead of using the chemical potential as a parameter to guarantee a constant number of electrons, it is possible to directly insert the aspired potential and obtain the number of electrons for that given potential. This is a very convenient way of determining a ΔN: After the new occupation numbers f_i have been obtained for the new number of electrons, the density matrix is modified by using Equation 3.

$$P_{\mu\nu} = \sum_i C_{\mu i} C_{i\nu} f_i \tag{7}$$

Next, the energy is again converged followed by another modification of the density matrix until convergence of the number of electrons (and thus the chemical potential) and the energy is achieved. However, while this scheme is appealing, the crucial point is the convergence of the overall scheme. A robust algo-

rithm is essential in any case, for simple systems like molecules and especially for complex examples like metallic nanoparticles. In Figure 1 the number of electrons with the number of SCF iterations is monitored if the scheme discussed above is applied to calculate the electronic structure of the O_2 molecule at an absolute potential of −3.71 V. Note that the absolute potential of the charge neutral O_2 with a bond distance of 1.21 Å calculated at the RI-BP86/def2-TZVP level of theory is −5.71 V. For all calculations in this paper the following convergence parameters were applied: The energy was converged up to 10^{-9} a.u., the maximal density change up to 10^{-5}, RMS density change up to 10^{-6} and the DIIS error up to 10^{-6} a.u. Furthermore, all calculations have been carried out without level shift for the virtual orbitals.

After the convergence of the initial charge state with 16 electrons is achieved, the number electrons is slightly increased. However, in the further course of the calculation the number of electrons oscillates between the minimum of 0 electrons and the maximum of 120 electrons. Hence, no convergence is observed, even for this very simple case.

The origin of this behavior is revealed in Figure 2, in which the dependence of the potential on the number of electrons is plotted according to Equation 2. For the red/solid exact curve, the potential was obtained by Equation 2 from converged calculations using fractional number of electrons and hence, is the exact $\mu(N)$. The orbital energies ε_i obtained from calculations with a N of 15, 16 and 17.5 electrons were used to approximate $\mu(N)$ by Equation 3. The slope calculated numerically by fractional charge states for O_2 shows a strong dependence of the potential on the number of electrons. However, the slope of $d\mu/dN$ calculated by the approximation using Equation 3 is much smaller (dashed green, blue and black line). This leads to a drastic overestimation of the change of the charge and causes erratic steps in the optimization of the charge of the system, impeding convergence of the algorithm.

A better approximation to obtain $d\mu/dN$ is the calculation of a new density matrix based on the old MO coefficients $C_{\mu i}^{N}$ but with a changed number of electrons by using Equation 8. This new density matrix is used to calculate a new Fock matrix and an approximated new energy (Equation 9).

$$\tilde{P}_{\mu\nu}^{N+\Delta N} = \sum_i C_{\mu i}^{N} C_{i\nu}^{N} \cdot \tilde{f}_i^{N+\Delta N} \tag{8}$$

$$E[\tilde{\rho}] = F[\tilde{\rho}] + \int v(r)\tilde{\rho}(r)dr \tag{9}$$

In Figure 3 the dependence of the potential on the number of electrons is plotted for O_2 by using this new approximation. Similar to Figure 2, the red/solid curve corresponds to the numerically calculated $\mu(N)$ (Equation 4) of converged calcula-

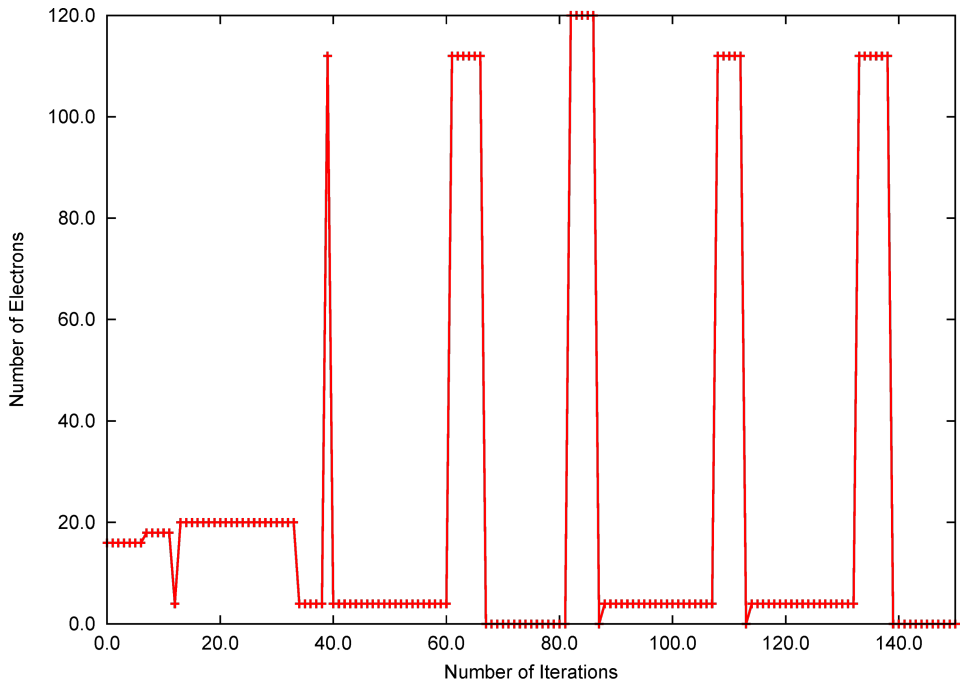

Figure 1: Evolution of the number of electrons with the number of iterations for O_2 if the potential dependent energy is computed by inserting the aspired μ into Equation 2.

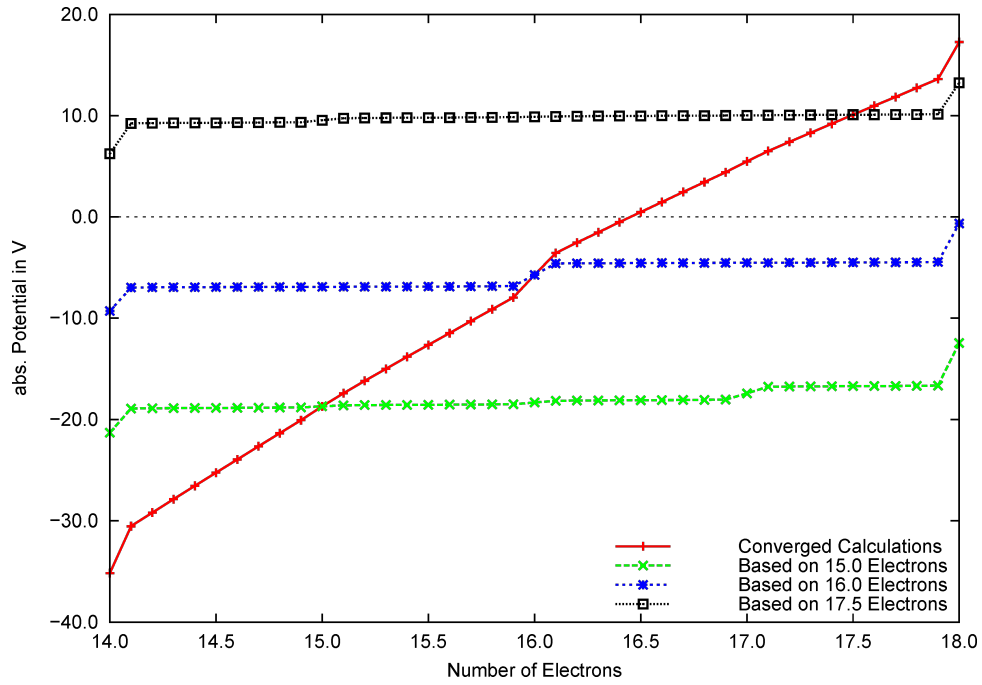

Figure 2: Change of the absolute potential for O_2 depending on the number of electrons, calculated numerically and approximated by Equation 3, respectively.

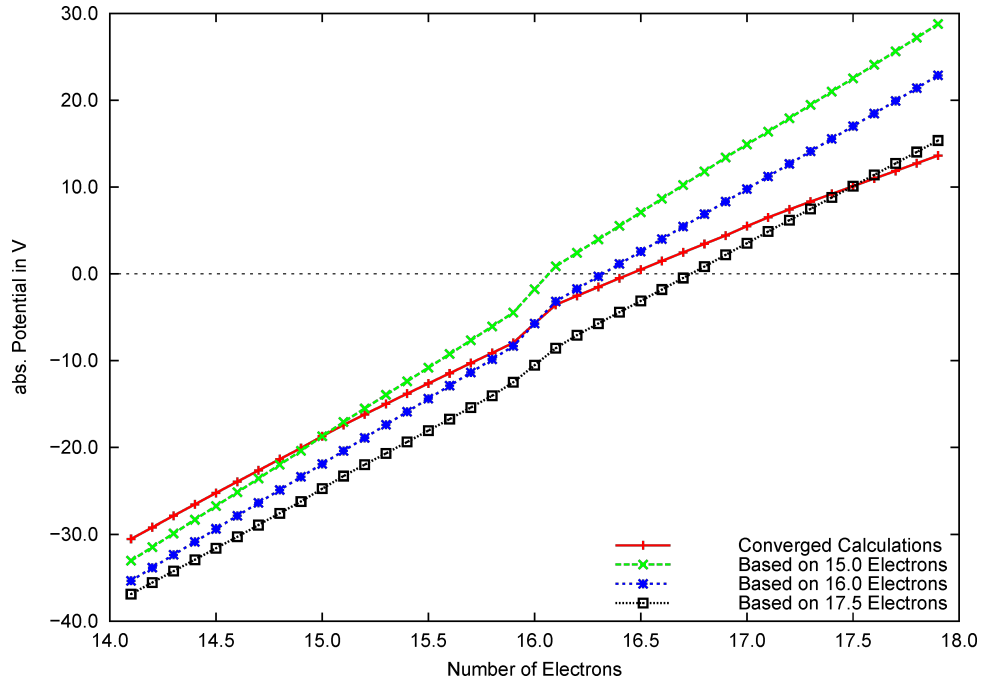

Figure 3: Chemical potential of the O_2 molecule, plotted against the number of electrons, calculated numerically and approximated by recalculation of the Fock matrix, respectively.

tions using a fractional N. Using the MO coefficients of the converged calculations with a N of 15.0, 16.0 and 17.5 electrons, approximated energies were calculated by using Equation 9. The approximated values of μ were obtained by numerical differentiation and are plotted with dashed lines. As can be seen, the approximation based on the recalculated Fock

matrices yields a much better approximation for the exact slope than the approximation based on the Fermi smearing formula. Moreover, the approximated slope is always larger than the exact $d\mu/dN$, circumventing the overestimation of the change with the number of electrons that was observed in the previous approximation.

As the function $E(N)$ exhibits a quadratic dependence on the energy, its derivative can easily be evaluated by a three-point scheme. For this purpose, the Fock matrix and the corresponding energy is calculated for three different points using the MO coefficients obtained for the current number of electrons. Assuming a quadratic form, an approximation for $\partial^2E/\partial N^2$ is obtained, which is then used to predict the number of electrons for the target chemical potential. Note that as a consequence, the computational costs of an iteration step approximately triple. However, it is not necessary to calculate a new number of electrons in every iteration, as several tests on smaller and larger model systems show that it is sufficient to converge the SCF equations to a certain extend by using a fixed number of electrons and only to adjust it every few iterations depending on the degree of convergence. Based on this, the scheme shown in Figure 4 was applied to a testset of molecules.

The potential obtained in this way is the absolute potential with the electron at rest in the vacuum as reference. It can be related to the experimentally achieved potential by a constant shift using the Trasatti scheme [33]. It should be noted that in actual applications, for which constant potential calculations will yield different numbers of electrons for the same system in different states, reaction enthalpies need to be calculated by adding the corresponding $e{\cdot}U$ correction, as discussed in a previous work [25].

Some final remarks about the validity of the overall scheme should be made at this point. The scheme presented here is a Grand Canonical Ensemble DFT approach that relies on a proper response of the system with respect to change in the number of electrons. It can be argued that typical functionals might not be well suited for this purpose. In molecular systems, for example, ionization potentials and electron affinities are often not well reproduced. DFT yields a continuous function of μ over N, though a step function is expected. Furthermore, the use of fractional electrons in the description of the system, as inherent to this approach, is not consistent with the ideas of quantized charge transfer in a real molecular system of isolated active sites on a surface. However, metallic systems at finite temperature with high or infinite density of states and small or vanishing bandgap, show a continuous change of the potential with the number of electrons. Furthermore, in the framework of a Grand Canonical approach the treated system is in contact with a bath of electrons, which models the situation of a subsystem in contact with a conducting environment. Thus, while limited in applicability, the approach is well suited for the treatment of metallic nanoparticles on conductive supports or within cluster approaches to model surface reactions. The developed algorithm has been implemented in the ORCA [34] programme package.

1. Start calculation for arbitrary N (preferentially charge neutral).
2. Converge free energy $E[\rho]$ to 10^{-5} and chemical potential of the current iteration step μ_{cur} (Equation 3) to 10^{-2}.
3. If current chemical potential not equal requested potential ($|\mu_{cur} - \mu_{aim}| > 10^{-3}$) approximate correct number of electron using the scheme:
   (a) Calculate two points $\tilde{N} = N \pm \Delta N$, with ΔN depends on deviation of the current μ_{cur} from the requested μ_{aim} as $\Delta N = |\mu_{cur} - \mu_{aim}| \cdot 0.2$.
   (b) Calculate test density matrices for $\tilde{N}$: $\tilde{P}_{\mu\nu} = \sum_i C_{\mu i} C^*_{\nu i} \cdot \tilde{f}_i$.
   (c) Recalculate Fock matrices and obtain test values of $E[\tilde{\rho}]$ for $\tilde{N}$.
   (d) Now three data points exists for $E(N)$, namely two approximated values $E[\tilde{\rho}]$ and the energy and potential of step 2. By fitting a second order polynomial to the data points an expression for $E(N)$ is obtained and by $\frac{dE}{dN} = \mu(N)$ an approximated dependence of μ over N is available. Using $\mu(N)$ an approximated value for N_{aim} corresponding to μ_{aim} is determined.
   (e) After five SCF cycles go back to step 2 using the new value for N.
4. If the requested chemical potential is obtained and the number of electrons has converged, the calculation has converged.

Figure 4: Scheme for a potential dependent calculation of the free energy.

Calculations on test systems

Using the new scheme, the above mentioned calculation for oxygen at a potential of −3.71 V was repeated. As shown in Figure 5, already the first approximation of the final number of electrons is fairly good (solid red curve). This is the case, even if a huge deviation of the requested chemical potential from the initial chemical potential exists. For O_2 at an extreme absolute potential of −25.71 V good convergence on 14.4 electrons is achieved within six updates of the number of electrons (dashed green curve). This is just one update more, compared to the calculation at −3.71 V.

The new scheme was tested for further examples like small organic molecules and metallic clusters (Figure 5). For all examples fast convergence of the number of electrons for the given potentials was achieved. For benzene, calculated at the RI-BP86/aug-ccPVTZ level of theory, convergence of the absolute potential and the energy was observed after 55 iterations. For the metal clusters Pt_4 and Pt_{10}, calculated at the RI-BP86/def2-TZVP level of theory, convergence was observed after 92 (−4 V) and 238 SCF iterations, respectively. Standard calculations for small molecules like oxygen or benzene using fixed number of electrons converge within 10–20 SCF iterations. If the calculations are carried out at fixed potential, the number of SCF iterations is approximately quintupled. However, systems with increasing metallic character, such as platinum clusters, show a slower convergence for a fixed number of electrons (50–70 iterations). For these systems, the number of SCF iterations approximately doubles if the calculation is carried out at fixed potential. This can be compared to a previous work [25] in which the energy of platinum clusters at a given potential was determined by an interpolation scheme. There, it is necessary to calculate the energy of the system at least for three different numbers of electrons in order to obtain a result for a given potential. In total, this amounts to (at least) threefold computational effort and hence the computational effort is reduced by using the new scheme.

One important aspect to note is the correlation between the calculated energy and the convergence of the absolute potential. Depending on the convergence criterium for the potential, the number of electrons N is also only converged with a certain error. For example, if the energy of O_2 is calculated at $\mu = -4$ V, starting with 16 or 15 electrons, respectively, the final number of electrons differs by $3.6 \cdot 10^{-5}$, if the potential is converged to 10^{-3} V. However, as the energy strongly depends on the number of electrons, this leads to a deviation of 0.01 kJ/mol in the final energies.

For systems such as metallic structures, for which $\mu(N)$ has a smaller slope than for oxygen, the resulting error in N for a given potential is larger, and hence the error of the calculated

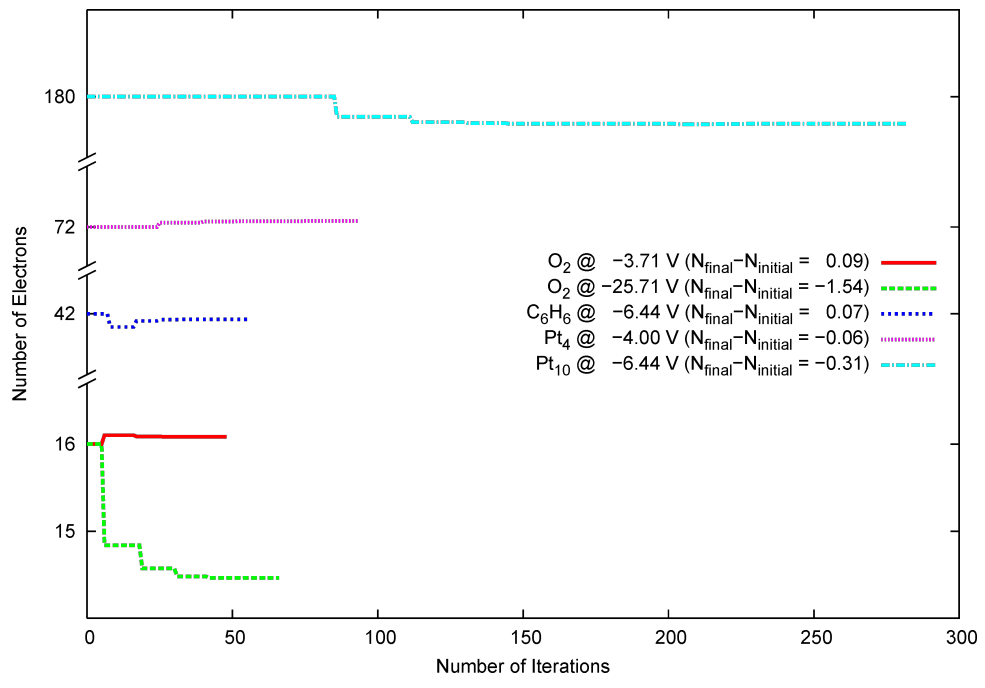

Figure 5: Convergence of the number of electrons with the SCF iterations for different systems. Note that the calculation for the charge neutral molecules with fixed number of electrons for O_2 converges within 7, for C_6H_6 within 13, for Pt_4 within 73 and for Pt_{10} within 177 SCF iterations, respectively.

energy increases. For instance, if the energy of a Pt_4 cluster is calculated at 1000 K over a potential range of −16 V to 4 V, with an initial charge of 0 and −1, respectively, the final energies for the same potential can differ by up to 5.0 kJ/mol, if the potential is converged up to 10^{-3} V. While for most purposes this error can be controlled by choosing the appropriate convergence criteria and consistent starting points for the calculation, the user should be aware of this behavior.

Conclusion

In this work, an SCF iteration scheme to calculate the electronic energy of a system at constant electrochemical potential in the framework of a Grand Canonical Ensemble DFT ansatz is presented. In contrast to common DFT calculations, that are carried out at a constant number of electrons N, the energy is calculated for a fixed electrochemical potential with a variable fractional number of electrons.

While earlier approaches require the calculation of the energy for different N [25-27], in the scheme presented here, the optimization of N is incorporated in the SCF iterations of the energy calculation. For this purpose it is decisive to find a good approximation for $d\mu/dN$ in order to obtain a good guess for the final N. The simple approach of estimating the correct N by inserting the requested μ into the Fermi–Dirac distribution function used in finite temperature DFT leads to an oscillatory behavior of N during the SCF iterations. A much better and still computationally simple approximation of N_{final} is obtained by numerical evaluation of $d\mu/dN$, recalculating the Fock matrix for different values for N during an additional update step. This way, a robust and efficient algorithm is obtained to carry out constant potential calculations in the framework of quantum chemical approaches.

Whether this model can be routinely applied in the computation of faradaic and non-faradaic electrochemical processes has to be subject to careful benchmarks, which is work in progress and will be published in forthcoming articles.

References

1. Busch, M.; Ahlberg, E.; Panas, I. *Catal. Today* **2013,** *202,* 114–119. doi:10.1016/j.cattod.2012.04.060
2. Busch, M.; Ahlberg, E.; Panas, I. *J. Phys. Chem. C* **2013,** *117,* 288–292. doi:10.1021/jp308982s
3. Escudero-Escribano, M.; Soldano, G. J.; Quaino, P.; Zoloff Michoff, M. E.; Leiva, E. P. M.; Schmickler, W.; Cuesta, Á. *Electrochim. Acta* **2012,** *82,* 524–533. doi:10.1016/j.electacta.2012.02.062
4. El-Sayed, A.-M.; Watkins, M. B.; Shluger, A. L.; Afanas'ev, V. V. *Microelectron. Eng.* **2013,** *109,* 68–71. doi:10.1016/j.mee.2013.03.027
5. Rossmeisl, J.; Chan, K.; Ahmed, R.; Tripković, V.; Björketun, M. E. *Phys. Chem. Chem. Phys.* **2013,** *15,* 10321–10325. doi:10.1039/c3cp51083b
6. Filhol, J.-S.; Doublet, M.-L. *Catal. Today* **2013,** *202,* 87–97. doi:10.1016/j.cattod.2012.04.023
7. Adriaanse, C.; Cheng, J.; Chau, V.; Sulpizi, M.; VandeVondele, J.; Sprik, M. *J. Phys. Chem. Lett.* **2012,** *3,* 3411–3415. doi:10.1021/jz3015293
8. Quaino, P.; Luque, N. B.; Soldano, G.; Nazmutdinov, R.; Santos, E.; Roman, T.; Lundin, A.; Groß, A.; Schmickler, W. *Electrochim. Acta* **2013,** *105,* 248–253. doi:10.1016/j.electacta.2013.04.084
9. Roman, T.; Groß, A. *Catal. Today* **2013,** *202,* 183–190. doi:10.1016/j.cattod.2012.06.001
10. Wilhelm, F.; Schmickler, W.; Nazmutdinov, R.; Spohr, E. *Electrochim. Acta* **2011,** *56,* 10632–10644. doi:10.1016/j.electacta.2011.04.036 61st Annual Meeting of the International-Society-of-Electrochemistry (ISE), Nice, FRANCE, SEP 26-OCT 01, 2010.
11. Oberhofer, H.; Reuter, K. *J. Chem. Phys.* **2013,** *139,* 044710. doi:10.1063/1.4816484
12. Kettner, M.; Schneider, W. B.; Auer, A. A. *J. Phys. Chem. C* **2012,** *116,* 15432–15438. doi:10.1021/jp303773y
13. Schneider, W. B.; Benedikt, U.; Auer, A. A. *ChemPhysChem* **2013,** *14,* 2984–2989. doi:10.1002/cphc.201300375
14. Leung, K. *Chem. Phys. Lett.* **2013,** *568–569,* 1–8. doi:10.1016/j.cplett.2012.08.022
15. Nazmutdinov, R. R.; Berezin, A. S.; Soldano, G.; Schmickler, W. *J. Phys. Chem. C* **2013,** *117,* 13021–13027. doi:10.1021/jp400037g
16. Nørskov, J. K.; Rossmeisl, J.; Logadottir, A.; Lindqvist, L.; Kitchin, J. R.; Bligaard, T.; Jónsson, H. *J. Phys. Chem. B* **2004,** *108,* 17886–17892. doi:10.1021/jp047349j
17. Rossmeisl, J.; Skúlason, E.; Björketun, M. E.; Tripkovic, V.; Nørskov, J. K. *Chem. Phys. Lett.* **2008,** *466,* 68–71. doi:10.1016/j.cplett.2008.10.024
18. Jacob, T. *Fuel Cells* **2006,** *6,* 159–181. doi:10.1002/fuce.200500201
19. Roudgar, A.; Eikerling, M.; van Santen, R. *Phys. Chem. Chem. Phys.* **2010,** *12,* 614–620. doi:10.1039/B914570B
20. Filhol, J.-S.; Neurock, M. *Angew. Chem., Int. Ed.* **2006,** *45,* 402–406. doi:10.1002/anie.200502540
21. Taylor, C. D.; Wasileski, S. A.; Filhol, J.-S.; Neurock, M. *Phys. Rev. B* **2006,** *73,* 165402. doi:10.1103/PhysRevB.73.165402
22. Kolb, D. M. *Prog. Surf. Sci.* **1996,** *51,* 109–173. doi:10.1016/0079-6816(96)00002-0
23. Vayenas, C. G.; Bebelis, S.; Neophytides, S. *J. Phys. Chem.* **1988,** *92,* 5083–5085. doi:10.1021/j100329a007
24. Wang, L.; Roudgar, A.; Eikerling, M. *J. Phys. Chem. C* **2009,** *113,* 17989–17996. doi:10.1021/jp900965q
25. Benedikt, U.; Schneider, W. B.; Auer, A. A. *Phys. Chem. Chem. Phys.* **2013,** *15,* 2712–2724. doi:10.1039/c2cp42675g
26. Lozovoi, A. Y.; Alavi, A.; Kohanoff, J.; Lynden-Bell, R. M. *J. Chem. Phys.* **2001,** *115,* 1661–1669. doi:10.1063/1.1379327
27. Bureau, C.; Lécayon, G. *J. Chem. Phys.* **1997,** *106,* 8821–8829. doi:10.1063/1.473947
28. Shiratori, K.; Nobusada, K. *J. Phys. Chem. A* **2008,** *112,* 10681–10688. doi:10.1021/jp803923f
29. Shiratori, K.; Nobusada, K. *Chem. Phys. Lett.* **2008,** *451,* 158–162. doi:10.1016/j.cplett.2007.11.081
30. Bonnet, N.; Morishita, T.; Sugino, O.; Otani, M. *Phys. Rev. Lett.* **2012,** *109,* 266101. doi:10.1103/PhysRevLett.109.266101

31. Parr, R. G.; Donnelly, R. A.; Levy, M.; Palke, W. E. *J. Chem. Phys.* **1978,** *68,* 3801–3807. doi:10.1063/1.436185
32. Vuilleumier, R.; Sprik, M.; Alavi, A. *J. Mol. Struct.: THEOCHEM* **2000,** *506,* 343–353. doi:10.1016/S0166-1280(00)00426-7
33. Trasatti, S. *Pure Appl. Chem.* **1986,** *58,* 955–966. doi:10.1351/pac198658070955
34. Neese, F. *Wiley Interdiscip. Rev.: Comput. Mol. Sci.* **2012,** *2,* 73–78. doi:10.1002/wcms.81

License and Terms

Beilstein Journal of Nanotechnology

Shape-selected nanocrystals for in situ spectro-electrochemistry studies on structurally well defined surfaces under controlled electrolyte transport: A combined in situ ATR-FTIR/online DEMS investigation of CO electrooxidation on Pt

Sylvain Brimaud*, Zenonas Jusys and R. Jürgen Behm

Full Research Paper

Open Access

Address:
Institut für Oberflächenchemie und Katalyse, Ulm University, Albert-Einstein-Allee 47, D-89081 Ulm, Germany

Email:
Sylvain Brimaud* - sylvain.brimaud@uni-ulm.de

* Corresponding author

Keywords:
CO oxidation; electrocatalysis; in situ spectro-electrochemistry; Pt; shape selected nanocrystals

Beilstein J. Nanotechnol. **2014,** *5,* 735–746.
doi:10.3762/bjnano.5.86

Received: 09 January 2014
Accepted: 09 May 2014
Published: 28 May 2014

This article is part of the Thematic Series "Electrocatalysis on the nm scale".

Associate Editor: P. Leiderer

Abstract

The suitability and potential of shape selected nanocrystals for in situ spectro-electrochemical and in particular spectro-electrocatalytic studies on structurally well defined electrodes under enforced and controlled electrolyte mass transport will be demonstrated, using Pt nanocrystals prepared by colloidal synthesis procedures and a flow cell set-up allowing simultaneous measurements of the Faradaic current, FTIR spectroscopy of adsorbed reaction intermediates and side products in an attenuated total reflection configuration (ATR-FTIRS) and differential electrochemical mass spectrometry (DEMS) measurements of volatile reaction products. Batches of shape-selected Pt nanocrystals with different shapes and hence different surface structures were prepared and structurally characterized by transmission electron microscopy (TEM) and electrochemical methods. The potential for in situ spectro-electrocatalytic studies is illustrated for CO_{ad} oxidation on Pt nanocrystal surfaces, where we could separate contributions from two processes occurring simultaneously, oxidative CO_{ad} removal and re-adsorption of (bi)sulfate anions, and reveal a distinct structure sensitivity in these processes and also in the structural implications of (bi)sulfate re-adsorption on the CO adlayer.

Introduction

Since the pioneering work of Bewick and coworkers [1,2], in situ infrared (IR) spectro-electrochemistry has been widely used to probe adsorbed species at the electrified solid/liquid interface under potential control. Among others, IR spectro-electrochemistry [3] was successfully employed to investigate the relations between electrode surface structure and the binding modes

of adsorbed species [4-10], to identify poisoning species and adsorbed intermediates formed during electrocatalytic reactions [2,11-13], and this way to unravel mechanistic details, or to resolve the structure of the water adlayer [14]. A major drawback of this method, at least for certain applications, is, however, that so far it is not possible to study electrochemical/electrocatalytic processes under enforced and well defined mass transport conditions on structurally well defined samples such as single crystalline electrodes. In the commonly applied external reflection configuration, where the working electrode is pressed against an IR-transparent window in order to minimize IR absorption by water in the aqueous electrolyte, it is possible to perform in situ spectroscopy (infrared reflection–absorption spectroscopy, IR-RAS) on single crystal surfaces, but the thin electrolyte layer precludes any significant mass transport [4-6]. On the other hand, mass transport of the electro-active species can be enforced and properly controlled employing the so-called internal reflection configuration (attenuated total reflection Fourier transform infrared spectroscopy, ATR-FTIRS) [12,15]. In this case, however, the working electrode consists of a structurally little defined polycrystalline metal film, which is directly deposited on the flat side of an IR-transparent reflecting element, as had been demonstrated, e.g., for Pt [12,16,17] or Au [18,19] films. We had later shown that in this geometry the reaction cell can be coupled in addition with a DEMS (differential electrochemical mass spectrometry) setup, allowing electrochemical measurements, IR spectroscopic detection of adsorbed species such as reaction intermediates or reaction side-products, and mass spectrometric detection of volatile reaction (side) products at the same time [15,20].

For spectro-electrochemical studies of reactions sensitive to mass transport effects, which includes many electrocatalytic reactions, it would be highly desirable to devise a way that allows us to use structurally better defined samples in an ATR configuration, e.g., to elucidate structural effects in the reaction. One possible approach would be use preferentially shaped nanoparticles of the respective material with well defined facet orientations (shape-selected nanocrystals), which are deposited on a chemically inert, IR transparent and electrically conducting film covering the ATR prism. Following these lines we have recently shown that ca. 10 nm (111)-Pt nano-octahedrons deposited on an Au film substrate, where the latter acts a chemically inert, but electrically conducting substrate, can be employed for in situ ATR-FTIRS investigations [21,22]. In that work we could provide first evidence that these working electrodes present voltammetric features and vibrational properties of adsorbed species which differ drastically from those of a polycrystalline Pt film and which are characteristic for a Pt(111) surface with a well ordered surface. In the present paper we will further explore the potential of this approach, extending this to nanoparticles with different shapes/facet orientations and to a more detailed characterization of the structural and electrochemical/electrocatalytic properties of these electrodes. Employing different types of shape-selected Pt nanocrystals (ca. 10 nm cubes, octahedrons and truncated octahedrons), we will quantitatively evaluate the contributions of different low index facet orientations to the respective properties, comparing results from electron microscopy, electrochemical measurements, in situ IR spectroscopic and mass spectrometric measurements. In the end, this aims at the possibility to conduct spectro-electrochemical studies under enforced and well controlled mass transport conditions on electrodes with well defined structural properties tailored for specific applications.

In the following, we will after a brief description of the experimental procedures and set-up, including the nanoparticle preparation, first describe the results of the structural characterization of 3 batches of differently shaped Pt nanoparticles by electron microscopy, and electrochemical techniques, including H-underpotential deposition as well Ge and Bi deposition (section 'Characterization of the Pt samples'). Subsequently, we will characterize the CO adsorption properties (section 'ATR-FTIRS characterization of structurally well defined Pt nanocrystals') and the re-adsorption of (bi)sulfate anions upon oxidative removal of CO_{ad} (CO_{ad} stripping) (section 'Monitoring sulfate re-adsorption during CO_{ad} oxidation') by combined in situ ATR-FTIRS and DEMS. The latter allows us to disentangle the contributions from the two processes, CO_{ad} oxidation and (bi)sulfate re-adsorption, to the Faradaic current for the different surface orientations, illustrating the potential of this approach.

Results and Discussion

Characterization of the Pt samples

For the present investigations we used three different batches of shape-selected Pt nanocrystals named after their dominant surface orientation. As illustrated in Figure 1, the hydrogen region voltammograms display current features which are characteristic of well ordered low index Pt surfaces [23,24]. Sharp and symmetric hydrogen sorption peaks are convincing indicators for both a well ordered Pt nanocrystal surface structure and the cleanness of the experimental setup and procedures. The hydrogen-region voltammograms obtained for such samples are approximated as weighted sum of the respective features of extended low Miller index single crystal electrode contributions. For more details we refer to [24,25] and references therein. Briefly, and focusing on the most significant current features, the (111)-NC sample contains 70% of ca. 10 nm octahedrons and exhibits the most pronounced broad peak at ca. 0.50 V, which is associated to (bi)sulfate adsorption on (111) oriented facets. On the other hand, the two peaks between 0.30

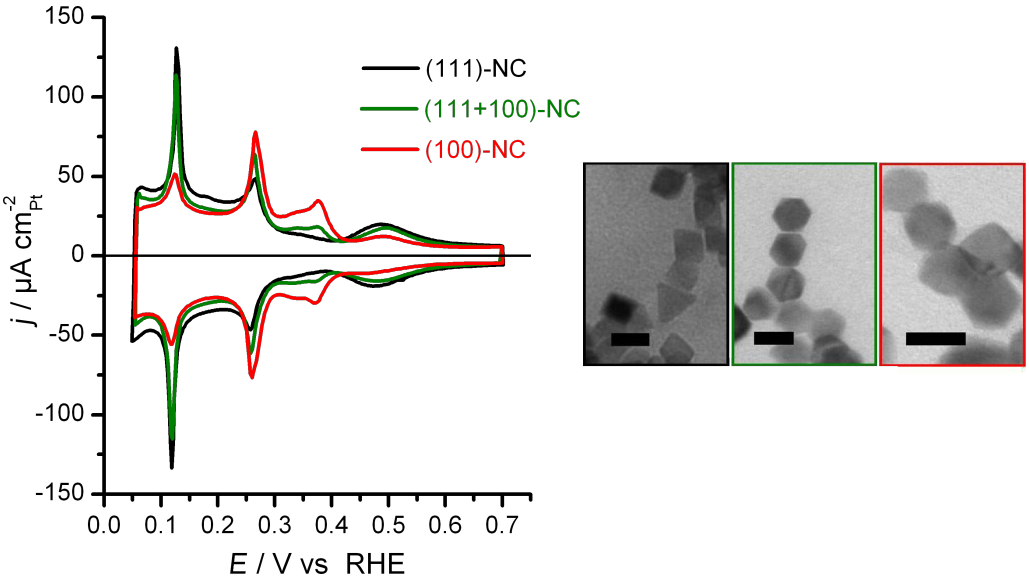

Figure 1: Left: Hydrogen-region voltammograms recorded at 50 mV s^{-1} in 0.5 M H_2SO_4. Black, green and red traces correspond to (111)-NC, (111+100)-NC and (100)-NC samples, respectively. Right: Representative BFTEM images for (111)-NC, (111+100)-NC and (100)-NC, respectively from left to right. The scale bar indicates 10 nm.

and 0.40 V vs RHE, which are characteristics of (100) oriented surfaces [26], are absent for the (111)-NC sample and particularly well-developed for the (100)-NC sample, where the latter one contains a significant amount of nanocubes with ca. 10 nm size. An "intermediate" (111+100)-NC sample containing essentially ca. 10 nm cuboctahedrons has also been prepared, its hydrogen region voltammogram displays current features which are a combination of both types described before. The relative amounts of the respective orientations obtained from a qualitative analysis of the H_{upd} peaks are in good agreement with the results of the analysis of the bright field transmission electron microscope (BFTEM) images (see Table 1).

Results from the more precise quantification by Ge and Bi adatom deposition, which specifically probe the contributions from ordered (100) and (111) surface orientations, respectively, are summarized in Table 2. They agree well with results from hydrogen region voltammograms and BFTEM. It is important

Table 1: Shape statistics from BFTEM analysis of the projected areas.

sample	2D projected area				
	regular hexagon	irregular hexagon	rhombus	square	others
(111)-NC	0%	12%	70%	0%	18%
(111+100)-NC	48%	18%	23%	0%	11%
(100)-NC	25%	31%	7%	22%	15%
plausible 3D body	cuboctahedron	truncated octahedron or cuboctahedron	octahedron	cube	others or undefined

Table 2: Fraction of ordered facets relative to the total surface area of the Pt nanocrystals, as determined by Bi and Ge adatom deposition, charge displaced (q_{dis}) during adsorption of CO at E_{ads} = 0.1 V, estimate of the potential of zero total charge (E_{pztc}), and the CO_{ad} saturation coverage (θ_{CO}) for each sample. In brackets are the uncertainties of the measurement as derived from repeated measurements.

sample name	fraction of (100) facets / %	fraction of (111) facets / %	q_{dis} / µC cm^{-2}	E_{pztc} / V	measured θ_{CO}
(111)-NC	6	49	148 (±4)	0.259 (±0.004)	0.66 (±0.03)
(111+100)-NC	17	32	150 (±1)	0.280 (±0.002)	0.69 (±0.03)
(100)-NC	37	16	146 (±3)	0.304 (±0.005)	0.72 (±0.03)

to realize that for all three samples the amount of well ordered facet area determined this way accounts for about 50% of the electrochemically active surface area, as determined by H_{upd}, with different ratios between (111) and (100) surface orientation depending on the nanocrystal shapes.

The charge displaced during CO adsorption at 0.10 V is about 150 μC cm^{-2} for all three samples investigated, independently of the Pt nanocrystal surface structure (see Table 2). This allows us to determine the E_{pztc} [27-29] for each of the working electrodes prepared from one of the three different batches of nanocrystals (see section 'Preparation and characterization of the Pt nanocrystals'). The resulting values for the E_{pztc} are 0.259 (±0.004) V, 0.280 (±0.002) V and 0.304 (±0.005) V for the (111)-NC, (111+100)-NC and (100)-NC samples, respectively (see also Table 2). The average charge for a polycrystalline electrode can be considered as a weighted sum of the contribution from each low-index facet orientation, weighted by their respective abundance [30,31]. This has to consider, however, also, contributions from the areas with non-perfect surface structure, including steps, edges etc., according to the Bi and Ge probing experiments contribute around 50% to the active surface area of each of the different batches of nanocrystals (see Table 2). Including this, the measured values agree well with the trend expected from the E_{pztc} values of the low-index Pt single crystal electrodes (0.15, 0.38 and 0.32 V for Pt(110), Pt(100) and Pt(111) in 0.5 M H_2SO_4, respectively [27]. Similar to the case of extended single crystal electrodes, E_{pztc} increases with the relative fraction of (100) facets for the nanocrystals investigated here (see Table 2).

In total, following the procedure developed by the Feliu group for the characterization of shape-selected Pt nanocrystals [24,25,29], we have three structurally well-defined and well-characterized samples of Pt nanocrystals available for the in situ IR investigations.

ATR-FTIRS characterization of structurally well defined Pt nanocrystals

Next, the adsorption properties of the structurally well defined Pt nanocrystals are characterized by FTIR spectroscopy, using adsorbed CO as probe molecule. For these measurements, the Pt nanocrystals are supported on a polycrystalline Au film predeposited on the flat side of a hemispherical Si prism for in situ ATR-IR investigations (see section 'Preparation and characterization of the Pt nanocrystals'). Before starting with the FTIR measurements, it is important to ensure that the experimental conditions, in particular the cleanness of sample and setup, resemble those in the beaker cell measurements. Figure 2 displays a comparison of the anodic part of the hydrogen-region voltammograms recorded in the beaker cell and in the thin-layer spectro-electrochemical flow cell for the three samples investigated. Obviously, they are identical. For investigations of the IR vibrational properties of adsorbed CO, gold films have the advantage that CO is adsorbed only in dynamic equilibrium with dissolved CO in the electrolyte [21,32]. Thus, after complete removal of CO from solution by purging of the flow

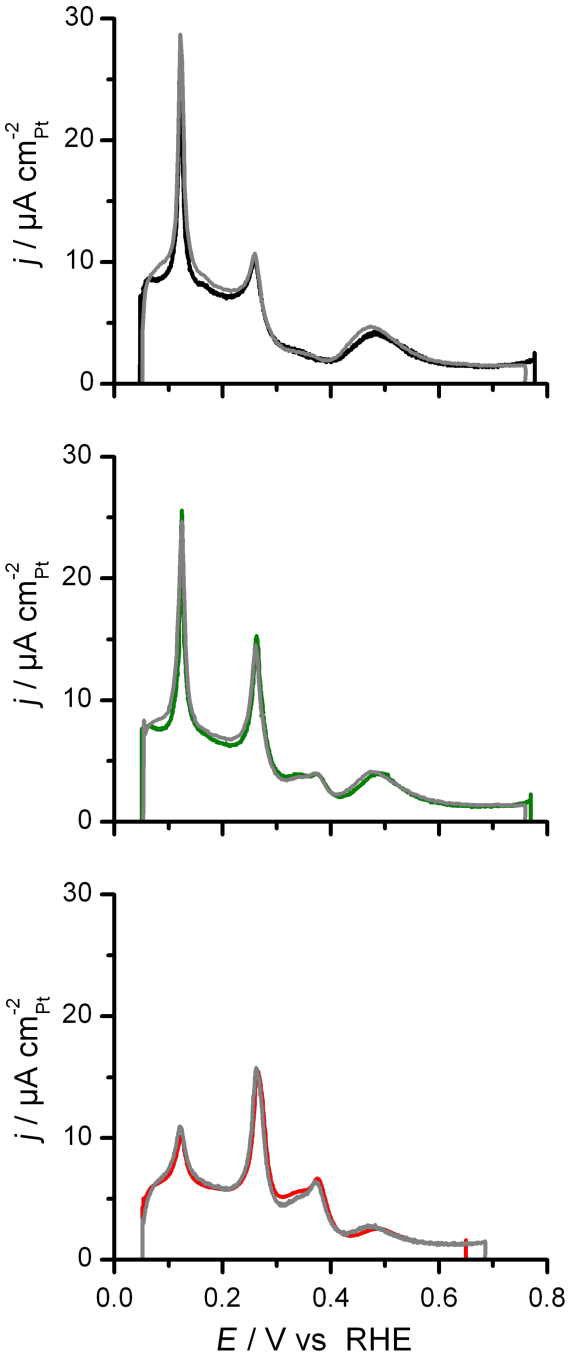

Figure 2: Comparison of the anodic scan of the hydrogen-region voltammograms recorded in the beaker cell (colored lines) and in the spectro-electrochemical flow cell (grey lines) at 10 mV s^{-1} in 0.5 M H_2SO_4. From top to bottom: (111)-NC, (111+100)-NC and (100)-NC.

cell with CO-free electrolyte, only the irreversibly adsorbed CO on the Pt nanocrystal surface remains.

Figure 3 compares ATR-FTIR spectra in the spectral regions for adsorbed CO and adsorbed (bi)sulfate anions recorded on the (111)-NC and (100)-NC samples. The inversion of the band polarity (abnormal IR effect) apparent from these spectra is well known for nanoparticle samples and has already been discussed elsewhere [21,33]. This does not, however, limit the interpretation of these spectra. After CO adsorption at 0.10 V and complete removal of dissolved CO, which was achieved by an electrolyte exchange under continuous potential control [12], two IR bands are observed in the 1500–2500 cm^{-1} region of the spectrum, which are due to linearly (CO_L, higher wave number) and bridge-bonded (CO_B, lower wave number) adsorbed CO, respectively [3,7,8,34]. For (111)-NC, the band corresponding to CO_L is blue-shifted by 4 cm^{-1} compared to that on (100)-NC while, oppositely, the band corresponding to CO_B is red-shifted by 10 cm^{-1}. The lower wave number obtained for CO_L adsorbed on the (100)-NC than on the (111)-NC sample agrees well with trends expected from CO adsorption on Pt(100) and Pt(111) surfaces [8,35,36]. Furthermore, we find a slightly smaller difference in wave numbers ($\Delta d\bar{\upsilon}_{CO} - dE$) between the two binding modes of CO_{ad} for (100)-NC than for (111)-NC. Also, the relative fraction of bridge-bonded CO_{ad} seems to be higher for the former nanocrystal sample than for the latter one. However, since the IR band intensity is known to not directly reflect the CO_{ad} coverage/population (bonding mode) [37], in particular not at high coverages, we will refrain from a more quantitative discussion. In total, the IR observations are fully consistent with in situ IR observations on CO_{ad} saturated low Miller index single crystal electrodes [8,35,36].

The IR spectral region characteristic of adsorbed (bi)sulfate (1050–1350 cm^{-1} [38,39]) is displayed in the right panel of Figure 3. Two bands are observed at ca. 1260 cm^{-1} and 1120 cm^{-1}, with different relative intensities depending on the surface structure of the respective nanocrystals. Inspection of previously published FTIR spectra obtained in an external reflection configuration on extended Pt single crystal electrodes [9,10] reveals that the band at higher wave number is characteristic for adsorption on Pt(111), while that at lower wave number is favoured for Pt(100). The different intensities in the two peaks reflect the influence of the different facet orientations. Thus, also in this case the IR data on shaped-selected nanocrystals are fully consistent with observations on extended single crystal electrodes.

Overall, the IR vibrational properties of adsorbed species (CO_{ad}, adsorbed (bi)sulfate) on shape-selected nanocrystals confirm the findings from electron microscopy and electrochemical measurements that the use of shape selected nanoparticles results in structurally well defined electrodes, with dominant structures equal to those of the respective single crystal electrodes. The absorbance by the underlying Au film is sufficiently low for in situ ATR-IR measurements, opening a door

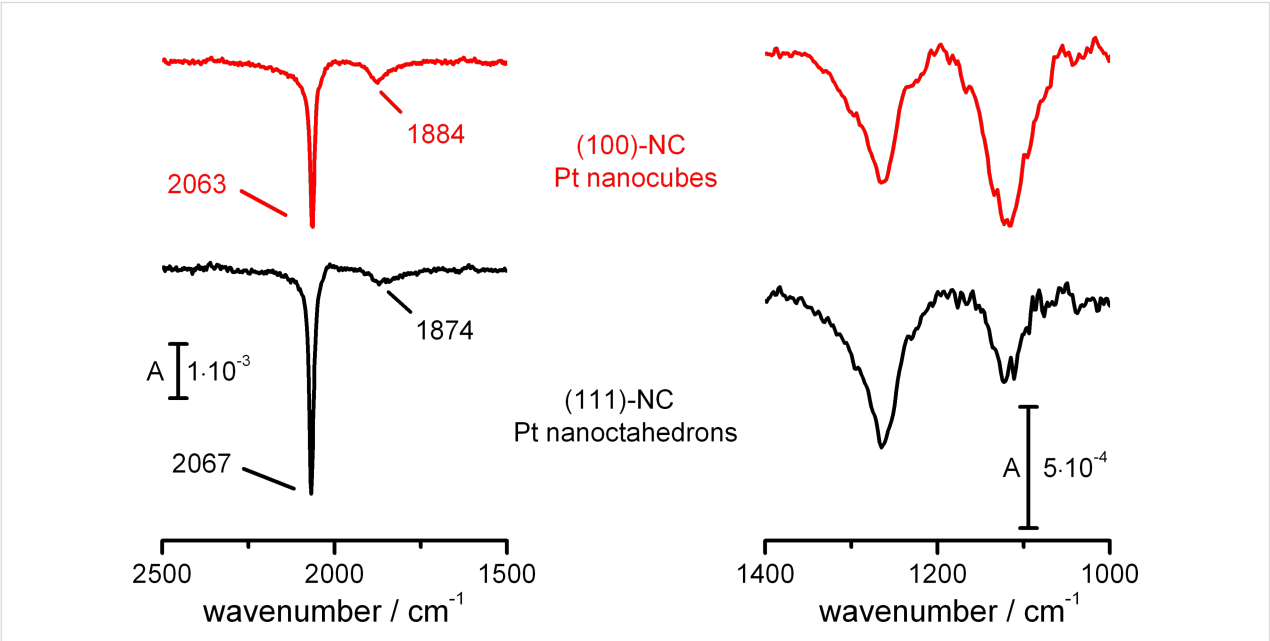

Figure 3: IR vibrational spectra of irreversibly adsorbed CO recorded at 0.10 V (left panel) and of adsorbed (bi)sulfate recorded at 0.75 V (right panel) on (100)-NC (top) and (111)-NC (bottom). R_0 was recorded at the same potential in the absence of CO (left panel). All experiments were conducted in 0.5 M H_2SO_4 and all spectra were acquired in the absence of dissolved CO.

for IR measurements on structurally well defined electrodes with tunable surface structure under enforced and controlled electrolyte mass transport.

Monitoring sulfate re-adsorption during CO_{ad} oxidation

As a first application of this newly developed tool for in situ spectro-electrochemical studies we investigated the potentiodynamic oxidation of a pre-adsorbed CO adlayer (CO_{ad} stripping). Combination of the thin-layer spectro-electrochemical flow cell with the DEMS setup allows for an online detection of the CO_2 produced upon CO_{ad} electro-oxidation. Results from potentiodynamic oxidative removal of CO_{ad}, which was pre-adsorbed at 0.1 V, are shown in Figure 4. The Faradaic currents recorded during the first and subsequent anodic scans are displayed in Figure 4a–c for the three samples investigated, the corresponding mass spectrometric (MS) currents (m/z = 44) resulting from detection of CO_2 are displayed in Figure 4d–f. For all samples, CO_{ad} electro-oxidation starts at 0.30 V, followed by the well-known pre-peak for CO_{ad} oxidation, and then by two oxidation peaks, whose maxima are located at ca. 0.61 and 0.67 V, respectively. The Faradaic current profiles for the CO_{ad} stripping agree well with those obtained in beaker cell measurements on similar nanocrystals [40,41]. Also the potentials at the maxima of the oxidation peaks measured during potentiodynamic oxidation at 1 mV s^{-1} are in good agreement data obtained at faster scan rates and $dE_{peak}/d(\log v)$ slopes reported previously [41]. The intensity of the second oxidation peak was found to be correlated with the fraction of (100) facets of the respective nanocrystal samples [41].

The MS current related to CO_2 detection can be transformed into the related Faradaic current from CO_{ad} oxidation via the collection efficiency K*. This is defined as the ratio between the MS current signal and the Faradaic current related to the respective process, multiplied by the number of electrons exchanged per product molecule in the reaction (in our case, oxidation of adsorbed CO to CO_2 leads to 2 electrons exchanged per CO_2 molecule) [20]. While in most cases K* is determined by comparing the charge under the oxidation peak corrected by a contribution of 20% from anion readsorption [42], we here followed a different route. In the present study, we determined the K* value by comparison of the Faradaic and mass spectrometric (m/z = 44) currents in the potential region 0.30–0.35 V, assuming that in this potential range, at the onset of CO_{ad} oxidation, Faradaic processes other than CO_{ad} electro-oxidation can be neglected, while at higher potentials other processes such as re-adsorption of anions or surface oxidation may take place as well [43-45]. An example of such kind of refined K* determination is shown Figure 5. In the pre-peak region (up to ca. 0.50 V), the perfect match between the Faradaic current for CO_2 production (determined using the K* value determined in the range from 0.30 to 0.35 V) and the measured Faradaic current for CO_{ad} oxidation supports the hypothesis that CO_{ad} electro-oxidation is the only Faradaic process occurring in this potential region. Thus, in the pre-peak

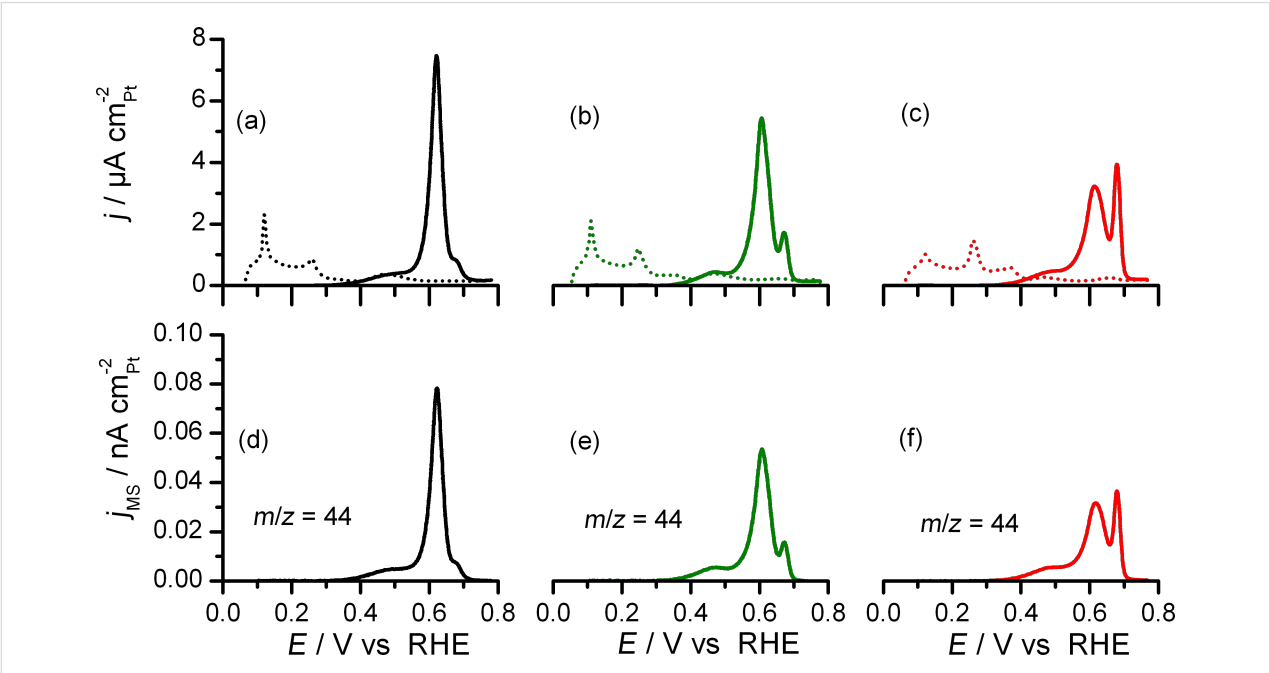

Figure 4: First (solid lines) and second (dashed lines) positive going scans of CO stripping voltammograms (a–c) and mass spectrometric current of the m/z = 44 signal (CO_2 detection) (d–f) for (111)-NC (a,d), (111+100)-NC (b,e) and (100)-NC (c,f). H_2SO_4 0.5 M, v = 1 mV s^{-1}.

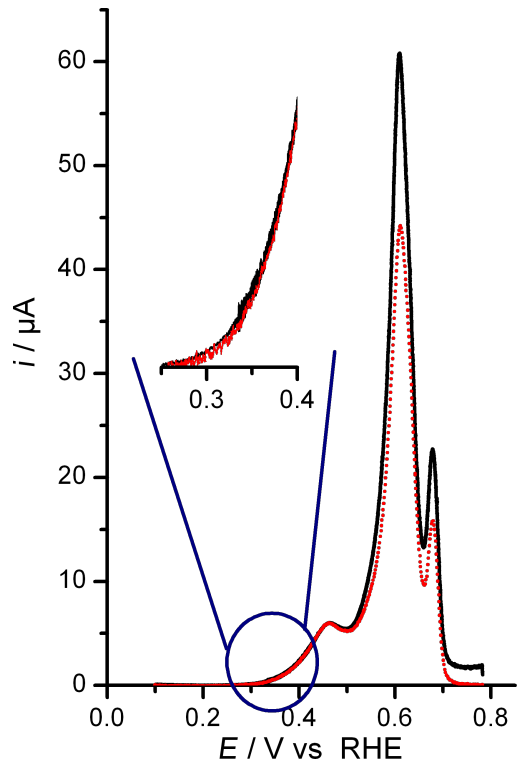

Figure 5: Normalized mass spectrometric current (m/z = 44, CO_2 detection, red dotted line) and Faradaic current (black solid line) acquired during the CO_{ad} stripping experiment on (111+100)-NC (v = 1 mV s^{-1}). The CO adlayer was formed by adsorption from CO saturated electrolyte at 0.10 V (0.5 M H_2SO_4).

region, the small fraction of CO_{ad} removed (see below) does not result in sufficiently opened Pt-CO adlayer allowing for (bi)sulfate anions readsorption [45]. The K* values obtained in this potential range were in the range between 2 and 3 × 10^{-5} for all experiments, which is in good agreement with previous findings on our experimental setup [20]. With further increase of the electrode potential, the normalized MS current from CO_2 detection deviates from the Faradaic current for CO_{ad} electro-oxidation. This indicates that another Faradaic process occurs, while CO_{ad} is removed by potentiodynamic oxidation. This difference is mainly attributed to (bi)sulfate anion re-adsorption and progressive double layer charging, which occurs while CO_{ad} is removed by potentiodynamic oxidation. Note that this direct procedure for determining the contribution of anion re-adsorption leads to results for the charge contribution from (bi)sulfate re-adsorption which are comparable with those of earlier (and more indirect) coulometric analysis (see below) [45,46]. Correspondingly, the difference between the normalized (mass spectrometric) current from CO_2 detection and the Faradaic current from CO_{ad} electro-oxidation reflects the current associated with (bi)sulfate anion re-adsorption and double layer charging, while CO_{ad} is increasingly removed from the surface.

Plots of the current associated to (bi)sulfate anions re-adsorption (and capacitive double layer charging) during potentiodynamic CO_{ad} oxidative removal are displayed in Figure 6 for the three samples of shape-selected nanoparticles investigated. To

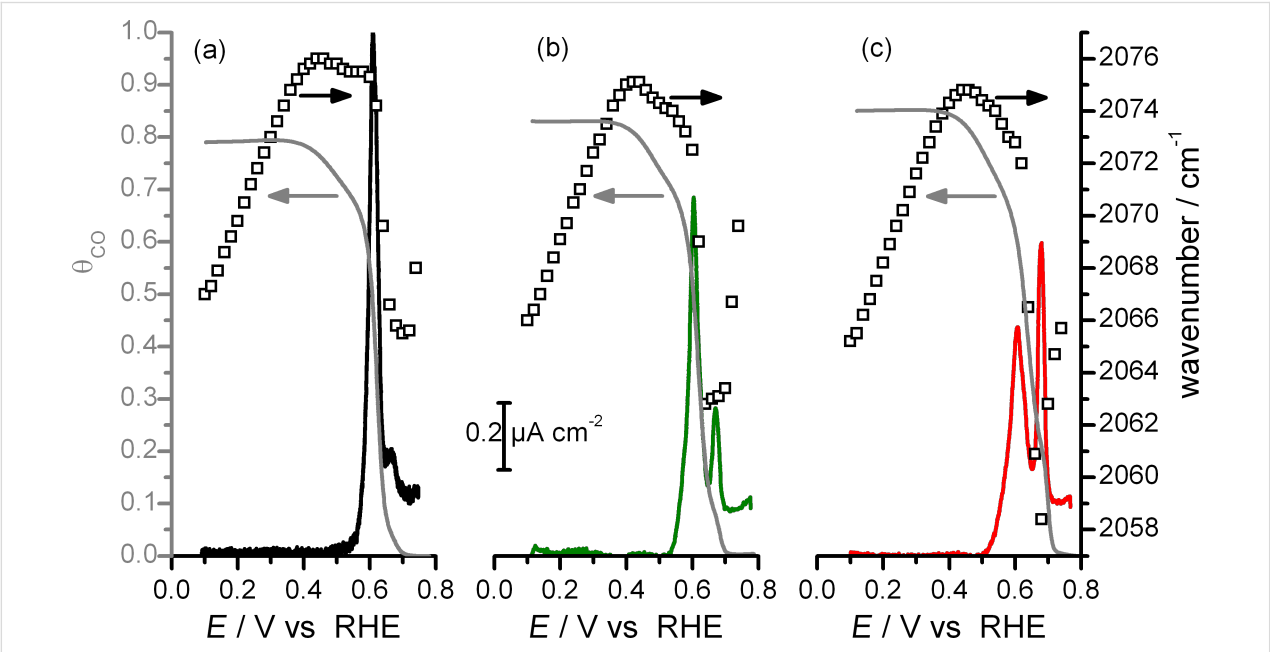

Figure 6: Plots of the currents from (bi)sulfate anions re-adsorption (colored traces), absolute CO_{ad} coverages (θ_{CO}, grey traces) and IR band frequencies for linearly adsorbed CO (open square) as function of the electrode potential for (111)-NC (a), (111+100)-NC (b) and (100)-NC (c) (0.5 M H_2SO_4, v = 1 mV s^{-1}).

the best of our knowledge, this is the first time that these currents have been measured directly.

The charge which is not related to CO_{ad} electro-oxidation in CO_{ad} stripping voltammogram is estimated to ca. 19% of the total charge, in good agreement with the value obtained from a pure coulometric analysis developed on Pt single crystalline electrodes (≈20%) [45]. In the latter method, the charge correction is determined via the so-called "double-layer" correction, where the sum of the charge displaced upon CO adsorption at the onset of hydrogen adsorption and of the charge in a base CV between that potential and the upper limit of the CO_{ad} stripping peak are subtracted from the total charge measured for the electrooxidation of a saturated CO adlayer. The absolute CO_{ad} coverage (θ_{CO} , with θ_{CO} = 1 for 1 CO_{ad} per Pt surface atom) resulting from the formation of a CO adlayer at 0.10 V can now be estimated from the ratio between the charge related to CO_{ad} electro-oxidation and double the charge related to H adsorption, and assuming a hydrogen saturation coverage of 0.77 at 0.05 V [47], independent of the Pt surface structure. The charge related to H adsorption can be determined from the Faradaic charge under the anodic part of the hydrogen region voltammogram, corrected for the charge associated to anion sorption (obtained from Figure 6) and the double layer capacitive contribution. The resulting saturation coverages of the CO adlayer formed at 0.10 V are tabulated in Table 2 and range between 0.6 and 0.7 CO_{ad} per Pt atom, in good agreement with findings for extended Pt single crystal surfaces/electrodes [45]. To illustrate the different potential dependences in CO_{ad} removal, we also plotted the evolution of the absolute CO_{ad} coverage as a function of the electrode potential during CO_{ad} stripping for the three nanocrystal samples (see Figure 6). Just as an example, at 0.64 V, 90%, 80% and 60% of the CO_{ad} has been removed from the nanocrystal surface for the samples (111)-NC, (111+100)-NC and (100)-NC, respectively.

The changes in the CO adsorption properties were monitored by following the frequency shifts of the IR band associated to linearly adsorbed CO, which are also plotted in Figure 6. They follow classical descriptions reported previously [5,34,43,48]. First, between 0.10 and 0.45 V, the CO_L band is linearly blue-shifted due to the effect of the applied electric field, i.e., reflecting the so-called Stark effect. The slope of between 30 and 33 cm^{-1} V^{-1} agrees well with previous findings on Pt surfaces [15,49,50]. Then, as the CO_{ad} coverage decreases, the CO_L band is dramatically red-shifted. This observation is generally interpreted as due to a stronger metal–CO_{ad} binding, caused by a lowering of the CO_{ad}–CO_{ad} lateral repulsion [5,34,48]. Finally, at potentials higher than 0.65 V, this changes again into a blue shift of the CO_L band, leading to a "U-shape" of the $d\bar{\upsilon}_{CO} - dE$ plot. It should be noted that, as shown Figure 6, the extent of amplitude of the "U-shape" depends on the structure of the nanocrystal surface, it is more pronounced as the fraction of (100) facets increases. This blue shift had been attributed to a compression of the remaining CO due to anion re-adsorption [43,44,51]. The plot of the current associated to anion re-adsorption displayed in Figure 6 supports this hypothesis. In fact, the intensity of the second peak of (bi)sulfate re-adsorption and the extent of the blue-shift at high potentials seem to be correlated, with both of them increasing as the fraction of ordered (100) area on the nanocrystal surface increases. The correlation between (bi)sulfate re-adsorption and CO_{ad} compression clearly illustrates the role played by anions for CO_{ad} bonding and for CO_{ad} electro-oxidation. Finally, the difference in anion re-adsorption for the three different samples illustrates also the structure sensitivity of this process.

Conclusion

Employing in situ ATR-FTIR spectroscopy and mass spectrometry in a combined ATR-FTIR/DEMS flow cell set-up, we could demonstrate that shape-selected and structurally well characterized nanocrystals deposited on a Au film/Si substrate offer an attractive opportunity for performing spectro-electrochemical and in particular spectro–electrocatalytic measurements under enforced and well controlled electrolyte mass transport conditions on structurally well defined electrode surfaces. The surface morphology and structure of the shape-selected nanocrystals, which are prepared by colloidal synthesis, can be varied in a controlled way over a wide range. TEM, electrochemical and in situ ATR-FTIR characterization agreeingly demonstrated that the surface of the nanocrystals consists predominantly of well ordered facets with low index orientation, whose relative contribution depends on the synthesis conditions. Comparison with extended single crystal electrodes revealed similar electrochemical and adsorption/reaction characteristics for low index facets and the corresponding extended single crystals, as evidenced by both voltammetric traces and the vibrational properties of adsorbed CO.

The possibility to prepare tailored model electrodes, whose active surface is dominated by one or more specific structural elements, offers new perspectives for spectro-electrochemical investigations of the relationship between reaction mechanism/kinetics, electrolyte mass transport and electrode surface structure. The potential of such kind of measurements is illustrated for potentiodynamic CO_{ad} oxidation, where the simultaneous online DEMS detection of the CO_2 produced during the oxidative removal of CO_{ad} and the measurement of the overall Faradaic current allow us to directly measure and separate the contribution from re-adsorption of (bi)sulfate anions to the Faradaic current. Finally, in situ ATR-FTIRS measurements performed in parallel reveal changes in the vibrational prop-

erties which can be traced back to the electrostatic Stark effect, changes in the CO_{ad} coverage and hence in the structure of the CO adlayer with increasing CO_{ad} removal, and finally similar changes induced by increasing re-adsorption of (bi)sulfate anions. Due to the strict time correlation between the different measurements the contributions from the different processes can be disentangled. Overall, this yields a detailed picture of the different processes occurring during the CO_{ad} oxidation reaction, on a molecular scale and specific for selected surface structures, which will be important for bulk reaction studies, e.g., of fuel cell relevant reaction, which are planned for the future.

While this was demonstrated for Pt nanocrystals, other metals are equally accessible, leaving this as a generally applicable approach for in situ spectro-electrochemical studies on structurally well defined electrodes under enforced and controlled electrolyte mass transport conditions.

Experimental

Preparation and characterization of the Pt nanocrystals

Batches of shape-selected Pt nanocrystals of different shapes were prepared by a colloidal synthesis method mainly developed by the El-Sayed group [52-54]. This synthesis method leads to ca. 10 nm sized nanocrystals with well ordered facets in low index orientations, whose voltammetric traces resemble those of flame annealed extended low Miller index single crystalline electrodes, as demonstrated previously by the Feliu group [25,40,55]. Prior to the synthesis, the reaction vessel was first cleaned by aqua regia to remove metal traces which could act as nucleation center, then with saturated alkaline solution to remove organic contaminants which could influence the growth process, and finally boiled in ultrapure water (MilliQ®, 18 MΩ cm). Briefly, the synthesis method consists of the reduction of a Pt salt (Alfa Aesar) dissolved in deaerated ultrapure water by hydrogen bubbling (5.0, Westfalen) in the presence of sodium polyacrylate (NaPA, M_w 2100, Sigma-Aldrich). The relevant synthesis parameters are given Table 3. After 10 min of hydrogen bubbling, the reaction vessel was sealed and left over night, protected from the light. Then, the precipitation of the nanocrystals was initiated by adding a few NaOH pellets. Cleaning of the nanocrystals was obtained by successive precipitation/redispersion in ultrapure water. Finally, the resulting batches of nanocrystals were stored in a few millilitres of ultrapure water. All chemicals and gases were used as received without any further purification.

Sizes and shapes of the nanocrystals were characterized by bright field transmission electron microscopy (BFTEM) (Philips CM 200 kV). A droplet of an aqueous suspension of nanocrystals was deposited on a carbonized Cu grid (Plano) and dried slowly. Free software (ImageJ, National Institute of Health / USA) was used to analyse the images.

The surface structure of the different batches of nanocrystals was furthermore characterized by electrochemical methods. The measurements were conducted in a classical three electrode beaker cell. The nanocrystals were deposited on a pure gold hemispherical bead by pipetting a droplet of water containing nanocrystals and subsequent drying under a N_2 flow. A qualitative picture of the Pt nanocrystals surface structure was obtained by potentiodynamic adsorption/desorption of hydrogen (in the so-called hydrogen region of the voltammogram). The surface areas of well ordered facets of specific orientation exhibited by the nanocrystal surface (total electrochemically active Pt surface area ca. 0.1 cm^2), were determined by coulometric analysis of the redox processes on a surface covered by a Ge or Bi adlayer generated by spontaneous deposition, following a method developed by the Feliu group and detailed in [56,57]. For determining the area of (100) oriented facets, we used spontaneous deposition of a Ge adlayer, which was performed by dipping the working electrode 5 min into a 10^{-2} M GeO_2 (Aldrich, 99.99% purity) containing 1 M NaOH solution. For determination of the (111) surface area, a similar process was employed using Bi deposition, where the working electrode was dipped for 5 min in saturated Bi_2O_3 (Aldrich, 99.99% purity) in 0.5 M H_2SO_4 solution. Subsequently, the modified working electrode was introduced into the electrochemical cell under potential control at 0.15 V. Then, the electrode was cycled a few times between 0.15 V and 0.60 V for the Ge-modified Pt electrodes and between 0.15 V and 0.75 V for the Bi-modified Pt electrodes, and the coulometric charge associated with the surface oxidation/reduction of the Bi/Ge adlayer was determined and correlated to the amount of (111)/(100) ordered domains [56,57].

Table 3: Relevant synthesis parameters and Pt precursors.

sample name	Pt precursor	NaPA/Pt ratio	initial pH	aging of the Pt solutions
(111)-NC	$H_2PtCl_6 \cdot 6H_2O$	5	7	1 day
(111+100)-NC	K_2PtCl_4	1	8	3 days
(100)-NC	K_2PtCl_4	12	7	3 days

The potential of zero total charge (E_{pztc}) was determined from the potential where the total charge passed in the base CV (hydrogen region) is equal to the charge displaced during CO adsorption at 0.10 V_{RHE} (q_{dis}). This provides a direct determination of the E_{pztc} [27-29].

Electrochemical setup

All electrochemical measurements, both in the beaker cell and in the in situ IR spectro-electrochemistry were conducted in O_2-free 0.5 M H_2SO_4 supporting electrolyte, and freshly prepared from ultrapure water (MilliQ®, 18 MΩ cm) and conc. H_2SO_4 (Suprapur, Merk). A home-made hydrogen reference electrode (RHE) served as reference electrode, and all potentials given in the paper are referenced versus RHE, a gold foil was used as counter-electrode. A Pine model AFRDE-5 analog potentiostat interfaced to a computer was used for potential control and data acquisition.

ATR-FTIR spectro-electrochemical measurements

The spectro-electrochemical setup and the dual thin-layer flow cell used in this study were described in detail in [12,20]. The in situ FTIRS measurements in an attenuated total reflection (ATR) configuration were carried out using a BioRad FTS 6000 spectrometer equipped with a HgCdTe (MCT) detector, cooled with liquid nitrogen. The spectral resolution was set to 4 cm^{-1}. The absorption is given in absorbance units defined as $A = -\log(R/R_0)$, where R and R_0 denote the reflectance at a given potential and at the reference potential, respectively. The respective reference potentials for R_0 are specified in the figure captions.

For the FTIRS measurements the Pt nanocrystals were deposited on a thin Au film serving as chemically inert and stable and electrically conducting substrate, which in turn is deposited on a Si prism. The Au films have to be thin enough to be FTIR transparent and thick enough to exhibit sufficient electric conductivity and fully cover the Si substrate. The gold thin film was prepared by electroless deposition on the flat plane of a Si prism, using the procedure published by Miyake et al. [18]. After polishing and cleaning of the Si prism, its flat surface was dipped into 40% NH_4F (BASF, Selectipure grade) in order to remove the oxide layer and to obtain a H-terminated Si surface, which improves the adhesion of the film. The gold plating solution consisted of a 1:1:1 mixture of 2% HF (Merck, suprapure grade), 0.03 M $NaAuCl_4$ (Alfa Aesar) and 0.3 M Na_2SO_3 + 0.1 M $Na_2S_2O_3$ + 0.1 M NH_4Cl (all from Merck, pro analysi grade). This freshly prepared solution was pipetted onto the Si–H surface at 50 °C. After 80 s, the resulting film was rinsed with ultrapure water and dried under a N_2 stream. After pipetting and drying a droplet of water-containing shaped-selected Pt nanocrystals on the gold film (electrochemically active Pt surface area ca. 10 cm^2), the Si prism was installed in the thin-layer cell by pressing its flat side via an O-ring spacer against the flow cell body. Particular attention was paid to the cleanness of the overall procedure in order to achieve similar experimental conditions as in the beaker cell measurements (see section 'ATR-FTIRS characterization of structurally well defined Pt nanocrystals').

DEMS setup and measurements

For online product detection, the second compartment of the flow cell was connected via a porous Teflon membrane to a differentially pumped quadrupole mass spectrometer from Pfeiffer Vacuum (QMS 422). A more detailed description of the DEMS setup is given in [58]. The determination of the K* factor necessary for converting mass spectrometric currents (here: CO_2 signal) into a Faradaic current (here: the Faradaic current for CO_{ad} oxidation) was described in the text.

Acknowledgements

This work was supported by the Deutsche Forschungsgemeinschaft via project BE 1201 / 17-1 and via the Research Group FOR 1376 (JU 2781 / 2-2, BE 1201 /18-2). We gratefully acknowledge Dr. J. Biskupek for the TEM measurements (Ulm University) and fruitful discussions with Dr. J. Solla-Gullón and Prof. J. M. Feliu (Univ. Alicante).

References

1. Bewick, A.; Kunimatsu, K.; Stanley Pons, B. *Electrochim. Acta* **1980,** *25,* 465. doi:10.1016/0013-4686(80)87039-3
2. Beden, B.; Lamy, C.; Bewick, A.; Kunimatsu, K. *J. Electroanal. Chem. Interfacial Electrochem.* **1981,** *121,* 343. doi:10.1016/S0022-0728(81)80590-6
3. Beden, B.; Lamy, C. In *Spectroelectrochemistry. Theory and Practice;* Gale, R. J., Ed.; Plenum Press, 1988; pp 189–261.
4. Leung, L.-W. H.; Wieckowski, A.; Weaver, M. J. *J. Phys. Chem.* **1988,** *92,* 6985. doi:10.1021/j100335a029
5. Chang, S. C.; Leung, L. W.; Weaver, M. J. *J. Phys. Chem.* **1989,** *93,* 5341. doi:10.1021/j100351a006
6. Leung, L.-W. H.; Weaver, M. J. *J. Phys. Chem.* **1989,** *93,* 7218. doi:10.1021/j100357a038
7. Kitamura, F.; Takeda, M.; Takahashi, M.; Ito, M. *Chem. Phys. Lett.* **1987,** *142,* 318. doi:10.1016/0009-2614(87)85114-X
8. Chang, S.-C.; Weaver, M. J. *J. Phys. Chem.* **1991,** *95,* 5391. doi:10.1021/j100167a010
9. Faguy, P. W.; Markovic, N.; Ross, J., Jr. *J. Electrochem. Soc.* **1993,** *140,* 1638. doi:10.1149/1.2221615
10. Hoshi, N.; Sakurada, A.; Nakamura, S.; Teruya, S.; Koga, O.; Hori, Y. *J. Phys. Chem. B* **2002,** *106,* 1985. doi:10.1021/jp012456o
11. Miki, A.; Ye, S.; Osawa, M. *Chem. Commun.* **2002,** 1500. doi:10.1039/B203392E
12. Chen, Y.-X.; Heinen, M.; Jusys, Z.; Behm, R. J. *Angew. Chem., Int. Ed.* **2006,** *45,* 981. doi:10.1002/anie.200502172
13. Iwasita, T. *J. Braz. Chem. Soc.* **2002,** *13,* 401. doi:10.1590/S0103-50532002000400002

14. Osawa, M.; Tsushima, M.; Mogami, H.; Samjeské, G.; Yamakata, A. *J. Phys. Chem. C* **2008,** *112,* 4248. doi:10.1021/jp710386g
15. Heinen, M.; Chen, Y.-X.; Jusys, Z.; Behm, R. J. *Electrochim. Acta* **2007,** *53,* 1279. doi:10.1016/j.electacta.2007.05.020
16. Miki, A.; Ye, S.; Sensaki, T.; Osawa, M. *J. Electroanal. Chem.* **2004,** *563,* 23. doi:10.1016/j.jelechem.2003.09.014
17. Cuesta, A.; Cabello, G.; Gutiérrez, C.; Osawa, M. *Phys. Chem. Chem. Phys.* **2011,** *13,* 20091. doi:10.1039/C1CP22498K
18. Miyake, H.; Ye, S.; Osawa, M. *Electrochem. Commun.* **2002,** *4,* 973. doi:10.1016/S1388-2481(02)00510-6
19. Cuesta, A.; Cabello, G.; Hartl, F. W.; Escudero-Escribano, M.; Vaz-Domínguez, C.; Kibler, L. A.; Osawa, M.; Gutiérrez, C. *Catal. Today* **2013,** *202,* 79. doi:10.1016/j.cattod.2012.04.022
20. Heinen, M.; Chen, Y. X.; Jusys, Z.; Behm, R. J. *Electrochim. Acta* **2007,** *52,* 5634. doi:10.1016/j.electacta.2007.01.055
21. Brimaud, S.; Jusys, Z.; Behm, R. J. *Electrocatalysis* **2011,** *2,* 69. doi:10.1007/s12678-011-0040-7
22. Brimaud, S.; Behm, R. J. *J. Am. Chem. Soc.* **2013,** *135,* 11716. doi:10.1021/ja4051795
23. Clavilier, J. In *Interfacial Electrochemistry, Theory, Experiment and Applications;* Wieckowski, A., Ed.; Marcel Dekker, 1999; pp 231–248.
24. Solla-Gullón, J.; Vidal-Iglesias, F. J.; Rodriguez, P.; Herrero, E.; Feliu, J. M.; Clavilier, J.; Aldaz, A. *J. Phys. Chem. B* **2004,** *108,* 13573. doi:10.1021/jp0471453
25. Solla-Gullón, J.; Rodríguez, P.; Herrero, E.; Aldaz, A.; Feliu, J. M. *Phys. Chem. Chem. Phys.* **2008,** *10,* 1359. doi:10.1039/B709809J
26. Armand, D.; Clavilier, J. *J. Electroanal. Chem. Interfacial Electrochem.* **1987,** *225,* 205. doi:10.1016/0022-0728(87)80014-1
27. Climent, V.; Gómez, R.; Feliu, J. M. *Electrochim. Acta* **1999,** *45,* 629. doi:10.1016/S0013-4686(99)00241-8
28. Climent, V.; García-Araez, N.; Herrero, E.; Feliu, J. *Russ. J. Electrochem.* **2006,** *42,* 1145. doi:10.1134/S1023193506110012
29. Chen, Q. S.; Solla-Gullón, J.; Sun, S. G.; Feliu, J. M. *Electrochim. Acta* **2010,** *55,* 7982. doi:10.1016/j.electacta.2010.03.050
30. Valette, G.; Hamelin, A. *J. Electroanal. Chem. Interfacial Electrochem.* **1973,** *45,* 301. doi:10.1016/S0022-0728(73)80166-4
31. Vorotyntsev, M. A. *J. Electroanal. Chem. Interfacial Electrochem.* **1981,** *123,* 379. doi:10.1016/S0022-0728(81)80512-8
32. Sun, S.-G.; Cai, W.-B.; Wan, L.-J.; Osawa, M. *J. Phys. Chem. B* **1999,** *103,* 2460. doi:10.1021/jp984028x
33. Chen, W.; Sun, S.-G.; Zhou, Z.-Y.; Chen, S.-P. *J. Phys. Chem. B* **2003,** *107,* 9808. doi:10.1021/jp034740g
34. Marković, N. M.; Ross, P. N., Jr. *Surf. Sci. Rep.* **2002,** *45,* 117. doi:10.1016/S0167-5729(01)00022-X
35. López-Cudero, A.; Cuesta, A.; Gutiérrez, C. *J. Electroanal. Chem.* **2005,** *579,* 1. doi:10.1016/j.jelechem.2005.01.018
36. López-Cudero, A.; Cuesta, Á.; Gutiérrez, C. *J. Electroanal. Chem.* **2006,** *586,* 204. doi:10.1016/j.jelechem.2005.10.003
37. Severson, M. W.; Stuhlmann, C.; Villegas, I.; Weaver, M. J. *J. Chem. Phys.* **1995,** *103,* 9832. doi:10.1063/1.469950
38. Nart, F. C.; Iwasita, T. *J. Electroanal. Chem.* **1992,** *322,* 289. doi:10.1016/0022-0728(92)80083-G
39. Lachenwitzer, A.; Li, N.; Lipkowski, J. *J. Electroanal. Chem.* **2002,** *532,* 85. doi:10.1016/S0022-0728(02)00759-3
40. Solla-Gullón, J.; Vidal-Iglesias, F. J.; Herrero, E.; Feliu, J. M.; Aldaz, A. *Electrochem. Commun.* **2006,** *8,* 189. doi:10.1016/j.elecom.2005.11.008
41. Brimaud, S.; Pronier, S.; Coutanceau, C.; Léger, J.-M. *Electrochem. Commun.* **2008,** *10,* 1703. doi:10.1016/j.elecom.2008.08.045
42. Jusys, Z.; Kaiser, J.; Behm, R. J. *Phys. Chem. Chem. Phys.* **2001,** *3,* 4650. doi:10.1039/B104617A
43. Marković, N. M.; Lucas, C. A.; Rodes, A.; Stamenković, V.; Ross, P. N. *Surf. Sci.* **2002,** *499,* L149. doi:10.1016/S0039-6028(01)01821-0
44. Tripkovic, D. V.; Strmcnik, D.; van der Vilet, D.; Stamenkovic, V.; Markovic, N. M. *Faraday Discuss.* **2009,** *140,* 25. doi:10.1039/B803714K
45. Gómez, R.; Feliu, J. M.; Aldaz, A.; Weaver, M. J. *Surf. Sci.* **1998,** *410,* 48. doi:10.1016/S0039-6028(98)00295-7
46. Angelucci, C. A.; Nart, F. C.; Herrero, E.; Feliu, J. M. *Electrochem. Commun.* **2007,** *9,* 1113. doi:10.1016/j.elecom.2007.01.012
47. Biegler, T.; Rand, D. A. J.; Woods, R. *J. Electroanal. Chem. Interfacial Electrochem.* **1971,** *29,* 269. doi:10.1016/S0022-0728(71)80089-X
48. Chang, S.-C.; Weaver, M. J. *Surf. Sci.* **1990,** *238,* 142. doi:10.1016/0039-6028(90)90072-G
49. Lambert, D. K. *Solid State Commun.* **1984,** *51,* 297. doi:10.1016/0038-1098(84)90691-4
50. Weaver, M. J. *Appl. Surf. Sci.* **1993,** *67,* 147. doi:10.1016/0169-4332(93)90307-W
51. Chen, Y.-X.; Heinen, M.; Jusys, Z.; Behm, R. J. *J. Phys. Chem. C* **2007,** *111,* 435. doi:10.1021/jp065508o
52. Petroski, J. M.; Wang, Z. L.; Green, T. C.; El Sayed, M. A. *J. Phys. Chem. B* **1998,** *102,* 3316. doi:10.1021/jp981030f
53. Petroski, J. M.; Green, T. C.; El Sayed, M. A. *J. Phys. Chem. A* **2001,** *105,* 5542. doi:10.1021/jp0019207
54. Petroski, J.; El Sayed, M. A. *J. Phys. Chem. A* **2003,** *107,* 8371. doi:10.1021/jp0300694
55. Solla-Gullón, J.; Vidal-Iglesias, F. J.; López-Cudero, A.; Garnier, E.; Feliu, J. M.; Aldaz, A. *Phys. Chem. Chem. Phys.* **2008,** *10,* 3689. doi:10.1039/B802703J
56. Rodriguez, P.; Herrero, E.; Solla-Gullón, J.; Vidal-Iglesias, F. J.; Aldaz, A.; Feliu, J. M. *Electrochim. Acta* **2005,** *50,* 3111. doi:10.1016/j.electacta.2004.10.086
57. Rodríguez, P.; Herrero, E.; Solla-Gullón, J.; Vidal-Iglesias, F. J.; Aldaz, A.; Feliu, J. M. *Electrochim. Acta* **2005,** *50,* 4308. doi:10.1016/j.electacta.2005.02.087
58. Jusys, Z.; Behm, R. J. *J. Phys. Chem. B* **2001,** *105,* 10874. doi:10.1021/jp011510y

Beilstein Journal of Nanotechnology

Adsorption and oxidation of formaldehyde on a polycrystalline Pt film electrode: An in situ IR spectroscopy search for adsorbed reaction intermediates

Zenonas Jusys* and R. Jürgen Behm

Full Research Paper

Open Access

Address:
Institute of Surface Chemistry and Catalysis, Ulm University, Albert-Einstein-Allee 47, D-89081 Ulm, Germany

Email:
Zenonas Jusys* - zenonas.jusys@uni-ulm.de

* Corresponding author

Keywords:
electrocatalysis; formaldehyde adsorption; formyl intermediate; in situ spectro-electrochemistry; Pt

Beilstein J. Nanotechnol. **2014,** *5,* 747–759.
doi:10.3762/bjnano.5.87

Received: 03 February 2014
Accepted: 30 April 2014
Published: 30 May 2014

This article is part of the Thematic Series "Electrocatalysis on the nm scale".

Associate Editor: J. J. Schneider

Abstract

As part of a mechanistic study of the electrooxidation of C1 molecules we have systematically investigated the dissociative adsorption/oxidation of formaldehyde on a polycrystalline Pt film electrode under experimental conditions optimizing the chance for detecting weakly adsorbed reaction intermediates. Employing in situ IR spectroscopy in an attenuated total reflection configuration (ATR-FTIRS) with p-polarized IR radiation to further improve the signal-to-noise ratio, and using low reaction temperatures (3 °C) and deuterium substitution to slow down the reaction kinetics and to stabilize weakly adsorbed reaction intermediates, we could detect an IR absorption band at 1660 cm^{-1} characteristic for adsorbed formyl intermediates. This assignment is supported by an isotope shift in wave number. Effects of temperature, potential and deuterium substitution on the formation and disappearance of different adsorbed species (CO_{ad}, adsorbed formate, adsorbed formyl), are monitored and quantified. Consequences on the mechanism for dissociative adsorption and oxidation of formaldehyde are discussed.

Introduction

The electrooxidation of organic C1 molecules, in particular of methanol, has been one of the most important topics in electrocatalysis over the last decades, both from a fundamental aspect as a model reaction for the oxidation of more complex organic molecules and because of the potential application of these compounds as fuel in direct oxidation fuel cells [1]. In the meantime, it has been generally accepted that for all three C1 species, methanol, formaldehyde and formic acid, the reaction proceeds in a dual pathway mechanism (methanol oxidation [2-5], formaldehyde oxidation [6], formic acid oxidation [7,8]), with an indirect pathway proceeding via formation and subsequent oxidation of CO_{ad} and a direct pathway, where the reac-

tion leads directly to CO_2. The latter pathway allows the reaction to proceed already at potentials where CO_{ad} electrooxidation is still kinetically inhibited. In addition to complete oxidation to CO_2, partial oxidation of methanol to formaldehyde and formic acid [9-12] and of formaldehyde to formic acid [6] have been identified as well as important contributions. These incomplete oxidation products may sensitively affect the reaction kinetics since they can i) be stepwise oxidized towards the final reaction product via a re-adsorption/further oxidation process [13-15], or ii) dissociatively adsorb to form CO_{ad}, resulting in higher CO_{ad} coverages and hence enhanced surface poisoning [16]. Early in situ IR spectroscopy studies of C1 molecule oxidation had demonstrated the formation of adsorbed CO in the reaction, which was identified as reaction inhibiting side product [17-20]. More recently, Osawa and co-workers [21-26] and later also other groups [27-33] reported the formation of adsorbed, bridge-bonded formate species during oxidation of all three C1 molecules on Pt film electrodes. The role of the adsorbed formate as possible reaction intermediate in formic acid oxidation was addressed extensively in both experimental [21,25-28,34] and theoretical [35-38] studies.

So far, however, the elementary reaction steps and in particular the nature of the reaction intermediate(s) are still under intense debate (see, e.g., [39] and [40]). It is generally accepted that the reaction proceeds via a sequence of dehydrogenation and oxidation steps, as it had been beautifully described in the formal reaction scheme put forward by Bagotzky et al. [41]. Clear experimental evidence for partly dehydrogenated species, e.g., by spectroscopic observation, however, is still missing. In two early in situ IR spectroscopy studies on methanol oxidation, the authors reported the observation of weak bands at 1215 and 1270 cm^{-1}, which they attributed to adsorbed $–CH_xOH$ [42] or –COH [43] intermediates, respectively. In later spectro-electrochemical studies, however, these features could not be reproduced, neither in an external reflection configuration (IRRAS), nor in highly sensitive surface enhanced IR spectroscopy measurements (SEIRAS) in an internal reflection configuration. Finally, the presence of hydrogen in the methanol adsorbate on an emersed polycrystalline Pt electrode was suggested from electrochemical thermal desorption mass spectrometry (ECTDMS) measurements based on the detection of carbon monoxide, hydrogen and traces of carbon dioxide during thermal desorption [44].

In a series of recent studies we have identified adsorbed acetyl with a characteristic band at about 1635 cm^{-1} or related species upon adsorption of higher alcohols on Pt electrodes (ethanol [45], ethylene glycol [46], 1-propanol [47], glycerol [48]) and demonstrated that they act as precursor for CO_{ad} and CO_2 formation. Based on these findings, a similar reaction path, involving the formation of an adsorbed formyl intermediate, may also be expected for adsorption/oxidation of the C1 molecules. Adsorbed formyl species were indeed predicted as reaction intermediates in functional theory based theoretical studies of the interaction of methanol with Pt electrode surfaces, whereas in other studies adsorbed hydroxymethylidyne or adsorbed formaldehyde were suggested as adsorbed reaction intermediates [49-52]. This will be discussed in more detail below.

In the present contribution we want to further explore the formation of reaction intermediates during interaction of C1 molecules with Pt. Based on our results on the adsorption and oxidation of C2 and C3 molecules, where adsorbed acetyl-type species were most clearly visible at potentials up to 0.4 V (vs the reversible hydrogen electrode, RHE) and in the initial stages of the adsorption process, when surface blocking by strongly adsorbed CO_{ad} species is negligible or less pronounced, we followed the initial build-up of adsorbed species upon admission of formaldehyde molecule containing electrolyte to the electrode via in situ ATR-FTIR spectroscopy, optimizing the experimental conditions for the detection of weakly adsorbed reaction intermediates. Since signals of adsorbed acetyl-type species were more pronounced for the adsorption and oxidation of aldehydes than of the corresponding alcohols [45-48,53,54], we will focus here on the interaction of formaldehyde with Pt. Findings of a similar type study on the adsorption and oxidation of formic acid on Pt, where the reaction intermediates are different, will be published elsewhere. The experiments were performed in a thin-layer spectro-electrochemical flow cell [28] at constant potential (0.0–0.4 V), using a thin-film Pt electrode. In order to enhance the sensitivity towards weakly adsorbed reaction intermediates, the experiments were performed employing p-polarized IR radiation to improve the signal-to-noise ratio, and at low reaction temperatures, between room temperature and 3 °C. Low temperatures not only enhance the surface coverage of weakly adsorbed species, but may also increase the time window available for measurements at low CO_{ad} coverage by slowing down the decomposition or further oxidation of the adsorbed reaction intermediate. For the same reason, we also performed comparable measurements using deuterium labeled formaldehyde. In addition, this also provides information on the nature of the adsorbate. The rates of the CO_{ad} build-up were quantified and the kinetic H/D isotope effect in CO_{ad} formation was determined as a function of the electrode potential and temperature.

In the following, we will, after a brief description of the experimental procedures, present time resolved series of ATR-FTIR spectra recorded at different temperatures and potentials and using both H and D labeled compounds. We will compare the

initial spectra to identify the adsorbed intermediates, followed by a discussion of the adsorption spectro-electrochemical transients. We will quantify the initial CO_{ad} formation rates from the respective molecules and their potential dependence to identify temperature effects and kinetic H/D isotope effect in the CO_{ad} formation reaction. Finally, the mechanistic implications of these findings for the C1 oxidation reaction will be discussed.

Results and Discussion

In situ ATR-FTIR spectra upon formaldehyde adsorption and oxidation

The temporal evolution of the ATR-FTIR spectra upon admission of either H2- or D2-formaldehyde to the Pt electrode surface at different temperatures (23 or 3 °C) and selected potentials (0.0 and 0.4 V) is shown in Figure 1. For better comparison, IR spectra acquired about 2 s after the admission of either H2- or D2-formaldehyde to the Pt electrode biased are plotted in Figure 2 for different potentials, isotopomers and temperatures. The temperature and isotope effects are illustrated in Figure 2a and Figure 2b for 0.0 V (2a) and 0.4 V (2b) adsorption potential, while the potential dependence of the initial spectra at 3 °C is depicted for D2- (c) and H2-formaldehyde (d) in Figure 2c and Figure 2d. Since the CO_{ad} coverage in the initial moments is still rather low, it is better possible to resolve bands of weakly adsorbed reaction intermediates, which otherwise may be overgrown by bands related to CO adsorption (see below).

The main characteristics of the spectra acquired at ambient temperature resemble those reported previously for ATR-FTIRS measurements in H_2SO_4 solution [23,24,32,55]. The bands at ca. 2010 cm^{-1} (at 0.0 V) are assigned to linearly bonded adsorbed CO (CO_L), with the exact wave number depending both on the CO_{ad} coverage and the electrode potential [56]. The bands at ca. 1805 cm^{-1} result from multiply bonded CO (CO_M). Bands related to displaced water, coadsorbed interfacial water or both, caused by the build-up of the CO adlayer, appear at wave numbers around 3500 cm^{-1} and at around 1620 cm^{-1} for the stretching and bending modes, respectively, in agreement with previous findings [21,57].

For adsorption at low potentials (0.0 to 0.3 V) and at low temperature, two weak broad positive bands appear at ca. 1420 and 1280 cm^{-1} with some residual intensity in between as well as a single broad band at around 1100 cm^{-1} (Figure 2c and

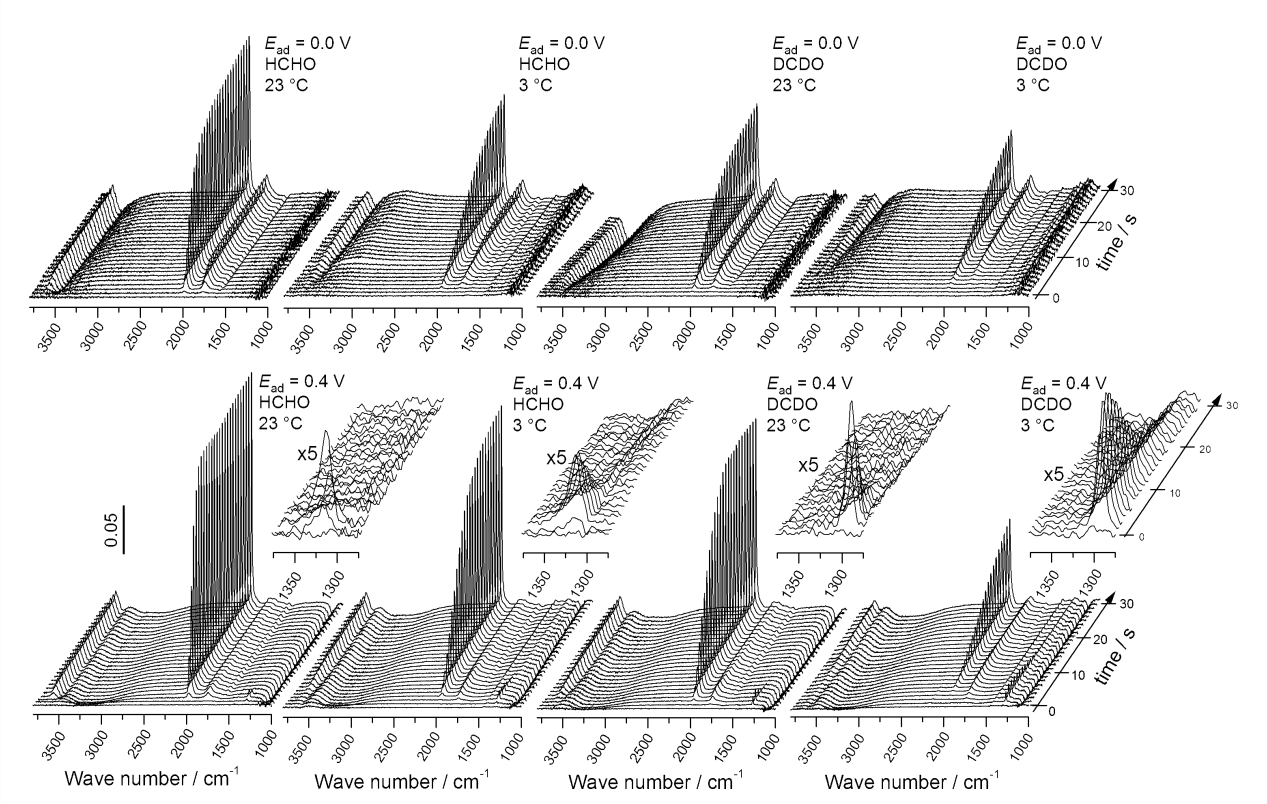

Figure 1: Temporal evolution of the ATR-FTIR spectra upon admission of 0.1 M H2- or D2-formaldehyde solution in 0.5 M $HClO_4$ at 0.0 V (upper panel) or 0.4 V (lower panel) to a Pt film electrode at different temperatures (for notations see figure). Insets: five-fold magnified temporal evolution of adsorbed formate band.

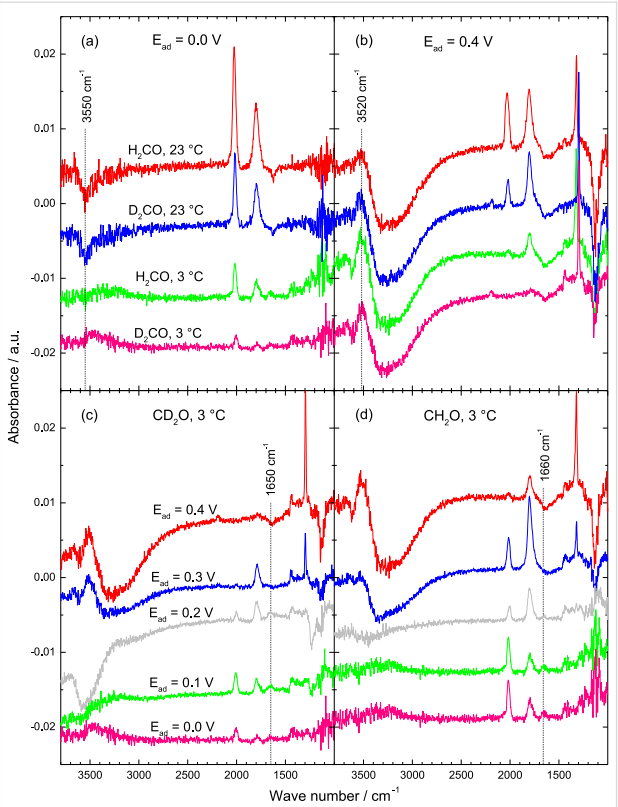

Figure 2: Initial ATR-FTIR spectra acquired ca. 2 s after admission of 0.1 M H2- or D2-formaldehyde solution in 0.5 M $HClO_4$ to a film Pt electrode at: 0.0 V (a) and 0.4 V (b) at 23 and 3 °C; at 0.0, 0.1, 0.2, 0.3 and 0.4 V for 0.1 M D2- (c) or H2-formaldehyde (d) at 3 °C temperature (see figure for notations).

Figure 2d). Bipolar bands at around 1425/1470, and around 1222/1245 cm^{-1} (positive/negative band) were reported previously for formaldehyde oxidation over a Pt(111) electrode [6]. Those authors tentatively assigned them to the symmetric deformation (scissoring) mode of a $–CH_2–$ (or $–O–CH_2$) group for the former and to the C–O stretching mode of a –COH group for the latter band in a methylene glycolate adspecies, which is adsorbed via two oxygen atoms. Due to the rather low intensity of these bands and their broad shape it is not possible to resolve the expected shift in wave number for the isotopomers (Figure 2). Note that these bands were not observed for room temperature adsorption (Figure 2a), although methylene glycol is equally present in the solution (see discussion below). Possible reasons herefore will be discussed below. At 0.3 V, and more strongly at 0.4 V, a pronounced negative band at ca. 1110 cm^{-1} developed, which is associated with the displacement of adsorbed perchlorate species [58]. It should be noted that adsorption of perchlorate was verified also by CO displacements transients, which showed a positive current at 0.1 and 0.2 V (H_{upd} displacement) and below, but a negative current at 0.3 and 0.4 V (adsorbed perchlorate displacement) (see Supporting Information File 1, Figure S1).

A distinct band at ca. 1320 cm^{-1} , which appears at 0.3 V and in particular at 0.4 V, has been assigned to the symmetric O–C–O vibration of a bridge bonded adsorbed formate [23,24,32,55]. This assignment is further supported by the corresponding shift of the band from 1320 to 1295 cm^{-1} when using deuterated formaldehyde (see the magnified insets in Figure 1).

A closer look at the initial IR spectra acquired at low adsorption potential (0.0 to 0.2 V, Figure 2c and Figure 2d) resolves a band at ca. 1650 cm^{-1} for D2-formaldehyde and at around 1660 cm^{-1} for H2-formaldehyde adsorption at 3 °C, which could be assigned to an adsorbed formyl species. A possible assignment of this band to water coadsorbed with CO_{ad} is unlikely due to the negligible CO_{ad} coverage in the initial stages of the adsorption process (see below). The assignment to adsorbed formyl is further supported by the red shift of the band by ca. 10 cm^{-1} upon deuteration of formaldehyde. This very weak band, whose intensity is close to the detection limit of the spectra, appeared reproducibly in a number of different experiments, both at 0.1 and 0.2 V adsorption potential, verifying that it is indeed due to absorption and not reflecting noise in the spectra.

The adsorbed formyl band is slightly less pronounced for adsorption of D2- than for H2-formaldehyde (Figure 2c and Figure 2d), which may reflect a kinetic H/D isotope effect (see section 'Formaldehyde adsorption: CO_{ad} formation rate and the kinetic H/D isotope effect' for kinetic isotope effects in the build-up of CO_{ad}), but the differences are in the limits of the detection and shall therefore not be discussed in more detail at this point. For increasing CO_{ad} coverage, which is rapidly reached for the fast dehydrogenation at ambient temperature (Figure 2a), this peak can not longer be resolved because of its overlap with a negative peak evolving at rather similar wave number. The latter is most likely related to the displacement of water from the surface by CO adsorption (bending mode of displaced water). Finally, in the high wave number region, we find a weak broad negative band at around 3550 cm^{-1}, whose appearance seems to be correlated with the formation of CO_{ad}. Therefore, it is associated with the O–H stretching mode of displaced interface water due to CO adsorption (see below and [58]).

The observation of an adsorbed formyl species agrees perfectly with the clear identification of adsorbed acetyl-type species, with a characteristic band at 1635 cm^{-1}, in a series of recent ATR-FTIR spectroscopy studies for adsorption of higher alcohols and aldehydes. [46-48,59-61]. In those studies, the barrier for C–C bond breaking stabilizes these acetyl-type adspecies against decomposition to CO_{ad}, which allows to reach higher coverages and band intensities of these species. We could

clearly demonstrate, by using deuterium [46,59] or ^{13}C labeling [59,61], that the band is indeed due to adsorbed acetyl species and not caused by water coadsorbed with CO_{ad}. In fact, even the red-shift upon deuteration of ca. 10 cm^{-1} obeserved in the present measurements agrees reasonably well with that obtained for deuterium labeled adsorbed acetyl species [46,59]. In the present case, the more facile C–H bond breaking leads to faster decomposition of the adsorbed formyl species, equivalent to a lower steady-state coverage. Overall, it was only possible to detect this species by combination of highly sensitive spectroscopy (SEIRAS using p-polarized light) and use of reaction conditions which slow down the rate for C–H bond breaking and the coverage of coadsorbed CO (low temperature, CO_{ad} free electrode at the initial stage of the adsorption transient = low CO_{ad} coverage).

The fact that observation and identification of adsorbed formyl species was possible only at low temperature and low potentials (Figure 2a and Figure 2c) implies that these intermediate species are highly reactive towards further dehydrogenation to the final stable state (CO_{ad}). The decomposition to CO_{ad} is obviously slowed down by lowering the reaction temperature, but apparently also by the presence of a high coverage adsorbed hydrogen adlayer at low potentials (0.0 V). The latter may stabilize the adsorbed intermediate by site blocking, leaving no empty sites for CHO_{ad} decomposition [62]. The comparable intensities in CHO_{ad} and CDO_{ad} in combination with the slower build-up of CO_{ad} from the D2-formaldehyde (see section 'Formaldehyde adsorption: CO_{ad} formation rate and the kinetic H/D isotope effect') can be understood if both adsorbed formyl formation and decomposition are slowed down upon deuteration. On an absolute scale, however, the intensity of this band and hence also the coverage of this species are still very low.

Adsorbed formyl species were indeed predicted as reaction intermediates in density functional theory based studies of the interaction of methanol with a Pt(111) surface [50]. The importance of water in the initial steps of dehydrogenation of methanol over Pt(111) via polarization of the hydroxyl due to hydrogen bond formation with a neighboring water molecule was addressed in [63]. This favors the cleavage of the C–H bond upon adsorption in a concerted step, together with the O–H hydrogen transfer to a water molecule, which finally results in an $HCHO_{ad}$ species. Density functional theory based calculations of the energy of dehydrogenation over solvated platinum surfaces were used to approximate the potential-dependent methanol dehydrogenation pathways over different low index Pt electrode surfaces [49]. These calculations revealed pronounced structural effects, in agreement with experimental findings. For Pt(111), they suggested the coexistence of two pathways, where the indirect pathway proceeds via formation of stable CO_{ad}, via an initial exothermic C–H cleavage step to adsorbed hydroxymethyl, which occurs over a wide potential range, and its subsequent exothermic dehydrogenation steps to form CO_{ad}. Another pathway ('incomplete dehydrogenation') was predicted to proceed via an initial O–H cleavage step to form adsorbed methoxy (which is expected to be competitive to C–H cleavage at quite positive potentials), followed by exothermic C–H cleavage to form adsorbed formaldehyde, which can subsequently desorb into solution. Similar type calculations, including water molecules and the electrode potential, implied that methanol dehydrogenation to CO_{ad} via a hydroxymethyl intermediate (initial C–H bond dissociation) is the lowest energy path, whereas the formation of a formaldehyde intermediate (initial C–H bond dissociation) is a minority pathway on a Pt(111) surface at 0.5 V (NHE) [51]. A recent detailed theoretical study on the stability, configuration and interconversion of formyl (CHO) and hydroxymethylidyne (COH) adsorbed on Pt(111) under a water bilayer suggested that CHO_{ad} is the only (meta-)stable form under these conditions, while the COH_{ad} configuration dissociates easily to CO_{ad} + H [52]. For CHO_{ad} on a bridge site under a water bilayer, only a single C–O bond vibration was calculated at wave numbers of 1250 cm^{-1} [52].

For an adsorption potential of 0.4 V (Figure 2b), the initial IR spectra exhibit distinct differences compared to the spectra recorded at lower potentials (0.0–0.2 V). This includes significantly less intense CO_{ad} related bands, a sharp positive band at around 1320 cm^{-1}, and a negative band at 1100 cm^{-1}, where the latter two are attributed (see discussion above) to bridge-bonded adsorbed formate and to displaced adsorbed perchlorate species, respectively. In the high wave number region, an apparently bipolar feature appears, with a pronounced broad negative feature in the range from ca. 2500 to 3500 cm^{-1} and a positive component developed at about 3520 cm^{-1} (Figure 2b). These two features are distinctly different from the weak negative band formed at lower potentials at 3550 cm^{-1} (Figure 2a). According to Osawa et al., the new bipolar feature can be explained by a positive band centered at 3550 cm^{-1} (water coadsorbed with CO_{ad}) superimposed on a broad negative band of the displaced water, which ranges from ca. 3700 to 2500 cm^{-1} [58]. For the present spectra, the positive peak may be due to water coadsorbed with adsorbed formates, since in the early stages (Figure 2b) the CO_{ad} coverages are negligible. This latter idea is supported by the fact that the spectral characteristics in this region are clearly different from those developed upon adsorption of CO dissolved in the solution, as found from comparison with the initial IR spectrum acquired upon adsorption of dissolved CO (see Supporting Information File 1, Figure S2). It should be noted that the wave number of this band (3520 cm^{-1}) is close to the value of around 3635 cm^{-1} predicted

(calculated) for the OH stretching mode of hydroxymethylidyne adsorbed on Pt(111) [52].

At this potential, there is no indication of any band at ca. 1660 cm^{-1} related to adsorbed formyl species (Figure 2a), despite of the much lower CO_{ad} coverage at short exposure times (Figure 2b, 2c and 2d). In this case, however, the rapid formation of adsorbed formates may lead to a negative band in this spectral range, due to displacement of interfacial water, which makes it impossible to resolve a possibly existent peak of adsorbed formyl in the early stages of the adsorption transient, despite of a very low CO_{ad} coverage. Hence, from the present data we can not decide, whether the missing band at 1660 cm^{-1} reflects the absence of adsorbed formyl species under these adsorption conditions or whether their signal is just overcompensated by the negative band of the displaced interfacial water.

Additional mechanistic insight comes from the time and potential dependent appearance and disappearance of the different features in these sequences of spectra. The transient appearance of the adsorbed formate band during the initial stages of formaldehyde admission to the Pt electrode surface at 0.3 V and 0.4 V (see the magnified insets in Figure 1 and transients in Figure 3) clearly indicates formaldehyde oxidation to formic acid under these conditions. Interestingly, the time span during which adsorbed formate is present on the surface correlates with the rate of CO_{ad} formation, with a longer presence of the formate band at a smaller CO_{ad} formation rate. The latter is reduced both by a lower adsorption temperature and/or by using deuterated formaldehyde. For the adsorption of D2-formaldehyde at 3 °C the adsorbed formate band exists over more than 10 seconds, whereas for H2-formaldehyde at 23 °C it instantaneously appears and vanishes within 1–2 seconds, together with a much faster CO_{ad} build-up. The transient appearance of adsorbed formate species is most easily explained by a mechanism where adsorbed CO increasingly blocks the surface for adsorption of the less strongly adsorbed formates. In agreement with that mechanism, the adsorbed formate band has essentially disappeared when a critical CO_{ad} coverage is reached, which is around 60% of the CO_{ad} saturation coverage independent of temperature and isotopomer.

The oxidation of formaldehyde to formic acid requires the addition of oxygen from the dissociative electrosorption of water, which, in contrast to Pt(100) [64], can essentially be ruled out on a polycrystalline Pt electrode at this low potential [65]. The absence of reactive OH_{ad} species on the electrode surface at these potentials can also be concluded from the constant CO_{ad} coverage after the adsorption transients, as evidenced by the unchanged CO_{ad} band intensity and wave number after switching back to the supporting electrolyte, between adsorption transients and subsequent CO_{ad} stripping experiments. Alternatively, one could envision a reaction pathway proceeding via adsorption of methylene glycol species, which are formed by hydration of formaldehyde in the solution phase [66,67]. Methylene glycol can be oxidized to adsorbed formates (formic acid) via a dehydrogenation step [6], without the need for OH_{ad} species. It is well known for methanol [4] and a series of higher alcohols that their dissociative adsorption on Pt surfaces is hindered by H_{upd} [45-48,60,61]. Correspondingly, one would expect that adsorption of methylene glycol is also inhibited by H_{upd}, blocking also oxidation of methylene glycol to formic acid at high H_{upd} coverages (low potentials). This fully agrees with the experimental findings, where the adsorbed formate band is absent for formaldehyde adsorption at <0.3 V (Figure 1).

The formic acid formed upon adsorption and oxidation of the hydrated form of formaldehyde can be further oxidized to CO_2. This was demonstrated by the transient CO_2 formation upon adsorption of formaldehyde on a Pt electrode at ambient temperature at potentials of 0.3 and 0.4 V [32], where CO_2 formation via an indirect pathway can be neglected. On the other hand, the strongly adsorbing carbonyl functional group of non-hydrated formaldehyde enables the dissociative adsorption to form CO_{ad} even at low potentials, e.g., via displacement of H_{upd}. At 0.4 V, where there is no more H_{upd} blocking, methylene glycol can also dissociatively adsorb to form CO_{ad}, via dissociation of two C–H bonds, assuming that it behaves similarly as other alcohols [45-48,60,61]. In addition, however, it could be oxidized to formic acid, which requires dissociation of a single C–H bond only, in an apparently facile dehydrogenation step.

Similar trends were also reported for the competing adsorption of formaldehyde and methanol using mixtures of carbon-labelled formaldehyde and methanol, which revealed a prevailing CO_{ad} formation from formaldehyde at low potentials (H_{upd} region), whereas in the double-layer region methanol was the dominant source for CO_{ad} formation [16]. Likewise, combining alcohol and aldehyde functional groups at different carbon atoms in a single molecule, in glycoladehyde, we obtained facile CO_{ad} formation at both low and high potential [68].

Overall, our data strongly support the idea that for understanding the interaction of formaldehyde with Pt electrodes, the coexistence of both the non-hydrated and hydrated form of formaldehyde in the bulk solution has to be considered. This is most clearly evident from the different trends in the potential dependence in formic acid (CO_2 formation) and in CO_{ad} formation, which was discussed above. In that case, the (possible) absence of the band related to adsorbed formyl, the lower CO_{ad}

coverage, and the transient appearance of adsorbed formates at 0.3 V and more pronounced at 0.4 V in combination may be explained by a simple mechanism, where dehydrogenation of formaldehyde to form CO_{ad}, which prevails at low potentials and proceeds via adsorbed formyl, is partly replaced by oxidation of the hydrated form of formaldehyde (methylene glycol) to formic acid at 0.3 and 0.4 V. The reaction proceeds until it is stopped by CO_{ad} development.

Further mechanistic insight comes from the absence of isotope mixing in adsorbed formates resulting from adsorption of D2-formaldehyde. If desorption of adsorbed formyl species were possible via re-hydrogenation and subsequent desorption of the resulting adsorbed formaldehyde, re-hydrogenation of CDO_{ad} by protons (from water) should result in the formation of a mixed D1H1-formaldehyde. Its subsequent hydration to D1H1-methylene glycol and re-adsorption and oxidation to formic acid would result in a mixture of both D1- and H1-formate species. Within the detection limits, this does not seem to be the case (see the magnified insets in Figure 1, and Figure 2b, where only a single band of D1-formate is resolved). Therefore, desorption of the formyl intermediate as formaldehyde (as a possible reason for the absence of the band at 1650 cm^{-1} for D2-formaldehyde adsorption at 0.3 (0.4) V and 3 °C in Figure 2c) is unlikely because of the absence of an adsorbed H1-formate isotopomer, at least at significant rates.

Formaldehyde adsorption and oxidation transients

The initial Faradaic current transients (upper panel) as well as the temporal evolution of the integral absorbances of linearly bonded CO_{ad} (CO_L, middle panel) and of bridge-bonded formate (bottom panel) obtained upon the admission of H2- (Figure 3a–f) or D2- (Figure 3g–l) formaldehyde to the Pt electrode (at about 10 s) are plotted in Figure 3. The electrode was biased at constant potentials of 0.0, 0.1, 0.2, 0.3 and 0.4 V, the data were recorded at room temperature (Figure 3a–c and Figure 3g–i) and 3 °C (Figure 3d–f and Figure 3j–l). The integral absorbances were evaluated from sequences of IR spectra, which were shown for representative potentials of 0.0 and 0.4 V in Figure 1.

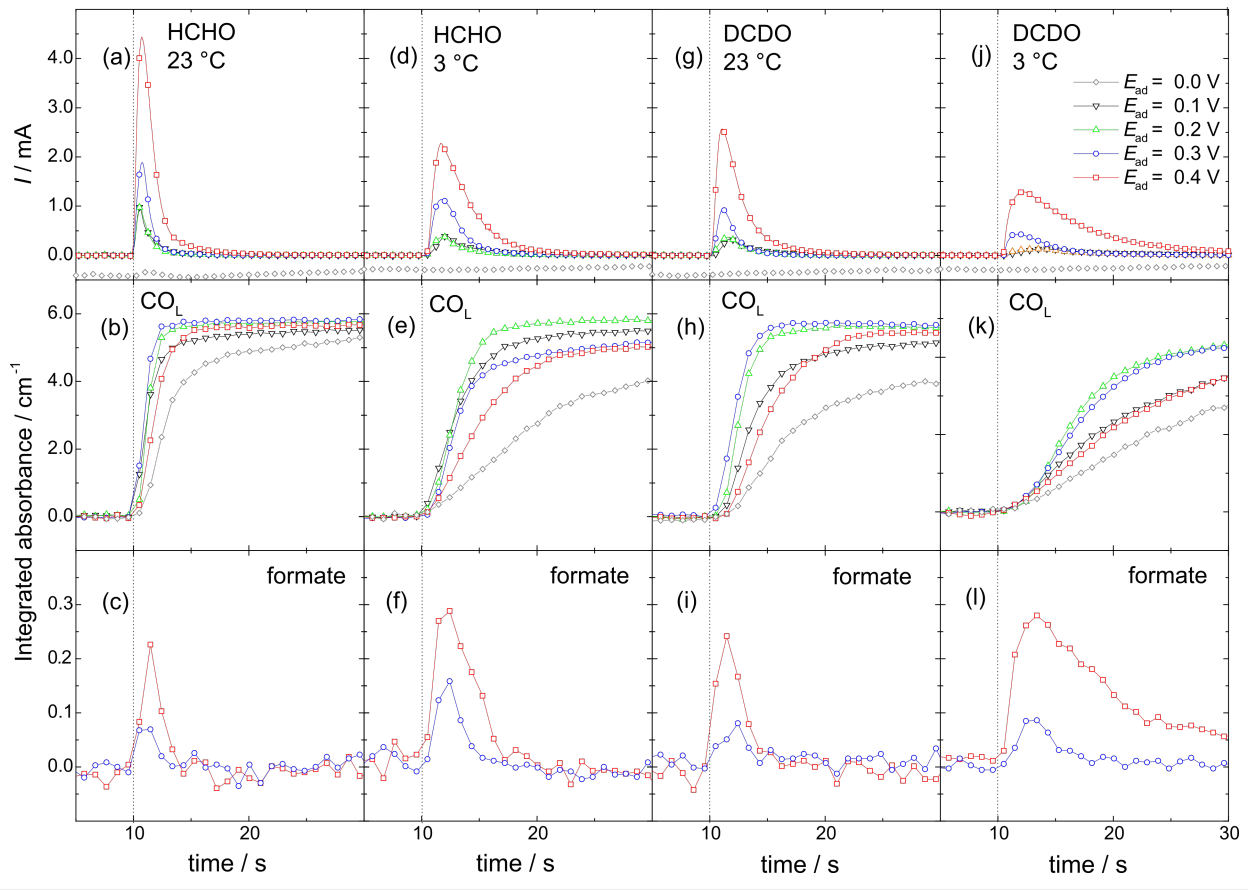

Figure 3: Transients of Faradaic current (upper panel) and integrated intensities of linearly bonded CO_{ad} (middle panel) and adsorbed bridge-bonded formate (for 0.3 and 0.4 V only) bands upon admission of 0.1 M H2- or D2-formaldehyde solution in 0.5 M $HClO_4$ to a Pt film electrode biased at 0.0, 0.1, 0.2, 0.3 and 0.4 V at 23 or 3 °C temperature (see figure for notations).

In general, the transients are similar to those recorded for formaldehyde adsorption in sulfuric acid solution at ambient temperature [16,32,55]. For adsorption at 0.0 V, the Faradaic current is governed by contributions from hydrogen evolution. The latter slightly decays with time, which can be explained by a build-up of CO_{ad} from dissociative adsorption of formaldehyde (see below). For potentials between 0.1 and 0.4 V, the Faradaic current increases steeply upon the admission of formaldehyde, passes a pronounced maximum and then decays in an approximately exponential form to zero. The Faradaic current peaks are highest and narrowest for H2-formaldehyde adsorption at ambient temperature. Both the temperature decrease and/or deuteration lead to lower maxima and peak broadening. The peak shape of the Faradaic current transients, specifically the decay after passing the maximum, indicates an increasing surface poisoning, most likely by the CO_{ad} resulting from the dissociative adsorption of formaldehyde. This is confirmed by the IR spectroscopy data (see CO_L transients below). The data presented so far clearly indicate that the Faradaic current peak results from at least three contributions: i) displacement of H_{upd} or adsorbed ClO_4 species, depending on the adsorption potential, ii) the formation of CO_{ad} from adsorbed formaldehyde or methylene glycol, and iii) oxidation of adsorbed formaldehyde (methylene glycol) to adsorbed formates or formic acid and eventually to CO_2. Formation of CO_{ad} from adsorbed formaldehyde will release two electrons upon formation of one CO_{ad} molecule, displacement of H_{upd} or adsorbed ClO_4 will release (consume) one electron per atom (molecule), oxidation to formate or formic acid will release two electrons per molecule, and oxidation to CO_2 four electrons per molecule. Because of the largely unknown product yields, in particular the yields of formic acid and CO_2 are unknown in these experiments, it is not possible to identify and quantify the contributions from the different product formation rates, in particular at 0.3 V and higher, where formate, formic acid, and CO_2 formation contribute increasingly. Nevertheless, due to the accumulation of reaction inhibiting CO_{ad}, which can not be oxidized at these potentials (≤0.4 V), the Faradaic current eventually decreases to zero.

The integrated intensities of the CO_L band plotted in the middle row of Figure 3 show a fast increase upon admission of the formaldehyde containing solution to the Pt film electrode, indicating an instantaneous onset of dissociative formaldehyde adsorption. For H2-formaldehyde adsorption at room temperature (Figure 3b), they approach saturation within a few seconds, except for 0.4 V where it takes a bit longer, whereas for the lower temperature and/or deuteration of formaldehyde the CO_{ad} build-up is slower, so that saturation may not be reached during the time of the transient (middle panel of Figure 3). Looking at the potential dependence, CO_{ad} formation seems to be fastest at 0.1–0.3 V, and is somewhat slower for higher and lower potentials. Importantly, the rate of the CO_{ad} development is clearly correlated with the width of the Faradaic current transients, which will be discussed below. It should be noted that the CO_{ad} formation due to dissociative adsorption of formaldehyde at 0.0 V decreases the current for hydrogen evolution only slightly (see above). Apparently, an efficient hydrogen evolution is possible even on largely CO_{ad} blocked electrode [69].

The integrated intensities of the bridge bonded adsorbed formate band are plotted in the lower panel of Figure 3 for 0.3 and 0.4 V adsorption potentials (for lower potentials the formate band is not resolved and therefore they are not included). As discussed before (see previous section), the transient appearance of the adsorbed formate band at these low potentials supports a mechanism where formaldehyde oxidation to formic acid proceeds via the hydrated form of formaldehyde (methylene glycol) and its interaction with the initially adsorbate-free electrode. At lower potentials, the electrode surface is largely blocked by H_{upd}, which inhibits the adsorption of alcohols [45-48,60,61] and thus the adsorption of methylene glycol.

The integrated absorbance of adsorbed formate (at adsorption potentials of 0.3 and 0.4 V) develops instantaneously upon exposure of the electrode to the reactant (Figure 3, bottom panel). After passing through a maximum, it decreases again until reaching the background level. As mentioned above, the duration of the adsorbed formate appearance is strictly correlated with the initial rate for CO_{ad} formation. It is shortest for the fastest CO_{ad} build-up (H2-formaldehyde adsorption at 23 °C, Figure 3a–c) and longest for the slowest build-up of CO_{ad} (D2-formaldehyde adsorption at 3 °C, Figure 3j–l). The transient appearance of the adsorbed formate species is typical of a self-poisoning behavior, in this case by adsorbed CO. which can displace the rather weakly bonded adsorbed formate species (see also the displacement of weakly adsorbed perchlorate indicated by the negative band at 0.3 and 0.4 V adsorption potential, Figure 1 and Figure 2b–d) and block the sites required for the further dehydrogenation of methylene glycol to formic acid [70]. Therefore, the adsorbed formate species should be considered as an indicator of methylene glycol oxidation to formic acid rather than as an active intermediate in formaldehyde oxidation to CO_2, as had been suggested earlier [23,24]. The active intermediate in this case are adsorbed methylene glycolates. The oxidation of methylene glycol to formic acid is responsible for the ongoing Faradaic current during the build-up of CO_{ad} at 0.3 and in particular at 0.4 V. Accordingly, the total charge in the Faradaic current transient is highest for the adsorption of D2-formaldehyde at low temperature at 0.4 V (see Figure 3j–l), where the build-up of CO_{ad} is slowest.

Formaldehyde adsorption: CO_{ad} formation rate and the kinetic H/D isotope effect

Figure 4 shows the potential dependence of i) the initial rates of the CO_{ad} build-up upon admission of the reacting molecule to the electrode surface (a), and of ii) the kinetic H/D isotope effect (b) found as the ratio of the initial rates for CO_{ad} build-up from the corresponding isotopomers H2- and D2-formaldehyde at 23 and 3 °C. The initial CO_{ad} formation rates were determined from the CO_L intensity increase (see Experimental section). In general, the rates for CO_{ad} formation from the dissociative adsorption of formaldehyde show a substantial effect of the adsorption potential, with lower values at 0.0 and 0.4 V, and higher values in the range 0.1–0.3 V. Furthermore, they decrease to about half upon lowering the temperature to 3 °C or upon deuteration of the C–H bond (Figure 4a). The ability of formaldehyde to dissociatively adsorb even on a largely H_{upd} covered Pt surface is related to the strong affinity of the carbonyl group (aldehyde function) to interact with metal surfaces, which was also found for a number of higher aldehydes [45,47,48,71]. Only at very high coverages of H_{upd}, as reached at 0.0 V and bulk evolution of H_2, the rate for dissociative formaldehyde decreases significantly. The metal–carbonyl interaction is sufficiently strong to displace reversibly adsorbed H_{upd} [45,47,48,68,72], which allows dehydrogenation of adsorbed formaldehyde molecules to CO_{ad} also on H_{upd} covered surfaces. The less pronounced decrease in the initial CO_{ad} formation rate at 0.4 V could be interpreted as result of a competing oxidation of hydrated formaldehyde (methylene glycol) to formic acid as discussed above, thereby lowering the CO_{ad} formation rate (from adsorbed formaldehyde).

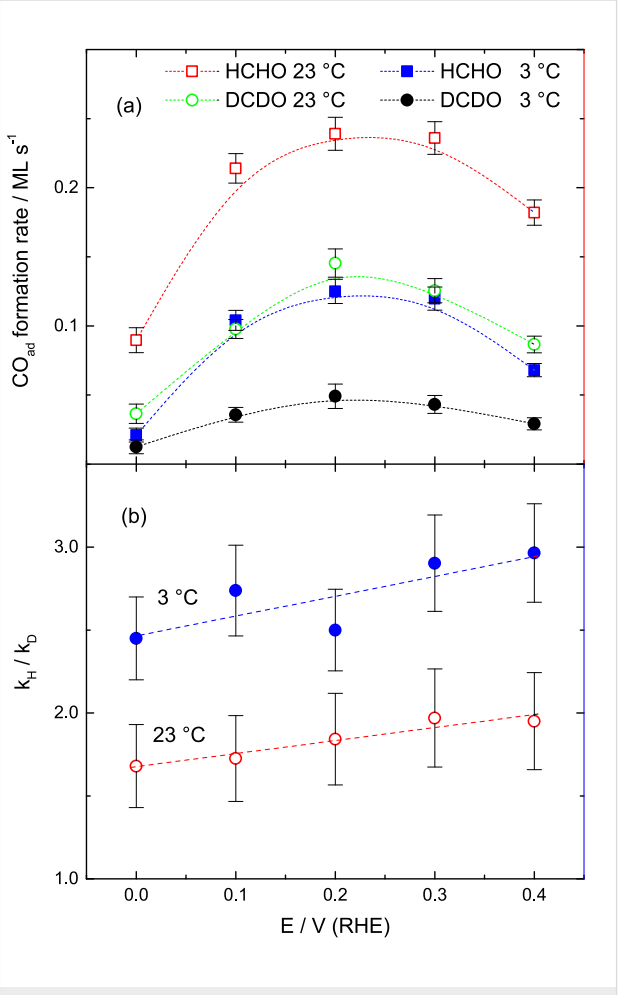

Figure 4: Initial CO_{ad} formation rates (a) and kinetic isotope effects for the CO_{ad} formation (b) upon admission of 0.1 M H2- or D2-formaldehyde to a Pt film electrode in 0.5 M $HClO_4$ at different potentials and temperatures (see figure for notations). Lines are included to guide the eye.

The decrease in the CO_{ad} formation rate upon formaldehyde dehydrogenation with temperature indicates a thermal activation of the C–H bond dissociation, whereas the decrease in the CO_{ad} formation rate upon deuterium substitution implies a primary kinetic H/D isotope effect (k_H/k_D). The observation of a kinetic isotope effect means that the C–H bond splitting appears in the rate determining step, which is either the first or the second hydrogen split-off. Previous theoretical work predicted a nearly barrier free spontaneous subtraction of the first hydrogen from adsorbed formaldehyde and a somewhat higher energy barrier for the dehydrogenation of the resulting adsorbed formyl [73]. This agrees with the experimental finding of adsorbed formyl species in the present work, since a fast dissociation of the second hydrogen would lead to a negligible coverage of the adsorbed intermediate.

The experimental k_H/k_D values, which are plotted in Figure 4b, range around 1.9 ± 0.4 for 23 °C and around 2.8 ± 0.5 for 3 °C, with slightly lower values at lower potentials. Importantly, the change of the selectivity in the dehydrogenation reaction from complete dehydrogenation (to CO_{ad}) at low potentials to incomplete dehydrogenation (to formic acid) at higher potentials does not induce any significant change in the k_H/k_D values, indicating that in both cases the C–H bond dissociation appears in the rate determining step.

The higher value of the kinetic H/D effect at lower temperature indicates a larger slow down of the C–D dissociation vs that for the C–H bond, as expected for a higher activation barrier.

Mechanistic implications

The results presented and discussed in the previous three sections lead us to the following conclusions on the interaction of formaldehyde with Pt:

1. An IR band compatible with an adsorbed formyl species, at ca. 1660 cm^{-1}, was detected for the first time for formaldehyde

adsorption as a band appearing at low potentials and low temperature (ca. 3 °C) in the initial stage of the adsorption (at very low CO_{ad} coverage). The assignment of this band to adsorbed formyl species is supported by the isotopic shift of the band to lower wave numbers upon D-labelling. Similarly to the adsorbed acetyl-type reaction intermediates, which we had identified during adsorption/oxidation of higher alcohols and aldehydes, the adsorbed formyl is proposed to act as precursor for CO_{ad} formation in formaldehyde adsorption, although we can not say from the present data whether this process proceeds directly or via interconversion to adsorbed hydroxymethylidyne. Although we can not detect the band assigned to adsorbed formyl at 0.4 V and higher potentials, due to the overlap with the negative band caused by displaced water (see Figure 2b–d), assumably, this pathway for CO_{ad} formation upon formaldehyde adsorption is active also at higher potentials.

2. Adsorbed formyl species are formed by dehydrogenation of adsorbed formaldehyde, according to $HCHO \rightarrow [HCHO]_{ad} \rightarrow CHO_{ad} + H^+ + e^-$. The other possible precursor, hydroxymethylidyne, does not interact sufficiently strong with Pt to be able to displace adsorbed H_{upd} at the low potentials where the adsorbed formyl species are detected (see also point 4).

3. The much lower absorption intensity and hence lower coverage of the adsorbed formyl species compared to that of the adsorbed acetyl-like species detected during adsorption/oxidation of longer chain alcohols/aldehydes is most easily understood by a lower barrier for C–H bond breaking for adsorbed formyl decomposition to CO_{ad} than that for C–C bond breaking required for adsorbed acetyl-type species, which leads to faster CO_{ad} formation and hence a lower steady-state coverage of adsorbed formyl species.

4. Oxidation of formaldehyde to formic acid on an adsorbate free Pt electrode is possible at potentials as low as 0.3 V, as evidenced by the transient observation of adsorbed bridge bonded formates in the initial stage of formaldehyde exposure to Pt. At later stages, the reaction is increasingly inhibited by CO_{ad} surface blocking. Considering that formation of active oxygen species from water is impossible at these potentials, we propose that under these conditions the reaction proceeds via dehydrogenation of adsorbed hydrated formaldehyde (methylene glycole), via $OH\text{-}CH_2\text{-}OH \rightarrow [\text{reaction intermediate}]_{ad} \rightarrow HCOOH + 2H^+ + 2e^-$. This is supported by the observation that at lower potentials this reaction is inhibited, since dissociative adsorption of alcohols on Pt is well known to be inhibited by adsorbed H_{upd}.

5. The kinetic isotope effect with k_H/k_D values of 1.9 ± 0.4 at 23 °C and 2.8 ± 0.5 at 3 °C in the initial CO_{ad} formation implies that C–H bond dissociation plays an important role in the rate-determining step for this process. The resulting k_H/k_D values exhibit no distinct potential dependence, despite of a pronounced potential dependence in the initial CO_{ad} formation rate in the range 0.0 to 0.4 V, indicating that the change of the dehydrogenation reaction selectivity from complete dehydrogenation (to CO_{ad}) at low potentials to incomplete dehydrogenation (to formic acid) at higher potentials does not induce any significant change in the k_H/k_D values. This in turn indicates that in both cases the C–H bond dissociation represents the rate determining step. The higher values of the kinetic H/D effect at lower temperature indicate a higher barrier for C–D dissociation than for C–H bond dissociation.

At present, we have no indication for pathways for formaldehyde oxidation to CO_2 other than via re-adsorption and further oxidation of formic acid or via oxidation of CO_{ad} (indirect pathway), although such direct pathways, e.g., via an adsorbed formyl assisted interaction and reaction with adjacent H_2O molecules, can not be ruled out. Calculations covering such scenarios are highly desirable and have been initiated.

Conclusion

In an effort to identify possible reaction intermediates in the formaldehyde oxidation reaction on Pt and their role in the reaction, we have investigated the interaction of formaldehyde with a polycrystalline Pt film electrode in the range of low potentials, up to 0.4 V, where the oxidation of CO_{ad} formed to CO_2 (indirect pathway) can be excluded. Employing in situ IR spectroscopy in an attenuated total reflection configuration (ATR-FTIRS) in a thin-layer flow cell, which allows for quick and efficient electrolyte exchange, the formation and disappearance of adsorbed species was monitored during spectro-electrochemical transients. The main results of measurements performed at low temperatures (3 °C) and using deuterium substitution in the C–H bond to optimize conditions for stabilizing weakly adsorbed reaction intermediates are: First, spectra obtained at low potentials indicate the existence of an adsorbed formyl intermediate, which is sufficiently strongly adsorbed to not be displaced by H_{upd}. This is in agreement with the adsorbed acetyl type reaction intermediate observed for higher alcohols and aldehydes, where the latter species was detected and identified as reaction intermediate for CO_{ad} formation. At higher CO_{ad} coverages/potentials this species is not detected any more since it is either increasingly displaced by CO_{ad} or because the signal is overgrown by a negative band due to CO_{ad} induced displacement of water from the interface. Second, the transient formation of formic acid/adsorbed formate upon interaction of formaldehyde with adsorbate free Pt already at potentials as low as 0.3 V, where reactive oxygen formation from H_2O can be excluded, points to a mechanism where the reaction proceeds

via dehydrogenation of the hydrated form of formaldehyde (methylene glycol) at these potentials. This is supported by the observation that at lower potentials formic acid/adsorbed formate formation is inhibited, but not CO_{ad} formation, if the first reaction proceeds via adsorption of a weakly adsorbed alcohol (diol) species, which is known to be inhibited by a H_{upd} adlayer, while the latter starts from adsorption of a more strongly interacting aldehyde, which is possible also on a H_{upd} blocked surface.

Experimental

The spectroscopy measurements were performed in a thin-layer flow cell in an attenuated total reflection (ATR) configuration described in detail in [28,32,74]. The cell was equipped with two Pt counter electrodes, located at the inlet and the outlet of the cell, respectively. A reversible hydrogen electrode (RHE) reference operated at ambient temperature was connected to the outlet of the cell via a Teflon capillary. To enable electrolyte exchange, two separate electrolyte supply bottles containing the supporting electrolyte (0.5 M $HClO_4$) and 0.1 M formaldehyde solution in the same supporting electrolyte, respectively, were connected to the common inlet port. The electrolyte flow (ca. 50 μL s^{-1}) was driven by the hydrostatic pressure of the supply bottles. The solutions were deareated by purging with high purity N_2. The temperature of the electrolyte in the glass jacketed and thermally isolated electrolyte bottles was controlled by a cryostat (Huber Compatible Control CC1, filled with Cryo30 - Lauda), which was set to −10 °C. This allowed to keep the electrolyte temperature in the thermostated supply bottles at ca. −5 °C. The resulting temperature in the non-thermostated flow cell, which was continuously flushed with the electrolyte, was slightly higher, around 3 °C, due to the heat transfer from the surroundings.

The Pt-film working electrode was prepared by electroless deposition of Pt [21] on the flat side of a semi-cylindrical Si prism. The working electrode was pressed against the planar Kel-F cell body via a circular gasket (ca. 0.1 mm thickness, inner diameter 12 mm, exposed electrode area ca. 1 cm^2, roughness factor ca. 5) to obtain a thin layer of electrolyte which can be effectively exchanged and allows a well defined mass transport from the inlet capillary positioned in the center of the cell body to six surrounding outlet capillaries located at the perimeter of the gasket [75]. The potential was controlled by a Pine Instruments potentiostate (Model AFRDE5).

The electrode surface was cleaned by cycling the potential between 0.06 and 1.5 V in 0.5 M $HClO_4$ at 100 mV s^{-1} scan rate, until the typical features of the Pt base cyclic voltammogram (CV) [76] were reproduced. The potential was then stopped at the desired adsorption potential in the negative-going scan and the electrolyte was switched to a 0.1 M solution of formaldehyde in 0.5 M $HClO_4$ for 3 min and then back to the supporting electrolyte. The supporting electrolyte was 0.5 M $HClO_4$, prepared from suprapure perchloric acid (Merck) and from Millipore MilliQ-water (18.2 MΩ cm), for formaldehyde solution we used an aqueous solution of paraformaldehyde (methanol-free, 16 wt % (Alfa Aesar)) for H-labelled formaldehyde and D2-paraformaldehyde (98 D%, Isotec) for D-labelled formaldehyde, respectively. To prepare the D2-formaldehyde solution, a proper amount of D2-paraformaldehyde was first dissolved in hot (ca. 80 °C) high purity water, then cooled down and diluted by 0.5 M $HClO_4$ to achieve a proper concentration.

For the ATR-FTIRS measurements we used a homemade mirror accessory within the sample chamber of a Varian 670i IR-spectrometer, equipped with a liquid nitrogen cooled mercury cadmium telluride (MCT) detector and an automated AutoPro5 polarizer set to 90° angle to transmit only surface-sensitive p-polarized radiation from the light source. The spectral resolution was set to 4 cm^{-1}, the temporal resolution was 1 s per spectrum (co-adding 5 interferograms). The absorbance was calculated as $A = -\log(R/R_0)$, with R representing the measured reflected intensity in the respective experiments, while R_0 describes the reflected intensities in pure supporting electrolyte at the respective adsorption potential. This results in positive bands for increased absorbance.

The quantitative evaluation of the CO_{ad} formation rates upon formic acid adsorption was based on the CO_{ad} intensity – CO_{ad} coverage relation derived in potential dependent calibration measurements performed earlier, where the IR band intensity of linearly bonded CO was related to the CO_{ad} coverage determined mass spectrometrically via the partial pressure change in CO upon adsorption of CO dissolved in the electrolyte at constant potential [77]. This gives a linear relation between CO_{ad} coverage and the absorbance of linearly adsorbed CO in the coverage range from 8 to 70% of the saturation coverage [59]. Accordingly, rates for CO_{ad} formation were evaluated from the slope of the intensity increase of the linearly bonded adsorbed CO with time at coverages >8% of the saturation coverage.

Supporting Information

Supporting Information File 1

CO adsorption transients and ATR-FTIR spectra at different potentials.
[http://www.beilstein-journals.org/bjnano/content/supplementary/2190-4286-5-87-S1.pdf]

Acknowledgements

Financial support by Deutsche Forschungsgemeinschaft (Research Unit FOR 1376, project JU 2781/2-1) is gratefully acknowledged.

References

1. Braunschweig, B.; Hibbitts, D.; Neurock, M.; Wieckowski, A. *Catal. Today* **2013,** *202,* 197–209. doi:10.1016/j.cattod.2012.08.013
2. Herrero, E.; Chrzanowski, W.; Wieckowski, A. *J. Phys. Chem.* **1995,** *99,* 10423–10424. doi:10.1021/j100025a054
3. Jarvi, T. D.; Stuve, E. M. Chapter 3. *Electrocatalysis;* Wiley-VCH: Heidelberg, Germany, 1998; pp 75–153.
4. Jusys, Z.; Behm, R. J. *J. Phys. Chem. B* **2001,** *105,* 10874–10883. doi:10.1021/jp011510y
5. Iwasita, T. Chapter 41. *Electrocatalysis;* Handbook of Fuel Cells, Vol. 2; John Wiley & Sons: Chichester, U.K., 2003; pp 603–624.
6. Batista, E. A.; Iwasita, T. *Langmuir* **2006,** *22,* 7912–7916. doi:10.1021/la061182z
7. Capon, A.; Parsons, R. *J. Electroanal. Chem. Interfacial Electrochem.* **1973,** *44,* 239–254. doi:10.1016/S0022-0728(73)80250-5
8. Parsons, R.; VanderNoot, T. *J. Electroanal. Chem. Interfacial Electrochem.* **1988,** *257,* 9–45. doi:10.1016/0022-0728(88)87028-1
9. Ota, K.-I.; Nakagawa, Y.; Takahashi, M. *J. Electroanal. Chem. Interfacial Electrochem.* **1984,** *179,* 179–186. doi:10.1016/S0022-0728(84)80286-7
10. Batista, E. A.; Malpass, G. R. P.; Motheo, A. J.; Iwasita, T. *Electrochem. Commun.* **2003,** *5,* 843–846. doi:10.1016/j.elecom.2003.08.010
11. Batista, E. A.; Malpass, G. R. P.; Motheo, A. J.; Iwasita, T. *J. Electroanal. Chem.* **2004,** *571,* 273–282. doi:10.1016/j.jelechem.2004.05.016
12. Zhao, W.; Jusys, Z.; Behm, R. J. *Anal. Chem.* **2012,** *84,* 5479–5483. doi:10.1021/ac203276f
13. Jusys, Z.; Kaiser, J.; Behm, R. J. *Langmuir* **2003,** *19,* 6759–6769. doi:10.1021/la020932b
14. Seidel, Y. E.; Schneider, A.; Jusys, Z.; Wickman, B.; Kasemo, B.; Behm, R. J. *Faraday Discuss.* **2009,** *140,* 167–184. doi:10.1039/b806437g
15. Seidel, Y. E.; Schneider, A.; Jusys, Z.; Wickman, B.; Kasemo, B.; Behm, R. J. *Langmuir* **2010,** *26,* 3569–3578. doi:10.1021/la902962g
16. Reichert, R.; Schnaidt, J.; Jusys, Z.; Behm, R. J. *ChemPhysChem* **2013,** *14,* 3678–3681. doi:10.1002/cphc.201300726
17. Lamy, C.; Léger, J.-M.; Clavilier, J.; Parsons, R. *J. Electroanal. Chem. Interfacial Electrochem.* **1983,** *150,* 71–77. doi:10.1016/S0022-0728(83)80191-0
18. Kunimatsu, K. *J. Electroanal. Chem. Interfacial Electrochem.* **1987,** *218,* 155–172. doi:10.1016/0022-0728(87)87013-4
19. Sun, S. G.; Clavilier, J. *J. Electroanal. Chem. Interfacial Electrochem.* **1988,** *240,* 147–159. doi:10.1016/0022-0728(88)80319-X
20. Lopes, M. I.; Fonseca, I. *J. Electroanal. Chem.* **1993,** *346,* 415–432. doi:10.1016/0022-0728(93)85028-F
21. Miki, A.; Ye, S.; Osawa, M. *Chem. Commun.* **2002,** 1500–1501. doi:10.1039/B203392E
22. Chen, Y. X.; Miki, A.; Ye, S.; Sakai, H.; Osawa, M. *J. Am. Chem. Soc.* **2003,** *125,* 3680–3681. doi:10.1021/ja029044t
23. Miki, A.; Ye, S.; Sensaki, T.; Osawa, M. *J. Electroanal. Chem.* **2004,** *563,* 23–31.
24. Samjeské, G.; Miki, A.; Osawa, M. *J. Phys. Chem. C* **2007,** *111,* 15074–15083. doi:10.1021/jp0743020
25. Samjeské, G.; Miki, A.; Ye, S.; Osawa, M. *J. Phys. Chem. B* **2006,** *110,* 16559–16566. doi:10.1021/jp061891l
26. Osawa, M.; Komatsu, K.-i.; Samjeské, G.; Uchida, T.; Ikeshoji, T.; Cuesta, A.; Gutiérrez, C. *Angew. Chem., Int. Ed.* **2011,** *50,* 1159–1163. doi:10.1002/anie.201004782
27. Chen, Y.-X.; Heinen, M.; Jusys, Z.; Behm, R. J. *Langmuir* **2006,** *22,* 10399–10408. doi:10.1021/la060928q
28. Chen, Y. X.; Heinen, M.; Jusys, Z.; Behm, R. J. *Angew. Chem., Int. Ed.* **2006,** *45,* 981–985. doi:10.1002/anie.200502172
29. Chen, Y.-X.; Heinen, M.; Jusys, Z.; Behm, R. J. *ChemPhysChem* **2007,** *8,* 380–385. doi:10.1002/cphc.200600520
30. Nakamura, M.; Shibutani, K.; Hoshi, N. *ChemPhysChem* **2007,** *8,* 1846–1849. doi:10.1002/cphc.200700244
31. Kuzume, A.; Mochiduki, Y.; Tsuchida, T.; Ito, M. *Phys. Chem. Chem. Phys.* **2008,** *10,* 2175–2179. doi:10.1039/B800243F
32. Heinen, M.; Jusys, Z.; Behm, R. J. Chapter 12. *Handbook of Fuel Cells;* John Wiley & Sons: Chichester, U.K., 2009; pp 183–214.
33. Okamoto, H.; Numata, Y.; Gojuki, T.; Mukouyama, Y. *Electrochim. Acta* **2014,** *116,* 263–270. doi:10.1016/j.electacta.2013.11.053
34. Jiang, J.; Scott, J.; Wieckowski, A. *Electrochim. Acta* **2013,** *104,* 124–133. doi:10.1016/j.electacta.2013.04.093
35. Neurock, M.; Janik, M.; Wieckowski, A. *Faraday Discuss.* **2009,** *140,* 363–378. doi:10.1039/b804591g
36. Gao, W.; Keith, J. A.; Anton, J.; Jacob, T. *J. Am. Chem. Soc.* **2010,** *132,* 18377–18385. doi:10.1021/ja1083317
37. Zhong, W.; Zhang, D. *Catal. Commun.* **2012,** *29,* 82–86. doi:10.1016/j.catcom.2012.09.002
38. Gao, W.; Mueller, J. E.; Jiang, Q.; Jacob, T. *Angew. Chem., Int. Ed.* **2012,** *51,* 9448–9452. doi:10.1002/anie.201203078
39. Housmans, T. H. M.; Wonders, A. H.; Koper, M. T. M. *J. Phys. Chem. B* **2006,** *110,* 10021–10031. doi:10.1021/jp055949s
40. Jusys, Z.; Behm, R. J. Chapter 13. *Fuel Cell Catalysis: A Surface Science Approach;* John Wiley & Sons: Chichester, U.K., 2009; pp 411–464.
41. Bagotzky, V. S.; Vassiliev, Yu. B.; Khazova, O. A. *J. Electroanal. Chem. Interfacial Electrochem.* **1977,** *81,* 229–238. doi:10.1016/S0022-0728(77)80019-3
42. Nichols, R. J.; Bewick, A. *Electrochim. Acta* **1988,** *33,* 1691–1694. doi:10.1016/0013-4686(88)80244-5
43. Iwasita, T.; Nart, F. C.; Lopez, B.; Vielstich, W. *Electrochim. Acta* **1992,** *37,* 2361–2367. doi:10.1016/0013-4686(92)85133-6
44. Wilhelm, S.; Vielstich, W.; Buschmann, H. W.; Iwasita, T. *J. Electroanal. Chem. Interfacial Electrochem.* **1987,** *229,* 377–384. doi:10.1016/0022-0728(87)85154-9
45. Heinen, M.; Jusys, Z.; Behm, R. J. *J. Phys. Chem. C* **2010,** *114,* 9850–9864. doi:10.1021/jp101441q
46. Schnaidt, J.; Heinen, M.; Jusys, Z.; Behm, R. J. *Catal. Today* **2013,** *202,* 154–162. doi:10.1016/j.cattod.2012.05.019
47. Schnaidt, J.; Heinen, M.; Jusys, Z.; Behm, R. J. *Electrochim. Acta* **2013,** *104,* 505–517. doi:10.1016/j.electacta.2012.12.139
48. Schnaidt, J.; Heinen, M.; Denot, D.; Jusys, Z.; Behm, R. J. *J. Electroanal. Chem.* **2011,** *661,* 250–264. doi:10.1016/j.jelechem.2011.08.011
49. Cao, D.; Lu, G.-Q.; Wieckowski, A.; Wasileski, S. A.; Neurock, M. *J. Phys. Chem. B* **2005,** *109,* 11622–11633. doi:10.1021/jp0501188

50. Kandoi, S.; Greeley, J. P.; Sanchez-Castillo, M. A.; Evans, T. S.; Gokhale, A. A.; Dumesic, J. A.; Mavrikakis, M. *Top. Catal.* **2006,** *37,* 17–28. doi:10.1007/s11244-006-0001-1
51. Janik, M.; Taylor, C.; Neurock, M. *Top. Catal.* **2007,** *46,* 306–319. doi:10.1007/s11244-007-9004-9
52. Árnadottir, L.; Stuve, E. M.; Jónsson, H. *Chem. Phys. Lett.* **2012,** *541,* 32–38. doi:10.1016/j.cplett.2012.05.024
53. Lai, S. C. S.; Kleyn, S. E. F.; Rosca, V.; Koper, M. T. M. *J. Phys. Chem. C* **2008,** *112,* 19080–19087. doi:10.1021/jp807350h
54. Gomes, J. F.; Bergamaski, K.; Pinto, M. F. S.; Miranda, P. B. *J. Catal.* **2013,** *302,* 67–82. doi:10.1016/j.jcat.2013.02.024
55. Chen, Y.-X., Heinen, M., Jusys, Z.; Behm, R. J. unpublished work.
56. Chang, S.-C.; Weaver, M. J. *J. Chem. Phys.* **1990,** *92,* 4582–4594. doi:10.1063/1.457719
57. Samjeské, G.; Komatsu, K.-i.; Osawa, M. *J. Phys. Chem. C* **2009,** *113,* 10222–10228. doi:10.1021/jp900582c
58. Osawa, M.; Tsushima, M.; Mogami, H.; Samjeské, G.; Yamakata, A. *J. Phys. Chem. C* **2008,** *112,* 4248–4256. doi:10.1021/jp710386g
59. Heinen, M. Ph.D. Thesis, Ulm University, 2010.
60. Schnaidt, J.; Heinen, M.; Jusys, Z.; Behm, R. J. *J. Phys. Chem. C* **2012,** *116,* 2872–2883. doi:10.1021/jp208162q
61. Schnaidt, J.; Jusys, Z.; Behm, R. J. *J. Phys. Chem. C* **2012,** *116,* 25852–25867. doi:10.1021/jp3086733
62. Strmcnik, D.; Tripkovic, D.; van der Vliet, D.; Stamenkovic, V.; Marković, N. M. *Electrochem. Commun.* **2008,** *10,* 1602–1605. doi:10.1016/j.elecom.2008.08.019
63. Hartnig, C.; Spohr, E. *Chem. Phys.* **2005,** *319,* 185–191. doi:10.1016/j.chemphys.2005.05.037
64. Climent, V.; Gómez, R.; Orts, J. M.; Feliu, J. M. *J. Phys. Chem. B* **2006,** *110,* 11344–11351. doi:10.1021/jp054948x
65. Wakisaka, M.; Suzuki, H.; Mitsu, S.; Uchida, H.; Wantanabe, M. *Langmuir* **2009,** *25,* 1897–1900. doi:10.1021/la803050r
66. Greenzaid, P.; Luz, Z.; Samuel, D. *J. Am. Chem. Soc.* **1967,** *89,* 749–756. doi:10.1021/ja00980a004
67. Sato, M.; Yamataka, H.; Komeiji, Y.; Mochizuki, Y. *Chem.–Eur. J.* **2012,** *18,* 9714–9721. doi:10.1002/chem.201200874
68. Schnaidt, J.; Heinen, M.; Jusys, Z.; Behm, R. J. *J. Phys. Chem. C* **2013,** *117,* 12689–12701. doi:10.1021/jp402986z
69. Leiva, E. P. M.; Santos, E.; Iwasita, T. *J. Electroanal. Chem. Interfacial Electrochem.* **1986,** *215,* 357–367. doi:10.1016/0022-0728(86)87028-0
70. Olivi, P.; Bulhões, L. O. S.; Léger, J.-M.; Hahn, F.; Beden, B.; Lamy, C. *Electrochim. Acta* **1996,** *41,* 927–932. doi:10.1016/0013-4686(95)00387-8
71. Wang, H.; Jusys, Z.; Behm, R. J. *Fuel Cells* **2004,** *4,* 113–125. doi:10.1002/fuce.200400014
72. Wang, H.; Jusys, Z.; Behm, R. J. *Electrochim. Acta* **2009,** *54,* 6484–6498. doi:10.1016/j.electacta.2009.05.097
73. Greeley, J.; Mavrikakis, M. *J. Am. Chem. Soc.* **2002,** *124,* 7193–7201. doi:10.1021/ja017818k
74. Heinen, M.; Chen, Y. X.; Jusys, Z.; Behm, R. J. *Electrochim. Acta* **2007,** *52,* 5634–5643. doi:10.1016/j.electacta.2007.01.055
75. Fuhrmann, J.; Linke, A.; Langmach, H.; Baltruschat, H. *Electrochim. Acta* **2009,** *55,* 430–438. doi:10.1016/j.electacta.2009.03.065
76. Breiter, M. W. *Electrochim. Acta* **1962,** *8,* 925–935. doi:10.1016/0013-4686(62)87047-9
77. Heinen, M.; Chen, Y. X.; Jusys, Z.; Behm, R. J. *Electrochim. Acta* **2007,** *53,* 1279–1289. doi:10.1016/j.electacta.2007.05.020

License and Terms

The definitive version of this article is the electronic one which can be found at:
doi:10.3762/bjnano.5.87

Beilstein Journal of Nanotechnology

Volcano plots in hydrogen electrocatalysis – uses and abuses

Paola Quaino[1,2], Fernanda Juarez[2], Elizabeth Santos[2,3] and Wolfgang Schmickler[*2]

Full Research Paper

Open Access

Address:
[1]PRELINE, Universidad Nacional del Litoral, Santa Fe, Argentina, [2]Institute of Theoretical Chemistry, Ulm University, D-89069 Ulm, Germany and [3]Faculdad de Matemática, Astronomía y Física, IFEG-CONICET, Universidad Nacional de Córdoba, Córdoba, Argentina

Email:
Wolfgang Schmickler[*] - wolfgang.schmickler@uni-ulm.de

* Corresponding author

Keywords:
electrocatalysis; hydrogen evolution; Sabatier's principle; volcano curve

Beilstein J. Nanotechnol. **2014,** *5,* 846–854.
doi:10.3762/bjnano.5.96

Received: 20 February 2014
Accepted: 28 May 2014
Published: 13 June 2014

This article is part of the Thematic Series "Electrocatalysis on the nm scale".

Guest Editor: R. J. Behm

Abstract

Sabatier's principle suggests, that for hydrogen evolution a plot of the rate constant versus the hydrogen adsorption energy should result in a volcano, and several such plots have been presented in the literature. A thorough examination of the data shows, that there is no volcano once the oxide-covered metals are left out. We examine the factors that govern the reaction rate in the light of our own theory and conclude, that Sabatier's principle is only one of several factors that determine the rate. With the exception of nickel and cobalt, the reaction rate does not decrease for highly exothermic hydrogen adsorption as predicted, because the reaction passes through more suitable intermediate states. The case of nickel is given special attention; since it is a 3d metal, its orbitals are compact and the overlap with hydrogen is too low to make it a good catalyst.

Introduction

Sabatier's principle [1] is one of the oldest rules in catalysis. For a two-step reaction passing through an adsorbed intermediate, like the hydrogen reaction, it states that the adsorption energy should be neither too high nor too low. If it is is too high (endothermic), adsorption is slow and limits the overall rate; if it is too low (exothermic), desorption is slow. In terms of hydrogen electrocatalysis it can be stated more precisely: at the equilibrium potential the free energy of adsorption of hydrogen from solution should be close to zero.

If Sabatier's principle is the only factor that governs a reaction, a plot of the reaction rate versus the free energy of adsorption of the intermediate results in a volcano curve. Starting from a high, positive (endergonic) energy of adsorption ΔG_{ad}, the rate at first rises with decreasing ΔG_{ad}; this is the ascending branch of the volcano. Near $\Delta G_{ad} \approx 0$ the rate passes through a maximum, and then starts to decrease as ΔG_{ad} becomes more exergonic (descending branch). Still, experimental evidence for a volcano relation in heterogenous catalysis is scarce. In electrochemistry,

Gerischer [2] and Parsons [3,4] were the first to point out that certain models for the hydrogen reaction predicted a volcano-like curve. However, it was Trasatti [5] who collected experimental data and constructed the first volcano curve for hydrogen evolution. Since experimental or theoretical data for hydrogen adsorption were not available at this time, he used the energy of hydride formation instead. His plot, which has been reproduced in many textbooks, is shown in Figure 1 and covers acid solutions. The reaction rate is expressed in terms of the exchange current density, which is proportional to the reaction rate at the equilibrium potential.

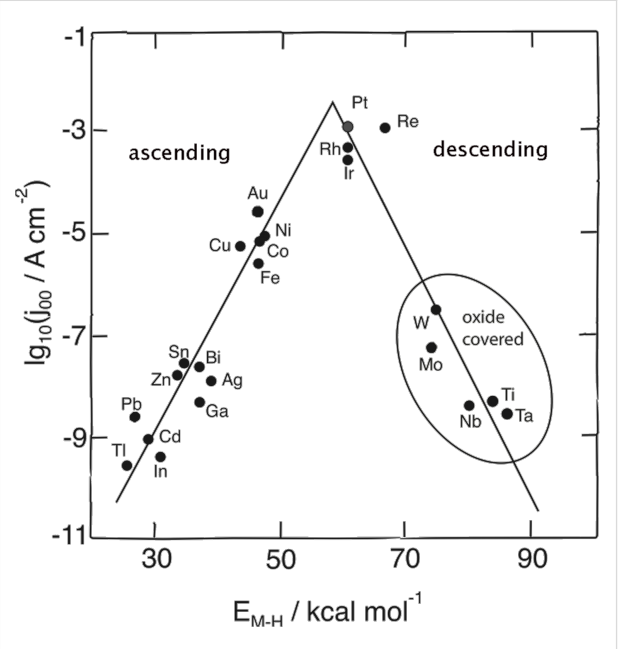

Figure 1: Trassati's volcano plot for the hydrogen evolution reaction in acid solutions. j_{00} denotes the exchange current density, and E_{MH} the energy of hydride formation. Data taken from [5].

The ascending branch of Trasatti's volcano plot is quite convincing; however, on the descending branch, there are only metals which are covered by an oxide film during hydrogen evolution, a fact that was not known at that time. Naturally, the presence of an oxide film reduces the reaction rate by several orders of magnitude. If we disregard the oxide-covered metals, there is no evidence for the descending branch.

In recent years, there has been much seismic activity, and several versions of volcano plots, not only for hydrogen evolution, have been constructed. In this article we shall critically consider the concepts behind and the experimental results for the hydrogen volcano plot, both in acid and in alkaline solutions. We will present our own ideas and show some new theoretical results for nickel, which in modern volcano plots is the only metal on the descending branch.

There is a parallelism between the concept of volcano plots in catalysis and outer sphere electron transfer reactions. According to Marcus' theory [6] a plot of the reaction rate versus the reaction free energy ΔG should pass through a maximum when $\Delta G \approx -\lambda$, where λ is the energy of solvent reorganisation of the reaction, and fall off for more exergonic reactions; the descending branch is known as the Marcus inverted region. While there are many electron transfer reaction which clearly show the ascending branch, there are very few examples where the inverted region has been observed. We shall return to this point.

Modern volcano plots

Before presenting a new version of the volcano plot, we would like to remind our readers of the mechanisms of hydrogen evolution and oxidation. In acid media, the first step in hydrogen evolution is always the Volmer reaction or electrochemical hydrogen adsorption:

$$\mathrm{H^+ + e^- \rightarrow H_{ad}} \qquad \text{(Volmer)} \tag{1}$$

while for the second step there are two possibilities:

$$\mathrm{H_{ad} + H_{ad} \rightarrow H_2} \qquad \text{(Tafel)} \tag{2}$$

$$\mathrm{H^+ + H_{ad} + e^- \rightarrow H_2} \qquad \text{(Heyrovsky)} \tag{3}$$

In alkaline solutions, the Volmer and Heyrovsky reactions are:

$$\mathrm{H_2O + e^- \rightarrow H_{ad} + OH^-} \qquad \text{(Volmer)} \tag{4}$$

$$\mathrm{H_2O + H_{ad} + e^- \rightarrow H_2 + OH^-} \qquad \text{(Heyrovsky)} \tag{5}$$

while the Tafel reaction stays the same.

Modern volcano plots, pioneered by the Nørskov group [7], use adsorption energies calculated by density functional theory (DFT). These are quite reliable for hydrogen adsorption – more so than experimental values – with an estimated error of ±0.1 eV. We have calculated these adsorption energies for a fair number of densely-packed metal surfaces, mostly fcc(111). In those cases, in which we considered the same metals, we obtained the same values as Nørskov et al. [7] within the usual DFT error. In contrast, the experimental values for the reaction rates measured by different groups sometimes vary by two orders of magnitude. The sources for our data are given in the appendix. We have not considered metals that are known be covered by oxide of hydroxide layers during hydrogen evolution.

The resulting plots are shown in Figure 2 both for acid and for alkaline solutions. Wherever there is a significant spread of

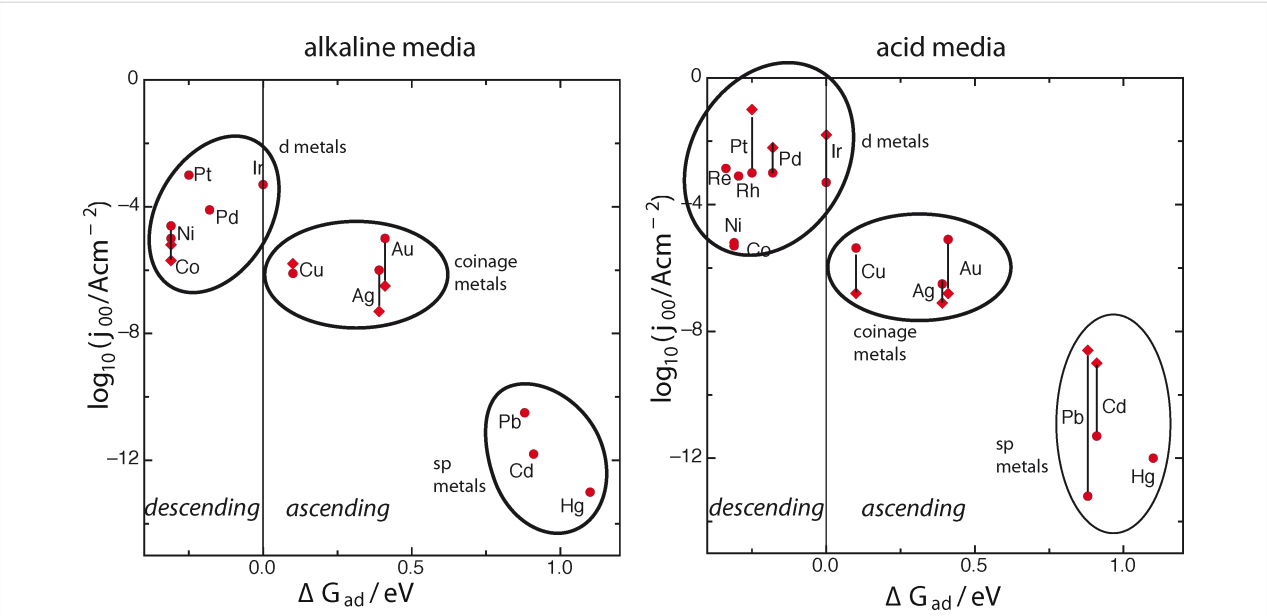

Figure 2: 'Volcano' plots for hydrogen evolution in acid and alkaline aqueous solutions. Note that ascending and descending branch are reversed with respect to Figure 1.

experimental data, we have indicated the corresponding error bars. There are more data for acid than for alkaline media, because the former are relevant for the most popular type of fuel cells, proton-exchange membrane (PEM) cells. Both plots look quite similar, but the fastest rates in acid solutions are somewhat faster than in alkaline. Neither of the plots bears any resemblance to a volcano, but there is a pronounced increase of the rate with decreasing (more favorable) ΔG_{ad} in the endergonic region. There is a clear separation into three groups: sp metals, which are the worst catalysts, coinage metals, which are intermediate, and the d metals, which contain the best catalysts, but also Ni and Co, which are mediocre.

A comparison with Trasatti's plot for acid media shows an overall similarity, once the oxide covered surfaces have been discarded from the latter, but also a few significant deviations. Some of these changes are due to new experimental values, others are caused by the fact, that the trends in hydride formation energies used by Trasatti do not always follow the hydrogen adsorption energies. An example for the latter is the position of nickel, an example for the former is the higher rate at silver in our plot, which is probably due to better sample preparation.

Discussion

Our group has developed its own theory of hydrogen electrocatalysis, based on a model Hamiltonian, quantum statistics and DFT, which we have reviewed in [8]. From our work we have derived three rules for a good catalyst:

- It should follow Sabatier's principle, $\Delta G \approx 0$ at the equilibrium potential;
- have a d band which spans the Fermi level;
- have a strong and long-ranged interaction between the d band and the hydrogen 1s orbital. A long range is important, because the electron transfer to the proton occurs at a certain distance, of the order of 0.5 Å, from the adsorption site [9].

These three conditions are not independent, since the position of the d band and the interaction strength also affect the energy of adsorption. Nevertheless, they can sometimes act against each other, as we shall show below. We proceed to discuss the plots of Figure 2 in the light of these principles. It is convenient to consider the three groups separately.

sp Metals

In the sp metals the d band lies so low that it plays no role in the bonding of hydrogen nor in electrocatalysis. This does not imply that the interaction of the d band with the adsorbed hydrogen is weak. For instance, in the case of Cd the interaction is sufficiently strong to produce nice bonding and antibonding peaks in the density of state (DOS) of the adsorbed hydrogen [10]. However, both bonding and antibonding states are filled, and hence this interaction does not contribute to the binding. In the absence of d band effects, we should expect this group of metals to follow Sabatier's principle. For alkaline solutions this is clearly the case, while for acid solutions the situation is not quite so clear. The difficulty with this groups of

metals is that measurable currents can only be obtained at high overpotentials, so that the determination of the exchange current density j_{00} requires an extrapolation over a large potential range. Further, on some metals like Pb and Cd there is a change in the slope of current–potential curves. Depending on which part of the curves are extrapolated, one obtains widely different values for j_{00}. Trasatti's [5] values are higher than those suggested by Petrii and Tsirlina [11] and nicely follow Sabatier's principle, while according to the latter group the reaction is slower on Pb than on Hg.

Of all the metals that we have investigated by using DFT, Hg is unique in that hydrogen is adsorbed on top; on all other metals it adsorbs at hollow sites. Also, it has the highest (least favorable) energy of adsorption. It must also be stated that the experimental values are quite old. Nowadays, there is a frantic search for good catalysts, and nobody is interested in sp metals, even though the most common car battery, the lead battery, only works because lead is such a bad catalyst for hydrogen evolution. Also, mercury once plaid a pivotal role as the electrode material for polarography, which used to be an important analytical technique. In fact, the only Nobel prize that has so far been awarded to an electrochemist was to Heyrovsky because of his work on polarography. In any case, in Trasatti's plot (Figure 1) the sp metals do follow Sabatier's principle quite well, and our plot supports this in alkaline solutions, while the data in acid solutions at least do not contradict this. Also, the fact that on these metals the Volmer reaction is the rate determining step [12] is quite in line with Sabatier's principle.

Coinage metals

The three coinage metals are mediocre catalysts; the experimental values for the exchange current densities also have to be extrapolated, but not over such a large potential range as is the case for the sp metals. Older data suffer from inadequate preparations of the electrode surface; for Ag and Au we have only considered experiments where the electrode had been treated by flame annealing. The spread of experimental data is much less than for the sp metals, and within experimental error the rates are about the same on all three metals, both in acid and in alkaline solutions. On Cu and Au, the Volmer reaction determines the rate, while on Ag the Volmer and Heyrovsky step are quite similar [12-17]. The Tafel reaction plays no role.

If the hydrogen evolution were governed by Sabatier's principle alone, copper, with $\Delta G_{ad} = 0.1$ eV, should be an excellent catalyst, better than platinum with $\Delta G_{ad} = -0.2$ eV. Its d band does not span the Fermi level, but ends about 0.1 eV below. So its position is not optimal, but close enough to make a contribution to the binding of hydrogen. However, as a third row element the orbitals of copper are compact; therefore the overlap with the hydrogen 1s orbital is short-ranged. As shown in Figure 3, the interaction of the copper d band with hydrogen has almost dropped to zero at a distance of the order of 1.4 Å, where electron transfer typically occurs [10]. The fact that the rate of hydrogen evolution is roughly the same on the three coinage metals is due to two opposing effects: The position of the d band and the energy of adsorption become more favorable in the order Au < Ag < Cu, while the coupling becomes weaker. Thus, the overall rates of the coinage metals are not governed by Sabatier's principle alone, and form a plateau rather than a volcano.

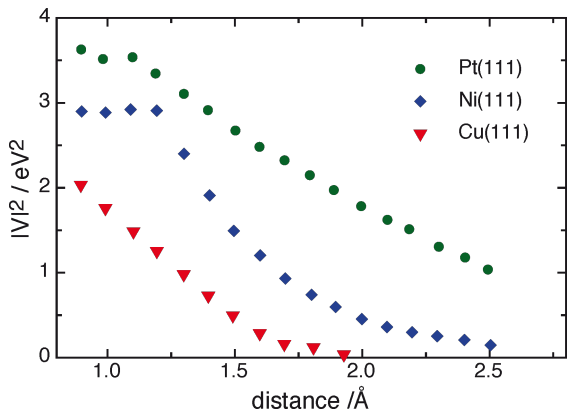

Figure 3: Square of the coupling constants between the H1s orbital and the d bands of Pt(111), Ni(111), Cu(111).

However, the difference in the rate constants for Cu(100) and Cu(111) in acid solutions, and also for Ag(100) and Ag(111), can be explained by Sabatier's principle. In both cases, the rate is somewhat faster on the (111) than on the (100) surfaces [15,18,19], and the adsorption energy is also lower on the more compact surfaces [20]. Theses differences are so small that we could not show them in our plot, but they are well established.

d Metals

By definition, the Fermi level of the d metals lies within the d band, so they fulfill at least one of our criteria for good catalysts. Indeed, with the exception of Co and Ni the rate is fast on all the metals that have been investigated – they are so fast that they are difficult to measure. In recent years, it has been claimed that the old values for Pt, Ir, Pd, as used by Trasatti [5] or Nørskov et al. [7], are too low because of mass transport limitations [21,22]. The new values correspond to the upper points in the error bars for these metals in Figure 2, while the lower points indicate the older values. None such measurements have been made for other metals of this group like Re and Rh, and the rates on these metals may well be higher than indicated. In any case, with the exception of Co and Ni, the rates are fast on these metals. They seem to be about one order

of magnitude faster in acid than in alkaline solutions, and they do not follow a volcano shape. Thus their behavior is not governed by Sabatier's principle alone.

We shall consider nickel and cobalt in detail later, and now focus on the other d metals. Starting from iridium, they ought to form the descending branch of the volcano, but obviously they do not. The reason is, that there are two distinct species: (1) The strongly adsorbed hydrogen, also called upd hydrogen (upd means *deposited at underpotentials*); it is the energy of this species that is generally used in volcano-type plots. (2) A weakly adsorbed species, also called opd hydrogen (opd means *deposited at overpotentials*). This topic is well reviewed in an article by Jerkiewicz [23]. With two states available, the reaction simply passes through the intermediate with the more favorable energy, and avoids the descending branch predicted by Sabatier's principle. At polycrystalline metals there are even more sites and therefore more options.

The relation between the two species is not simple, since the energy of the weakly adsorbed hydrogen depends on the coverage with the upd species. The best investigated case is Pt(111) in acid solutions, where the strongly adsorbed hydrogen is clearly visible in the cyclic voltammogram at potentials above the onset of hydrogen evolution; the total coverage of this species reaches about 70% in this region. However, the weakly adsorbed species has also been detected by infrared spectroscopy above the hydrogen evolution region [24]. So the adsorption of the weakly adsorbed species sets in before the coverage with the other one is complete. This is important, because the two species repel each other, and with increasing coverage of upd hydrogen both the energy of the opd species and the activation energy for the Tafel reaction increase noticeably. Therefore, a DFT calculation for the free energy of adsorption of the weakly adsorbed species in the presence of a monolayer of upd hydrogen gives often quite high (unfavorable) values for the the adsorption energy of the former species. We have discussed this point in detail in a a recent communication [25], where we have also calculated the isotherms for both species of adsorbed hydrogen on Pt(111). In any case, the interaction between the two species makes it quite difficult to calculate the adsorption free energy of the true intermediate state by DFT.

In the introduction, we mentioned a similarity between the volcano plots predicted by Sabatier's principle, and the free energy relation predicted by Marcus' theory for outer sphere electron transfer. It was very difficult to prove the existence of the Marcus inverted region at high reaction free energies, because in most reactions the electron can be transferred to a state with a higher, and thus more favorable, energy. In fact, this is the reason why the Marcus inverted region cannot be observed at metal electrodes, where in the highly exothermic region the electron can pass to the multitude of empty states that lie above the Fermi level [26]. Similarly, it is difficult to find an electrode material that follows the descending branch of the volcano curves, because the metals with a strong affinity to hydrogen usually have more than one adsorbed states, and the reaction passes through the more favorable ones. Nickel and cobalt are the only metals that lie on the descending branch, and they are worth a special look.

Nickel

Nickel and cobalt are very similar, and we focus on Ni(111), which is the densest and most stable surface. Nickel is one of the few metals that are spin polarized, and the d bands for spin up and spin down are shifted with respect to each other, even though they have the same shape (see Figure 4). This has a marked effect on the spin polarization of a hydrogen atom in front of the surface. On the densest-packed surface of most metals, spin polarization of the H1s orbital vanishes at about 2.4 Å [10,27]. In contrast, on Ni(111) spin polarization persists to much shorter distances. As an example, we show the densities of states (DOS) at a distance of 1.6 Å. For the two spin states of H1s, the DOS have almost the same shape but are shifted with respect to each other. Each spin orbital interacts principally with its d band counterpart on nickel, and exhibits clear bonding and antibonding peaks. At shorter distances, the spin polarization of hydrogen vanishes gradually, and is absent when the atom is adsorbed at a distance of 0.9 Å.

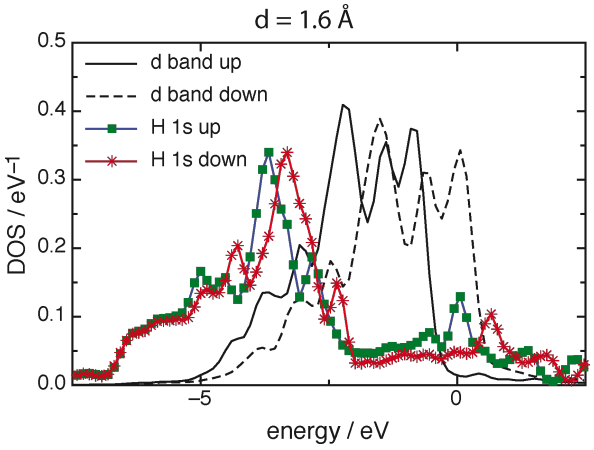

Figure 4: Densities of states of the d bands of Ni(111) and of the 1s spin orbitals of a hydrogen atom at a distance of 1.6 Å from the surface.

Nickel is a 3d metal, in the same row as copper. This entails that its orbitals are compact, and the interaction with the hydrogen atom falls off rapidly with distance [25], even though

the adsorption energy is quite favorable (see Figure 3). The most favorable adsorption site is the (111) hollow site. The next best site, which corresponds to weakly adsorbed hydrogen, is on top, has an adsorption energy of 0.9 eV, in the presence of a monolayer of strongly adsorbed hydrogen, and is thus highly unfavorable. Therefore hydrogen evolution must pass through the strongly adsorbed hydrogen, and thus follows Sabatier's principle, while the other d metals (except cobalt) can escape by passing through intermediates with a higher energy.

We have calculated the free energy surface for hydrogen adsorption (Volmer reaction) on Ni(111) from our own theory. The calculations follow exactly our previous works [10,25], to which we refer for the details. In Figure 5 the surface has been plotted as a function of two coordinates: of the distance of the reactant from the surface, and of the solvent coordinate q, which characterizes the state of the solvent. In our normalization a solvent coordinate of value q indicates, that the solvent would be in equilibrium with a reactant of charge $-q$. Thus, the initial state of the reaction is a proton of charge one, which corresponds to $q = -1$, and is situated at large distances. The final state is an adsorbed, uncharged hydrogen atom with $q = 0$ on the metal surface. During the course of the reaction, the solvent is reorganized [6], and the system passes through a saddle point. At the equilibrium potential for hydrogen evolution the corresponding energy of activation is about 0.48 eV, which makes for a fast reaction. However, at this potential the reaction is exergonic by about 0.32 eV. Experimentally, on nickel and cobalt the Volmer–Heyrovsky mechanism has been found to operate, with the Heyrovsky step being rate-determining [28,29]. This agrees with our observations, that the Volmer step should be fast, and is perfectly in line with Sabatier's principle.

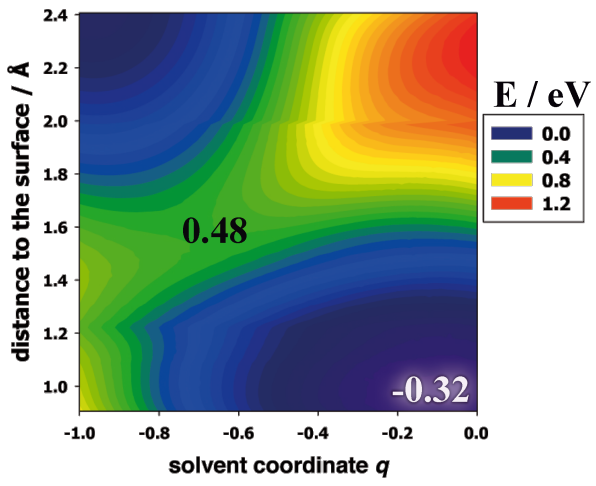

Figure 5: Free energy surface for the Volmer reaction on Ni(111) in acid solution at the equilibrium potential for hydrogen evolution.

Final remarks

There is no doubt that Sabatier's principle is sound, but the position of the d band and the details of its interaction with hydrogen are just as important. On the ascending branch of the plot, where ΔG_{ad} becomes more negative, these factors usually work in parallel, with the exception of the coinage metals, which have roughly the same rates because of the compensating effects discussed above. However, given the uncertainty of the experimental values, one can always draw a straight line starting somewhere near mercury and ending near platinum, which looks quite convincing even though the maximum is not at iridium, where it ought to be. The difficulty lies with the descending branch: When the oxide-covered metals are left out, only nickel and cobalt show the predicted decrease. On the other metals the reaction simply passes through intermediate states with higher energies.

A referee raised the valid question, why hydrogen evolution on oxide-covered metals has not been investigated systematically. There are several good reasons: (1) In an electrochemical environment, the oxide films on metal surfaces are not crystalline, but amorphous. In addition, they often incorporate OH and water. A good overview is given in [30]. (2) DFT studies on perfect oxides have shown, that often hydrogen is adsorbed as a proton, and is often incorporated into the film. WO_3 is a good example for this effect [31]. (3) The experimental data are affected by the charge transport through the film, which is very difficult to correct for [32]. Therefore, for this class of electrodes it is impossible to relate DFT data for hydrogen adsorption with experimental data.

Besides the original work of Trasatti, several other volcano-type plots have appeared in the literature. There is no point in giving a complete list, so we mention a few that we think particularly valuable. The Nørskov group [7] was the first to use adsorption free energies calculated by DFT, and thus produced a more reliable and larger set of energies. The main difference between their plot and ours is, that we have added a few sp metals, used more recent data for Pt, Pd, and Ir, and left out the oxide-covered metals. Another volcano plot was presented by the same group in [33]. It was obtained by kinetic modelling based on the assumption that in all cases the Tafel reaction (Equation 2) is the rate-determining step, and that the Volmer reaction is always in equilibrium – as we have mentioned above, only Pt(111) and rhenium in acid solutions actually follow this path. Sheng et al. [34] have proposed a volcano plot for alkaline solutions. All of these plots lose their volcano shapes, once the oxide-covered metals are deleted.

Besides hydrogen adsorption energies, correlations have been proposed with a host of other metal characteristics: work func-

tion, latent heat of melting, lattice constants, etc. A fairly complete list has been given by Petrii and Tsirlina [11] and makes for an amusing read. They are not based on any sound principle like Sabatier's, and it is not surprising that none of them has been successful [12].

For practical applications in fuel cells, the problem is not hydrogen oxidation but oxygen reduction, which is slow and inefficient. The full reduction involves four electron transfer steps, and possibly other chemical steps. The overall rate on a given substrate depends strongly on the pH value, and is also affected by anions. It is not surprising, that the details of the mechanism are still very much a subject of debate. Nevertheless, several attempts have been made to construct volcano plots for oxygen reduction as well. Really this topic is outside of the scope of this paper, so we just make a few brief comments meant as food for thought.

A principal difficulty is the lack of reliable data. Older data have been collected by Kinoshita [35], but the values obtained by different groups on similar systems differ widely. Therefore, it is not surprising that the volcano plot quoted most often is purely theoretical, calculated by the Nørskov group on the basis of a thermodynamic model for acid solutions [36]. Since this reaction contains so many steps, it is not clear which adsorption energy should be plotted on the x axis. This group has opted for the energy of adsorption of atomic oxygen; other candidates such as OH or OOH adsorption energies show decent linear correlations with oxygen adsorption.

In acid solutions, the first and rate-determining step is:

$$O_2 + H^+ + e^- \rightarrow HO_2 \quad (6)$$

In the outer sphere mode this reaction has a standard equilibrium potential of −0.046 V SHE, which has to be compared with the standard potential for oxygen reduction at pH 0, 1.229 V SHE. Obviously, on a good catalyst for this reaction the adsorption energy must be of the order of 1 eV – which is exactly the energy of adsorption of OOH on Pt(111) [37]. We have replotted the theoretical activities as calculated by Nørskov et al. [36] in Figure 6 as a function of the OOH adsorption energy, which seems the more natural descriptor to us. The resulting plot still looks more or less like a volcano, but it is not as nice as in the original paper, since the correlation between O and OOH adsorption energies is not perfect. As for experimental data, there is one consistent set of data for the oxygen reduction in 85% phosphoric acid; this was once a popular solution because of the phosphoric acid fuel cell. We have plotted the corresponding data in the same figure. There are some obvious similarities and differences, which we shall not discuss. For obvious reasons the theoretical points form the nicer volcano. Finally we remark, that a recent volcano plot correlating experimental data with OH adsorption energies is not convincing [38], because the experimental data mix results obtained in acid and in alkaline solutions, even though, for example, oxygen reduction on gold and silver are many orders of magnitude faster in alkaline than in acid solutions.

In summary: Volcano plots are a valiant attempt to understand catalytic reactions with the aid of a single descriptor, typically the energy of adsorption of a single intermediate. However, the kinetics of complex reactions are not so simple.

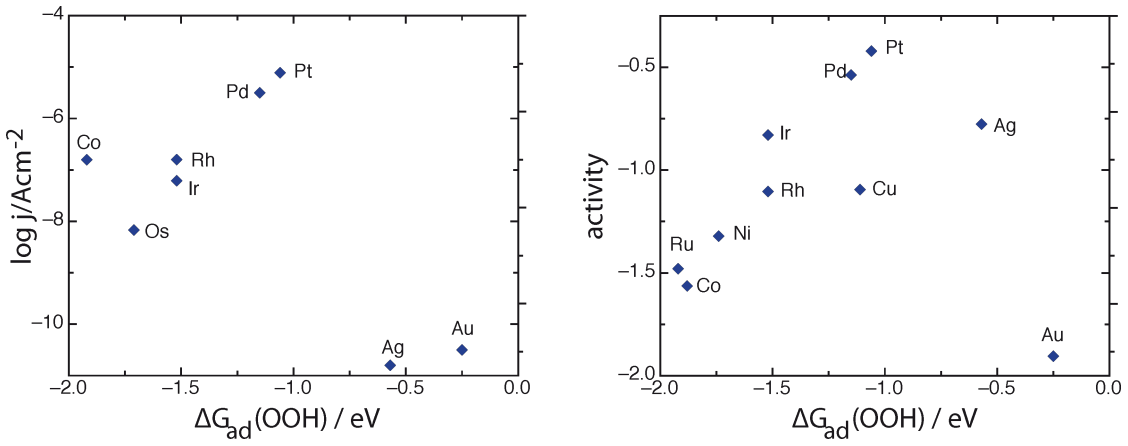

Figure 6: Oxygen reduction on various substrates in acid solutions. Left: logarithm of the current at 800 mV NHE in 85% phosphoric acid at 25°C plotted versus the adsorption energy of OOH on (111) surfaces; experimental data from Appleby [39], adsorption energies from [37]. Right: electrode activity (theoretical) for oxygen evolution in acid solutions versus OOH adsorption energy. The activity is proportional to the logarithm of the rate constant; the corresponding values have been taken from [36].

Appendix

Sources of the experimental data for hydrogen evolution

sp Metals

All values for alkaline solutions are from Petrii and Tsirlina [11]; values for acid solutions are from the same source and from Trasatti [5]. The latter values are systematically higher than the former for reasons explained above.

Coinage metals

Values for acid solutions are from Norskøv et al. [7]; for alkaline solutions they are from Sheng et al. [34].

d Metals

Values for alkaline solutions are again form Sheng et al. [34]. Those for acid solutions are from Norskøv et al. [7]; for Pt, Ir, Pd we have also taken values from Chen and A. Kucernak [21] and Gasteiger et al. [22]; the latter are higher than the older values for reasons explained above.

Acknowledgements

Financial supports by the Deutsche Forschungsgemeinschaft (Schm 344/34-1,2, SA 1770/1-1,2, and FOR 1376), and by an exchange agreement between the DAAD-Mincyt are gratefully acknowledged. The authors thank CONICET for continued support. E. S. acknowledges PIP-CONICET 112-20100001-00411, and PICT-2012-2324 (Agencia Nacional de Promoción Científica y Tecnológica, FONCYT, préstamo BID) for support, while P.Q. thanks CAID 501 201101 00276 LI UNL for support. A generous grant of computing time from the Baden-Württemberg grid is gratefully acknowledged.

References

1. Sabatier, F. *La catalyse en chimie organique;* Berauge: Paris, 1920.
2. Gerischer, H. *Bull. Soc. Chim. Belg.* **1958,** *67,* 506. doi:10.1002/bscb.19580670714
3. Parsons, R. *Trans. Faraday Soc.* **1958,** *54,* 1053. doi:10.1039/tf9585401053
4. Parsons, R. *Catalysis in Electrochemistry, from Fundamentals to Strategies for Fuel Cell Development;* John Wiley & Sons: Hoboken, NJ, USA, 2011.
5. Trasatti, S. *J. Electroanal. Chem.* **1972,** *39,* 163. doi:10.1016/S0022-0728(72)80485-6
6. Marcus, R. A. *J. Chem. Phys.* **1956,** *24,* 966. doi:10.1063/1.1742723
7. Nørskov, J. K.; Bligaard, T.; Logadottir, A.; Kitchin, J. R.; Chen, J. G.; Pandelov, S.; Stimming, U. *J. Electrochem. Soc.* **2005,** *152,* J23. doi:10.1149/1.1856988
   See also the comment on this paper: Schmickler, W.; Trasatti, S. *J. Electrochem. Soc.* **2006**, *153*, L31. doi:10.1149/1.2358294
8. Santos, E.; Quaino, P.; Schmickler, W. *Phys. Chem. Chem. Phys.* **2012,** *14,* 11224. doi:10.1039/c2cp40717e
9. Santos, E.; Schmickler, W. *Angew. Chem., Int. Ed.* **2007,** *46,* 8262. doi:10.1002/anie.200702338
10. Santos, E.; Lundin, A.; Pötting, K.; Quaino, P.; Schmickler, W. *Phys. Rev. B* **2009,** *79,* 235436. doi:10.1103/PhysRevB.79.235436
11. Petri, O. A.; Tsirlina, G. A. *Electrochim. Acta* **1994,** *39,* 1739. doi:10.1016/0013-4686(94)85159-X
12. Kuhn, A. T.; Mortimer, C. J.; Bond, G. C.; Lindley, J. *J. Electroanal. Chem.* **1972,** *34,* 1. doi:10.1016/S0022-0728(72)80496-0
13. Gerischer, H.; Mehl, W. *Z. Elektrochem.* **1955,** *59,* 1049.
14. Hamelin, A. *J. Electroanal. Chem.* **1987,** *223,* 171. doi:10.1016/0022-0728(87)85258-0
15. Eberhardt, D.; Santos, E.; Schmickler, W. *J. Electroanal. Chem.* **1999,** *461,* 76. doi:10.1016/S0022-0728(98)00093-X
16. Ruderman, A.; Juarez, M. F.; Soldano, G.; Avalle, L. B.; Beltramo, G.; Giesen, M.; Santos, E. *Electrochim. Acta* **2013,** *109,* 403. doi:10.1016/j.electacta.2013.07.112
17. Ruderman, A.; Juarez, M. F.; Avalle, L. B.; Beltramo, G.; Giesen, M.; Santos, E. *Elecrochem. Commun.* **2013,** *34,* 235. doi:10.1016/j.elecom.2013.06.023
18. Doubova, L. M.; Trasatti, S. *J. Electroanal. Chem.* **1999,** *467,* 164. doi:10.1016/S0022-0728(99)00060-1
19. Batrakov, V.; Dittrikh, Y.; Popov, A. *Elektrokhimiya* **1972,** *8,* 640.
20. Santos, E.; Pötting, K.; Lundin, A.; Quaino, P.; Schmickler, W. *ChemPhysChem* **2010,** *11,* 1491. doi:10.1002/cphc.200900808
21. Chen, S.; Kucernak, A. *J. Phys. Chem. B* **2004,** *108,* 13984. doi:10.1021/jp048641u
22. Rheinländer, P.; Henning, S.; Herranz, J.; Gasteiger, H. *ECS Trans.* **2013,** *50,* 2163. doi:10.1149/05002.2163ecst
23. Jerkiewicz, G. *Prog. Surf. Sci.* **1998,** *57,* 137. doi:10.1016/S0079-6816(98)00015-X
24. Kunimatsu, K.; Senzaki, T.; Samjeske, G.; Tsushima, M.; Osawa, M. *Electrochim. Acta* **2007,** *52,* 5715. doi:10.1016/j.electacta.2006.12.007
25. Santos, E.; Hindelang, P.; Quaino, P.; Schulz, E. N.; Soldano, G.; Schmickler, W. *ChemPhysChem* **2011,** *12,* 2274. doi:10.1002/cphc.201100309
26. Schmickler, W.; Tao, N. *Electrochim. Acta* **1997,** *42,* 2809. doi:10.1016/S0013-4686(97)00084-4
27. Mizielinki, M. S.; Bird, D. M.; Persson, M.; Holloway, S. *J. Chem. Phys.* **2005,** *122,* 084710. doi:10.1063/1.1854623
28. Bicelli, L. P.; Romagnani, C.; Rosania, M. *J. Electroanal. Chem.* **1975,** *63,* 238. doi:10.1016/S0022-0728(75)80296-8
29. Gonzales, E. R.; Avaca, L. A.; Tremiliosi-Filho, G.; Machado, S. A. S.; Ferreira, M. *Int. J. Hydrogen Energy* **1994,** *19,* 17. doi:10.1016/0360-3199(94)90173-2
30. Morrison, R. *Electrochemistry at Semiconductor, Oxidized Metal Electrodes;* Plenum Press: New York, NY, USA, 1980.
31. Wang, F.; Valentin, C. D.; Pacchioni, G. *J. Phys. Chem. C* **2012,** *116,* 10672. doi:10.1021/jp302210y
32. Joncich, M. J.; Stewart, L. S.; Posey, F. A. *J. Electrochem. Soc.* **1965,** *112,* 717. doi:10.1149/1.2423674
33. Skúlason, E.; Tripkovic, V.; Björketun, M. E.; Gudmundsdóttir, S.; Karlsberg, G.; Rossmeisl, J.; Bligaard, T.; Jónsson, H.; Nørskov, J. K. *J. Phys. Chem. C* **2010,** *114,* 18182. doi:10.1021/jp1048887
34. Sheng, W.; Myint, M.; Chen, J. G.; Yan, Y. *Energy Environ. Sci.* **2013,** *6,* 1509. doi:10.1039/C3EE00045A
35. Kinoshita, K. *Electrochemical oxygen technology;* Wiley-Interscience: New York, NY, USA, 1992.
36. Nørskov, J. K.; Rossmeisl, J.; Logadottir, A.; Lindqvist, L.; Kitchin, J. R.; Bligaard, T.; Jónsson, H. *J. Phys. Chem. B* **2004,** *108,* 17886. doi:10.1021/jp047349j

37. Yu, T. H.; Hofmann, T.; Sha, Y.; Merinov, B. V.; Myers, D. J.; Heske, C.; Goddard, W. A., III. *J. Phys. Chem. C* **2013,** *117,* 26598. doi:10.1021/jp4071554
38. Viswanathan, V.; Hansen, H. A.; Rossmeisl, J.; Nørskov, J. K. *ACS Catal.* **2012,** *2,* 1654. doi:10.1021/cs300227s
39. Appleby, A. J. *Surf. Sci.* **1971,** *27,* 225. doi:10.1016/0039-6028(71)90175-0

License and Terms

Beilstein Journal of Nanotechnology

Double layer effects in a model of proton discharge on charged electrodes

Johannes Wiebe*[1] and Eckhard Spohr*[2]

Full Research Paper

Open Access

Address:
[1]Faculty of Chemistry, Duisburg-Essen University, D-45117 Essen, Germany and [2]Faculty of Chemistry and Center for Computational Sciences and Simulation (CCSS), Universität Duisburg-Essen, D-45117 Essen, Germany

Email:
Johannes Wiebe* - johannes.wiebe@uni-due.de;
Eckhard Spohr* - eckhard.spohr@uni-due.de

* Corresponding author

Keywords:
electrocatalysis; interfacial electrochemistry; proton discharge; reactive force field; trajectory calculations

Beilstein J. Nanotechnol. **2014,** *5,* 973–982.
doi:10.3762/bjnano.5.111

Received: 14 February 2014
Accepted: 10 June 2014
Published: 07 July 2014

This article is part of the Thematic Series "Electrocatalysis on the nm scale".

Guest Editor: R. J. Behm

Abstract

We report first results on double layer effects on proton discharge reactions from aqueous solutions to charged platinum electrodes. We have extended a recently developed combined proton transfer/proton discharge model on the basis of empirical valence bond theory to include specifically adsorbed sodium cations and chloride anions. For each of four studied systems 800–1000 trajectories of a discharging proton were integrated by molecular dynamics simulations until discharge occurred. The results show significant influences of ion presence on the *average* behavior of protons prior to the discharge event. Rationalization of the observed behavior cannot be based solely on the electrochemical potential (or surface charge) but needs to resort to the molecular details of the double layer structure.

Introduction

One of the most fundamental electrochemical reactions is proton discharge from an aqueous solution to a charged electrode, which is the first step of the hydrogen evolution reaction. This basic electrocatalytic reaction and its dependence on the nature and the surface structure of the electrode, on impurities and the electrolyte has been extensively studied for more than 100 years [1]. A theoretical description of the reaction is particularly difficult, since the proton interacts strongly with the aqueous environment. The ability of the proton to attach to single water molecules as a hydronium ion or to larger clusters of molecules such as the so-called Zundel and Eigen cations, $H_5O_2^+$ and $H_9O_4^+$, respectively, and their fast interconversion through the Grotthuss hopping mechanism [2-5] opens up myriads of different reaction pathways for this reaction step. It is thus impossible to – even approximately – separate the reactive complex from the environment, which forms the basis of many theoretical treatments of reactivity in the condensed phase.

A microscopic treatment of electrocatalytic reactivity needs to accommodate the simple facts that (i) there is a multitude of possible reaction pathways in (ii) an ever changing environment that (iii) interacts strongly and 'chemically' rather than weakly and physically with the reactive complex at (iv) very different electrostatic environments near electrodes of (v) very different nature, composition and geometry. Recently we started to investigate proton transfer and discharge at charged electrodes on the basis of reactive force field molecular dynamics (MD), which allows us at present to incorporate for a given model the first four of these requirements into a molecular model. As a starting system we chose a simple platinum (111) surface, because experimentally the platinum surface exhibits one of the highest exchange current densities for the proton discharge reaction. Much research effort in electrocatalysis is directed towards replacing this expensive electrocatalyst with cheaper materials and – ideally simultaneously – to further improve the efficiency of the catalyst. In addition, platinum was deemed suitable because substantial simulation work has been done on this system before.

Much work has been done in recent years by using mostly quantum mechanical density functional theory (DFT) to study adsorbate energetics and geometries on many different catalysts and different catalyst surface geometries. In this context water adsorbates and bilayers have been studied extensively. The electrostatic potential has been introduced either through the implementation of sophisticated boundary conditions [6], through balancing of net electrode charges by electrolyte charges [7,8] or through electrostatic reference methods [9,10]. Chen and Sprik [11] have recently reviewed the current state of such approaches in the context of electronic energy level alignment.

The large number of possible proton transfer paths in the fluxional hydrogen bonding network of the aqueous solution makes the use of quantum chemistry-based approaches difficult but possible. The approach has been pushed forward successfully by the Otani group [12-15], but is limited to the study of few trajectories due to the huge computer time requirements. We chose instead a reactive force field procedure to statistically study the large number of proton transfer pathways by developing empirical valence bond (EVB) force fields for Grotthuss style proton migration and proton discharge at the water/Pt(111) [16,17] and the water/Ag(111) interface [18]. The first EVB models were developed by Warshel to study proton transfer mechanisms in biological systems [19-21]. This methodology was later extended by various groups to study proton dynamics in water [22,23] in a chemically intuitive picture, in which the proton state is described as (to a first approximation) a time-dependent superposition of Eigen, $H_9O_4^+$, and Zundel, $H_5O_2^+$, cations. Multistate generalizations of this simple picture were later applied to a variety of physical, chemical and biological problems [24-28]. In order to utilize the methodology for highly acidic environments such as a fuel cell membrane, the approach was, on the other hand, extremely simplified towards a minimal two-state model, in which the proton is either attached to a single water molecule as a H_3O^+ ion or to two molecules as a $H_5O_2^+$ ion [29,30].

The simple two-state EVB model was then combined with a very approximate and qualitative representation of the proton transfer to the surface and the motion of the (discharged) hydrogen atom on the Pt(111) surface. The final MD model can be practically applied in MD simulations of the electrochemical interface. Among other things, it is Hamiltonian in nature and conserves total energy. We have studied in this way proton discharge by straightforward simulation of ensembles of reactive proton trajectories, which all start from a proton equilibrated in the 'bulk' (center) of the water slab and migrate towards the charged surface, where they become discharged subsequently. Over the range of surface charge densities that could be simulated, an approximately exponential (or Tafel like) dependence of the microscopically defined rate on the surface charge density was found. Also, comparing a similarly constructed model for the Ag(111) surface showed that the corresponding rates for the silver surface are much smaller than those for the platinum surface. While this seems to be in agreement with the experimental evidence that hydrogen evolution on silver is much slower than on platinum [31,32], it may also be the consequence of model limitations, as both models were constructed in different ways.

In the present manuscript we extend these studies to investigate the influence of ions (Na^+ and Cl^- ions) in the first water layer in contact with the electrode as a first step towards understanding how electrolytes influence proton discharge. In the next section we briefly summarize the details of the simulation procedure. This is followed by the discussion of key results and some concluding remarks.

Details of the calculations

Our recent publications on a reactive force field model for proton transfer and proton discharge on platinum surfaces on the basis of the empirical valence bond (EVB) approach dealt with idealized water films containing an excess proton on negatively charged platinum and silver surfaces [16-18,33]. Those references describe the models in details, in particular also how parameters for the force field terms were obtained by fitting analytical functions to the data of quantum chemical calculations. The systems were realized as a water film consisting of 512 water molecules plus one excess Zundel complex, $H_5O_2^+$,

in contact with a static platinum slab with (111) surface geometry, consisting of 4 layers with 64 platinum atoms per layer. The surface charge density of the platinum electrode was chosen such that discharge reactions take place on a time scale suitable for MD simulations (within a few tens or hundreds of picoseconds).

Here now we augment the simulated systems by introducing one or two Na^+ or Cl^- ions into the aqueous double layer on the negatively charged electrode surfaces. Specifically, we studied four different systems: double layers with 1 or 2 adsorbed Cl^- ions and one with a single adsorbed Na^+ ion; in addition a reference system consisting of a pure water adsorbate layer was studied. In order to prevent desorption of the negatively charged Cl^- ions from the negatively charged platinum surface, the Cl^- ions had to be tethered to specific positions on the surface. The tethering of anions does not try to mimic a realistic bonding situation. Rather, it is a simple way to achieve a localized negative charge on the negative surface. Another alternative would have been to keep the position of the anions fixed.

Once adsorbed, the Na^+ ion, on the other hand, did never desorb from the surface but was free to diffuse within the adsorbate water layer. Hence, while the anions are specifically tethered to a site on the surface, the cation is free to move laterally and, in principle, can desorb. Nevertheless, in the following, we use the term 'adsorbed' for both cations and anions.

For each system, 1000 trajectories (only 800 for the system with 1 Cl^- ion) were integrated until a time of 2.5 ps *after* the discharge reaction. The platinum surface charge in contact with the pure water film was $-5e$, homogeneously distributed over the area of the slab ($A = 2.22 \times 1.923\ nm^2$), which corresponds to a surface charge density of $\sigma = -18.8\ \mu C\ cm^{-2}$. Here, $e = |e|$ is defined as the (positive) absolute value of the electron charge. In the systems with 1 and 2 Cl^- ions, each ion carries its full negative charge. The focus of the present work did not reach towards consideration of the electrochemically well-established effect of partial charge transfer, which has been investigated in particular for halogen adsorbates [34]. The magnitude of the homogeneous surface charge was reduced correspondingly by one or two elementary charges e so that the total charge of the double layer (homogeneous plus specifically adsorbed charge) was again $-5e$. For the Na^+ system, the positive elementary charge of the adsorbate ion was not compensated. Instead the homogeneous surface charge was kept at $-5e$ so that the total charge of the surface (homogeneous plus specifically adsorbed) amounted to $-4e$.

The water–water, water–hydronium, water–platinum and hydronium–platinum interactions underlying the 9-state EVB model were the same as in the previous work, in which they are described in detail [16]. In the spirit of a maximally simplified model, ion–water and ion–platinum interactions were described by simple Lennard-Jones plus point charge models with ionic Lennard-Jones parameters taken from [35], which were combined with the Lennard-Jones parameters of the water model. Ion–platinum Lennard-Jones parameters were chosen as $(\varepsilon, \sigma) = (0.218, 2.93)$ for Na^+ and (1.345, 3.35) for Cl^-, which, together with a harmonic tether potential for the Cl^- ions guaranteed that the ions stayed adsorbed in the surface layer of the water molecules. Here, ε is in units of $kJ \cdot mol^{-1}$ and σ in units of nm. In this work, the 9-state EVB model is constructed as the combination of the Walbran and Kornyshev two-state EVB model for proton transport [29] with a model of the hydrogen interaction with the metal surface, which is parametrized by seven distinct EVB basis states. The model describes states in which a proton is bound to water molecules and states in which a (neutralized) hydrogen atom interacts with the surface and superpositions thereof. The proton charge, and particularly its change during the neutralization reaction, is compensated by a corresponding negative charge on the metal slab.

Far from the electrode only the two charged states can contribute to the EVB ground state so that the state of a proton is a time-dependent superposition state of two different H_3O^+ states. The proton complex thus dynamically moves between more hydronium and more Zundel like states. In this situation the metal states do not contribute, since the coupling elements to the metal states vanish. After the proton has discharged, its state is a superposition of 7 equivalent hydrogen states in which the atom binds to one of the 7 metal atoms of a hexagonal surface cluster. The number of these states was chosen as the minimal number of hydrogen states that allow for a continuous motion of the hydrogen atom between on-top, hollow, and bridge sites. Shortly before the discharge reaction after the proton has migrated close to the metal surface, the coupling between the protonic and the (discharged) surface states sets in and the full 9-dimensional Hamiltonian matrix is diagonalized. We furthermore make the assumption that the system always stays on the adiabatic ground state potential energy surface, which we obtain as the lowest energy eigenvector of the Hamiltonian matrix. All further details of this model can be found in [16].

In the adiabatic ground state simulations performed here, proton transfer and proton discharge occur mainly when the environment of the proton provides adequate configurations that make the outcome of a proton hop favorable. Thus, the barrier for proton motion is usually small so that proton tunneling is less important than in many other cases. However, there is evidence for quantum effects due to the delocalized nature of the protons,

in particular from ab initio MD simulations [4,36,37]. Such calculations show that an adequate incorporation of the wave nature of atoms shifts the (broad) distributions of internal states towards states in which the center of proton charge is more delocalized over two or more water molecules. The two-state EVB model [29] shows indeed a preference for more delocalized (Zundel like) states [38], which is thus a (possibly fortuitous) feature of our model, which on average incorporates some of the quantum effects in an empirical way.

According to estimates we made in [17] the surface charge densities used in our computer simulations falls within the range of hydrogen underpotential deposition (UPD). In particular, at the negative surface charge densities studied here, one can expect the existence of a hydrogen UPD layer and fast discharge, which is indeed consistent with the results of the model. Recent DFT calculations by the Groß group [34] showed that the existence of such a layer moves the water layer to larger distances from the surface and shows a somewhat larger orientational order of the water molecules, which was attributed by the authors to be the result of weakened water–metal interactions in the presence of the hydrogen layer. The differences of the orientational distributions are small, so that we do not expect qualitative differences in the fast reorientation dynamics that accompany the proton discharge step [17]. Thus the overall effect of the presence of the hydrogen layer on the Volmer discharge step should not be large and is furthermore expected to be similar for all studied systems. We have thus chosen not to incorporate the additional complexity of a UPD layer into the model Hamiltonian.

Results

Figure 1 shows a system snapshot for the system with two adsorbed chloride ions, about 1 ps before a proton transfer event. The instantaneous Zundel complex is marked as spheres whereas regular water molecules are represented as sticks.

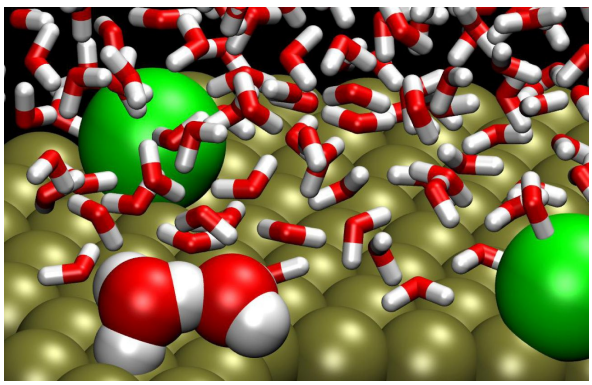

Figure 1: Snapshot for a water film with two adsorbed Cl^- ions (green).

The most obvious observable to study with our simulation setup is the time until discharge. The distribution of discharge times is rather broad, which has also been observed for the pure water case [17]. Figure 2 shows the distribution of reaction times for three simulations with a total surface charge of $-5e$. In the pure water simulation, the entire surface charge is homogeneously spread over the metal slab. In the simulations with one (two) contact adsorbed tethered chloride ions, $-4e$ ($-3e$) of the slab charge are homogeneously spread over the metal and the remaining one (two) negative charge(s) are centered on the ions. Note that in the present study we have disregarded the fact that the ions, which are adsorbed at the electrochemical interface, usually carry only a partial charge, which is a consequence of the fact that the bond of halide atoms with the metal surface has partially covalent character. Thus, the studied systems represent the idealized case of no partial charge transfer (PCT).

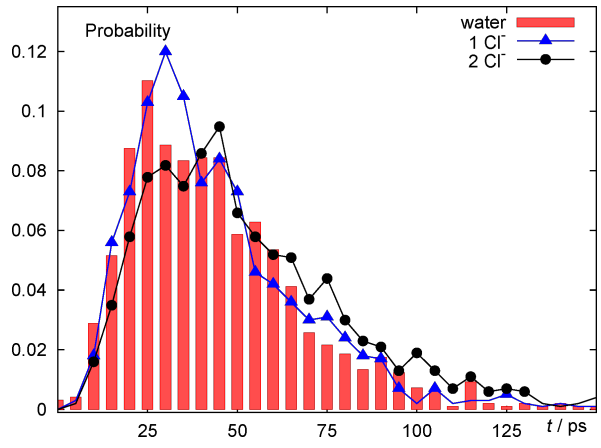

Figure 2: Distribution of discharge times (represented as probabilities to observe discharge within a 5 ps time interval) for a system of pure water (red boxes), of one fully charged adsorbed Cl^- ion (blue triangles) and two fully charged adsorbed Cl^- ions (black circles). In all three cases the total surface charge was $-5e$ and, consequently, the homogeneous surface charge density corresponded to $-5e$, $-4e$ and $-3e$, respectively.

All three distributions are rather similar. Most trajectories react during a time interval of about 25 to 70 ps. However, there is also a trend for the systems with adsorbed chloride to exhibit longer reaction times. This becomes quite apparent, when comparing pure water (red bars) with the 2 Cl^- case (black circles); the 1 Cl^- case falls in between. Whether or not the slight dependence on ion concentration in the adsorbate layer is due to differences in the average electric fields, which drive proton motion in solution, or the consequence of a site-blocking effect, which might play a role if the proton approaches the negative chloride centers in 'head-on' collisions, cannot be decided on the basis of these data (see below).

In the model setup implemented here, in which trajectories start in the center of the water film and protons subsequently migrate towards the charged electrode surface until they become discharged, one can obtain average properties over trajectories in at least two fundamentally different ways: In the first method the trajectories are aligned in a straightforward manner at their starting position. Thus, the average of some observable O over trajectories i, $\langle O\rangle(t)$ is calculated according to

$$\langle O\rangle(t) = \frac{1}{N}\sum_{i}^{N} O_i\left(t - t_{0_i}\right), \qquad (1)$$

where the sum runs over all trajectories and t_{0_i} denotes the initial time of the ith trajectory run.

Figure 3 shows the average distance of the particular proton which, at any given time, is eligible to be transferred to a neighbouring water molecule, and which is ultimately discharged by transfer to the metal surface. After an initial induction period (during which the proton is, on average, accelerated towards the surface) the curve assumes an approximately linear slope in the time interval between about 30 and about 60 ps. This behavior is indicative of the drift regime characteristic for a charged ion migrating in a homogeneous electric field. Thus, proton motion in this regime is dominated by the *mean* electric field (which can be calculated, e.g., by solving Poisson's equation with the charge density obtained by the average ionic densities), while the instantaneous electric field acting on the proton is fluctuative in nature. Beyond about 60 ps there is an approximately exponential decay of the curve as the inset of the curve shows. This behavior is the consequence of the different possible outcomes of the trajectories in the vicinity of the surface, which exhibit a broad distribution of times, during which the proton carrying complex is adsorbed in the contact water layer but does only dissociate after a configuration suitable for discharge occurs fluctuatively. Note that, in order to avoid excessive noise for long times (when few trajectories contribute to the average, since many trajectories have been terminated already after discharge), we have artificially extended each terminated trajectory by using the constant final value of the transferred proton. With this procedure, the curve must approach a constant value corresponding to the average adsorption distance at infinitely long times. The Na^+ ion deposited initially on the negatively charged surface did never desorb from the electrode. In the simulations with negative ions one or two Cl^- ions were tethered to the surface, since otherwise the ions would have desorbed due to the strong Coulomb repulsion from the homogeneous electrode charge. Note that in the simulations with the anions the overall surface charge was the same as for the pure

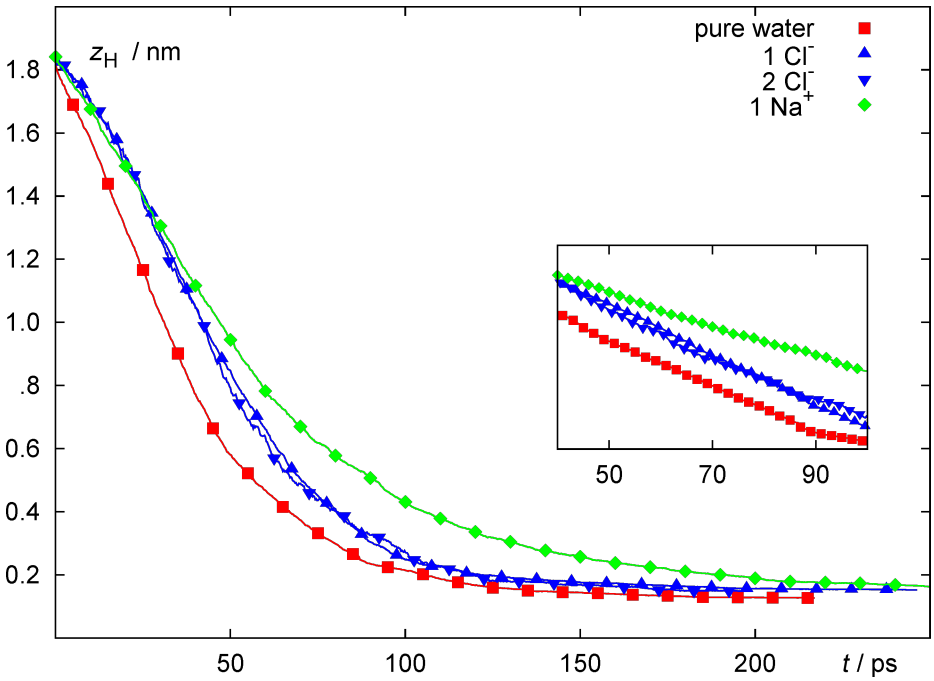

Figure 3: Average proton distance from the metal surface z_H as a function of time for pure water (red squares), one or two adsorbed Cl^- ions (blue triangles) and one adsorbed Na^+ (green diamonds). All ions carry a full positive or negative charge. The total surface charge is $-4e$ for the Na^+ system and $-5e$ for all other systems. Trajectories are aligned and averaged at their starting time. Inset: logarithmic scale.

water case, corresponding to a total of −5 elementary charges (corresponding to a surface charge density of −18.8 μC·cm^{-2}). The presence of the Na^+ ion, on the other hand, reduced the total charge of −5*e* (from the homogeneous part) to a total of −4*e*, corresponding to a total surface charge density of −14.4 μC·cm^{-2}.

The general behavior of the curves is similar. However, compared to the pure water case, the induction period seems to be slightly longer for the systems with adsorbed chloride. As could already be inferred from Figure 2, the presence of the chloride ions delays the approach of the proton to the surface relative to the pure water case, in spite of the fact that the total surface charge is identical in all cases. For the Na^+ simulation the intermediate slope of the curve is the smallest, in line with the fact that the net surface charge density is reduced and thus the driving force for migration and discharge is smaller than in the other cases.

Figure 3 can provide some information about the time scale of the proton approach to the surface and its residence time in the first adsorbed water layer. However, it does not provide any obvious insight into the nature of the discharge reaction. In order to probe the short time behavior immediately before and immediately after the reaction, we have calculated averages over trajectories in a different way: we have aligned the trajectories at their respective time of reaction rather than at the start time. Thus, an alternative definition of a trajectory average

$$\left\langle \tilde{O} \right\rangle (t) = \sum_i O\left(t - \tau_{R_i}\right) \tag{2}$$

can be used to assume a reaction-centered view of events. τ_{R_i} denotes the reaction time of the *i*th trajectory. Thus, comparison is not made based on some (more or less) arbitrary starting time in the past, but around the time of the reaction specific for each trajectory. This is consistent with the picture of chemical reactions as isolated rare events, for which it should suffice to study the behavior of the system from shortly before to shortly after the event. Here, we define the reaction time τ_{R_i} as the time, when the sum of the weights of all metal EVB states is for the first time larger than 0.9 in trajectory *i*, in other words, when more than 90% of the proton charge has been transferred to the surface. In a previous work [17], it was established that once this point has been reached, the discharge process is essentially complete.

Figure 4 shows the corresponding data for $z_H(t)$ for the time interval from −7.5 ps to +2.5 ps, i.e., for the last 10 ps of the

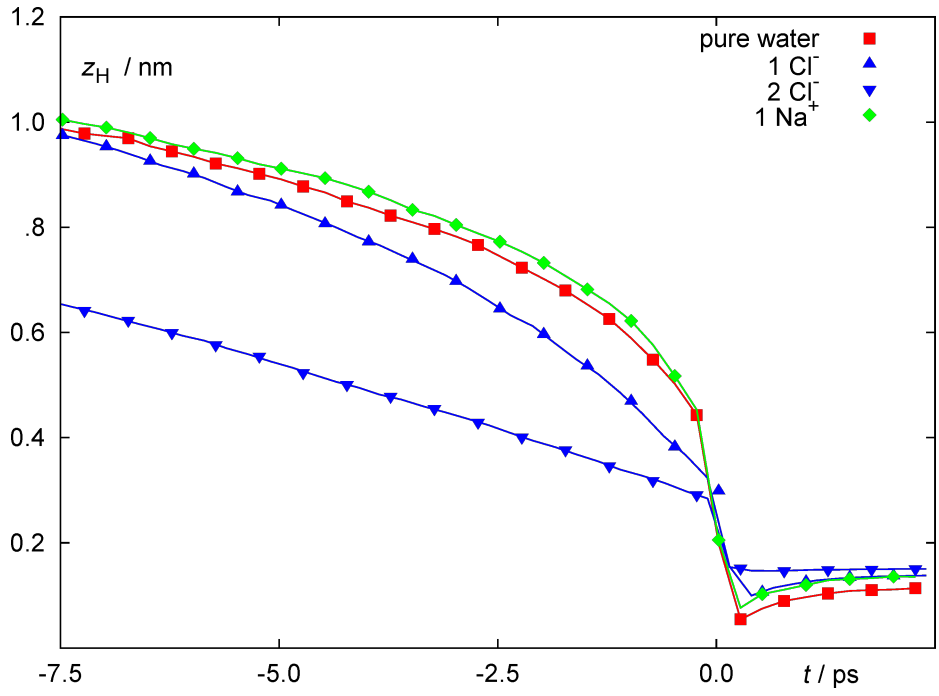

Figure 4: Average proton distance from the metal surface z_H as a function of time for pure water (red squares), one or two adsorbed Cl^- ions (blue triangles) and one adsorbed Na^+ (green diamonds). All ions carry a full positive or negative charge. The total surface charge is −4*e* for the Na^+ system and −5*e* for all other systems. Trajectories are aligned at the time of reaction, which is the zero of time, and averaged.

reactive trajectories. All trajectories were terminated 2.5 ps after the discharge reaction took place. The curves show significant differences for the different simulated systems. Quite expectedly, all curves have in common that the final step, when the proton moves out of its position as a proton in the first water layer to the state of an adsorbed hydrogen (which is much closer to the surface layer of platinum atoms), is very rapid and occurs within a few femtoseconds, a timespan not resolved in this representation.

If one first focuses on the behavior *after* the reaction, one notes that, due to excessive kinetic energy produced as a consequence of the exothermic discharge reaction, the average proton distance immediately after the reaction is rather small and then relaxes to its equilibrium value further away from the top platinum layer. This behavior is particularly pronounced for pure water and for the Na^+ simulations. These two simulations also show the fastest final decrease of the average proton distance from the surface in the time interval *before* the reaction takes place. Apparently the proton is accelerated (on average) from a position in the second or in the third layer immediately before the reaction. This supports earlier conclusions that the reaction mechanism at high driving force (i.e., at high surface charge densities) does not require a (fluctuative) reorientation of water molecules in the first layer to take place. Rather, once the proton can be transferred into the adsorbed water layer, proton discharge follows (almost) instantaneously. Although our model does not allow truly simultaneous proton transfer (all proton transfer steps are sequential), the quick succession of several such steps is an indication that such a simultaneous transfer mechanism might be possible in reality.

Interestingly the curves for the pure water simulation and the single Na^+ ion simulation are very similar before the reaction takes place. Thus, shortly before the reaction the proton motion is not (or only very slightly) affected by the presence of the adsorbed Na^+ ion. A possible interpretation of this behavior could be the following: the proton is unlikely to be discharged in the immediate vicinity of the positive site, because it is repelled by the positive charge of the Na^+ ion. Consequently, the proton trajectories most likely 'bend around' the contact adsorbed cation. Once the proton is 'sufficiently' close to the surface (apparently the second or third layers fulfill this condition already) the proton trajectory is strongly affected by the field of the homogeneous surface charge, while the repulsive field of the Na^+ ion plays a minor role in bending the proton trajectory away from the Na^+ ion. Thus, close to the surface, the driving force for proton discharge on the metal electrode with an adsorbed Na^+ ion is rather similar to the one in the absence of the cation, even though the net electrode charge is different by one elementary charge.

Chloride ions, on the other hand, behave qualitatively different. The simulation with a single Cl^- ion clearly shows a much slower approach of the proton to the electrode surface than in the case of the clean surface. The effect is even more significant in the presence of two contact-adsorbed chloride ions. In the latter case the curve shows an almost linear dependence of the average proton distance on time, which indicates that a simultaneous (or, since truly simultaneous transfer is not possible in our model, almost simultaneous) proton transfer from a water molecule in the second layer to one in the first layer and from there to the metal is of minor importance. Note again, that the electrode surfaces in the simulations of the proton with 0, 1, and 2 Cl^- ions all carry the same total charge. Thus the difference in behavior shortly before the reaction indicates significantly different local electrostatic potentials and fields. This demonstrates one possible way in which local double layer effects can modify electrochemical reactions in addition to the influence of the external electrode potential.

Figure 5 shows the lateral positions of the discharging proton above the metal surface as crosses for each individual trajectory on the left at reaction time (time $t = 0$ in Figure 4). The right figure shows the probability density of the proton transfer event as a function of the proton position at discharge *projected* onto the surface and mapped into a surface elementary cell. Note that the potential energy surface of a discharged hydrogen atom on platinum is relatively flat so that the H atom is very mobile. For the pure water case (top) discharge events are observed above all surface sites. However, discharge from straight above individual metal atoms is most probable, because this is the most probable adsorption site for the water molecule and the most probable direction to transfer the proton is along the direction from the oxygen atom to the surface. This behavior is more pronounced in the case of two adsorbed Cl^- ions. In this case on-top proton transfer is significantly increased compared to all other adsorption sites. This is, however, in part a consequence of the more ordered water layer structure induced by the two adsorbed ions. The distribution functions within the elementary cell on the right reflect this as well. While for the pure water interface, proton transfer within the elementary cell occurs almost homogeneously everywhere, there is a clear prevalence for on-top sites for the case of two adsorbed Cl^- ions.

Figure 6 shows indeed that there is a preference for the location of proton discharge to be closer to the anion than to the cation. The figure shows, as a function of the radius r the cumulative probability for proton discharge to occur within this distance from the adsorbed ion. For all distances shown, the probability is higher around the chloride ion than around the sodium ion, but overall this preference is not very pronounced.

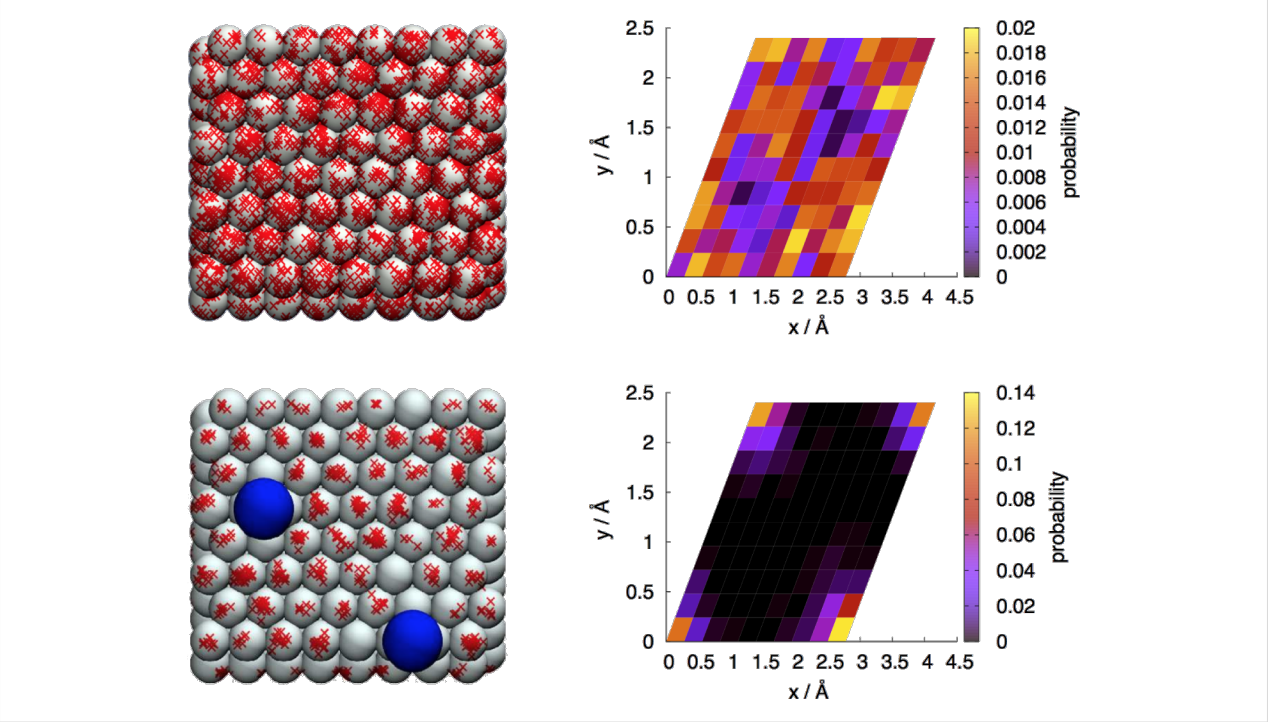

Figure 5: Lateral proton positions at the instant of discharge marked as red × symbols (left) and probability distributions of the proton positions at discharge mapped into a single surface elementary cell (right) for an interfacial layer consisting of pure water (top) and of two solvated Cl^- ions (bottom).

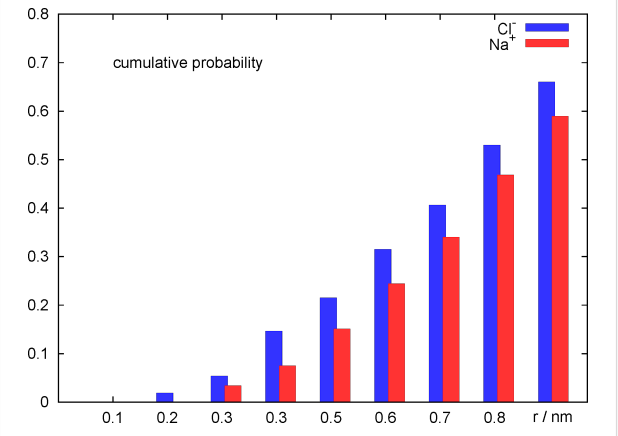

Figure 6: Cumulative probability to observe proton discharge within a radius *r* around the Na^+ ion (red) and the Cl^- ion in the system with only one adsorbed Cl^- ion (blue).

Discussion

We have compared reactive trajectory calculations of proton discharge from aqueous solutions to charged platinum electrodes for pure water, for adsorbate layers with single Na^+ and Cl^- ions, and for an adsorbate layer with two Cl^- ions. All ions have their full positive or negative elementary charge, so that no effects of partial charge transfer to the surface are included in the model. No bulk electrolyte is present that is capable of screening the surface charge. The sole difference between the different systems is the composition of the adsorbate water layer and distribution and magnitude of the negative electrode charge.

For the series of 0, 1 and 2 Cl^- ions the overall charge of the combined electrode/adsorbate ion system, which the approaching proton experiences, is identical, because the same total charge was distributed differently between the surface (as a homogeneous surface charge) and the ions (as point charges at the ion site). Nevertheless, significant differences can be observed. The distribution of reaction times, and thus the average, shifts towards higher values with increasing Cl^- concentration. Thus, not only the overall long-range electrode potential but also the local charge distribution plays a role for the reactivity. This is probably not so much a consequence of site blocking but rather of enhanced interaction of the proton complex with the negative chloride ions. This interaction manifests itself for instance in Figure 4 where it becomes obvious that the proton approaches the surface much more slowly in the presence of one Cl^- ion as compared to water, and even more slowly in the presence of two Cl^- ions.

On the other hand, shortly before the discharge step occurs, the presence of the sodium ion plays a minor role, as can be seen from the time dependence of the mean approach distance, which is very similar in the presence of the sodium ion when

compared to pure water, in spite of the fact that the total charge of the surface and the adsorbate layer is smaller in the presence of Na^+. The similarity between the two curves in Figure 4 may be a consequence of the fact that the approaching positively charged proton avoids the positively charged Na^+ ion. As Figure 6 shows, this effect is indeed present, but it appears to be rather weak. In fact, the proton approaches the surface even slightly faster when the Na^+ ion is present in the double layer.

The presence of the ionic adsorbates has an ordering effect on the surrounding water molecules (analogous to the one observed by the Gross group for water around an OH group on a Ru surface by using DFT calculations [39]), which is evident from the correlation of the proton discharge sites with the ions and with the on top water site in Figure 5.

In summary our calculations show that, aside from the obvious influence of the interfacial or electrode charge density, structural features of the double layer also have an influence on the electrochemical reactivity, represented here through the proton discharge reaction and its dependence on the composition of the adsorbed water layer. This is an example of a double layer effect which influences the interfacial structure and dynamics beyond the simple one-dimensional potential drop at the interface.

Acknowledgements

We gratefully acknowledge financial support by DFG within the framework of the DFG Research Unit 1376 “Elementary reaction steps in electrocatalysis: Theory meets experiment”. We are also grateful for support by the Cluster of Excellence RESOLV (EXC1069) funded by the Deutsche Forschungsgemeinschaft. Computations were in part performed at the UDE Cray computer operated by CCSS.

References

1. Tafel, J. *Z. Phys. Chem.* **1905,** *50,* 641–712.
2. Agmon, N. *J. Phys. Chem. A* **2005,** *109,* 13–35. doi:10.1021/jp047465m
3. Voth, G. A. *Acc. Chem. Res.* **2006,** *39,* 143–150. doi:10.1021/ar0402098
4. Marx, D. *ChemPhysChem* **2006,** *7,* 1848–1870. doi:10.1002/cphc.200600128
5. Marx, D.; Chandra, A.; Tuckerman, M. E. *Chem. Rev.* **2010,** *110,* 2174–2216. doi:10.1021/cr900233f
6. Otani, M.; Sugino, O. *Phys. Rev. B* **2006,** *73,* 115407. doi:10.1103/PhysRevB.73.115407
7. Karlberg, G. S.; Jaramillo, T. F.; Skúlason, E.; Rossmeisl, J.; Bligaard, T.; Nørskov, J. K. *Phys. Rev. Lett.* **2007,** *99,* 126161. doi:10.1103/PhysRevLett.99.126101
8. Rossmeisl, J.; Skúlason, E.; Björketun, M. E.; Tripkovich, V.; Nørskov, J. K. *Chem. Phys. Lett.* **2008,** *466,* 68–71. doi:10.1016/j.cplett.2008.10.024
9. Taylor, C. D.; Wasileski, S. A.; Filhol, J.-S.; Neurock, M. *Phys. Rev. B* **2006,** *73,* 165402. doi:10.1103/PhysRevB.73.165402
10. Filhol, J.-S.; Neurock, M. *Angew. Chem., Int. Ed.* **2006,** *45,* 402–406. doi:10.1002/anie.200502540
11. Cheng, J.; Sprik, M. *Phys. Chem. Chem. Phys.* **2012,** *14,* 11245–11267. doi:10.1039/c2cp41652b
12. Sugino, O.; Hamada, I.; Otani, M.; Morikawa, Y.; Ikeshoji, T.; Okamoto, Y. *Surf. Sci.* **2007,** *601,* 5237–5240. doi:10.1016/j.susc.2007.04.208
13. Otani, M.; Hamada, I.; Sugino, O.; Morikawa, Y.; Okamoto, Y.; Ikeshoji, T. *J. Phys. Soc. Jpn.* **2008,** *77,* 024802. doi:10.1143/JPSJ.77.024802
14. Otani, M.; Hamada, I.; Sugino, O.; Morikawa, Y.; Okamotode, Y.; Ikeshojiae, T. *Phys. Chem. Chem. Phys.* **2008,** *10,* 3609–3612. doi:10.1039/b803541e
15. Ikeshoji, T.; Otani, M.; Hamada, I.; Okamoto, Y. *Phys. Chem. Chem. Phys.* **2011,** *13,* 20223–20227. doi:10.1039/c1cp21969c
16. Wilhelm, F.; Schmickler, W.; Nazmutdinov, R. R.; Spohr, E. *J. Phys. Chem. C* **2008,** *112,* 10814–10826. doi:10.1021/jp800414f
17. Wilhelm, F.; Schmickler, W.; Spohr, E. *J. Phys.: Condens. Matter* **2010,** *22,* 175001. doi:10.1088/0953-8984/22/17/175001
18. Wilhelm, F.; Schmickler, W.; Nazmutdinov, R.; Spohr, E. *Electrochim. Acta* **2011,** *56,* 10632–10644. doi:10.1016/j.electacta.2011.04.036
19. Warshel, A.; Weiss, R. M. *J. Am. Chem. Soc.* **1980,** *102,* 6218–6226. doi:10.1021/ja00540a008
20. Hwang, J.-K.; King, G.; Creighton, S.; Warshel, A. *J. Am. Chem. Soc.* **1988,** *110,* 5297–5311. doi:10.1021/ja00224a011
21. Åqvist, J.; Warshel, A. *Chem. Rev.* **1993,** *93,* 2523–2544. doi:10.1021/cr00023a010
22. Lobaugh, J.; Voth, G. A. *J. Chem. Phys.* **1996,** *104,* 2056–2069. doi:10.1063/1.470962
23. Sagnella, D. E.; Tuckerman, M. E. *J. Chem. Phys.* **1998,** *108,* 2073–2083. doi:10.1063/1.475586
24. Vuilleumier, R.; Borgis, D. *J. Chem. Phys.* **1999,** *111,* 4251–4266. doi:10.1063/1.479723
25. Schmitt, U. W.; Voth, G. A. *J. Chem. Phys.* **1999,** *111,* 9361–9381. doi:10.1063/1.480032
26. Brancato, G.; Tuckerman, M. E. *J. Chem. Phys.* **2005,** *122,* 224507. doi:10.1063/1.1902924
27. Wu, Y.; Chen, H.; Wang, F.; Paesani, F.; Voth, G. A. *J. Phys. Chem. B* **2008,** *112,* 467–482. doi:10.1021/jp076658h
28. Day, T. J. F.; Soudackov, A. V.; Čuma, M.; Schmitt, U. W.; Voth, G. A. *J. Chem. Phys.* **2002,** *117,* 5839–5849. doi:10.1063/1.1497157
29. Walbran, S.; Kornyshev, A. A. *J. Chem. Phys.* **2001,** *114,* 10039–10048. doi:10.1063/1.1370393
30. Commer, P.; Cherstvy, A. G.; Spohr, E.; Kornyshev, A. A. *Fuel Cells* **2003,** *2,* 127–136. doi:10.1002/fuce.200290011
31. Eberhardt, D.; Santos, E.; Schmickler, W. *J. Electroanal. Chem.* **1999,** *461,* 76–79. doi:10.1016/S0022-0728(98)00093-X
32. Doubova, L. M.; Trasatti, S. *J. Electroanal. Chem.* **1999,** *467,* 164–176. doi:10.1016/S0022-0728(99)00060-1
33. Schmickler, W.; Wilhelm, F.; Spohr, E. *Electrochim. Acta* **2013,** *101,* 341–346. doi:10.1016/j.electacta.2013.01.146
34. Roman, T.; Groß, A. *Catal. Today* **2013,** *202,* 183–190. doi:10.1016/j.cattod.2012.06.001
35. Heinzinger, K.; Bopp, P.; Jancsó, G. *Acta Chim. Hung.* **1985,** *121,* 27–53.

36. Tuckerman, M. E.; Chandra, A.; Marx, D. *J. Chem. Phys.* **2010,** *133,* 124108. doi:10.1063/1.3474625
37. Knight, C.; Voth, G. A. *Acc. Chem. Res.* **2012,** *45,* 101–109. doi:10.1021/ar200140h
38. Kornyshev, A. A.; Kuznetsov, A. M.; Spohr, E.; Ulstrup, J. *J. Phys. Chem. B* **2003,** *107,* 3351–3366. doi:10.1021/jp020857d
39. Schnur, S.; Groß, A. *New J. Phys.* **2009,** *11,* 125003. doi:10.1088/1367-2630/11/12/125003

License and Terms

BEILSTEIN JOURNAL OF NANOTECHNOLOGY

Restructuring of an Ir(210) electrode surface by potential cycling

Khaled A. Soliman[1,2], Dieter M. Kolb[1,§], Ludwig A. Kibler[*1] and Timo Jacob[1]

Full Research Paper

Open Access

Address:
[1]Institut für Elektrochemie, Universität Ulm, 89069 Ulm, Germany and [2]Permanent address: Electrochemistry and Corrosion Laboratory, Physical Chemistry Department, National Research Centre, Cairo, 12622, Egypt

Email:
Ludwig A. Kibler[*] - ludwig.kibler@uni-ulm.de

* Corresponding author
§ Dieter M. Kolb (1942–2011)

Keywords:
CO adlayer oxidation; cyclic voltammetry; Ir(210) single crystal; potential cycling; scanning tunnelling microscopy; surface restructuring

Beilstein J. Nanotechnol. **2014,** *5,* 1349–1356.
doi:10.3762/bjnano.5.148

Received: 10 March 2014
Accepted: 21 July 2014
Published: 25 August 2014

This article is part of the Thematic Series "Electrocatalysis on the nm scale".

Guest Editor: R. J. Behm

Abstract

This study addresses the electrochemical surface faceting and restructuring of Ir(210) single crystal electrodes. Cyclic voltammetry measurements and in situ scanning tunnelling microscopy are used to probe structural changes and variations in the electrochemical behaviour after potential cycling of Ir(210) in 0.1 M H_2SO_4. Faceted structures are obtained electrochemically as a function of time by cycling at a scanrate of 1 $V \cdot s^{-1}$ between −0.28 and 0.70 V vs SCE, i.e., between the onset of hydrogen evolution and the surface oxidation regime. The electrochemical behaviour in sulfuric acid solution is compared with that of thermally faceted Ir(210), which shows a sharp characteristic voltammetric peak for (311) facets. Structures similar to thermally-induced faceted Ir(210) are obtained electrochemically, which typically correspond to polyoriented facets at nano-pyramids. These structures grow anisotropically in a preferred direction and reach a height of about 5 nm after 4 h of cycling. The structural changes are reflected in variations of the electrocatalytic activity towards carbon monoxide adlayer oxidation.

Introduction

The surface structure of metal electrodes is a decisive factor for kinetics of many electrochemical processes and electrocatalytical reactions [1-3]. Since the behaviour of polycrystalline material is often quite complex, relations between the surface structure of an electrode and its activity for a given reaction are typically investigated in experiments by using clean and well-defined model systems, such as single crystal surfaces [4-6], epitaxially grown monolayers [7,8] or preferentially-shaped nanoparticles [9]. In all cases, detailed protocols have been established for the reproducible preparation of these model electrodes, which have been extensively characterized in recent years.

The development of so-called electrochemical surface science has shown that the geometric surface structure of metals is often identical under ultrahigh-vacuum (UHV) conditions and in contact with an electrolyte. However, there are several examples for which the stability of electrode surfaces is limited to certain potential regions or reaction conditions. Among these are (i) reconstructed surfaces of Au and Pt single crystals [10,11], (ii) structural changes in operando, e.g., for hydrogen evolution at PdAu nanoparticles [12], (iii) removal of islands by adsorbates, such as electrochemical annealing of Au(100) by adsorbed chloride [13,14], (iv) dissolution of metals at positive potentials and restructuring by oxidation–reduction cycles [15,16]. Thus, morphological changes between thermodynamically stable structures can be induced for example by temperature, electrode potential or specific adsorption.

Unlike reconstruction phenomena, the faceting of surfaces leads to structures, which exist in the bulk lattice already. In earlier studies, we have examined the electrochemical behaviour of Ir single crystals [17,18], including thermally-induced faceted Ir(210) [19,20]. Besides the laborious preparation under UHV conditions [21,22], faceted Ir(210) can easily be obtained outside a UHV chamber by inductive heating and cooling in nitrogen gas atmosphere [19,20]. Such thermally-induced faceted Ir(210) has been characterized by cyclic voltammetry and in situ scanning tunnelling microscopy (STM) [20]. Thus, very similar surface structures with nanometer-scale pyramids consisting of (110) and {311} facets could be prepared in- and outside a UHV chamber. It was found that the presence of oxygen is crucial for the faceting process on Ir(210) [21,22].

Theoretical calculations for the Ir(210) system, based on first principles, provided supportive information. It was shown that, due to the anisotropy in surface free energy for the different Ir surface orientations, the adsorption of more than 0.5 ML oxygen causes the formation of nano-pyramids exhibiting (110) and {311} faces to be thermodynamically more stable than the original Ir(210) substrate [19,23]. Based on density functional theory calculations it was predicted that the faceting process of Ir(210) can also be induced by the electrode potential [19].

Here, we present a combined electrochemical and in situ STM study of Ir(210), which demonstrates that the faceted surface is not only stable in a certain potential region, but can also be obtained electrochemically. The simple polarization of Ir(210) at positive potentials did not lead to the formation of facets. However, potential cycling into the surface oxidation potential region leads to a restructuring of the Ir(210) surface. Carbon monoxide adlayer oxidation was chosen as a structure-sensitive reaction to study the electrocatalytic activity of restructured Ir(210) surfaces compared to non-restructured Ir(210).

Experimental

A cylindrical Ir(210) single crystal (4 mm in diameter and thickness, MaTecK Jülich, Germany) was used both for electrochemical and in situ STM investigations. Before each measurement, the single crystal was annealed at 1700 °C by inductive heating in a stream of nitrogen gas (5.0, MTI IndustrieGase AG, Neu-Ulm, Germany) mixed with carbon monoxide (4.7, MTI) or hydrogen (5.0, MTI). The annealing temperature was controlled (contact-free) by an infrared pyrometer (Infratherm IGAR 12-LO, IMPAC Infrared GmbH, Frankfurt am Main, Germany). After short cooling in the same gas mixture, the single crystal was transferred under nitrogen atmosphere to the electrochemical cell. The crystal was immersed under potential control into 0.1 M H_2SO_4 at −0.1 V vs SCE and brought to a stable hanging-meniscus configuration. The CO adlayer was anodically stripped in a single voltammetric scan up to 0.7 V. Surface quality and cleanliness were assured by recording reproducible current–potential curves in the hydrogen adsorption region. Subsequently, the crystal was transferred to the STM cell, while a droplet of electrolyte protected its surface. The solutions were prepared from H_2SO_4 (Merck, suprapur) and ultrapure water (18.2 MΩ·cm at 25 °C, total oxidizable carbon < 1 ppb as recorded with an A10 TOC Monitor, Millipore). The electrolytes were purged with nitrogen gas. The electrochemical measurements were performed in a conventional three-electrode glass cell. A saturated calomel electrode (SCE) and a Pt wire were used as the reference and counter electrodes, respectively. Pt wires were used for the STM cell as counter and pseudo-reference electrodes. The STM images were recorded with a Digital Instruments Nanoscope III (Digital Instruments, Santa Barbara, California). For the preparation of the STM tips, a Pt/Ir wire (80/20) was etched in 4.5 M NaCN and coated with an electrophoretic paint to reduce Faradic currents at the tip/electrolyte interfaces below 50 pA.

Results and Discussion

Electrochemical behaviour of Ir(210)

Annealing and cooling of Ir(210) in a nitrogen gas atmosphere containing trace amounts of oxygen was shown earlier to induce surface faceting, which can be avoided by adding a reducing gas, such as hydrogen [19,20]. In this study, CO was mixed to the cooling gas in order to start with a non-faceted surface. In this case, a CO adlayer is formed on the Ir surface, which survives the transfer to the electrochemical cell and which can easily be stripped of at positive potentials, as described in section Experimental.

Figure 1 shows typical cyclic voltammograms of the freshly-prepared Ir(210) single crystal electrode in 0.1 M H_2SO_4 after anodic stripping of the CO adlayer. There are three current peaks in the hydrogen adsorption region located at −0.04, −0.18

and −0.25 V. As in the case of low-index planes of Ir, these peaks are assigned to hydrogen adsorption/desorption combined with (bi)sulphate desorption/adsorption, respectively [5,17,18]. In contrast to low-index Ir surfaces [5], there are no very sharp voltammetric peaks for the relatively open (210) surface orientation.

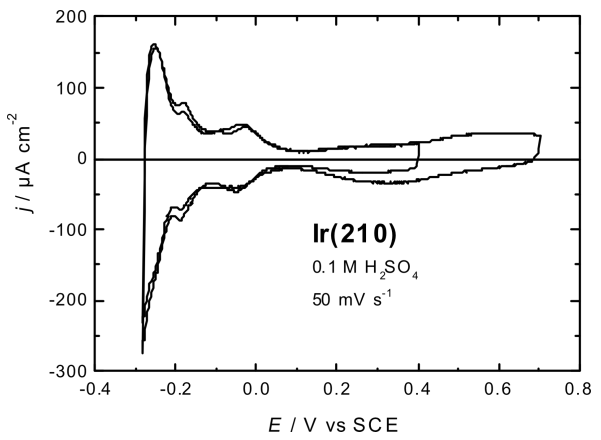

Figure 1: Cyclic voltammograms of Ir(210), which was annealed and cooled in a N_2 + CO mixture, after anodic stripping of the CO adlayer in 0.1 M H_2SO_4. Scan rate: 50 mV·s^{-1}.

The total charge density in the hydrogen adsorption region is around 300 μC·cm^{-2}, as reported earlier [20]. Surface oxidation, including the adsorption of O/OH, starts at potentials more positive than 0.1 V. A rather broad peak for reduction of the oxidized surface is centred at 0.3 V. Stable voltammograms with reproducible hydrogen adsorption peaks were obtained by keeping the positive potential limit below 0.4 V. Annealing and cooling in the presence of CO leads to very similar current–potential curves as for H_2-cooled Ir(210) [20], although the CO adlayer has to be removed in a single scan into the positive potential region.

In situ STM of Ir(210) surfaces

The effect of the cooling atmosphere after annealing of noble metal single crystal electrodes has been investigated earlier for Pt(111) [24], Pt(100) and Pt(110) surfaces [6]. It was reported that the use of CO as a cooling gas for Pt(110) leads to the formation of an unreconstructed (1×1) surface [6,25], while cooling in N_2 preserves the reconstructed Pt(110) surface [6]. The influence of the reducing cooling gases (H_2 or CO) on the surface structure of Ir(210) in 0.1 M H_2SO_4 was studied by in situ STM measurements.

Figure 2a and Figure 3a display topographic images of Ir(210) in 0.1 M H_2SO_4 after preparation by inductive heating and

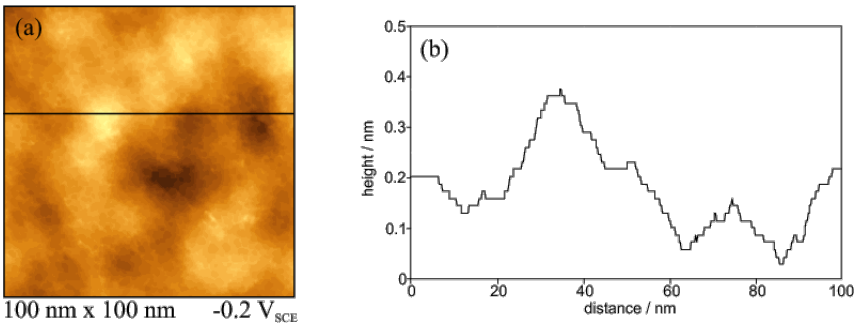

Figure 2: (a) in situ STM image of CO-cooled Ir(210) in 0.1 M H_2SO_4 at −0.2 V. (b) Height profile along the line shown in (a).

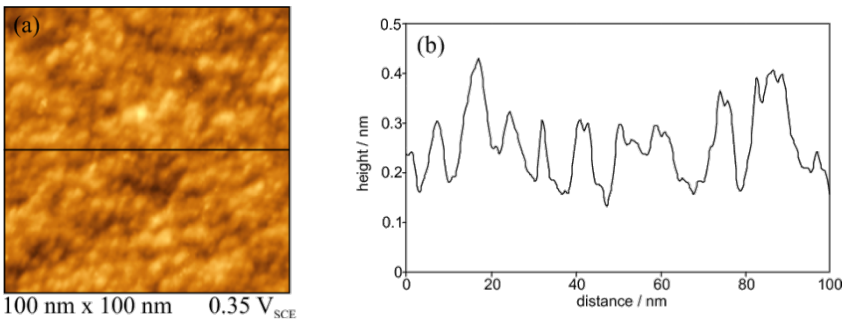

Figure 3: in situ STM image of H_2-cooled Ir(210) in 0.1 M H_2SO_4 at 0.35 V. (b) Height profile along the line shown in (a).

cooling down in the presence of CO and H_2, respectively. Bright spots in these images represent higher areas, while dark ones represent lower surface regions of Ir(210). In contrast to low-index Ir surfaces such as Ir(111) [26], the STM images in Figure 2a and Figure 3a do not show wide terraces separated by monoatomic high steps. Rather small flat surface regions appear for CO-cooled Ir(210), as seen in the height profile shown in Figure 2b.

The height profile shown in Figure 3b indicates that the density of surface defects is higher for the H_2-cooled Ir(210) surface than that for the CO-cooled surface (Figure 2b). This structural difference is not obvious from the current–potential curves in Figure 1, which are basically identical with those for Ir(210) prepared by H_2–cooling [20]. However, it will be shown below that the cooling gas (CO or H_2) has a strong impact on the electrocatalytic activity of Ir(210) towards CO adlayer oxidation (see below in Figure 8). The high density of atomic steps and kinks of H_2-cooled Ir(210) is very similar to that of other high index planes, as in the case of Pt(210) [9]. Since LEED patterns obtained for a clean Ir(210) surface under UHV show a (1×1) structure [21], we assume that unreconstructed Ir(210) surfaces are also obtained after annealing and cooling in CO or H_2.

Potential cycling effects on Ir(210) surface

Previous theoretical studies predicted an electrochemical facet formation, i.e., potential-induced, on Ir(210) surface upon adsorption of oxygen [19]. First experiments revealed, however, that a simple polarization of Ir(210) in 0.1 M H_2SO_4 at potentials more positive than 0.1 V, i.e., in the region of oxygen adsorption/surface oxidation, did not lead to the expected structural changes.

The formation of facets by potential cycling has been extensively studied with platinum [27-32], rhodium [33] and gold surfaces [34-36]. Accordingly, the Ir(210) single crystal electrode was subjected to potential cycling at scan rates between 0.05 and 2 $V \cdot s^{-1}$ in 0.1 M H_2SO_4 in the potential region between −0.28 to 0.7 V for different periods of time up to 4 h. In the following, we present results obtained with a scan rate of 1 $V \cdot s^{-1}$, which show the most obvious effects. As representative examples, Figure 4 shows the effect of potential cycling for 1 min and 60 min on the voltammograms of Ir(210) in 0.1 M H_2SO_4.

Cycling the Ir(210) electrode for 1 min caused only slight changes in the voltammogram, as can be seen by comparing Figure 4 with Figure 1. However, the voltammogram of the Ir(210) electrode subjected to 60 min of potential cycling showed an increase of the peak current intensities at −0.18 and −0.04 V concurrently with a decrease of the peak current at

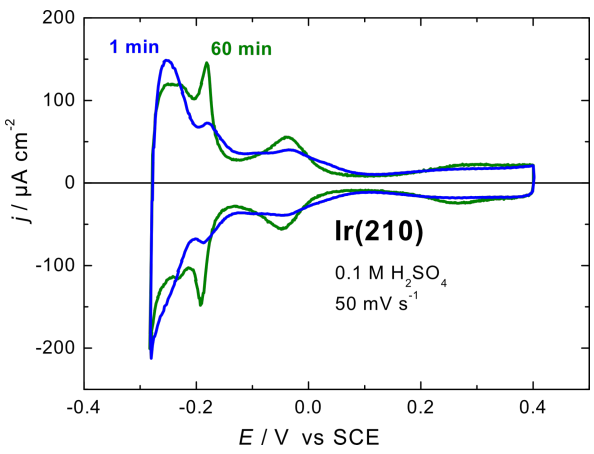

Figure 4: Current–potential curves for Ir(210) in 0.1 M H_2SO_4 after cycling at 1 $V \cdot s^{-1}$ between −0.28 and 0.7 V. Scan rate: 50 $mV \cdot s^{-1}$.

−0.25 V. The noticeable increase in the former two peaks (at −0.18 and −0.04 V) indicates the possible formation of (311) facets [20], because the peak at −0.18 V is characteristic of Ir(311) [5].

Figure 5 displays quantitative changes in hydrogen adsorption peak heights as a function of the cycling time. This graph demonstrates formal kinetics of facet formation or surface restructuring of Ir(210) in 0.1 M H_2SO_4. The increase of the peak current at −0.18 V is a good indication for (311) facet formation, as mentioned above. The charge densities in the hydrogen adsorption region of Ir(210) electrode after 1 min of potential cycling are practically the same as for the freshly-prepared Ir(210) electrode (300 $\mu C \cdot cm^{-2}$), although both surfaces before and after cycling have different structures as depicted by the in situ STM images (see below).

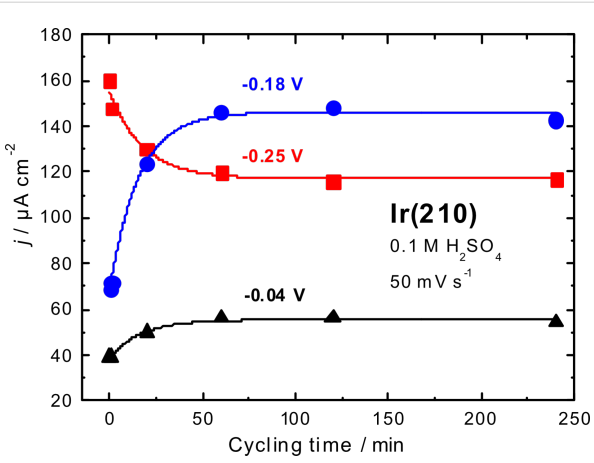

Figure 5: Current densities for hydrogen adsorption peaks of Ir(210) in 0.1 M H_2SO_4 as a function of the potential cyclic time. The curves show non-linear fits according to first order laws.

A significantly higher charge density (345 μC·cm^{-2}) was determined for the hydrogen adsorption region of the Ir(210) crystal after 60 min of potential cycling. This is a clear indication for changes in the morphology and roughness of the Ir(210) surface. Only very slight changes were seen in the voltammograms of Ir(210) for cycling times longer than 60 min (Figure 5). Nevertheless, there are still detectable changes in the surface structure of Ir(210) after longer cycling times (see below in Figure 6), which escape from the voltammetric analysis.

As mentioned above, potentiostatic polarization of a freshly-prepared Ir(210) electrode for example at 0.7 V did not lead to changes in the hydrogen adsorption peaks. While a sufficiently high coverage of oxygen species should be obtained under these conditions, potential cycling provokes the desired movement of surface atoms [36]. In addition, though faceting is thermodynamically driven, it is hindered (and limited) by the kinetic barriers involved in the atom rearrangement at the surface [37]. Thus, not only a critical adsorbate (here oxygen) coverage is required but also appropriate activation, allowing the system to overcome the kinetic barriers in the process of facet formation [23]. The voltammetric peak at −0.18 V for Ir(210) after potential cycles, which indicates (311) facets, is not as sharp as that of thermally-induced faceted Ir(210) [20]. While thermal activation is effective, electrochemical activation by potential cycling at room temperature seems to work, however less pronounced or less well-defined. Electrochemical treatment including potential cycling of Ir(210) in 0.1 M HCl did not lead to comparable changes, probably because adsorbed chloride hinders oxygen adsorption.

In situ STM of Ir(210) after repetitive fast potential cycles

The change in surface topography of Ir(210) by repetitive oxidation–reduction potential cycles has been investigated by using in situ STM. Figure 6 shows the corresponding images of Ir(210) in 0.1 M H_2SO_4 after cycling for 1 min, 20 min, 60 min

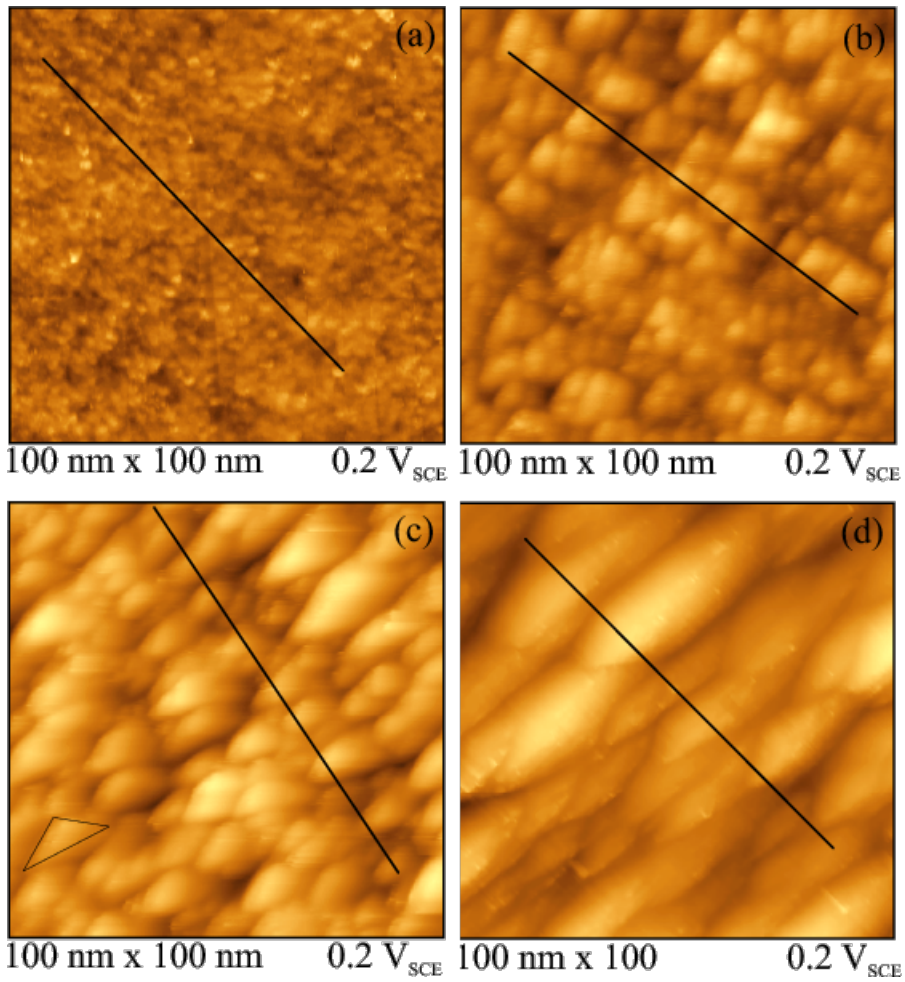

Figure 6: In situ STM images (100 × 100 nm^2) of CO-cooled Ir(210) surface in 0.1 M H_2SO_4 after cycling between −0.28 and 0.7 V at 1 V·s^{-1} for (a) 1, (b) 20, (c) 60 and (d) 240 min.

and 240 min. The series of STM images indicates that the surface morphology is gradually changing with cycling time. Already after 1 min of potential cycling (Figure 6a), the surface becomes rougher compared to the untreated surface (Figure 2). Cycling for 20 min leads to the formation of small triangular structures (Figure 6b), which resemble the well-defined surface structure of thermally faceted Ir(210) [20].

Ermanoski et al. showed that for the thermally-faceted Ir(210) surface the angles between the pyramidal faces and the (210) substrate obtained by LEED are in good agreement with the theoretical tilt angles of 19.3° and 18.4° for (311) and (110) facets, respectively [22]. While these tilt angles of the facets were verified experimentally both under UHV and electrochemical conditions [20,21], the presence of a superstructure on Ir(110) facets consisting of a stepped double-missing-row reconstruction also leads to a smaller tilt angle of only around 7° [21,37]. Figure 7 presents the cross section profiles for the potential-induced faceted Ir(210) surface along the solid lines marked in Figure 6. The lines scans indicate that the Ir(210) surface is completely facetted electrochemically. Since the tilt angles range from 6 to 28° and show clear variations in a single STM image, the electrochemically facetted Ir(210) surfaces are not as well-defined as the faceted surfaces obtained after thermal activation.

Increasing the cycling time to 60 min resulted in the formation of larger triangular structures (see black triangle in Figure 6c), which cover the whole Ir(210) surface (Figure 6c). These triangular structures are very similar to the thermally-induced faceted Ir(210) surface [19,20] and to samples prepared under UHV conditions [22]. For the case of 240 min potential cycling, anisotropic groove structures are formed that seem to be even more stable than the triangular structure under the chosen experimental conditions (Figure 6d). However, the two CVs of Ir(210) in sulfuric acid after 60 and 240 min of potential cycling are practically indistinguishable. Still, we compared our cyclic voltammograms (e.g., those in Figure 4) obtained by potential cycling to those of extended vicinal Ir single crystal surfaces [5]. There are striking similarities with Ir(320), Ir(310) and Ir(410), for example.

CO adlayer oxidation on Ir(210)

Studies of CO oxidation on single crystal electrodes are of practical as well as fundamental interest. From the electrocatalytic point of view, CO is the most prominent intermediate species responsible for the poisoning of metallic catalysts [38]. Understanding the mechanism of the CO oxidation on single crystal electrodes may lead to a deeper insight into the relation between surface structure and electrocatalytic activity. Therefore, we chose carbon monoxide as a structure-sensitive probe of the electrocatalytic activity of restructured Ir(210), subjected to potential cycles.

Figure 8 shows linear sweep voltammograms for CO adlayer oxidation at Ir(210) in 0.1 M H_2SO_4 before and after the potential cycling treatment. The peak potential for CO adlayer oxidation on the CO-cooled Ir(210) electrode lies at 0.46 V (Figure 8), whereas there are two distinct oxidation peaks at 0.25 V and 0.4 V for the H_2-cooled Ir(210) electrode (Figure 8).

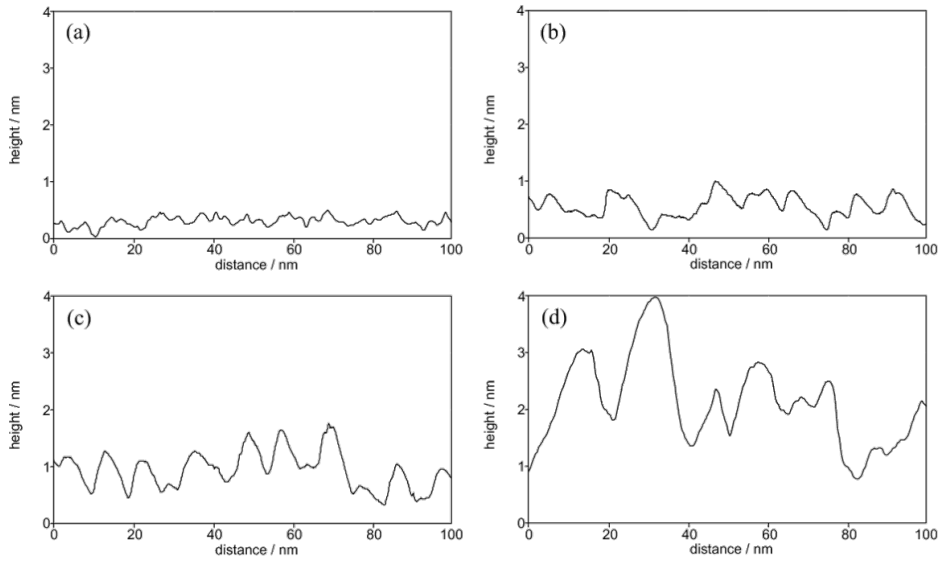

Figure 7: Height profiles of the CO-cooled Ir(210) surface in 0.1 M H_2SO_4 after cycling between −0.28 and 0.7 V at 1 $V \cdot s^{-1}$ for (a) 1, (b) 20, (c) 60 and (d) 240 min.

It was supposed that diffusion of reaction partners may be involved in the oxidation reaction mechanism [19]. So far, we were not able to identify the type of surface defects, which act as active centers for CO oxidation on H_2-cooled Ir(210). However, these sites are absent at the CO-cooled Ir(210) surface, which explains the higher overpotential. After applying oxidation–reduction cycles, the peak potential for the CO adlayer oxidation is shifted to lower values compared to the CO-cooled Ir(210) (Figure 8). The peak potentials for CO adlayer oxidation are 0.45 V, 0.43 V, 0.39 and 0.4 V after potential cycling for 1, 20, 60 and 240 min, respectively. Thus, the restructured, electrochemically facetted Ir(210) surfaces are clearly more active than the planar Ir(210) electrode obtained by inductive heating and subsequent cooling in CO atmosphere. Several explanations might be suggested to account for the observed behaviour. Among the important parameters is the change in binding energy of adsorbed CO from 2.46 eV on Ir(210) to 2.19 eV on Ir(311) [39]. This should be directly reflected by the relatively facile oxidation of CO at the facetted surface enriched with (311) faces compared to the untreated planar Ir(210) electrode. Another reason attributed to the enhancement is the structural change produced by the oxidation–reduction cycles, resulting in an enrichment of oxygen-containing species on the surface at lower overpotentials, which is essentially required for CO oxidation. The structural changes are very clear from the in situ STM image of Ir(210) surface before and after potential cycling, see Figure 2 and Figure 6, respectively.

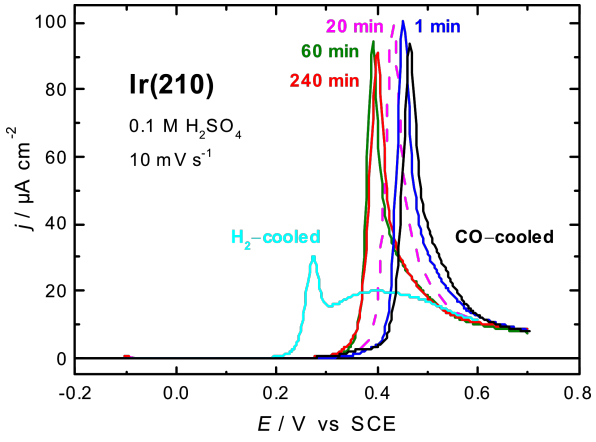

Figure 8: Current–potential curves for CO adlayer oxidation on Ir(210) in 0.1 M H_2SO_4 before and after changing the surface morphology by potential cycling. Scan rate: 10 mV·s^{-1}.

It should be mentioned that the Ir(210) electrode, annealed and cooled down in hydrogen atmosphere, is far more active than the restructured Ir(210) surfaces presented here and is also more active than the thermally-induced faceted Ir(210) surfaces [19]. However, so far we could not identify the reactive sites, which enhance CO adlayer oxidation significantly. It is also seen in Figure 3, that the density of defects on the H_2-cooled surface is higher than on the CO-cooled one. This is also in agreement with the results obtained under an UHV system in which a planar Ir(210) surface was found to be more active than faceted Ir(210) for CO oxidation to form CO_2 [40]. CO adlayer oxidation turns out to be much more structure-sensitive than the electrochemical processes taking place in dilute sulfuric acid, for example hydrogen adsorption. We would like to mention that potential cycling of the H_2-cooled Ir(210) lead to similar electrochemical surface faceting as for the CO-cooled Ir(210) surface.

Conclusion

In the present study, we have explored electrochemical facet formation on Ir(210). Potential cycling of Ir(210) single crystal electrode in 0.1 M H_2SO_4induces surface restructuring. Different structure types are forming as a function of cycling time. Triangular structures are obtained after 20 min and/or 60 min of potential cycling between −0.28 and 0.7 V, while an anisotropic groove structure is formed after 240 min. The restructured Ir(210) surfaces are more active towards the CO adlayer oxidation than planar Ir(210), which has been prepared by inductive heating and cooling in CO atmosphere. Annealing of Ir(210) and cooling in the presence of hydrogen leads to the most active surface for CO adlayer oxidation in this study. The enhanced electrocatalytic activity is probably related to a lower CO binding energy, a higher surface roughness and a larger amount of defect sites on the faceted Ir(210) surface. The results verify the theoretical prediction that faceting of Ir(210) is possible under electrochemical conditions.

Acknowledgements

We gratefully acknowledge the financial support of the Deutsche Forschungsgemeinschaft (DFG) by FOR-1376, JA1072/6-1 and KO576/25-1 (”Elektrochemische Untersuchungen zur potential-induzierten Oberflächenfacettierung“).

References

1. Arvia, A. J.; Salvarezza, R. C.; Triaca, W. E. *J. New Mater. Electrochem. Syst.* **2004,** *7,* 133–143.
2. Marković, N. M.; Ross, P. N., Jr. *Surf. Sci. Rep.* **2002,** *45,* 117–229. doi:10.1016/S0167-5729(01)00022-X
3. Koper, M. T. M. *Nanoscale* **2011,** *3,* 2054–2073. doi:10.1039/c0nr00857e
4. Hara, M.; Linke, U.; Wandlowski, T. *Electrochim. Acta* **2007,** *52,* 5733–5748. doi:10.1016/j.electacta.2006.11.048
5. Furuya, N.; Koide, S. *Surf. Sci.* **1990,** *226,* 221–225. doi:10.1016/0039-6028(90)90487-S
6. Kibler, L. A.; Cuesta, A.; Kleinert, M.; Kolb, D. M. *J. Electroanal. Chem.* **2000,** *484,* 73–82. doi:10.1016/S0022-0728(00)00065-6

7. Kibler, L. A.; El-Aziz, A. M.; Hoyer, R.; Kolb, D. M. *Angew. Chem., Int. Ed.* **2005,** *44,* 2080–2084. doi:10.1002/anie.200462127
8. Calle-Vallejo, F.; Koper, M. T. M.; Bandarenka, A. S. *Chem. Soc. Rev.* **2013,** *42,* 5210–5230. doi:10.1039/c3cs60026b
9. Tian, N.; Zhou, Z.-Y.; Sun, S.-G. *J. Phys. Chem. C* **2008,** *112,* 19801–19817. doi:10.1021/jp804051e
10. Kolb, D. M. *Prog. Surf. Sci.* **1996,** *51,* 109–173. doi:10.1016/0079-6816(96)00002-0
11. Kolb, D. M. *Electrochim. Acta* **2000,** *45,* 2387–2402. doi:10.1016/S0013-4686(00)00328-5
12. Okube, M.; Petrykin, V.; Mueller, J. M.; Fantauzzi, D.; Krtil, P.; Jacob, T. *ChemElectroChem* **2014,** *1,* 207–212. doi:10.1002/celc.201300112
13. Dakkouri, A. S. *Solid State Ionics* **1997,** *94,* 99–114. doi:10.1016/S0167-2738(96)00499-7
14. Kibler, L. A.; Kleinert, M.; Kolb, D. M. *Surf. Sci.* **2000,** *461,* 155–167. doi:10.1016/S0039-6028(00)00569-0
15. Arvia, A. J.; Canullo, J. C.; Custidiano, E.; Perdriel, C. L.; Triaca, W. E. *Electrochim. Acta* **1986,** *31,* 1359–1368. doi:10.1016/0013-4686(86)87046-3
16. Komanicky, V.; Menzel, A.; Chang, K.-C.; You, H. *J. Phys. Chem. B* **2005,** *109,* 23543–23549. doi:10.1021/jp0541516
17. Pajkossy, T.; Kibler, L. A.; Kolb, D. M. *J. Electroanal. Chem.* **2005,** *582,* 69–75. doi:10.1016/j.jelechem.2005.03.019
18. Pajkossy, T.; Kibler, L. A.; Kolb, D. M. *J. Electroanal. Chem.* **2007,** *600,* 113–118. doi:10.1016/j.jelechem.2006.04.016
19. Kaghazchi, P.; Simeone, F. C.; Soliman, K. A.; Kibler, L. A.; Jacob, T. *Faraday Discuss.* **2009,** *140,* 69–80. doi:10.1039/B802919A
20. Soliman, K. A.; Simeone, F. A.; Kibler, L. A. J. *Electrochem. Commun.* **2009,** *11,* 31–33. doi:10.1016/j.elecom.2008.10.017
21. Ermanoski, I.; Pelhos, K.; Chen, W.; Quinton, J. S.; Madey, T. E. *Surf. Sci.* **2004,** *549,* 1–23. doi:10.1016/j.susc.2003.10.052
22. Ermanoski, I.; Kim, C.; Kelty, S. P.; Madey, T. E. *Surf. Sci.* **2005,** *596,* 89–97. doi:10.1016/j.susc.2005.08.024
23. Kaghazchi, P.; Jacob, T.; Ermanoski, I.; Chen, W.; Madey, T. E. *ACS Nano* **2008,** *2,* 1280–1288. doi:10.1021/nn800210v
24. Lebedeva, N. P.; Koper, M. T. M.; Feliu, J. M.; Van Santen, R. A. *Electrochem. Commun.* **2000,** *2,* 487–490. doi:10.1016/S1388-2481(00)00062-X
25. Wakisaka, M.; Asizawa, S.; Yoneyama, T.; Uchida, H.; Watanabe, M. *Langmuir* **2010,** *26,* 9191–9194. doi:10.1021/la101330x
26. Wan, L.-J.; Hara, M.; Inukai, J.; Itaya, K. *J. Phys. Chem. B* **1999,** *103,* 6978–6983. doi:10.1021/jp991112j
27. Biegler, T. *J. Electrochem. Soc.* **1967,** *114,* 1261–1262. doi:10.1149/1.2426465
28. Kinoshita, K.; Lundquist, J. T.; Stonehart, P. *J. Electroanal. Chem.* **1973,** *48,* 157–166. doi:10.1016/0368-1874(73)85091-9
29. Ross, P. N., Jr. *J. Electrochem. Soc.* **1979,** *126,* 67–77. doi:10.1149/1.2128990
30. Canullo, J. C.; Triaca, W. E.; Arvía, A. J. *J. Electroanal. Chem.* **1984,** *175,* 337–340. doi:10.1016/S0022-0728(84)80370-8
31. Cerviño, R. M.; Triaca, W. E.; Arvia, A. J. *J. Electroanal. Chem.* **1985,** *182,* 51–60. doi:10.1016/0368-1874(85)85439-3
32. Galindo, M. C.; Perdriel, C. L.; Martins, M. E.; Arvia, A. J. *Langmuir* **1989,** *5,* 165–170. doi:10.1021/la00085a031
33. Méndez, E.; Castro Luna, A. M.; Cerdá, M. F.; Mombrú, A. W.; Zinola, C. F.; Martins, M. E. *J. Solid State Electrochem.* **2003,** *7,* 208–216. doi:10.1007/s10008-002-0299-y
34. Perdriel, C. L.; Arvia, A. J.; Ipohorski, M. *J. Electroanal. Chem. Interfacial Electrochem.* **1986,** *215,* 317–329. doi:10.1016/0022-0728(86)87025-5
35. Rodríguez Nieto, F. J.; Andreasen, G.; Martins, M. E.; Castez, F.; Salvarezza, R. C.; Arvia, A. J. *J. Phys. Chem. B* **2003,** *107,* 11452–11466. doi:10.1021/jp0353542
36. Köntje, C.; Kolb, D. M.; Jerkiewicz, G. *Langmuir* **2013,** *29,* 10272–10278. doi:10.1021/la4018757
37. Kaghazchi, P.; Fantauzzi, D.; Anton, J.; Jacob, T. *Phys. Chem. Chem. Phys.* **2010,** *12,* 8669–8684. doi:10.1039/C000766H
38. Koper, M. T. M.; Lai, S. C. S.; Herrero, E. Mechanisms of the Oxidation of Carbon Monoxide and Small Organic Molecules at Metal Electrodes. In *Fuel cell catalysis;* Koper, M. T. M., Ed.; John Wiley & Sons: New York, NY, USA, 2009; pp 159–208.
39. Chen, W.; Bartynski, R. A.; Kaghazchi, P.; Jacob, T. *J. Chem. Phys.* **2012,** *136,* 224701-1–224701-10. doi:10.1063/1.4723811
40. Chen, W.; Ermanoski, I.; Jacob, T.; Madey, T. E. *Langmuir* **2006,** *22,* 3166–3173. doi:10.1021/la053183h

License and Terms